Multiple star formation:

Chemistry, physics and coevality

ISBN: 978-94-028-0786-8

Multiple star formation:

Chemistry, physics and coevality

Proefschrift

ter verkrijging van
de graad van Doctor aan de Universiteit Leiden,
op gezag van Rector Magnificus prof.mr. C.J.J.M. Stolker,
volgens besluit van het College voor Promoties
te verdedigen op woensdag 1 november 2017
klokke 15:00 uur
door

Nadia Mariel Murillo Mejías
(穆美蓉)

geboren te San José, Costa Rica
in 1988

Promotiecommissie

Promotores:	Prof. dr. E. F. van Dishoeck	
	Prof. dr. S.-P. Lai	National Tsing Hua University Academia Sinica, Taiwan
Overige leden:	Prof. dr. H.V.J. Linnartz	
	Prof. dr. H.J.A. Rottgering	
	Prof. dr. M.R. Hogerheijde	
	Prof. dr. S. S. R. Offner	University of Massachusetts, USA
	Dr. J. Jørgensen	University of Copenhagen, Denmark
	Dr. N. Sakai	Riken Insitute, Japan

To those who look up at the sky
and wonder why the stars twinkle

Front cover: Illustration by author with the image “Young stars in their baby blanket of dust: ρ Ophiuchi" (NASA/JPL-Caltech/Harvard-Smithsonian) in the background

Contents

Chapter 1

Introduction

1.1 Observing multiplicity in stars

Multiple stars have been studied for millennia, with the earliest documented observation being from the Egyptians, who unknowingly recorded the variability and calculated the period of Algol between 1244 to 1163 B.C. (Jetsu & Porceddu 2015). Double stars were often of interest to astronomers who observed them with the naked eye. Although some of the double stars were pairs of chance alignment, another fraction were visual binaries. The development of the telescope provided a window to further the study of multiple stars, with many close pairs being discovered and the finding that some variable stars, such as Algol, were in fact multiple stars. Calculation of the probability of random alignment along the line of sight suggested that many of these double stars were actuall physically close in proximity (Michell 1767). With periodic observations of double stars spanning 25 years, Herschel (1803) proved that many of the known double stars were in truth physically bound systems, providing rough estimates of orbital periods. Surprisingly, the first eclipsing binary to be observed was also reported by Herschel (1803).

As instrumentation progressed, so did the study of multiple stars and their characteristics, proving to be important laboratories for the measurement of stellar properties. Multiplicity of stars has been found across the entire mass range, increasing proportionally with mass (Duchêne & Kraus 2013). These systems produce several interesting phenomena in evolved stars, for example dust and gas shells of evolved stars (e.g. Maercker et al. 2012), type Ia supernovae, and one of the mechanisms to form binary black holes (Breivik et al. 2016). Early theories on the formation of multiple systems suggested gravitational capture as a formation mechanism. However, this method proved challenging since dense clusters of stars are needed, as well as a third body for conservation of energy (Tohline 2002). Observations into the depths of molecular clouds in wavelengths other than optical provide crucial information as to how multiple stellar systems form. Infra-red and radio surveys of star forming regions in recent decades have detected multiplicity from pre-main sequence stars down to the embedded stage of star formation (e.g. Looney et al. 2000; Chen et al. 2009; Tobin et al. 2016b). Simply put, multiple stellar systems are born.

Many pieces to the puzzle of multiple star formation are still missing. While fragmentation is proposed as the main formation mechanism (Tohline 2002), when and

how it occurs is still not clear, as are the factors that hinder or favour fragmentation. These aspects are important since they influence the consequent evolution and structure of the system. The physics and chemistry of multiple stellar systems from birth to main sequence are also aspects that need to be studied to understand how these systems evolve. Disks play a key role in the evolution of protostars by accreting matter onto the protostar and can fragment to form close multiple protostellar systems. When disks form is thus a question of interest to star formation in general. The embedded phase of star formation provides the ideal place to start the study of multiple systems, since the conditions of formation are mostly intact and the structure that will dictate the evolution of the system is taking shape. This thesis presents work addressing the above questions, using submillimeter observations and infrared archival data coupled with chemical and physical models.

1.2 Low-mass star and disk formation

Stellar nurseries for low-mass stars are relatively nearby, at distances of less than 500 pc from the Sun, allowing high-resolution observations that can disentangle the structure and reveal the secrets of star formation. Low-mass stars ($M_{\rm star}$ <2 $M_\odot$) are formed in dense cloud cores of dust and gas with number densities in the range of 10^4 to 10^5 cm^{-3} and diameters of about 0.1 pc. These cloud cores are typically located along the density peaks in filamentary structures (André et al. 2010; Kennicutt & Evans 2012) within cold molecular clouds (10 – 20 K). Recent studies find that clustered star formation is located at the site of bundles of filaments, which funnel material into the forming cluster. Stars can also form in isolation in so-called Bok Globules, compact clumps of dust and gas with masses less than 100 $M_\odot$. The ρ Ophiuchus molecular cloud ($d \sim 120\pm$ 4.5; Loinard et al. 2008) is a good example of clustered star formation, while the Perseus molecular cloud ($d \sim 235 \pm 18$ pc; Hirota et al. 2008, 2011) exhibits a range of environments with NGC1333 being clustered while B1, L1448 and L1455 are more sparse with some relatively isolated cloud cores (34 and 6 YSO pc^{-2} for clustered and non-clustered, respectively; Plunkett et al. 2013).

Low-mass star formation begins with a rotating cloud core of dust and gas, with its density usually peaking in the center (Shu et al. 1987) and characterized by being very cold and having high deuteration due to freeze-out of molecules such as CO (Crapsi et al. 2005). Accumulation of material onto the starless cloud core eventually causes gravity to be the dominant force. Once the Jeans criteria are satisfied, the cloud core begins gravitational collapse (Figure 1). The first collapse produces a stable core termed the First Hydrostatic Core (FHSC) (Larson 1969), a short lived phase (100 – 1000 yr, Masunaga & Inutsuka 2000; Tomida et al. 2010) with a low mass central object (0.01–0.1 $M_\odot$, Saigo et al. 2008; Tomida et al. 2010) that is rather compact and dim (<0.1 $L_\odot$ and 5–20 AU radius, Masunaga et al. 1998; Saigo et al. 2008) but capable of driving an outflow (Price et al. 2012). Several possible candidates of this object have been found (see Dunham et al. 2011 for comparison of several candidates), but none confirmed given the ambiguity to identify them even from their spectral energy distributions (Commerçon et al. 2012).

As the temperature in the FHSC rises due to compression, H_2 begins to dissociate and triggers a second collapse, which eventually forms the so-called Second Hydrostatic Core (Larson 1969), more commonly known as an embedded protostar or a Class 0 object (André et al. 1993). The deeply embedded object obtains most of its energy from

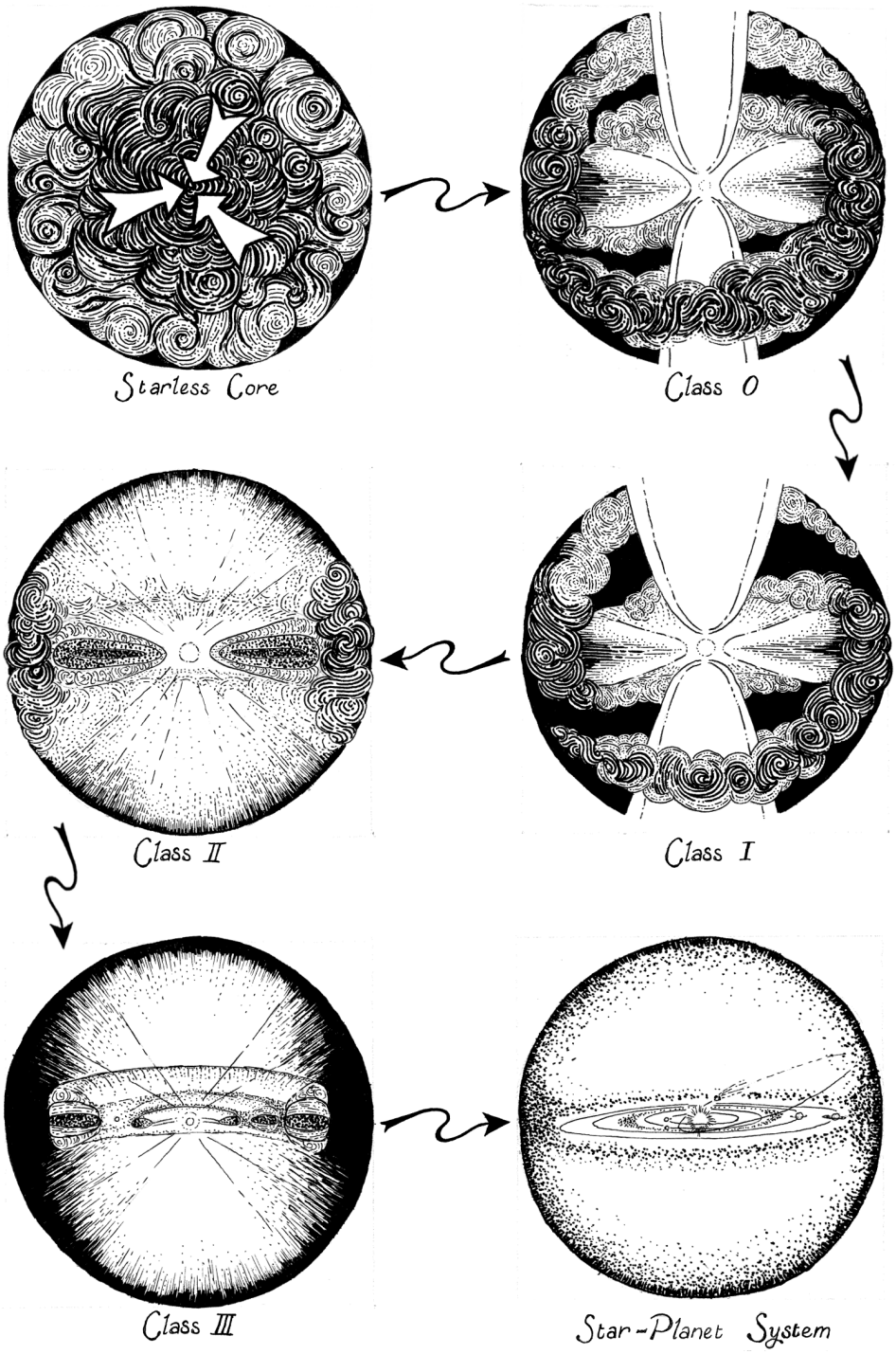

Figure 1: Single star formation and evolutionary path from collapsing cloud core to protostar, to young stellar object and finally to a star-planet system (Drawing by author).

Table 1: Phases of star formation

	Class			Stage	
	$T_{\rm bol}$ K	$\alpha_{\rm IR}$	$\frac{L_{\rm submm}}{L_{\rm bol}}$	Mass relation	Age yr
0	$T \leq 70$	...	> 0.005	$M_{\rm env} >> M_*$	10^5
I	$70 < T \leq 650$	$\alpha > 0$	< 0.005	$M_{\rm env} < M_*$	10^5 – 10^6
II	$650 < T \leq 2800$	$0 > \alpha >$ -1.5	< 0.005	$M_{\rm env} < 0.1$ M$_\odot$	10^6 – 10^7
III	...	-1.5 $> \alpha$	...	No accretion	

accretion. Highly collimated jets are driven by sources in this phase. The molecular outflow and its cavity are thought to be produced by the swept up and heated gas in the wake of the jet. The cavity carves out parts of the envelope, exposing material to radiation from the forming star and promoting the build up of a chemically rich and complex envelope. These jets and outflows are thought to be product of the accretion process and magnetic fields (Frank et al. 2014).

Observations found that in the late phases of embedded star formation, rotationally supported disks were commonplace (e.g. Hogerheijde 2001; Jørgensen et al. 2009; Yen et al. 2013), while flattened continuum structures, i.e., disk-like structures or pseudo-disks, were found in the early phases of embedded star formation (e.g. Jørgensen et al. 2009; Enoch et al. 2011). This leads to the expectation that rotationally supported disks formed towards the end of the embedded star formation phase. Models suggested that only small disks formed at early times (Terebey et al. 1984) or were hindered by magnetic breaking when the magnetic fields and core rotation axis were aligned (Mellon & Li 2008; Krumholz et al. 2013). However, recent observations found a large, rotationally-supported disk towards deeply embedded protostars (Tobin et al. 2012b; Yen et al. 2017, Chapter 1.6 of this thesis), hinting at the possibility that disks form in the early embedded phases of star formation.

As material is accreted onto the protostar and the outflow progressively widens the cavity (Arce & Sargent 2006), the envelope mass is gradually reduced and the overall temperature rises. This increases the chemical complexity throughout the envelope, but at the same time pushes the envelope material onto the disk plane. Eventually the disk, now termed protoplanetary disk, is all that remains around the protostar as the envelope has been fully dispersed and the outflow is no longer observable. The protostar begins hydrogen burning in this phase, reaching the zero age main sequence line, and becoming a star. If the protoplanetary disk has enough material and appropriate conditions, planets may begin to form through the coagulation of dust and attracting the gas that remains in the disk. Finally as the disk is dispersed, the remainder is a young main sequence low-mass star orbited by a system of newly formed planets.

The different phases of star formation are classified into *Stages* or *Classes*. Table 1 lists the criteria for classification into Stages and Classes. Stages are based on the ages of the protostar and the mass relation between the star M_* and envelope $M_{\rm env}$. However the masses of these structures are not always directly measurable from observations. On the other hand, Classes are determined by observational parameters, namely the spectral energy distribution (SED) and the parameters derived from it. Such parameters are the bolometric temperature $T_{\rm bol}$, infrared spectral index $\alpha_{\rm IR}$ be-

tween 2 to 20 μm, and the ratio of submillimeter luminosity, which is defined as the luminosity for $\lambda \geq 350$ μm, to bolometric luminosity $L_{\rm submm}/L_{\rm bol}$. The difficulty of the classification of star formation phases using Classes is that the SED, and thus parameters derived from it, is sensitive to the geometry of the protostellar source along the line of sight (Crapsi et al. 2008). Additionally, not all parameters can be used for all phases of star formation. Regardless of the disadvantages, Classes are widely used in literature. While both methods of classification describe similar phases of star formation, they are not uniquely correlated. For example, the luminosity ratio $L_{\rm submm}/L_{\rm bol}$ is meant to reflect the envelope to central protostar mass ratio $M_{\rm env}/M_*$ (André et al. 1993; Froebrich 2005), but a Class II object with a significant disk can cause the luminosity ratio to be large despite the protostar having little envelope mass. The boundary conditions for Stages and Classes are listed in Table 1. Enoch et al. (2009b) further defined sub-classes based on $T_{\rm bol}$ from averaged SEDs observed from protostars in Perseus, Ophiuchus and Serpens.

The current picture described in this section works well to explain single low-mass star formation. However, multiple stars are the more common outcome of star formation. It is then necessary to study how multiple stars affect the process of star formation, and adjust our picture accordingly.

1.3 Multiple low-mass star formation

1.3.1 Definitions

Aiming to have consistency in the research presented in this thesis, the definitions of the key terms used throughout the description of multiple low-mass star formation are given here. Some of the terms are illustrated in Figure 2.

Multiplicity or ***multiple*** is used to refer to a system consisting of two or more components or sources, whether protostellar or stellar. The terms binary, triple and higher-order multiples are thus implicitly merged into this term. The ***multiplicity fraction*** thus means the number of systems in a region that are composed of two or more components in comparison with all the systems in the same region. This can be expressed as

$$MF = \frac{B + T + Q + ...}{S + B + T + Q + ...} \tag{1.1}$$

while the ***companion star fraction*** expresses the average number of companions per system and is given by

$$CSF = \frac{B + 2T + 3Q + ...}{S + B + T + Q + ...} \tag{1.2}$$

For both fractions, S, B, T and Q stand for singles, binaries, triples and quadruples (Reipurth et al. 2014).

A ***protostellar system*** is defined as a protostar and its surrounding immediate environment composed of a disk, envelope and bipolar outflow, and can be either single or multiple. A ***single protostellar system*** or ***single protostar***, as the name suggests, is a protostellar system with a single, central, heating source. On the other hand, a ***multiple protostellar system*** or ***multiple protostar*** here refers to two or more gravitationally bound protostellar sources composing one system. Multiple systems share a common envelope, and in some cases, a common disk, however each

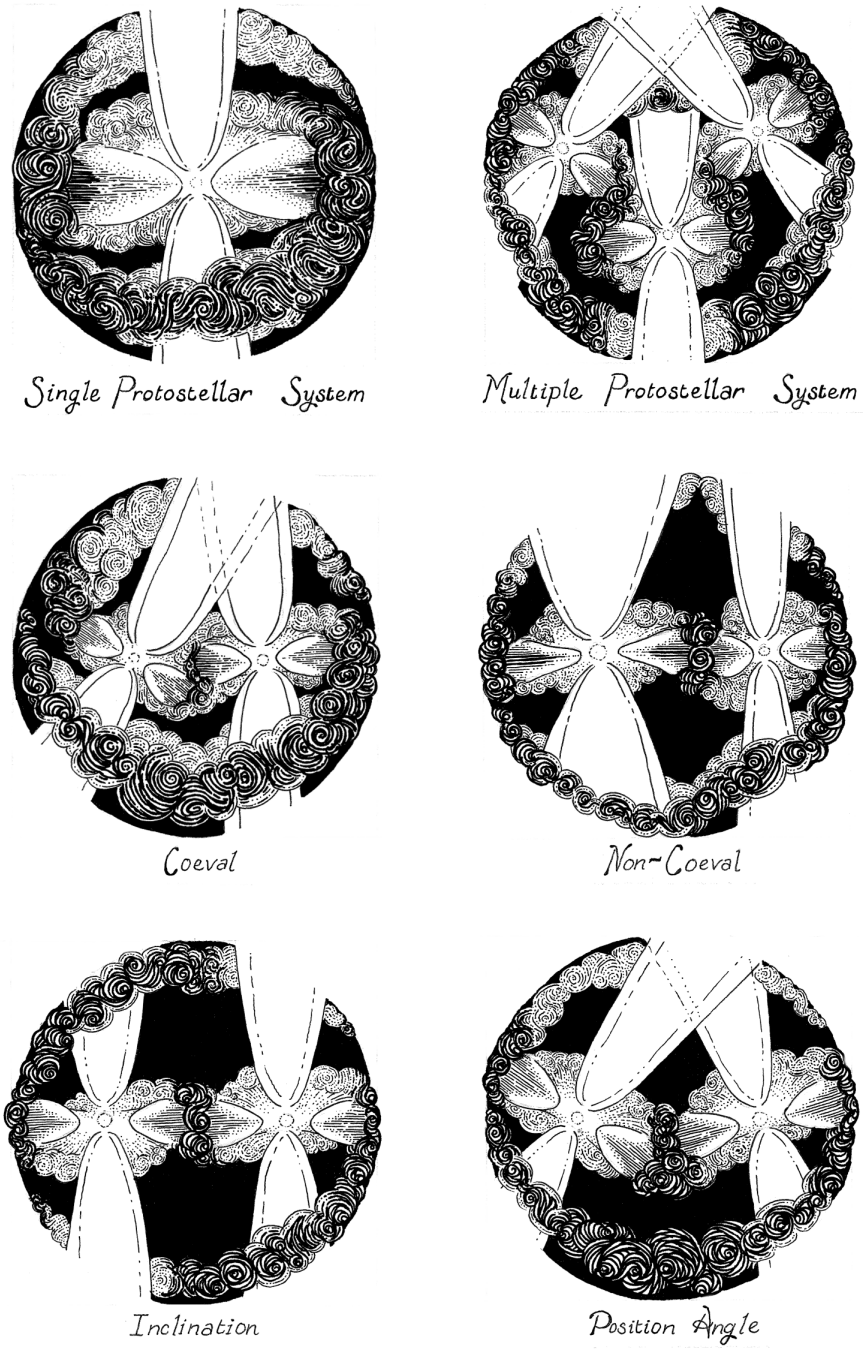

Figure 2: Definitions used in this thesis (Drawing by author).

component tends to drive an outflow of its own. We assume that a group of protostars are gravitiationally bound, unless there is evidence to the contrary, if they are observed to have a common cloud core in single dish observations. To be considered a multiple protostellar system, a group of protostars must have several continuum and molecular emission observations which independently confirm its multiplicity, e.g., observations of outflow, envelope and continuum. This is necessary to avoid protostellar systems being identified as multiple protostellar systems due to observational artifacts or background objects.

Regarding multiple protostellar systems, a ***resolved multiple system*** is a system whose multiple components can be resolved with the observations being discussed. Conversely, the separate components of an ***unresolved multiple system*** cannot be distinguished from the data being used. This distinction is important when considering the parameters derived from observations, for example the evolutionary stage, bolometric luminosity ($L_{\rm bol}$) and temperature ($T_{\rm bol}$), since the quantities derived for unresolved multiple systems are arithmetic averages of the components in the system.

The ***position angle*** is the orientation of the axes of an object on the plane of the sky. In contrast, ***inclination*** is the orientation of the axes of an object along the line of sight of the observer. This difference is important when considering the geometry of the system and its effect on the observations. ***Geometry*** here refers to the configuration of the system from the point of view of the observer. This aspect is crucial to determine the physical properties and evolutionary stage of a protostar (e.g. Crapsi et al. 2008).

Coevality is defined as the relative evolutionary stages of the components that make up a multiple protostellar system, accounting for the SED, derived properties, geometry and physical structure of the cloud core. A ***coeval system*** is a multiple protostellar system whose components show similar evolutionary stages relative to each other. On the other hand, the components of a ***non-coeval system*** have different evolutionary stages. The ***frequency of (non-)coevality*** is defined as the fraction of multiple systems whose components show similar evolutionary stages. This is expressed as a ratio of (non-)coeval systems over the total number of systems considered. For triple and higher-order multiple systems, the coevality of the components in the system is counted $n-1$ times, where n is the number of resolved components, in order to account for the coevality of all the components in the system. For example, for a triple system with two components in the Class 0 stage and the third in the Class I stage, it is counted once as coeval and once as non-coeval.

1.3.2 Observations

Multiple protostellar systems have been surveyed from the pre-main sequence stage to the deeply embedded phase of star formation. These surveys are carried out in continuum, from infrared to (sub)millimeter to radio observations (see Sec. 1.5.1). Surveys of Class I up to pre-main sequence multiple protostellar systems using infrared observations (Haisch et al. 2002, 2004; Barsony et al. 2003; Connelley et al. 2008a,b) and optical (Hartigan & Kenyon 2003; Connelley et al. 2009), found companion fractions between 18 to ∼50%, varying with evolutionary stage and separation, with separations ranging from 14 to 4500 AU. Surveys of deeply embedded multiple protostllar systems need to be done in (sub)millimeter in order to detect young protostars. Using interferometry, separations down to a few 10 AU can be probed. Fewer surveys have

been conducted towards embedded protostars, with relatively small samples (Looney et al. 2000; Chen et al. 2013; Tobin et al. 2013b). These surveys found that embedded protostellar systems present much higher multiplicity and companion fractions (64 ± 8% and 91 ± 5%, respectively; Chen et al. 2013) for separations larger than 1800 AU. These values are lower limits due to the completeness of the sample with respect to separation.

Recently, Tobin et al. (2016b) conducted an unbiased survey of the Perseus molecular cloud at 8 mm and 1 cm using the Very Large Array, probing separations between 15 to 10000 AU. Tobin et al. (2016b) found multiplicity and companion fractions of 0.57 ± 0.09 and 1.2 ± 0.2, respectively, in Class 0 multiple systems, while both fractions drop to 0.23 ± 0.08 for the Class I systems. Placing all the results from surveys of multiple protostellar systems together, it appears that the multiplicity frequency declines as the protostellar systems evolve and age (see review in Reipurth et al. 2014). This decline in multiplicity and companion fractions would suggest that multiple protostellar system evolution is dynamical, for example by ejecting components (Reipurth 2000; Goodwin & Whitworth 2007) and decaying orbits (Bate et al. 2002).

While continuum surveys of multiple protostellar systems can reveal information about multiplicity and companion fractions, as well as separation distribution, little information on the physical and chemical structure of multiple protostellar systems can be obtained. Only a handful of multiple protostars have been studied in-depth, reporting the structure of outflows, envelope chemistry and kinematics, interaction between components and magnetic fields, or disentangling the bonafide components in the system. Some 'well-studied' systems include NGC1333 IRAS4A (Choi et al. 2010; Ching et al. 2016); NGC1333 IRAS2A (Tobin et al. 2015); NGC1333 SVS13 (Chen et al. 2009); L1448 N (Kwon et al. 2006; Tobin et al. 2016a); L1448 C (Hirano et al. 2010); B1-b (Hirano & Liu 2014; Gerin et al. 2015); IRAS16293 (Jørgensen et al. 2011, 2016); and VLA1623 (Murillo & Lai 2013). Many of these systems appear to show non-coeval components (e.g. NGC1333 SVS13, B1-b and VLA1623)[1]. Even more interesting is the observations by Tobin et al. (2016a) which found evidence of recent disk fragmentation in L1448 N, a clear sign of non-coevality.

Non-coeval embedded protostellar systems would indicate that fragmentation is occurring at different times during the star formation process. Observations of pre-main sequence binaries found a tendency of so-called mixed pairs, such as classical and weak-lined T-Tauri binaries or one component having a disk with no accretion, which were thought to have different ages (Duchêne et al. 1999; Kenyon & Hartmann 1995; Hartigan & Kenyon 2003). Binaries containing Class I and II components were also found (McCabe et al. 2006). Furthermore, an age coevality frequency of two-thirds was found in the Taurus-Auriga region (Kraus & Hillenbrand 2009). However all these studies suffer from two main issues, i) the samples are composed mainly of pre-main sequence binaries that, as previously mentioned, have undergone dynamical evolution which erases much of the original formation conditions; and ii) the coevality was determined from isochrones which have large uncertainties (Soderblom et al. 2014). Studies of coevality at the earliest embedded phase have not been done, due to technical difficulties, but are needed to address when fragmentation occurs. In relation to this, observations looking for signs of fragmentation in pre-stellar cloud cores have been

[1]While it may appear that IRAS16293 has non-coeval components, it must be noted that the A and B sources most likely have perpendicular inclinations, that is B is face-on, while A is close to edge on (Jørgensen et al. 2016), making the comparison of evoultionary stage rather difficult (Crapsi et al. 2008).

carried out. Some have not found clear signatures of structures that can lead to fragmentation (Schnee et al. 2010; Dunham et al. 2016), while others do show structure in starless cores (Pineda et al. 2015; Kirk et al. 2017).

The combination of continuum surveys and observations of the physics and chemistry of multiple protostellar systems are needed to address the open questions in the formation and evolution of these systems, and of star formation in general. Additionally, observations can place constraints on theory, and in turn models can provide a set of parameters and signatures that can be observed to test the results of simulations.

1.3.3 Theory, models and fragmentation

Early theories of the formation of multiple stellar systems suggested capture as the main mechanism (see Tohline 2002 for review). However, multiple stars formed through capture require high stellar densities, like those in globular clusters, and would produce one ejected star for each binary formed due to energy conservation. Additionally, this mechanism does not explain how isolated or higher order multiples form, or the observations of embedded multiple protostellar systems. Together with the low protostellar densities in protoclusters, capture is discarded as the main formation mechanism of multiple stars.

Models have indicated that fragmentation is the most likely mechanism of multiple protostellar system formation (Figure 3). Tohline (2002) divided fragmentation into two categories, prompt and delayed. Prompt fragmentation would occur during the initial collapse of the cloud core. In contrast, an instability in the envelope or disk would trigger further collapse in the surrounding structure of a formed protostar and this would be termed delayed fragmentation. Several numerical simulations of fragmentation have included additional physical processes, such as turbulence (e.g. Goodwin et al. 2004; Offner et al. 2010, 2016), episodic accretion and disk fragmentation (e.g. Stamatellos & Whitworth 2009b; Stamatellos et al. 2011), rotational fragmentation (e.g. Hennebelle et al. 2004; Machida et al. 2008; Klapp et al. 2014) and magnetic fields (e.g. Nakamura & Li 2003), to name a few.

The turbulent fragmentation scenario (Offner et al. 2010) proposes that perturbations caused by turbulence in the starless cloud core will produce several density enhancements that will in turn generate multiple protostellar components upon collapse, but with large separations on the scale of $\sim$1000 AU. Close systems could then be formed through decrease of the orbit radius as the multiple protostar evolves. This is expected to generate observable signatures in pre-stellar cloud cores (Offner et al. 2012a). Some such structures have been found in some regions (Pineda et al. 2015; Kirk et al. 2017), but not in other regions like Chameleon (Schnee et al. 2010; Dunham et al. 2016). It is possible that the cores in Chameleon are unbound and not collapsing, while those in ρ Ophiuchus are undergoing collapse. Another way to test turbulent fragmentation is through the coevality of multiple protostars with separations of $\sim$1000 AU or more. If these systems tend to be coeval, turbulent fragmentation may be a very likely formation scenario.

Disk fragmentation proposes that instabilities (Toomre $Q < 1$) in protostellar disks can lead to collapse and formation of a companion source (Stamatellos & Whitworth 2009a; Kratter et al. 2010), producing multiple protostellar systems with separations on the scale of disk sizes, $\sim$100 AU. Several processes can affect instabilities in the disk, for example episodic accretion (Stamatellos et al. 2011) and heating of the disk

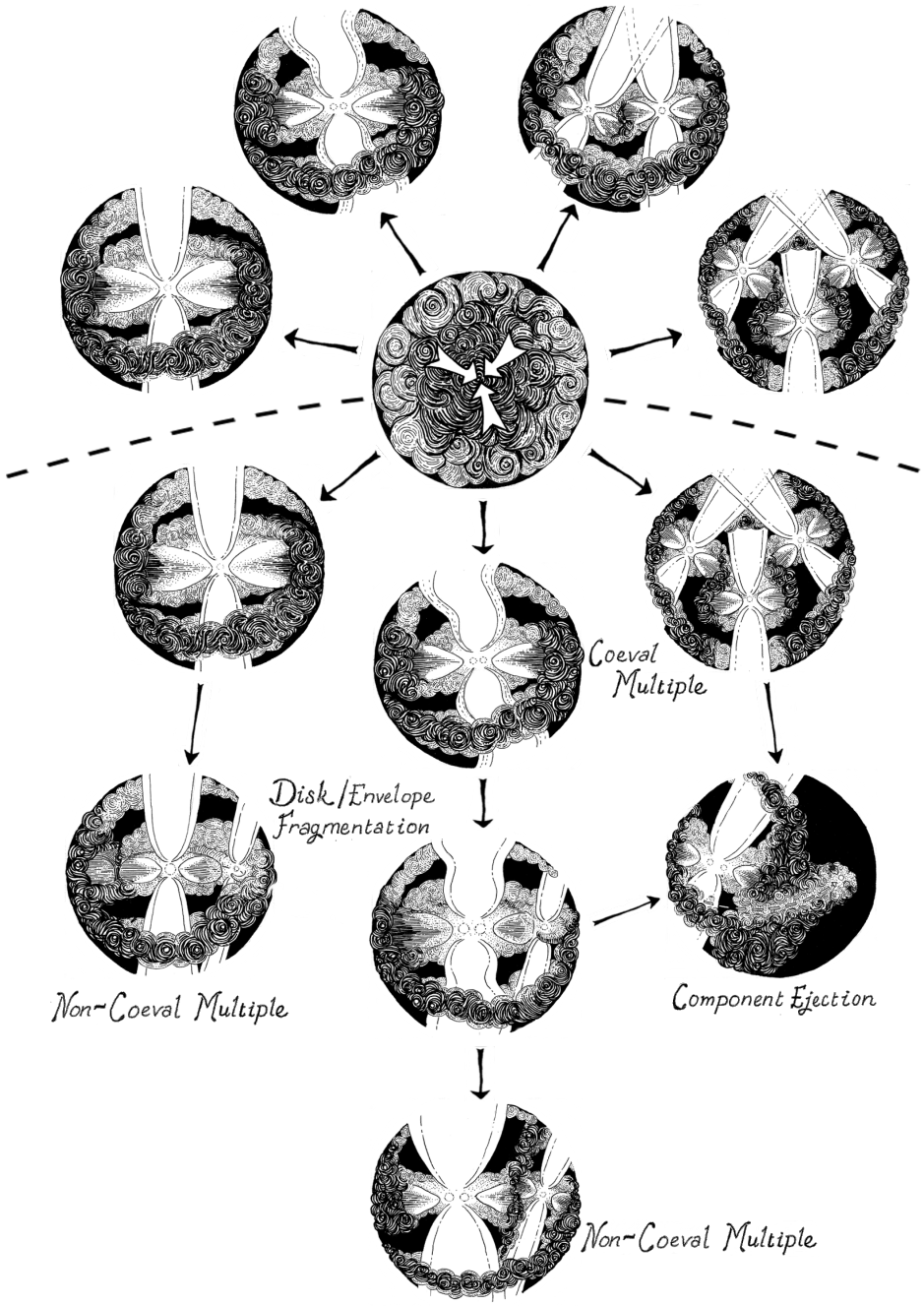

Figure 3: Picture of star formation including the different fragmentation methods leading to multiple star formation. Above the dashed line, the initial collapse of the cloud core produces a stable protostellar system, and for the case of multiples, gravitationally bound. Below the dashed line, the system produced in the initial collapse can further fragment. For protostellar systems with triple or higher multiplicity, interaction between the components can lead to ejection of a component, or a stable system that is gravitiationally bound. (Drawing by author).

(Bate 2009; Offner et al. 2009; Stamatellos & Whitworth 2009b). The close multiple protostars generated in this way can also produce wide multiples (separations >100 AU) through orbital decay (Bate et al. 2002). Observations reported by Tobin et al. (2016a) provide evidence for the viability of this mechanism, as do the reports of large rotationally supported disks in embedded protostars (Tobin et al. 2013c, This thesis).

Recently, thermal feedback and heating of the gas and dust have been raised as important factors in star formation in general, and specifically for fragmentation (see review by Krumholz et al. 2014 and references therein). Early models showed that dynamical collapse and fragmentation were halted by heating due to increase in the opacity of the cloud core, the so-called opacity limit for fragmentation. Accretion can heat the surrounding gas, even as early as accretion during the FHSC, thus fragmentation can be suppressed before the protostellar object forms. If the cloud core is heated by the internal source above 100 K, a good part of fragmentation will be hindered. Numerical simulations, such as that by Bate (2012), show how quickly the gas can be heated by the formation of a single protostar. This can cause fragmentation, and consequently the formation of multiple protostars, to be considerably reduced. Observations of multiple protostellar systems cannot yet determine whether the results of simulations are fully reflected by forming stars. Evidence for gas heating at 1000 AU scales has been obtained from observations of high-J CO lines which indicate that UV-heated gas is mainly located around the outflow cavity (Yıldız et al. 2012, 2015). The presence of observed embedded multiple protostars that show indications of non-coevality would hint at the presence of an additional mechanism playing a role. Furthermore, the recently fragmented disk observed by Tobin et al. (2016a) would suggest that instabilities could overcome heating-suppressed fragmentation, since a circumbinary disk is most certainly heated above 100 K, both from the central binary and through accretion.

Given the broad range of configurations, multiplicity and companion fractions, and coevality, it is most likely that multiple protostellar systems do not form through one single mechanism, but from a combination of turbulent and disk fragmentation (Kratter 2011), with density, temperature and magnetic fields all playing a role.

1.3.4 Current picture of multiple star formation

Combining the results from observations and models, the picture of single star formation can be adjusted to include the common outcome of multiple protostars (Figure 3). Rather than be a unique linear process, star formation branches depending on whether the initial collapse produces a stable system and if the conditions are favourable for further fragmentation or not. Upon initial collapse, turbulence can generate density irregularities in the cloud core leading to the formation of several protostellar sources within a common cloud core. This would produce coeval systems, as the components of the system form at practically the same time, and evolve simultaneously. On the other hand, a single protostar can form, and instabilities in the disk or cloud core would trigger fragmentation and collapse to form an additional protostar. The result would be a non-coeval multiple protostellar system with components at different evolutionary phases. It is also possible that both mechanisms occur in the same system, causing a multiple protostar to have both coeval and non-coeval components.

The evolutionary process would differ as well. For a multiple protostar that ejects a component, the orbit will become tighter and the ejected source will have truncated

accretion (Stamatellos & Whitworth 2009a). If the multiple protostar does not disintegrate, it will be likely that the envelope will be dispersed much faster than for a single protostar, or dispersed completely for one component and remain almost intact in the companion. This will in turn affect the formation of planets in later stages, since the protoplanetary disk mass and size will vary with the evolution of the system, and can be mostly dispersed for one component but not the other (Akeson & Jensen 2014).

1.3.5 Open questions in multiple star formation

Our understanding of multiple star formation is progressing along with observations and the constraints they place on models. This thesis addresses the questions of disk formation, the physicochemical structure, and the coevality of multiple protostellar systems. Nevertheless, there are many pieces to the puzzle that are still missing and require further work to address the questions. Here a brief description of some open questions is given.

A fundamental question that has yet to be answered is whether all the observed protostellar systems that show multiplicity are gravitationally bound. The difficulty of answering this question lies in the reliable measurement of masses from the individual components, and resolving those individual components. The best way to derive the protostellar mass is through the study of rotationally supported disks. Current technical capabilities allow surveys of disks in embedded protostellar systems (Yen et al. 2015) and to disentangle the multiplicity of these systems down to 15 AU (Tobin et al. 2016b), thus this question can be addressed for systems where the disk can be characterized and the central mass determined.

An open question related to the formation mechanism of multiple protostellar systems is the moment when fragmentation occurs. In other words, does fragmentation happen during the initial collapse, after one protostar has formed, or a combination of both. This is closely related to the factors that favour or hinder fragmentation. Heating, magnetic fields and outflows are some factors that are thought to have an impact on whether fragmentation occurs. Heated gas would reduce the chance of fragmentation in a cloud core. The magnetic field configuration is expected to affect disk formation which in turn affects disk fragmentation and the formation of close multiples. Outflows are proposed to be capable of triggering collapse in neighboring cloud cores (Barsony et al. 1998), although this might be in disagreement with the first factor mentioned, since shocked gas and dust is heated up rather quickly.

Directly related to the formation mechanisms and the factors that play a role, is what dictates the level of multiplicity. Why do some cloud cores produce higher order multiples while others produce only binaries or singles? One possible parameter could be the size and density distribution of a cloud core, since a small cloud core with a central density distribution would be expected to produce a single or a close binary, whereas an elongated cloud core with several density peaks might collapse to form multiple protostars. Structure in the starless cloud core could also lead to fragmentation. Magnetic fields and gas heating are also expected to influence the level of multiplicity.

In a multiple protostellar system, the components interact with each other, the time scale depending on their configuration. This can lead to ejection of components, redistribution of the configuration and material, as well as quicker dispersal of the en-

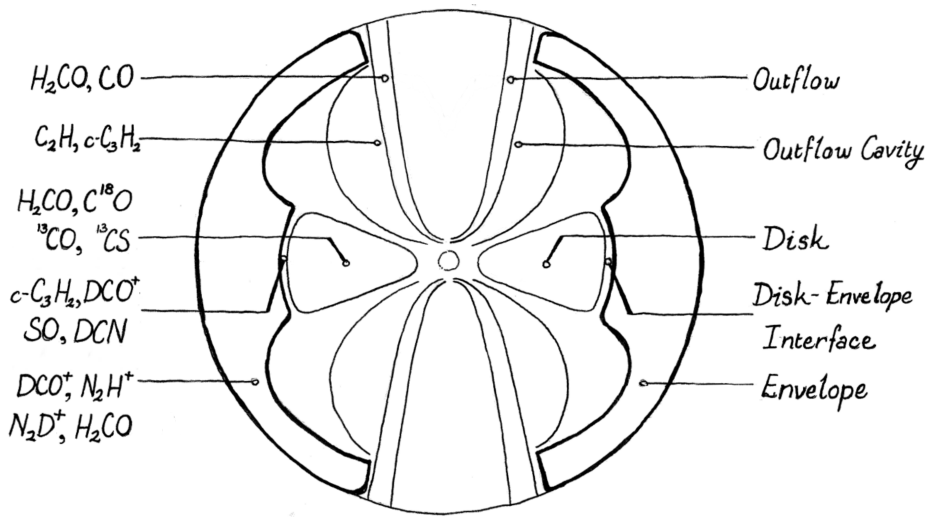

Figure 4: Regions of a protostellar system and molecules that have been observed to trace the different structures (Drawing by author).

velope and disk of one or all components in the system. Thus, the initial configuration of the embedded phase may not endure to the pre-main sequence stage. Additionally, non-coeval systems might evolve differently than coeval systems, due to interaction. While it is tricky to study the evolution of multiple protostars, it is of interest to study these systems at different evolutionary stages, and compare them with single protostars at the same evolutionary stages, to understand how multiplicity affects star formation in general. For example, it could be explored if there is some degree of competitive accretion in multiple protostars, even more so in non-coeval systems.

Rotationally supported disk formation is a question for star formation in general and are of interest since they are the precursors of protoplanetary disks. How early they form will affect the structure of the disk. Recent observations suggest disks can form as early as the Class 0 stage. With the disk also comes the possibility of multiple protostar formation through disk fragmentation. Thus, while the disk can influence the multiplicity of a protostellar system, it is unclear how the multiplicity of a system affects the formation of disks. Harris et al. (2012) suggest that the star-disk tidal interactions and the accretion processes during the formation of the multiple system both contribute to the evolution and formation of protoplanetary disks, and eventually planets. Several rotationally supported disks have been observed centered around one of the components of a multiple protosellar system, thus indicating that multiplicity does not hinder the formation of disks. However, if companions help form or determine the size of the disks is yet unknown.

1.4 Chemistry as a tool

Molecules are a strong tool in the study of star formation. Molecular emission lines are excellent probes of physical conditions and structure in astrophysical objects (Figure 4). Different molecular species can be sensitive to either temperature or density

depending on the molecular structure and the mechanism to (de)populate the energy levels. For example, some energy levels of H_2CO are (de)populated by collisions alone, making them a good thermometer, since collision rates are determined by temperature. On the other hand, molecules such as c$-C_3H_2$ are dependent on critical density for populating its energy levels, making it sensitive to density up to its critical density and then temperature sensitive.

Rather than a specific physical structure always being traced by a particular molecule, the chemical reactions, temperatures and densities needed to produce molecular species dictate what regions they trace. Thus, if a protostellar structure is often detected in a particular molecule, for example rotationally supported disks traced by $C^{18}O$, it is indicative that these structures have similar physical conditions. DCO^+, N_2H^+ and N_2D^+ are good tracers of cold ($\sim$20 K) regions where CO freezes out, whereas c$-C_3H_2$ and CCH trace warm (50 – 100 K) and/or UV-irradiated regions due to their chemistry (Jansen 1995; Sakai & Yamamoto 2013). Examples of the regions traced by each molecules are shown in Figure 4. The chemical production and destruction paths, which can be at high or low temperatures, gas-phase, surface reactions or a combination, can alter the conditions where a molecular species is produced. This aspect must be considered when analyzing observations. DCO^+ is an example of production via two paths, at temperatures below 30 K when CO freezes out (Mathews et al. 2013) and from reactions in the warmer disk surface (Favre et al. 2015).

Additionally, molecular line emission can probe the kinematics of the region they are tracing, as well as processes such as shocks around the disk (e.g. Sakai et al. 2014a), episodic accretion (e.g. Jørgensen et al. 2015; Frimann et al. 2017), infall (e.g. Schnee et al. 2010; Tobin et al. 2012a; Mottram et al. 2014) and molecular outflows (e.g. Arce & Sargent 2006; Kristensen et al. 2012; Lee et al. 2016). These phenomena could not be detected from continuum alone, and are crucial to understand the formation and evolution of stars. Kinematics of rotationally supported disks traced from molecular emission provide the only direct way to measure central protostellar masses (e.g., Tobin et al. 2012b). Central protostellar masses are crucial for determination of evolutionary stage (Table 1), but also to determine if an observed multiple protostellar system is gravitationally bound. Ratios of molecular species and transitions are thought to provide evolutionary indicators (e.g. Emprechtinger et al. 2009; Crapsi et al. 2005; Schnee et al. 2013).

Combining observations of molecular emission with dust continuum provide a full picture of the structure of a protostellar system. The non-detection of molecular emission can also tell as much as the detection, since the lack of a molecule can be product of the presence of another species which causes the molecule's destruction or if the molecule itself or its chemical parent are frozen out onto the dust grains. Detection of emission at a given transition but not at a higher transition is indicative of the physical conditions, since the material being traced may not have the temperature or density to populate the upper energy levels of the molecule.

1.5 Methods

1.5.1 Observations

Young, deeply embedded protostars are comparatively cooler than their pre-main sequence counterparts. Enshrouded by dense envelopes, the light from the central source

cannot be observed directly and heats its surroundings up to a few hundred Kelvin. Thus these systems can only be observed at wavelengths longer than a few microns, for example, Class 0 sources are generally observed to have emission at wavelengths $\geq$24 μm. Therefore these systems need to be studied with (sub)millimeter and infrared telescopes. The former are ground-based while the latter, due to the atmosphere blocking the mid- and far-infrared wavelengths, are space-borne.

The structures of a protostellar system, that is the disk, envelope and outflow, span sizes from a few AU to fractions of a parsec. To have a complete view of a protostellar system, it is then necessary to observe them at different resolutions. Single dish observations will probe the outer envelope and large scale outflow, while interferometric observations reveal the inner AU scale structure. Both are used in this thesis.

Observations using the Submillimeter Array (SMA) in Hawaii, the Atacama Large Millimeter/submillimeter Array (ALMA) in the Chajnantor plateau, Atacama dessert, Chile, and the Atacama Pathfinder Experiment also in Atacama, are presented in this work. The typical resolution of the observations presented in this work are in the range of 0.8" to 0.5", tracing scales of $\sim$100 to 60 AU in ρ Ophiuchus molecular cloud, and 200 to 125 AU in the Perseus star forming region. Additionally, archival data taken by the Spitzer Space Telescope for the legacy project "From Cores to disks (c2d)" and by the Herschel Space Observatory for the guaranteed time project "Gould Belt Survey" are also used in conjunction with (sub)millimeter observations. Typical resolution from Herschel Space Observatory PACS photometric maps is of about 7", resulting in scales of 1700 AU being traced in the Perseus star forming region.

1.5.2 Spectral energy distribution (SED)

The evolutionary stage of a protostellar system can be studied from the spectral energy distribution (SED). Based on studies of protostellar objects at different evolutionary stages and models of protostellar evolution, the SED shape changes as the protostar evolves. This is mainly due to the fact that as the central source becomes hotter, the black body component of the SED moves to shorter wavelengths and the (sub)millimeter emission, which is dominated by the envelope and later the disk, becomes weaker as these structures disperse. Thus, analyzing the SED peak location, infrared spectral index α_{IR} and ratio of submillimeter to bolometric luminosity $L_{\rm submm}/L_{\rm bol}$, as well as the shape are useful in determining the evolutionary stage of a protostellar source. While these characteristics can give information on the evolutionary stage, care must be taken that the observed SED is not product of an unresolved multiple protostellar system, since this would provide averaged parameters and not the real conditions of the observed protostellar source.

1.5.3 Physical and chemical models

Comparison of observations with models provide a deeper understanding of the protostellar system being observed. This is because the conditions in the model can be changed and the result examined and compared, thus providing not only the conditions that match the observations, but also how a change in these parameters would alter the outcome. When models are simplified to the basic elements, while not all details are taken into account, they can identify the main factors that generate the observed conditions.

In the research presented in this thesis, two simple models are used, an analytical time-independent chemical network and a thin disk model. The first is used to study the formation and destruction of DCO^+ by considering only the main chemical species and reactions needed. The second provides a physical description of disk structures driven by a central protostar, simplifying the structure to a flat disk. In our model, different velocity structures can be studied, including a combination of these with a critical radius $R_{\rm crit}$ denoting the point where the transition occurs. Both models are then passed through radiative transfer programs and convolved to the beam of the observations so that the model can be directly compared to the observations.

1.6 This thesis

In recent decades, several continuum surveys have provided a view into the multiplicity of protostellar systems from the early embedded phase to the pre-main sequence stage. The chemical structure of the envelope, on the other hand, has only been studied for a few dozen systems and not always with the same molecular species, making the comparison and determination of the physical structure difficult. Chemistry serves as a tool to probe the physical conditions of a protostellar system, and thus is necessary for addressing the many open questions in multiple low-mass star formation. The motivation behind this thesis is to systematically study low-mass multiple protostellar systems, placing special focus on their coevality and the chemistry to reveal their physical structure. Constructing the SED of each component in a multiple protostellar system and then comparing them provides a way to study the coevality of multiple protostars. In order to study the chemical and physical structure, the same set of molecular species are targeted for the multiple protostars studied. These molecules are selected to probe the different regions of a protostellar cloud core, namely the cold and warm regions of the envelope (N_2H^+, N_2D^+, DCO^+, c$-C_3H_2$, C_2H and H_2CO), the disk ($C^{18}O$, ^{13}CO) and the heated gas (^{13}CO 6–5, c$-C_3H_2$). In addition to the multiple protostellar systems studied, a couple of single protostars are included in order to do a comparison of the physical and chemical structure of single and multiple protostars.

With this motivation in mind and aiming to look at some basic aspects in the formation and evolution of multiple protostars, this work addresses five main questions:

- When do disks form?
- How do disks impact the chemical structure of protostellar systems?
- What is the frequency of coevality in multiple protostellar systems?
- What is the chemical and physical structure of multiple protostellar systems and how do they compare to single protostars?
- Is there a temperature-fragmentation relation in protostellar systems?

A brief outline of the subsequent chapters together with their respective titles in this thesis follows.

Chapter 2 – A Keplerian disk around a Class 0 source: ALMA observations of VLA1623A

Rotationally supported disks are an important structure for star formation. They are observed to be common around pre-main sequence stars and Class I protostellar systems. Disk-like structures in continuum have been detected in Class 0 protostars, and more recently, indications of rotationally supported disks in deeply embedded sources. VLA1623 is a non-coeval triple protostellar system located in L1688 in ρ Ophiuchus ($d \sim 120$ pc). The three components of the system are VLA1623A, B and W. VLA1623A, the prototypical Class 0 source, is deeply embedded and young, driving a remarkable outflow in the south-east to north-west direction. VLA1623B, separated 1.1" from A, is relatively cold and depleted of most molecular emission, but has evidence of driving an outflow and is expected to be the youngest of the three. The component to the west separated by 10", VLA1623W, appears to be older than A and B, with less circumstellar material. ALMA Cycle 0 Early Science observations towards VLA1623 detected a disk-like structure traced in $C^{18}O$ 2–1 centered on source A. Using a thin disk model with the addition of foreground coupled with radiative transfer, the $C^{18}O$ emission is modelled. The thin disk model allows different velocity structures to be probed, including free-fall, infall and Keplerian, plus a combination of these by setting a critical radius $R_{\rm crit}$. We find that the $C^{18}O$ emission centered on VLA1623A has an outer radius of 180 AU. The structure is best described by a Keplerian disk with a radius of at least 150 AU, a central mass of 0.2 $M_\odot$, and an inclination of i =55°. The velocity structure of the outer 30 AU cannot be determined unambiguously due to resolution. The weak magnetic field, misaligned with respect to the outflow direction, may have helped form the disk. Comparison with other Class 0 sources reported of driving Keplerian disks shows VLA1623A to be the youngest, thus driving the youngest Keplerian disk yet found.

Chapter 3 – The physical and temperature structure of the disk-envelope interface: evidence for disk shadowing from ALMA DCO^+ observations of VLA1623

Rotationally supported disks can form in the embedded phase of protostars. Since the protostellar envelope at this stage is not negligible, the presence of the disk must produce an impact on the envelope. Previous observations of L1527 suggest that a shock occurs at the point where the disk and envelope meet, the disk-envelope interface, which may alter the chemistry of the region. It is then of interest to study whether a shock occurs in all cases and to what extent does the disk alter the envelope structure. ALMA Cycle 0 12m array observations of DCO^+ 3–2, done simultaneously with $C^{18}O$ 2–1, detect clumpy structures bordering the Keplerian disk centered on VLA1623A. Temperature and density models constrained by continuum data and source SED, place the peak of DCO^+ at about 5" offset from the source where the temperature falls below 20 K. However the observed peak is located at 3" away from the position of VLA1623A, closer than expected. A simple analytic time-independent chemical network coupled with the temperature and density profile of VLA1623 is used to model the observed DCO^+ emission. The peak of DCO^+ is only reproduced with a drop in temperature of a factor of 1.5, making the temperature in the region between 11 to 16 K. Altering the density or the CO freeze-out region does not alter

the position of the DCO^+ peak. Shadowing of the envelope by the disk can cause a decrease in temperature, encouraging the formation of cold-chemistry molecules like DCO^+. These results are further confirmed by ALMA Cycle 2 ACA observations, which show DCO^+ emission along the outflow axis to be best described by the spherically symmetric constant CO abundance models. This highlights the drastic impact that the disk has on the envelope and its temperature structure.

Chapter 4 – Tracing the cold and warm physico-chemical structure of deeply embedded protostars: IRAS 16293-2422 versus VLA 1623-2417

A sketch of the physical structure and evolution of low-mass protostars has been outlined and well-studied. However, the physico-chemical structure is still quite blurry, and the factors that influence the chemical complexity even more so. Motivated by this question, two Class 0 protostellar systems, IRAS 16293-2422 and VLA 1623-2417 are studied in depth using ALMA observations. The observations for IRAS 16293-2422 are part of the PILS program (PI Jes Jørgensen) and complemented with SMA observations. For VLA 1623-2417, the data used here were observed during ALMA Cycle 0 and 2 using the 12m array and the Atacama Compact Array (ACA). Both systems are multiple, deeply embedded and located in the ρ Ophiuchus molecular cloud. IRAS 16293-2422 is very luminous, whereas VLA 1623-2417 is considerably dimmer. Focus is placed on the cold and warm envelope of the two protostellar systems, which are traced by DCO^+, c$-C_3H_2$, C_2H, N_2H^+ and N_2D^+. DCO^+ is found to trace the outer edge of disk(-like) structures for one of the components in both systems. The rest of the molecules do not coincide in spatial distribution, but are located in regions with similar physical conditions. VLA 1623-2417 presents little emission, to the point that N_2D^+ and N_2H^+ are not detected. The presence of a rotationally supported disk in VLA 1623-2417 can cause the outer envelope to be very cold due to disk shadowing, reducing the chemical complexity of the envelope and confining any warmer gas along the outflow cavity, where c$-C_3H_2$ is traced. IRAS 16293-2422, on the other hand, being more luminous could heat up the envelope to a larger extent than VLA 1623-2417, but the disk would still shield part of the envelope, producing the observed spatial distributions. Thus, the presence of disks can have a lasting impact not only on the temperature structure of the protostar, but on the chemical complexity.

Chapter 5 – Do siblings always form and evolve simultaneously? Testing the coevality of multiple protostellar systems through SEDs

Fragmentation is widely accepted as the formation mechanism of multiple protostars. It is still debated, however, when fragmentation occurs and if all multiple protostars form and evolve contemporaneously. Surveys of pre-main sequence binaries suggest a non-coevality frequency of about 33% with the use of isochrones, however, dynamical evolution can erase the conditions of formation. Studying the coevality in young protostars requires an alternate method than that used for pre-main sequence stars due to their embedded nature. Looking at the relative evolutionary phases of the components in a multiple protostar can provide insight into the issue of coevality. We study the protostars in the Perseus molecular cloud. This star forming region has been

widely studied in molecular line emission and continuum, and the multiplicity of the region has been recently well studied down to separations of 15 AU. The SEDs for all identified protostellar systems in the Perseus molecular cloud are constructed using data from literature and extracted fluxes from Herschel PACS maps. Parameters such as $T_{\rm bol}$, $\alpha_{\rm IR}$ and $L_{\rm submm}/L_{\rm bol}$ are derived from each SED as well. However, SEDs and derived parameters alone cannot determine whether a system is coeval or not, since the SED is affected by geometry. Thus, physical parameters, inclination and the physical structure of the protostellar system must be accounted for when studying coevality. A non-coevality frequency of 1/3 is found in the region on scales of $\geq$1700 AU, with higher order multiple protostars tending to have non-coeval components, while binaries are more coeval. This places constraints on formation mechanisms for higher order multiples, and at the same time raises the question of what factors enhance fragmentation in some systems but not others.

Chapter 6 – The role of environment and gas temperature in the formation of multiple protostellar systems

Hydrodynamical simulations with the inclusion of radiative feedback show that heated gas tends to suppress fragmentation. Thus, when a protostar forms and heats its surrounding environment, fragmentation should be reduced almost entirely and multiple protostellar systems with non-coeval components should be greatly reduced. However, from the construction and comparison of SEDs in multiple protostellar systems, it was found that 1/3 of the time multiple protostars are non-coeval (Chapter 5). For this to occur, an already formed protostar or binary protostar must undergo further collapse of its envelope or disk, both of which are expected to be heated by the already formed protostar(s). The question is then raised if non-coeval multiple protostars are cooler than single and coeval multiple protostars. Aiming to address this question, the outer envelope of a sample of multiple and single protostellar systems is studied with APEX observations. The molecules targeted include DCO^+, c$-C_3H_2$ and H_2CO with APEX-1 (216 GHz), which are good indicators of temperature in the different regions of the protostar. We find that the outer envelope of multiple protostellar systems is more chemically rich than that of single protostars, even for molecules associated with warm chemistry. Our observations show no clear correlation between temperature and fragmentation, but instead non-coeval multiple protostellar systems present larger cold gas reservoirs. These results suggest that mass, rather than temperature, plays a role in fragmentation.

The conclusions of this thesis can thus be summarized as follows:

1. Large, rotationally supported disks can form in the early embedded phase (Chapter 2).

2. Disks alter the chemical composition of the envelope by altering the temperature profile of the cloud core along the disk plane (Chapter 3).

3. The chemical structure of the protostellar system does not depend on the evolutionary stage, but on the temperature profile, with the disk being the main controlling factor of the temperature (Chapters 3 & 4).

4. Of multiple protostellar systems in Perseus, 2/3 are coeval, implying that 1/3 of the time there are conditions in multiple protostellar systems that lead to further fragmentation. The coevality frequency is independent of separation down to $\geq$1700 AU, but higher order multiples tend to be non-coeval while binaries tend to be coeval (Chapter 5).

5. In Perseus, the outer envelope of multiple protostellar systems are more chemically rich than that of close binary and single protostars, however the temperature for both types of systems is similar, hinting at a lack of temperature-fragmentation relation (Chapter 6).

The results obtained in this thesis provide useful constraints on the formation and evolution of multiple protostellar systems, adding small pieces to the puzzle of multiple low-mass star formation and evolution. However, the target sample used in this work is small, and mainly focused on the Perseus star forming region, with two additional systems from Ophiuchus, VLA1623 and IRAS16293. This sample needs to be expanded, for example to Orion, if we are to understand the formation and evolution of multiple protostellar systems. A method to probe multiple protostars can be derived from the work presented here. The envelope and disk are studied with a set of molecules that are good tracers of the various regions of temperature and density, for example DCO^+, N_2H^+ and N_2D^+ for the cold outer envelope, H_2CO, c$-C_3H_2$ and C_2H for the warm regions and CO and its isotopologues for the disk and outflow kinematics. This kind of survey can be readily done with the current technical capabilities of ground-based (sub)millimeter telescopes, both in the northern and southern hemispheres, that have receivers in the 230 and 345 GHz range. Advances in instrumentation will allow higher sensitivities and resolutions, but the larger scales need to be understood before we can make sense of the finer details. Additionally, the combination of single dish and interferometers can probe from the outer envelope to the disk, revealing the structure of the cloud core. The coevality of multiple protostellar systems is determined through the construction of the SED of each component. However, complete SEDs are limited by the available far-infrared data. Sub-arcsecond resolution far-infrared data is crucial to examine the coevality of multiple protostars with separations larger than 7".

Model constraints can also be derived from the work presented in this thesis. For example, the frequency of non-coevality can be integrated into simulations of multiple low-mass star formation, with additional consideration that non-coevality occurs in higher-order multiples as well as the early formation of disks in multiple protostars. Another example of a constraint to include into models would be the weak relation between temperature and fragmentation, and how the presence of a disk alters the temperature profile in star formation in general.

Multiplicity in stars is ubiquitous. Understanding how multiple stars form and evolve will lead to a complete picture of star formation, and also to a better understanding of stars.

Chapter 2

A Keplerian disk around a Class 0 source

ALMA observations of VLA1623A

Murillo, N. M., Lai, S.-P., Bruderer, S.,
Harsono, D. and van Dishoeck, E. F.
2013, A&A, 560, 103

Abstract

Context Rotationally supported disks are critical in the star formation process. The questions of when do they form and what factors influence or hinder their formation have been studied but are largely unanswered. Observations of early-stage YSOs are needed to probe disk formation.

Aims VLA1623 is a triple non-coeval protostellar system, with a weak magnetic field perpendicular to the outflow, whose Class 0 component, VLA1623A, shows a disk-like structure in continuum with signatures of rotation in line emission. We aim to determine whether this structure is in part or in whole a rotationally supported disk, i.e. a Keplerian disk, and what its characteristics are.

Methods ALMA Cycle 0 Early Science 1.3 mm continuum and $C^{18}O$ 2-1 observations in the extended configuration are presented here and used to perform an analysis of the disk-like structure using PV diagrams and thin disk modeling with the addition of foreground absorption.

Results The PV diagrams of the $C^{18}O$ line emission suggest the presence of a rotationally supported component with a radius of at least 50 AU. Kinematical modeling of the line emission shows that the disk out to 180 AU is actually rotationally supported, with the rotation described well by Keplerian rotation out to at least 150 AU, and the central source mass is $\sim$0.2 $M_\odot$ for an inclination of 55°. Pure infall and conserved angular momentum rotation models are excluded.

Conclusions VLA1623A, a very young Class 0 source, presents a disk with an outer radius $R_{\rm out} = 180$ AU with a Keplerian velocity structure out to at least 150 AU. The weak magnetic fields and recent fragmentation in this region of ρ Ophiuchus may have played a leading role in the formation of the disk.

2.1 Introduction

Disks are key actors in the formation of stars. They are crucial for accretion and angular momentum distribution in the early stages and for planet formation in the later stages. Rotationally supported disks have been observed using molecular lines in the Class II stage of star formation (Mannings & Sargent 1997; Guilloteau & Dutrey 1998; Guilloteau et al. 1999; Qi et al. 2004; Hughes et al. 2009; Rodriguez et al. 2010), while continuum disk-like structures, the so-called pseudo-disks, are reported in Class 0 objects (Jørgensen et al. 2009; Enoch et al. 2009a, 2011). This leads to the expectation that rotationally supported or Keplerian disks evolve from pseudo-disks between the Class 0 and II stages.

Idealized, non-magnetized conditions for a collapsing isothermal core suggest that a small rotating disk ($R_{\rm out} < 100$ AU) should form as early as the Class 0 stage and grow as $R \propto t^3$, where t is time since collapse (Terebey et al. 1984). Adding magnetic fields to the problem offers varied results. Ideal MHD shows that magnetic field breaking can hinder disk formation (Mellon & Li 2008); however, if the magnetic field and rotation axes are misaligned, rotationally supported disks may form since the magnetic breaking efficiency is reduced (Hennebelle & Ciardi 2009; Krumholz et al. 2013). Consideration of non-ideal MHD effects and their role in disk formation has been explored, but there is no clear solution (Li et al. 2011).

Despite the observational relations and predictions obtained from simulations, it is still unclear when disks actually begin to form and to what degree factors, such as magnetic fields and fragmentation, hinder or encourage the formation of rotationally supported disks.

While observations of (sub-) Keplerian disks in Class I YSOs (Hogerheijde 2001; Brinch et al. 2007; Lommen et al. 2008; Jørgensen et al. 2009; Takakuwa et al. 2012; Yen et al. 2013) support the expectation that disks form between the Class 0 and II stages, recent observations have found indications that rotationally supported disks may be present as early as the Class 0 stage (NGC1333 IRAS4A: Choi et al. 2010; L1527: Tobin et al. 2012b; VLA1623: Murillo & Lai 2013). Interestingly, hour-glass-like magnetic fields are present in NGC1333 IRAS4A (Girart et al. 2006; Hull et al. 2014a) and in the large scale in L1527 (Davidson et al. 2011), while magnetic fields perpendicular to the outflow direction are present in VLA1623 (Holland et al. 1996; Hull et al. 2013, 2014a) and in the small scale in L1527 (Hull et al. 2014a). Additionally, while NGC1333 IRAS4A and VLA1623 are confirmed multiples, it is unclear whether L1527 is a protobinary (Loinard et al. 2002) or a single protostar. This brings back the question of what factors play a role in the formation of a Keplerian disk and if the combination of these factors is more relevant than the evolutionary stage of a protostar when it comes to the formation of a disk.

VLA1623 is a triple non-coeval protostellar system (Murillo & Lai 2013; Chen et al. 2013) with a prominent outflow (André et al. 1990) located in ρ Ophiuchus ($d \sim 120$pc, Loinard et al. 2008). VLA1623 is composed of three continuum sources: VLA1623A, a deeply embedded Class 0 source with no emission shortward of 24 μm; VLA1623B, a very cold and compact source separated 1.1″ from VLA1623A; and VLA1623W, a Class I source at a projected distance of 10" from VLA1623A. SMA observations of VLA1623 revealed that the easternmost component, VLA1623A, has a disk-like structure in $C^{18}O$ and $C^{17}O$ that was mimicked in continuum. Furthermore, VLA1623A's disk shows a velocity gradient characteristic of rotation. A simple eyeball analysis

Table 1: VLA1623's 1.3 mm continuum fluxes measured with ALMA

Source	R.A.	Decl.	Peak mJy beam^{-1}	Integrated mJy
VLA1623A	16:26:26.390	-24:24:30.688	93.1	201.3±1.2
VLA1623B	16:26:26.309	-24:24:30.588	93.5	96.3±0.7
VLA1623W	16:26:25.636	-24:24:29.488	21.6	37.3±0.9

of the position-velocity diagrams of the $C^{17}O$ and $C^{18}O$ emission by Murillo & Lai (2013) suggested that the disk was rotationally supported, most likely exhibiting pure Keplerian rotation. They concluded that further analysis is required to distinguish the pseudo-disk $v \propto R^{-1}$ pattern from the rotationally supported $v \propto R^{-0.5}$ profile.

In this paper, we present Atacama Large Millimeter/submillimeter Array (ALMA) Early Science Cycle 0 observations of VLA1623A in 1.3 mm continuum and $C^{18}O$ emission. The results of the $C^{18}O$ ALMA observations are consistent with previous Sub-Millimeter Array (SMA) $C^{18}O$ observations in that they both show the disk-like structure and velocity gradient centered on VLA1623A. However, the sensitivity and spatial and velocity resolutions of the detection are significantly increased and improved due to ALMA's capabilities. To determine whether the $C^{18}O$ emission is tracing a rotationally supported disk about VLA1623A, we performed position-velocity diagram analysis and modeled the $C^{18}O$ emission in order to determine the extent to which the observed structure is rotationally supported.

2.2 Observations

We observed VLA1623 (pointing coordinates α=16:26:26.419 δ=-24.24.29.988 J2000) with the Atacama Large Millimeter/submillimeter Array (ALMA) during the early science Cycle 0 period on April 8, 2012. Observations were done in Band 6 (230 GHz) using the extended configuration, consisting of 16 antennae with a maximum baseline of ∼400m, for a total observing time of one hour and a duty cycle of 58%. Calibration was done with 3C 279, 1733-130, and Titan for bandpass, gain, and flux calibration, respectively. The spectral configuration was set up to observe four molecular lines: DCO^+ (3-2), $C^{18}O$ (2-1), N_2D^+ (3-2), and ^{12}CO (2-1), in addition to continuum. No significant N_2D^+ emission was detected. In this paper we only analyze and discuss the results of $C^{18}O$ and continuum. The remaining lines will be discussed in future papers. The spectral configuration provided a velocity resolution of 0.0833 km s^{-1} for $C^{18}O$.

Reduced data were received on June 15, 2012. We redid the data calibration and reduction using the standard pipeline for single-pointing observations. Comparison of the delivered data and our recalibrated data shows consistency in the continuum flux levels. The synthesized beam size is $0.79'' \times 0.54''$ for the continuum and $0.79'' \times 0.61''$ for $C^{18}O$, providing enough resolution to resolve the continuum and line emission from each source.

We compare the 1.3mm continuum observations obtained with ALMA (this work) and SMA (Murillo & Lai 2013). To compare, VLA1623B's integrated flux is used since it was the most sensitive to the flux calibrations. We use the same region and task (CASA's imstat task) to measure the integrated flux for both datasets. For the SMA

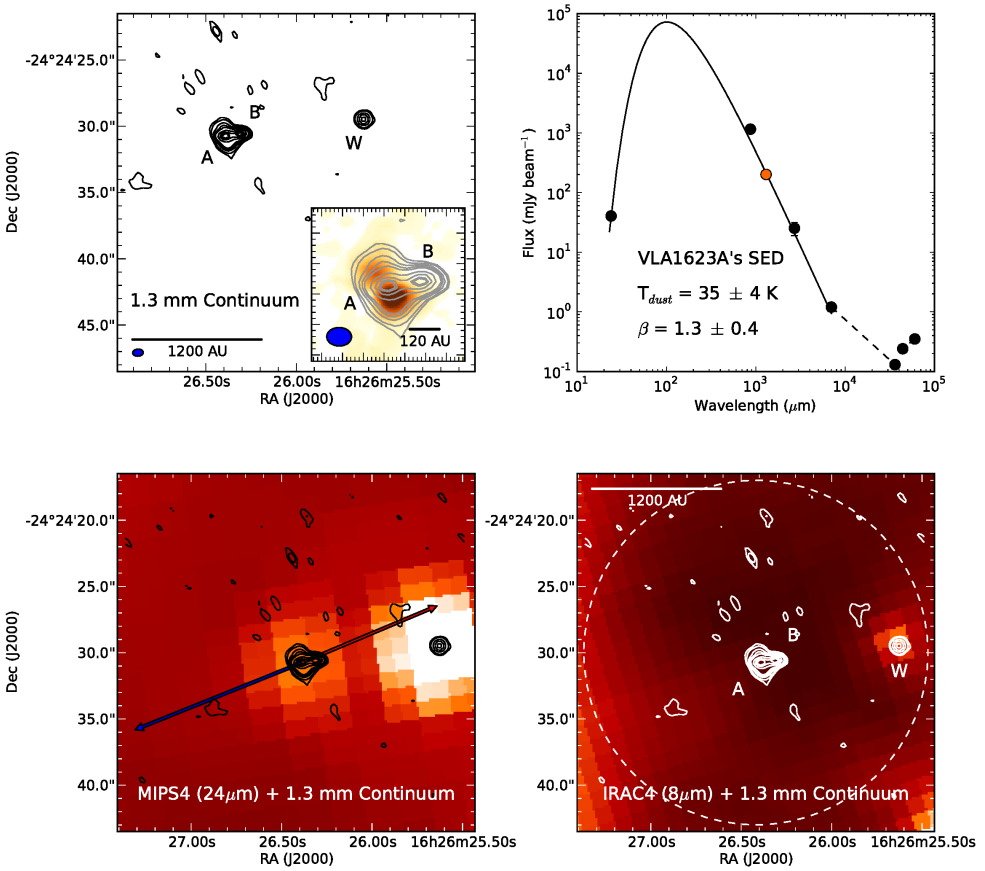

Figure 1: VLA1623 in continuum: *Top left:* ALMA 1.3 mm continnum, three components are observed: VLA1623A, B, and W. While B and W are observed to be compact, A shows an extended and flattened component. The inset shows a zoom-in of VLA1623A and B (black contours), overlaid with intensity-integrated $C^{18}O$ (2-1) (halftone). Contours are in steps of 3σ, 5σ, 10σ, 15σ, 20σ, 40σ, 60σ, and 78σ, with σ=1 mJy beam^{-1}. *Top right*: VLA1623A's SED; the orange point indicates VLA1623A's integrated continuum flux obtained from our ALMA observations. The solid line is the best fit of a single-temperature graybody fit, and the resulting parameters are indicated in the figure. Flux uncertainties are usually smaller than the plot symbols. *Bottom left*: ALMA 1.3 mm continuum contours overlaid on Spitzer MIPS1. Contours are the same as in the top left figure. Red and blue arrows indicate the red- and blue-shifted large-scale outflow direction. *Bottom right*: ALMA 1.3 mm continuum contours overlaid on Spitzer IRAC4. Contours are the same as in the top left figure. The dashed circle indicates the field of view of the ALMA observations.

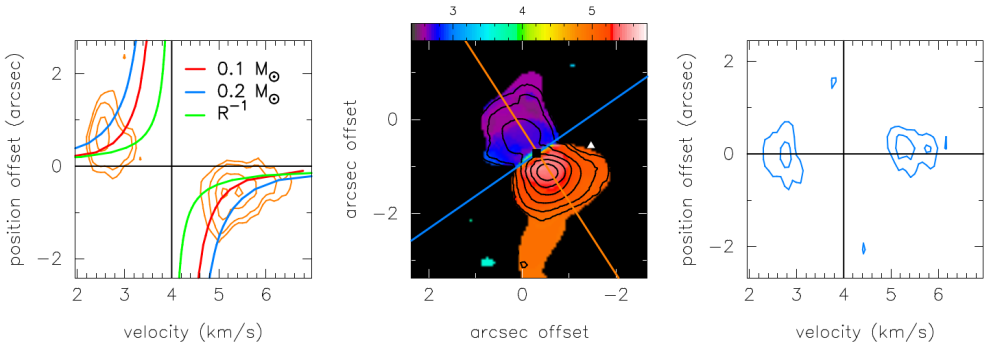

Figure 2: Observed $C^{18}O$ (2-1): *Left*: Pure Keplerian rotation curves ($v \propto R^{-0.5}$, red and blue) and infall ($v \propto R^{-1}$, green) are overlaid on the PV diagram. This suggests that the emission may be rotationally supported with $M_* \sim$ 0.1-0.2 $M_\odot$. *Center*: $C^{18}O$ velocity map (Moment 1, halftone) and intensity integrated (Moment 0, contours) maps. Contours are in steps of 3σ, 5σ, 10σ, 15σ, 20σ and 25σ with σ = 13 mJy beam^{-1}. VLA1623A and B's positions are marked with a square and triangle, respectively. Orange and blue lines indicate the image-space PV diagram cuts at PA = 35° (left) and 125° (right), respectively. *Right*: Lack of velocity gradient suggests no outflow contamination on the $C^{18}O$ emission. In both PV diagrams contours are in steps of 3σ, 5σ, 10σ and 15σ where σ = 19 mJy beam^{-1} and the black lines indicate the systemic velocity and position of VLA1623A.

data, VLA1623B has an integrated flux of 96.8±0.7 mJy, while for the ALMA data, VLA1623B has an integrated flux of 96.3±0.7 mJy. This shows that both observations are consistent.

JCMT observations towards VLA1623 by Jørgensen et al. (2002) detected $C^{18}O$ (2-1) with a flux of 12.1 K km s^{-1} (174 Jy km s^{-1}, with 14.46 Jy/K). Our $C^{18}O$ (2-1) detection with ALMA has a flux of 13 Jy km s^{-1}. Thus, we recover ∼8% of the total single-dish detected flux.

2.3 Results

2.3.1 1.3 mm continuum

ALMA 1.3 mm continuum observations detect three continuum sources (Fig. 1, top left), in agreement with previous SMA observations (Murillo & Lai 2013; Chen et al. 2013). The easternmost source, VLA1623A, shows an elongated and flattened morphology peaking in the center, with the elongation perpendicular to the outflow direction (Fig. 1, top left insert). VLA1623A is detected at 24 μm, but shows no emission shortward of 24 μm (Fig. 1, bottom row). VLA1623B, located to the west of VLA1623A and separated by 1.1″, is compact and shows no discernible infrared emission (Fig. 1, bottom row) suggesting that it is deeply embedded and cold. The westernmost source, VLA1623W (∼10″ separation), is observed to be compact and dimmer than the other two sources in millimeter, but is bright in the infrared (Fig. 1, bottom row). Although VLA1623W is located at the edge of the field of view in our ALMA observations, it is a ∼20σ detection, and its flux and position coincide with previous detections of this source, so we consider it a genuine detection. Peak and integrated fluxes of each source are listed in Table 1. Integrated fluxes for each source

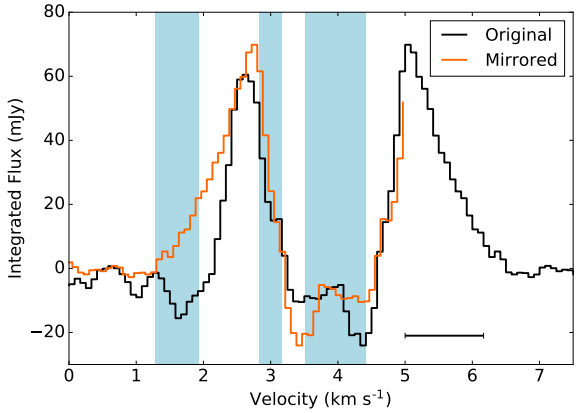

Figure 3: $C^{18}O$ (2-1) line profile. The unaltered spectral profile (black) is overlaid with a portion of the spectral profile mirrored about 4.0 km s^{-1} (orange). Light blue rectangles mark the widths obtained from the best- fit thin disk model (Table 3) of the foreground material (1.6 and 3 km s^{-1}) and the envelope (4.0 km s^{-1}). The horizontal line between 5 and 6.5 km s^{-1} shows the velocity range used for the UV-space PV diagram.

were obtained by integrating the continuum emission over a region the size of the source out to 3σ. In this paper, we focus on VLA1623A, whose SED is shown in the top right of Fig. 1.

2.3.2 $C^{18}O$ (2-1)

The $C^{18}O$ (2-1) emission towards VLA1623A shows an elongated and flattened structure perpendicular to the outflow direction, following the same shape as VLA1623A's 1.3 mm continuum emission (Fig. 1, top left insert, Fig. 2, center). Results and discussion of the $C^{18}O$ emission towards VLA1623B and W are presented in Appendix 2.A.

The $C^{18}O$ emission about VLA1623A exhibits a velocity gradient along the major axis, with blueshifted material to the NE and redshifted material to the SW in the velocity range of 2 to 6.5 km s^{-1} (Fig. 2). The results of our ALMA observations presented here are consistent with SMA observations of $C^{18}O$ (2-1) toward VLA1623A (Murillo & Lai 2013). In comparison, however, our ALMA observations have higher sensitivity (rms noise = 18 mJy $beam^{-1}$) and velocity resolution (0.0833 km s^{-1}) than previous SMA observations (rms noise = 42 mJy $beam^{-1}$ and velocity resolution = 0.275 km s^{-1}). ALMA's higher sensitivity and velocity resolution allow us to obtain a better view of the structure being traced and a deeper kinematical analysis. In addition, the high sensitivity allowed detecting previously unknown filament-like features, located to the north and south of VLA1623A's $C^{18}O$ disk structure (Fig. 2, center). These features may be the beginnings of a disk wind (Klaassen et al. 2013).

The observed velocity gradient along the major axis suggests rotation (Fig. 2 left and center), as previously suspected from the SMA detection of $C^{18}O$. Furthermore, lack of a velocity gradient along the outflow axis indicates that the observed $C^{18}O$ line emission is tracing only the envelope and/or disk structure (Fig. 2 right).

The ρ Ophiuchus region is known to have several layers of foreground clouds along the line of sight (Loren 1989), as shown by studies toward cores B and E in ρ Ophiuchus (Loren 1989; Boogert et al. 2002; van Kempen et al. 2009b). However, there are

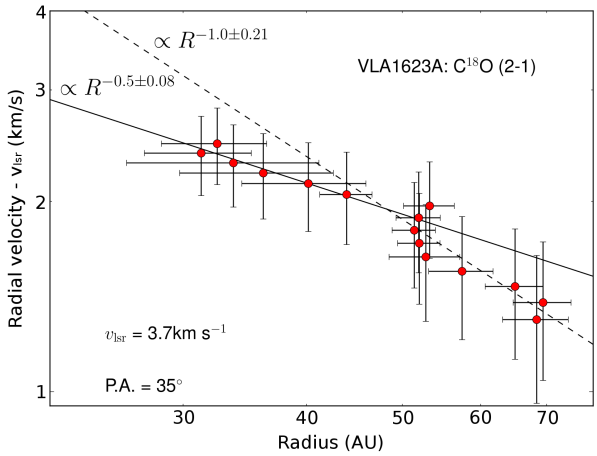

Figure 4: UV-space PV diagram of $C^{18}O$. v_{lsr} = 3.7 km s^{-1} . The red points indicate the redshifted ($v > 5.0$ km s^{-1}) emission. The velocity range covered in this diagram is indicated in Fig. 3. Blueshifted emission ($v < 2.8$ km s^{-1}) is not included in the diagram since it is strongly affected by foreground emission (see Fig. 3 and Sect. 2.3.2). The points are fit with a power law of the form $v = aR^n$. The solid line shows the fit to the high-velocity points ($v > 5.7$ km s^{-1}), while the dashed line shows the fit to the low-velocity points ($v < 5.7$ km s^{-1}). This suggests that the pure Keplerian disk extends to a radius of 50 AU.

no current studies of the foreground of VLA1623 (ρ Ophiuchus core A). From JCMT observations toward VLA1623, it is difficult to determine the position of absorbing material given the dense and active region (Jørgensen et al. 2004). Determining the foreground over a large area from single-dish data requires a more in-depth study beyond the scope of this paper. Thus to estimate the positions of the absorbing material, we compared the original and mirrored spectra (Fig. 3). From line observations, Mardones et al. (1997) and Yu & Chernin (1997) report VLA1623's systemic velocity v_{lsr} to be between 3.4 to 3.8 km s^{-1}. Mirroring the spectra about this range of v_{lsr} does not produce a symmetric spectra, however. We instead find that the $C^{18}O$ spectra is better mirrored about 4.0 km s^{-1}, which would suggest that VLA1623's v_{lsr} might be 4.0 km s^{-1}. We then consider the full range of v_{lsr} = 3.4 to 4.0 km s^{-1} in this work. Regarding the absorbing material, it is clear from Fig. 3 that there is absorption at velocities near 2 and 3 km s^{-1}, as well as absorption towards the systemic velocity. The absorption at the systemic velocity is either due to absorption caused by VLA1623's outer envelope or to resolved-out emission. On the other hand, the absorptions near 2 and 3 km s^{-1} are more likely to be due to foreground clouds. These foreground clouds "eat out" some of the blueshifted emission, causing the observed red- and blueshifted $C^{18}O$ emission to seem asymmetric towards VLA1623A.

2.4 Analysis

2.4.1 Position-velocity diagrams

The first and most common way of analyzing the kinematics of line emission is through position-velocity (PV) diagrams. Here we perform image-space and UV-space PV

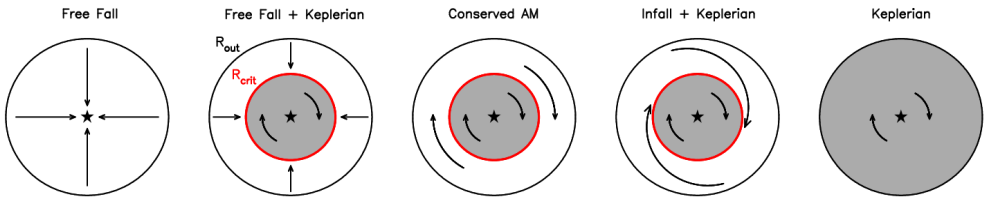

Figure 5: Cartoon illustrating the velocity structure distribution in the disk, shown here face on, for each model examined.

diagrams. Image-space PV diagrams project the line-emission 3D data cube into a 2D plane along a cut, defined by position angle (PA) and source position, over the structure of interest. UV-space PV diagrams, on the other hand, are constructed by fitting, channel by channel, the UV visibilities of the line emission to find the peak position in each channel (Lommen et al. 2008; Jørgensen et al. 2009). The peak positions of each channel are then rotated to the PA along the velocity gradient, projected onto PV space and fit with a power law in log-log space. The resulting PV diagram and power law fit provide insight into the kinematic structure of the line emission.

The $C^{18}O$ velocity integrated map (Fig. 2, center) shows a velocity gradient along the major axis (PA = 35±15°) of the structure, perpendicular to the outflow. The image-space PV diagram along the structure's major axis (Fig. 2, left) is characteristic of a rotating structure around a 0.1 to 0.2 $M_\odot$ object, with pure infall clearly providing a worse fit. The rotation curves in Fig. 2 (left panel) do not account for inclination effects.

Figure 4 shows the UV-space PV diagram of the $C^{18}O$ emission. The blueshifted emission is excluded from the diagram since it is strongly affected by foreground emission (Fig. 3, also see Sect. 2.3.2) at higher velocities. Thus we only fit the redshifted points, with velocities greater than 5.0 km s^{-1}. The velocity range of points used is shown in Fig. 3. The data points are fit with a power law of the form $v = aR^n$, and we find that the UV-space PV diagram is independent of the inclination angle of the structure. The entire range of possible $v_{\rm lsr}$ (3.4 to 4.0 km s^{-1}) was fit. The results of the fit for any $v_{\rm lsr}$ are within the error of the fit presented here, which uses the mean $v_{\rm lsr}$, 3.7 km s^{-1}. Thus we find that the high-velocity points ($v > 5.7$ km s^{-1}) are well fit by $v \propto R^{-0.5\pm0.08}$, giving a central protostellar mass M_* of 0.22±0.02 $M_\odot$. On the other hand, the low-velocity points (5 km $s^{-1} < v < 5.7$ km s^{-1}) are well fit by $v \propto R^{-1}$. This suggests that there is a turnover point at 50 AU, where the inner parts, i.e. $R \leq 50$ AU, are under the effect of pure Keplerian rotation and the outer parts are undergoing infall. In the following section, we argue that the lower velocity points are affected by optical depth and absorption, and that R can be larger.

2.4.2 Modeling of $C^{18}O$ (2-1)

Based on the results from the PV diagrams, which suggest there is a rotationally supported component in the observed $C^{18}O$ emission, we proceed to further investigate the structure and its kinematics using an analytical thin disk model with the addition of absorbing foreground material. The model does not include radiative transfer or excitation since the goal is to study the kinematics and structure of the observed disk.

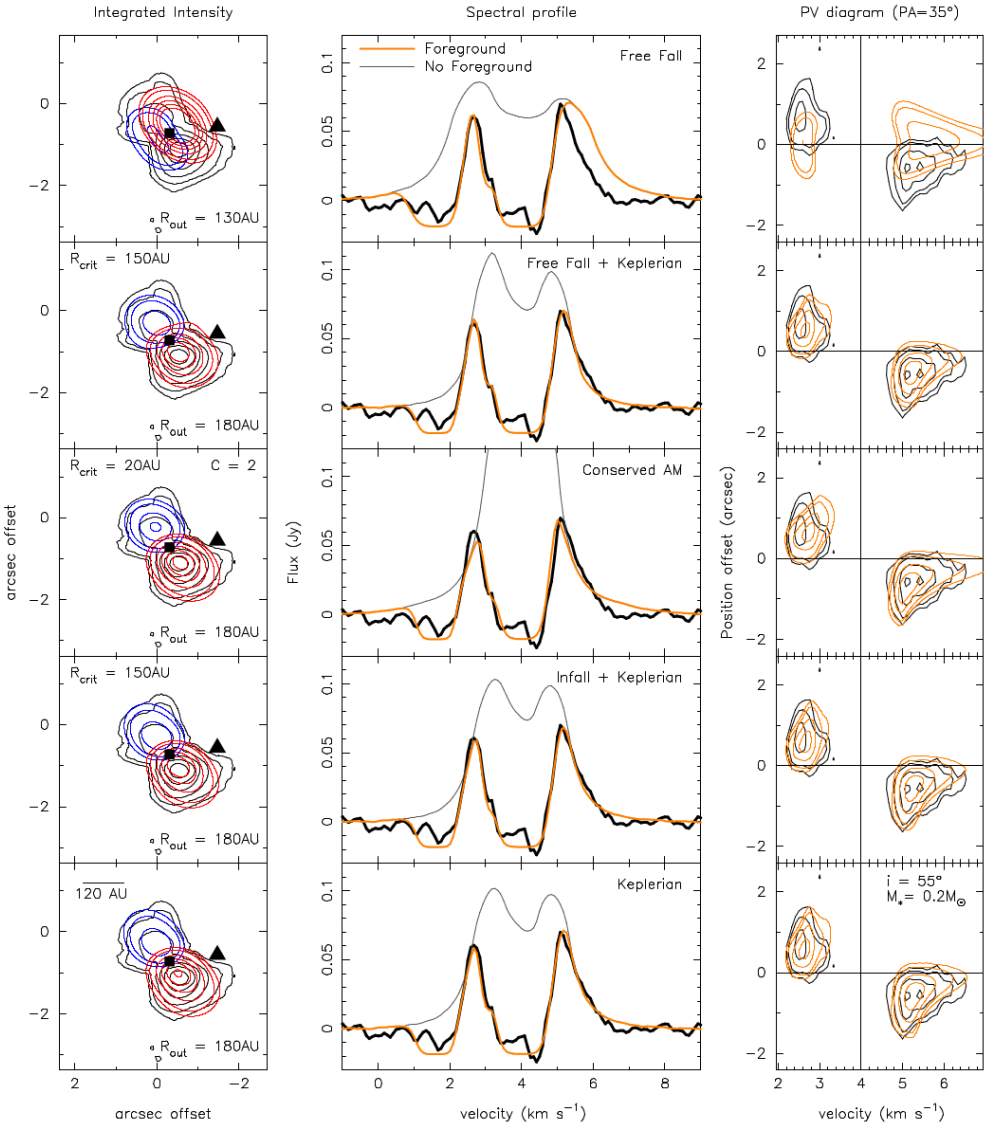

Figure 6: Comparison of $C^{18}O$ observations (black lines) with a thin disk model (colored lines) that includes foreground components. The left column shows moment 0 maps with the red and blue lines showing red and blueshifted emission, respectively. Source positions are marked as in Fig. 2. The middle column compares the spectral profiles with and without foreground. The right column presents the image-space PV diagrams. The models shown here have two foreground components (at 1.6 and 3.0 km s^{-1}) and the resolved out envelope component (at 4.0 km s^{-1}). Contours both for observations and models are the same as those in Fig. 2. M_* and i for all models are shown in the last panel.

Table 2: Best fit thin disk model results

Parameter	Free fall	Free fall + Keplerian	Conserved AM	Infall + Keplerian	Keplerian
i (degrees)	55	55	55	55	55
$R_{\rm out}$ (AU)	130	180	180	180	180
$R_{\rm crit}$ (AU)	...	150	20	150	...

The input parameters include the outer radius $R_{\rm out}$ of the disk, source position, PA, inclination i of the disk, the mass of the central source M_*, and the temperature and column density gradients of the disk surface. Generated maps are convolved to the observed clean beam. The model output is in the form of position-position-velocity (xyv) data cubes in FITS format.

For all of the models we fix the central protostellar mass $M_* = 0.2$ M$_\odot$, which was obtained from the PV diagram analysis (see Sect. 2.4.1), and the position angle to 35°, since these parameters are well constrained from the PV diagrams (see Sect. 2.4.1 and Figs. 2 and 4). We set $v_{\rm lsr} = 4.0$ km s^{-1}, which is the symmetry axis of the spectrum. The distance is set to 120 pc, and the source position is set slightly offset by $0.02'' \times 0.04''$ to the SW from VLA1623A's position to match the center of the C^{18}O emission, i.e. the rotation axis.

Other free parameters in the model are line width $v_{\rm width}$, inclination i, and outer radius $R_{\rm out}$. These values are constrained to best fit the observations. The attempted value ranges for each parameter are 0.1 km s^{-1} $\leq v_{\rm width} \leq$ 1.0 km s^{-1}; 0° (face-on) $\leq i \leq$ 90° (edge-on); 100 AU $\leq R_{\rm out} \leq$ 200 AU. The best fit for almost all models was obtained with $v_{\rm width} = 0.2$ km s^{-1}, $i = 55°$, and $R_{\rm out} = 180$ AU, except for the free-falling disk model, where $R_{\rm out} = 130$ AU. Since we do not have a way to constrain the temperature and column density gradients, we assume the observed emission is optically thin, and set the density as a constant and adjust the temperature gradient to match the observed spectral profile.

As discussed in Sect. 2.3.2, we suspect the presence of absorbing material along the line of sight of VLA1623, which would affect the observed emission and spectral profile, and thus influence the model fitting. From the data presented here we can not be completely certain of the characteristics of the absorbing material. Thus, we adjust the model velocities, peak opacity, and widths of the foreground clouds aiming to best fit the observed spectral profile. We assume that the foreground clouds only absorb with opacity following a Gaussian-like profile of the form

$$\tau(v) \propto \exp\left(-0.5\left(\frac{v - v_0}{\sigma}\right)^2\right). \tag{2.1}$$

By adjusting the absorbing material parameters to fit the observed spectral profile, we find that the best results are obtained by introducing three absorbing layers, one corresponding to the envelope at 4.0 km s^{-1}, and two corresponding to possible foreground clouds at 1.6 and 3.0 km s^{-1}. The characteristics of the absorbing material for each model are listed in Table 3.

To study the kinematical structure of the disk, we modeled five cases: (1) free-falling disk, (2) free-falling outer disk plus inner Keplerian disk, (3) conservation of angular momentum (AM), (4) infalling ($v \propto R^{-1}$) outer envelope plus inner Keplerian

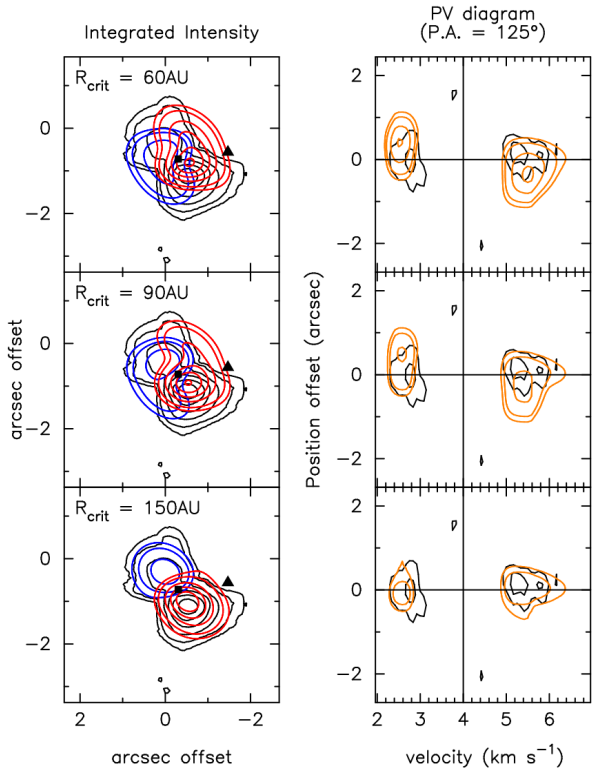

Figure 7: Free fall plus Keplerian case for three different $R_{\rm crit}$. The best fit model (color) to the data (black) is obtained as $R_{\rm crit}$ approaches $R_{\rm out}$. Right panels show PV diagram along outflow direction (P.A. = 125°). All contours and the model at $R_{\rm crit}$ = 150 AU are the same as in Fig. 6.

Table 3: Absorbing material for best fit thin disk model

	Free fall	Free fall + Keplerian	Conserved AM	Infall + Keplerian	Keplerian
Envelope					
velocity (km s^{-1})	4.0	4.0	4.0	4.0	4.0
opacity	7.0	7.0	7.0	7.5	7.0
width (km s^{-1})	0.9	0.99	0.99	0.99	0.99
Foreground 1					
velocity (km s^{-1})	1.6	1.6	1.6	1.6	1.6
opacity	5.0	5.0	5.0	5.0	5.0
width (km s^{-1})	0.89	0.64	0.62	0.64	0.64
Foreground 2					
velocity (km s^{-1})	3.0	3.0	3.1	3.05	3.0
opacity	0.39	0.29	0.29	0.29	0.29
width (km s^{-1})	0.39	0.34	0.34	0.34	0.34

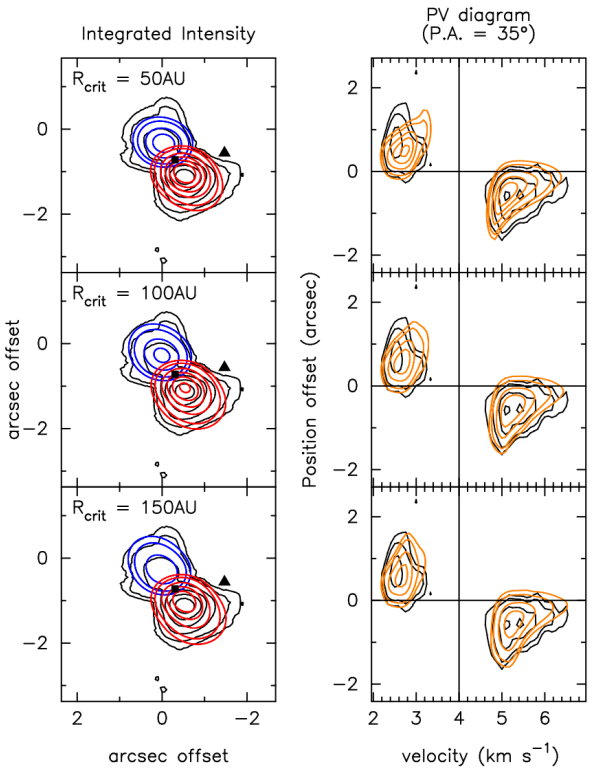

Figure 8: Infall plus Keplerian case for three different $R_{\rm crit}$. The best fit model (color) to the data (black) is obtained as $R_{\rm crit}$ approaches $R_{\rm out}$. Right panels show PV diagrams along the disk's major axis (P.A. = 35°). All contours and the model at $R_{\rm crit}$ = 150 AU are the same as in Fig. 6.

disk, and (5) pure Keplerian disk. For Cases 2, 3, and 4, we define a critical radius $R_{\rm crit}$ parameter (1 AU $\leq R_{\rm crit} < R_{\rm out}$) that defines the radius at which the transition from one velocity structure to the other occurs. Figure 5 illustrates the velocity structure distribution of each of the modeled cases. In Sect. 2.4.3 we briefly describe each model and the results obtained.

Figure 6 presents the best fitting results for the five cases modeled. We overlay the observed and modeled spatial distribution, spectral profile, and image-space PV diagram. Model spectral profiles are shown both with and without foreground absorption. The image-space PV diagram for each model was constructed along the disk's major axis. The best fit parameters obtained for each of the models are shown in Fig. 6 and listed in Table 2. To determine the best fit model of all five cases examined, we first compared each model and observations by eye and then through the residuals obtained by subtracting the channel maps of the observations and model. We deemed the model with the least residual the best fit (discarding the filaments to the north and south). Appendix 2.B shows the channel map for each model, compared with observations and the corresponding residual.

2.4.3 Model results

Free falling disk: In the very early stages of star formation, the envelope of a protostar is thought to be under free fall collapse. Thus, if there was any disk-like structure around the protostar at this stage, its motion would be that of free fall as well, i.e. a free-falling disk (Fig. 5). In our model, we study a free-falling disk structure where all motions are confined to the plane of the disk. The velocity structure within the disk structure is described as

$$v_{\rm ff}^{r} = \sqrt{\frac{2GM_{*}}{R}}. \tag{2.2}$$

In Fig. 6, the top row shows the thin disk model under free fall. Figure 10 shows the channel map of the model and the residual. It is clear that the pure free fall case does not fit the observed $C^{18}O$ emission, since the velocity gradient is along the outflow direction, which is not the case in the observations. In addition, the wings in the spectral profile of this model are broad compared to the observed spectral profile.

Free fall plus Keplerian rotation: This case represents the formation of a rotationally supported disk in a young protostar whose outer disk is in free fall collapse (Figure 5). To describe the velocity structure transition, we use the parameter $R_{\rm crit}$, where $R < R_{\rm crit}$ produces

$$v_{\rm rot}^{\phi} = \sqrt{\frac{GM_{*}}{R}} \tag{2.3}$$

and $R \geq R_{\rm crit}$ is described by Eq. 2.2.

For this case, we experimented with different critical radii $R_{\rm crit}$ to determine if the observed emission is a combination of Keplerian rotation and free fall (Fig. 7). We find that the free fall region ($R > R_{\rm crit}$) is clearly visible unless $R_{\rm crit}$ approximates $R_{\rm out}$. Similar to the pure free fall case, the outer free fall region produces a velocity gradient along the outflow direction, which is visible in the PV diagram (Fig. 7); however, we do not observe any velocity gradient along the outflow direction in the $C^{18}O$ structure (Fig. 2, right). In addition, the $C^{17}O$ (3-2) emission observed with SMA (Murillo &

Table 4: Class 0 sources with disk

Parameter	NGC1333 IRAS4A2[a]	L1527	VLA1623A	Ref.
i (degrees)	10.7	∼85	55	1,2,3
$R_{\rm out}$ (AU)	310	90	180	1,2,3
M_* ($M_\odot$)	0.08±0.02	0.19±0.04	0.22±0.02	1,2,3
$M_{\rm env}$[b] ($M_\odot$)	5.6	0.9	0.8	4,5
M_*/M_{env}	0.01	0.2	0.28	...
$T_{\rm bol}$ (K)	51	44	10	1,5,3
$L_{\rm bol}$ ($L_\odot$)	1.9±0.9	1.97	1.1±0.2	1,2,6
$L_{\rm submm}/L_{\rm bol}$[c] (%)	3.6	0.8	1.2	...

References. (1) Choi et al. (2010); (2) Tobin et al. (2012b); (3) this work; (4) Froebrich (2005); (5) Kristensen et al. (2012); (6) Murillo & Lai (2013)
[(a)] $T_{\rm bol}$ and $L_{\rm bol}$ parameters are for NGC1333 IRAS4A, Choi et al. (2010) assumes IRAS4A2 contributes half of the $L_{\rm bol}$. [(b)] $M_{\rm env}$ is the total envelope mass of each system. [(c)] $L_{\rm submm}/L_{\rm bol} > 0.5\%$ is characteristic of Class 0 source (Froebrich 2005; André et al. 1993).

Lai 2013) shows a velocity gradient indicative of rotation, thus the outer part of the observed structure is not under free fall. Figs. 7 and 11 compare this model and the observations in detail, which show that only at $R_{\rm crit} = 150$ AU does the model closely approximate the observations.

Conserved Angular Momentum (AM): This case examines whether VLA1623A's $C^{18}O$ structure is described well by rotation with conserved angular momentum (Fig. 5), for example if the initial angular momentum of the cloud were conserved during collapse. The velocity structure in the inner region $R < R_{\rm crit}$ is given by Eq. 2.3, while at $R \geq R_{\rm crit}$ it is described by

$$v^{\phi}_{\rm AM} = C\sqrt{\frac{GM_*}{R_{\rm crit}}}\frac{R_{\rm crit}}{R} \tag{2.4}$$

where C is a constant indicating the increase in the Keplerian velocity at $R_{\rm crit}$.

For this model, we find that $C = 2$ with $R_{\rm crit} = 20$ AU provides the closest fit to the observations. In comparison to the other cases examined, this model produces broader wings and higher velocities at smaller radii, effects visible in the spectral profile and the PV diagram, respectively (Fig. 6). Additionally, from the spectral profile shown in Fig. 6, it is seen that this model does not correctly reproduce the blueshifted peak. Changing the C parameter does not resolve this issue, and changing the line width also broadens the wings. Furthermore, even though from the intensity integrated map the spatial distribution appears to fit the observations, inspecting the channel map residuals shows that the model does not quite agree with the observations (Fig. 12). Thus we determine that this scenario does not match the observations.

Infall plus Keplerian rotation: This case is similar to the free fall plus Keplerian case, but with the outer part of the envelope infalling onto the rotationally supported disk (Fig. 5). We consider this model a possibility from the results of the UV-space PV diagram (Fig. 4), which shows an inner region under Keplerian rotation and an outer region of infall, with a critical radius of ∼50 AU. Thus, for the inner rotating region (i.e. $R < R_{\rm crit}$) the velocity structure is described by Eq. 2.3, and for the outer

infalling region ($R \geq R_{\rm crit}$) it is given by

$$v^r_{\rm infall} = \sqrt{\frac{GM_*}{R_{\rm crit}}}\frac{R_{\rm crit}}{R}. \quad (2.5)$$

As in the free fall plus Keplerian case, we ran the model with different critical radii $R_{\rm crit}$ to determine how far each of the velocity structures extends (Fig. 8). Similar to the free fall plus Keplerian case, we find that the best fit occurs as $R_{\rm crit}$ approaches $R_{\rm out}$, with the best fit having $R_{\rm crit} = 150$ AU (Figs. 6 and 8). The discrepancy between the $R_{\rm crit}$ obtained from the modeling (150 AU) and that of the UV-space PV diagram from observations (50 AU) may be due to the low-velocity points being greatly affected by optical depth and absorption of the envelope. Keplerian rotation out to at least 150 AU represents a best fit scenario for the observed $C^{18}O$ emission. Because of the large $R_{\rm crit}$, it is difficult to distinguish this scenario from the following case. In Fig 13 the channel map comparison and residual between this model and the observations are shown.

Pure Keplerian rotation: In this case we model a Keplerian disk around a central protostar (Fig. 5). This velocity structure has been observed starting in Class I protostars and is common among Class II protostars. The velocity structure is given by Eq. 2.3.

We find this case to fit the observed $C^{18}O$ emission well, as the model agrees with the observations spatially, in the spectral profile and in the image-space PV diagram (Fig. 6). However, it is difficult to determine whether this scenario is considerably better than the infall plus Keplerian case. We discuss this further in the next section. In Fig. 14 the channel map comparison and residual between this model and the observations are shown.

2.5 Discussion

Our ALMA observations of VLA1623 reveal that the Class 0 component of this system, VLA1623A, has a disk structure in $C^{18}O$ (2-1) with an outer radius of 180 AU. Thin disk modeling with the addition of foreground indicates that the disk structure is most certainly Keplerian out to a radius of 150 AU. For the outer 30 AU, it is uncertain whether the velocity structure may be undergoing infall ($v \propto R^{-1}$) or pure Keplerian rotation. This uncertainty is due to the low S/N (5σ) in the outer edges of the observed disk structure, while the inner regions of the disk have a higher S/N (10 to 25σ), thus a better and more reliable fit is obtained in the inner parts of the observed structure. The presence of such a large Keplerian disk raises the question of how disks are formed in the early stages of protostellar evolution.

Regardless of the model, neither the infall plus Keplerian case nor the pure Keplerian case reproduces the weak filament-like structures to the north of the blueshifted emission (v = 2.3 to 2.47 km s^{-1}) and south of the redshifted emission (v = 4.8 to 4.97 km s^{-1}) (Figs. 2, 13, and 14). These structures may be produced by a disk wind (Klaassen et al. 2013) or material entrained by the outflow.

The idealized non-magnetized isothermal sphere collapse model of Terebey et al. (1984) suggests that disks may form during the early protostellar stages. As previously mentioned, under these conditions, the disk's centrifugal radius R_c is expected to grow proportional to t^3, where t denotes the time since collapse. To calculate the time since

collapse for $R_c = 150$ AU, we use the equation from Belloche (2013)

$$R_c(\mathrm{AU}) = 39 \left(\frac{\Omega}{4 \times 10^{-14} \text{ rad s}^{-1}} \right)^2 \left(\frac{a}{0.2 \text{ km s}^{-1}} \right) \left(\frac{m_{*+d}}{1 \text{ M}_\odot} \right)^3 \tag{2.6}$$

where Ω is the initial cloud core rotation rate, a is the sound speed, and $m_{*+d} = 0.975 \frac{a^3}{G} t$. Assuming VLA1623 has a rotation rate $\Omega = 4 \times 10^{-14}$ rad s$^{-1,}$ and the sound speed in the core is of $a = 0.2$ km s^{-1}, we obtain $t = 8.5 \times 10^5$ yr for a centrifugal radius of 150 AU. However, the old age obtained through this method is inconsistent with the expected age from T_{bol} (Ladd et al. 1998) and the estimated Class 0 lifetime obtained by Evans et al. (2009), which is on the order of 10^5 yr, although they conceded that for ρ Ophiuchus the lifetime is 4×10^4 yr, an order of magnitude lower than the age calculated above. Furthermore, based on outflow observations, VLA1623's dynamical timescale is between 0.2 and 2.5 $\times$ 10^4 yr (André et al. 1990; Nakamura et al. 2011). This indicates that there are other factors that enhance the formation of the disk. Possible factors that can influence disk formation may be fragmentation, turbulence, or the misalignment of the magnetic field and rotation axis. For the first factor, fragmentation, there is little work done on how fragmentation can enhance or hinder disk formation, with most work focusing on how a disk fragments. However, there may be a possible relation given that two of the three Class 0 sources reported as having rotationally supported disks are confirmed multiples (see Sect. 2.1 and below). The introduction of turbulence and its effect on disk formation from low to high masses has been studied by Seifried et al. (2013), finding that turbulence can encourage disk formation even when strong magnetic fields are present. Nakamura et al. (2011) studied the outflow generated turbulence in ρ Ophiuchus' main cloud, concluding that outflows can influence the dense cores significantly. However, from Nakamura et al. (2011) or this work, there is not enough information to determine the degree of influence that turbulence has on the formation of VLA1623A's disk. At present we can neither examine further nor rule out the role of turbulence. The last factor, magnetic field misalignment, is considered in-depth below.

Magnetic fields are expected to influence the formation of protostellar disks in the early stages of protostar formation. It it thus of interest to look into the magnetic field configuration of VLA1623. Holland et al. (1996) observed 800 μm polarization with the JCMT, finding a 2% polarization and a magnetic field perpendicular to the outflow direction. Hull et al. (2014a) also observed the field to be perpendicular to the outflow down to 2" resolution with CARMA observations. Murillo & Lai (2013) carried out polarization observations with the SMA (compact configuration, resolution $\sim 1.5''$) but found no significant detection. From these results, we infer that the magnetic field towards VLA1623 is not aligned with the rotation axis of VLA1623A's disk, and the field strength may be low. Krumholz et al. (2013) find that rotationally supported disks should form as early as the Class 0 stages with sizes of 100 AU or larger when the magnetic field direction and the disk's rotational axis misalignment are large and the magnetic field strength is low. The presence of a fairly large rotationally supported disk around VLA1623A is consistent with the Krumholz et al. (2013) predictions, given VLA1623A's misalignment of 84° between magnetic field direction and rotational axis (Hull et al. 2013). In addition, the disk size is sensitive to the initial cloud density profile, with centrally concentrated profiles favoring larger disks. Moreover, the discrepancy between magnetized models of disk formation and VLA1623A's disk may be due to the sink particle parameters used to represent the forming protostar in

the models (Machida et al. 2014).

Two other Class 0 sources have been reported as presenting a Keplerian disk structure: NGC1333 IRAS4A2 and L1527. The characteristics of these sources are listed in Table 4 along with VLA1623A's characteristics. It should be noted that the parameters for NGC1333 IRAS4A2 are obtained under the assumption that this source contributes half of the bolometric luminosity and that both sources in the NGC1333 IRAS4A binary have the same bolometric temperature. Thus, in comparisson, VLA1623A is noticeably younger than L1527, based on the bolometric temperature and luminosity ratio. On the other hand, we cannot determine the relative evolutionary stages of VLA1623A and NGC1333 IRAS4A2 with certainty. We can assume, however, that VLA1623A is younger than NGC1333 IRAS4A2 based on the bolometric temperature. It must be noted, though, that the inclination angle of a protostar can affect the calculated parameters and thus affect the derived evolutionary parameters. Given that all three sources have different inclination angles, this may well affect the comparison. However, it is very possible that VLA1623A's disk is the youngest disk among the three sources, given that VLA1623A is still deeply embedded and shows no emission shortward of 24μm.

2.6 Conclusions

We have presented ALMA Cycle 0 Early Science Band 6 extended configuration observations of $C^{18}O$ (2-1) and continuum towards VLA1623. From these observations, we found three continuum sources that are consistent with previous observations and $C^{18}O$ emission centered at VLA1623A with signatures of rotation and an outer radius of 180 AU. Through PV diagram analysis and modeling of the observed $C^{18}O$, we determine that the emission traces a Keplerian disk out to 150 AU around a 0.2±0.02 $M_\odot$ protostar. The weak magnetic field and its misalignment with the disk's rotational axis may have increased the chances of disk formation at such an early stage. There may also be the possibility that fragmentation played a role in the early disk formation, but this is unclear from the results obtained here. Comparison of evolutionary indicators of VLA1623A with those of the other Class 0 sources showing indications of Keplerian disks suggest that VLA1623A's disk may be the youngest among the Class 0 Keplerian disks. Our results show that disks, and more precisely rotationally supported or Keplerian disks, can be formed in the Class 0 stage of protostellar evolution even with fairly large radii. However, our results also hint that the environmental factors play a larger role than evolutionary stage in the formation of disks.

Appendix

2.A VLA1623W

In our ALMA observations, we detect VLA1623W in continuum (see Sect. 2.3.1 and Fig. 1) and in $C^{18}O$ line emission (Fig. 9), which was previously undetected with SMA observations. The emission is weak, peaking at 5σ in the channel maps and at 13σ in the intensity integrated map, and it has a velocity range of about -0.5 to 1 km s^{-1}. Noteworthy is VLA1623W's apparent systemic velocity $v_{\rm lsr}$ between 0 and 1 km s^{-1}, which differs from VLA1623A's systemic velocity by 3 to 4 km s^{-1}. VLA1623W's

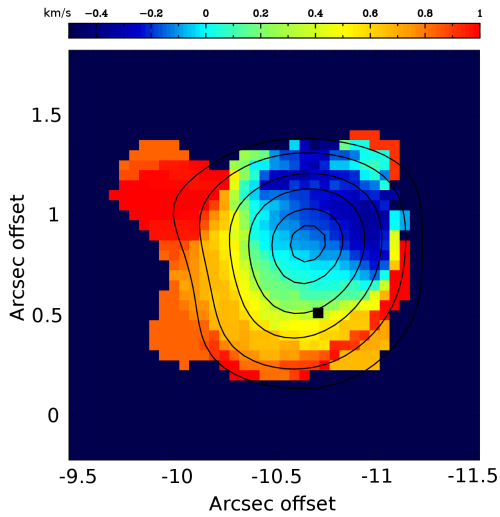

Figure 9: Integrated intensity (Moment 0, contours) and velocity (Moment 1, halftone) maps of $C^{18}O$ (2-1) detection towards VLA1623W. The position of VLA1623W is marked with a black square. Contours are in steps of 3σ, 5σ, 8σ,10σ, 12σ, and 13σ with $\sigma = 13$ mJy beam^{-1}.

$v_{\rm lsr}$ is difficult to determine with certainty since the emission appears to be strongly affected by foreground material (see Sect. 2.3.2) and the low S/N of the detection. Finally, no $C^{18}O$ emission was detected towards VLA1623B (Fig. 1, top left inset), which is consistent with previous CO depletion findings (Murillo & Lai 2013).

The velocity gradient of VLA1623W's $C^{18}O$ emission appears to be consistent with a rotationally supported disk structure, and given that VLA1623W is classified as a Class I source (Murillo & Lai 2013), this is very likely. However, since the emission is very close to the edge of the field of view (Fig. 1) and is affected by foreground absorption, we are limited in carrying out kinematical analysis of the emission.

Finally the large difference in systemic velocity from VLA1623A and B may suggest one of two scenarios. First, VLA1623W is not part of the system, but is instead a foreground or nearby source, that due to projection effects seems to be part of the system. However, Dzib et al. (2013) rule out the possibility of VLA1623W (or VLA1623B) being a foreground or background object due to its proper motion. Second, due to three-body interaction, VLA1623W was ejected from the closer binary of VLA1623A and B (Reipurth 2000). This possibility is very likely, given that VLA1623B may be a very recent formation, which would have caused the binary, now triple, to become unstable and eject one of the components. This ejection would cause VLA1623W to lose some of its envelope mass and appear more evolved, since one of the classification criteria is the envelope to central star mass ratio. The loss of mass would also make it more visible in the infrared and affect its evolution.

2.B Comparison of thin disk models and observations

In this appendix, we present the channel map comparison for each model and observations, as well as the residual obtained from subtracting the model from the observations. The figures presented below are a supplement to Fig. 6 in order to gauge the best-fitting model of the observed emission. All figures below show the blueshifted emission in the velocity range of 2.3 to 3 km s^{-1}, while the redshifted emission is in the velocity range of 4.8 to 6.5 km s^{-1}.

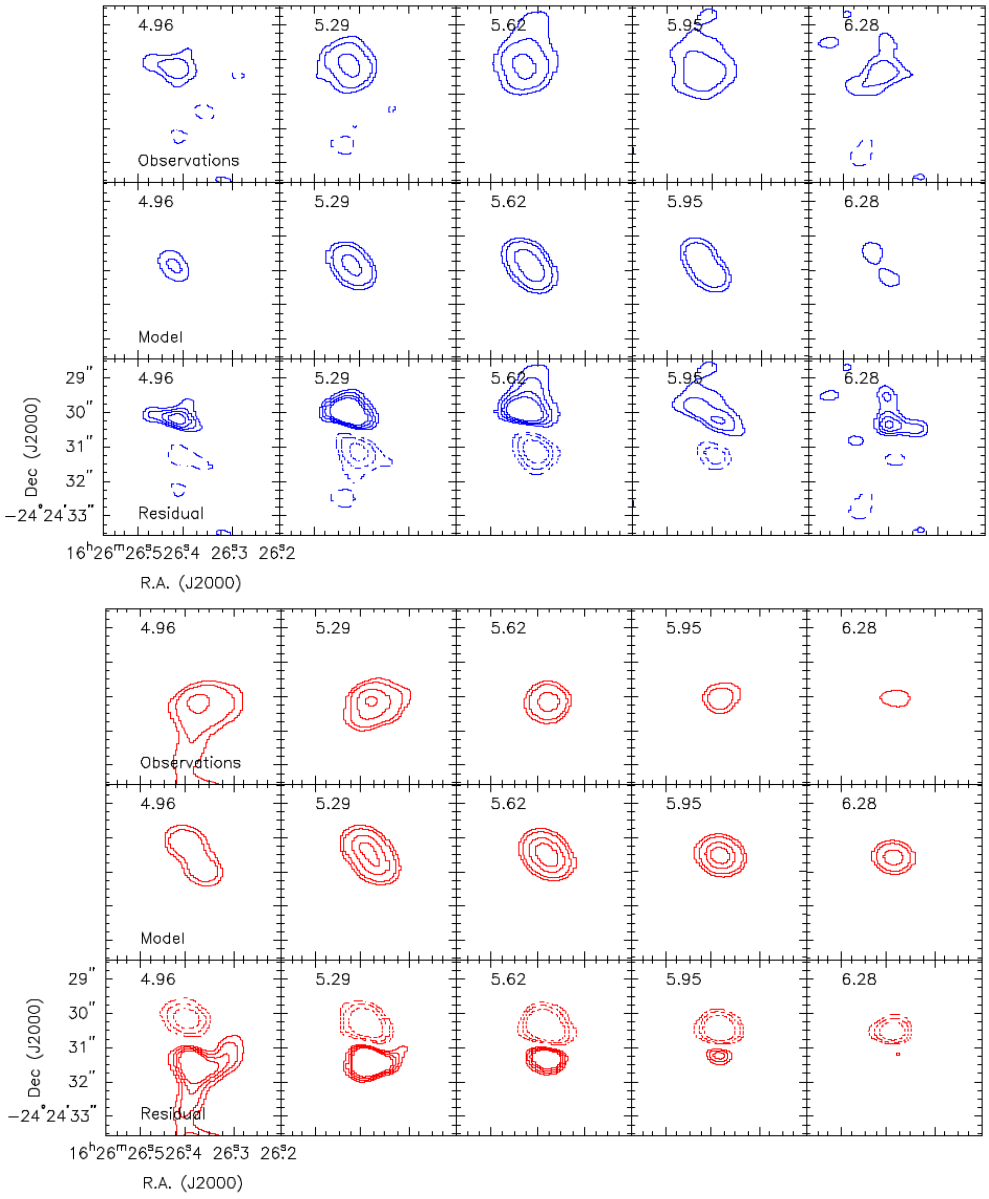

Figure 10: Channel maps of $C^{18}O$ observations (top), free falling disk model shown in Figure 6 (middle) and residual (bottom panel). The blue contours show the blueshifted emission and the red contours the redshifted emission. Number labels on the top of each panel indicate the velocity of that channel. Channels are binned to a velocity resolution of 0.16 km s^{-1} for the blueshifted emission, and 0.33 km s^{-1} for the redshifted emission for better display. Contours are in steps of 3σ, 5σ, 10σ, 15σ, 20σ and 25σ for the observations and model channel maps, and -8σ, -5σ, -3σ, 3σ, 4σ, 5σ and 6σ for the residual channel map, where $\sigma = 19$ mJy $beam^{-1}$.

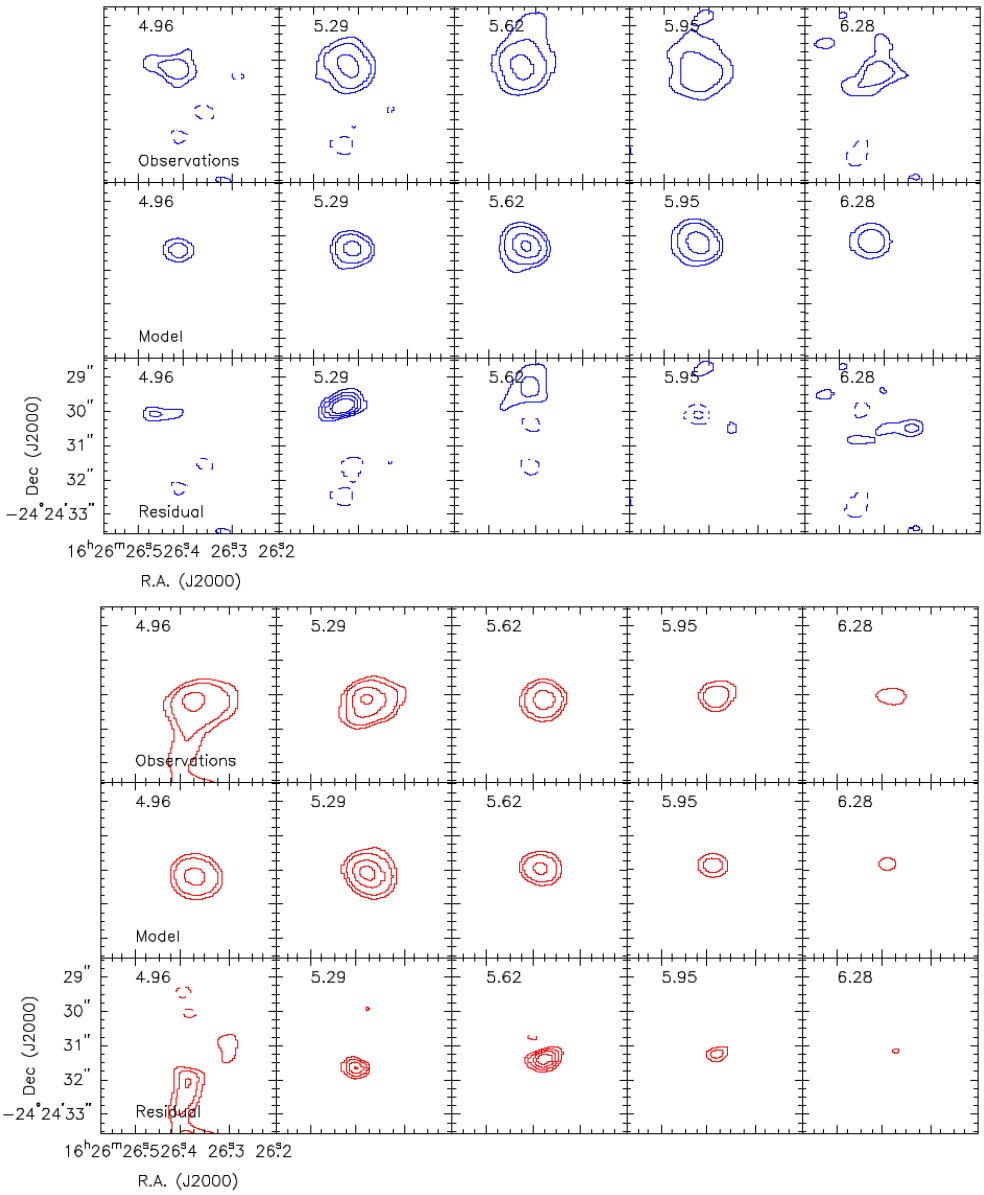

Figure 11: Same as Figure 10 but for the free fall plus Keplerian disk model shown in Figure 6.

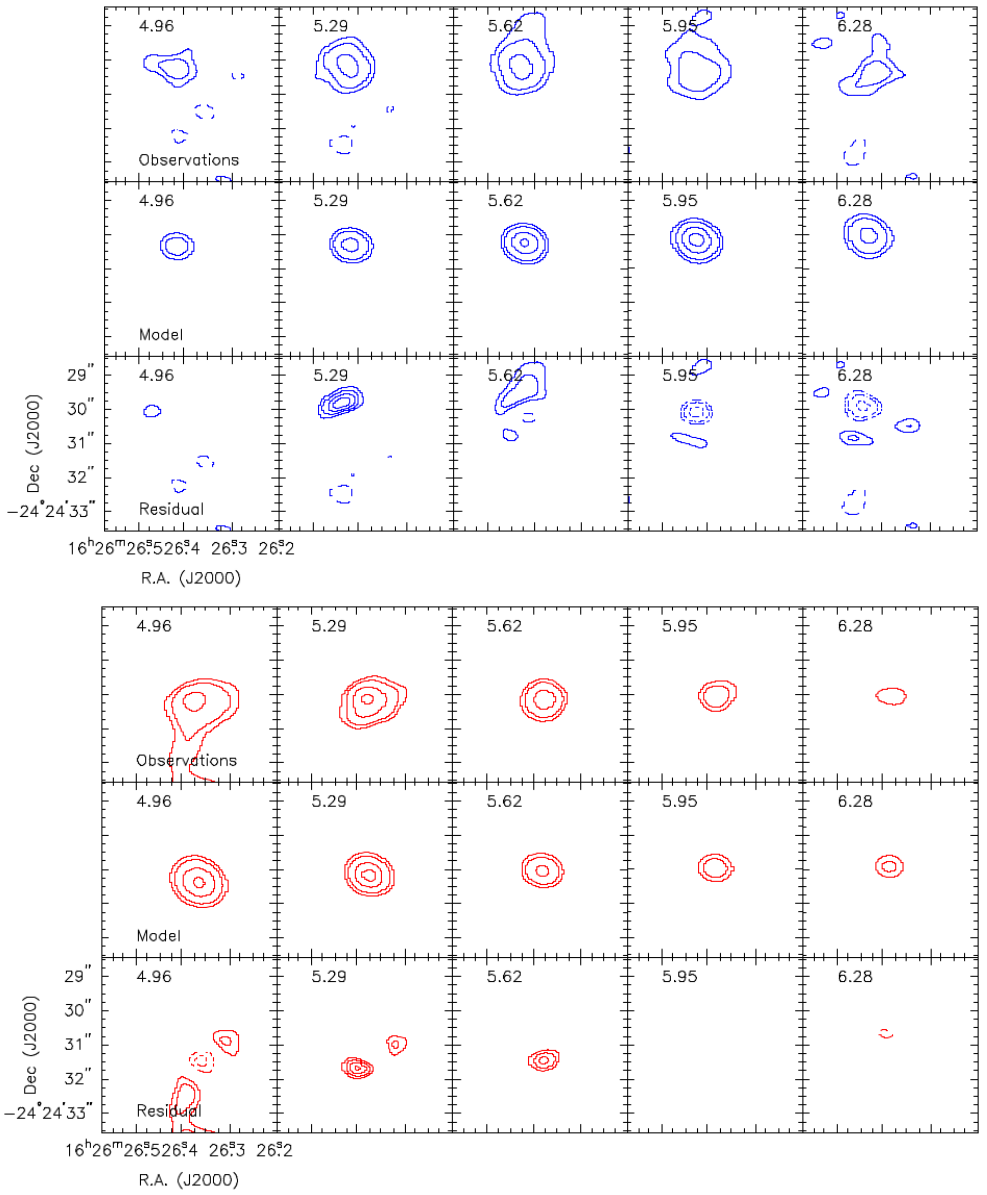

Figure 12: Same as Figure 10 but for the Conserved Angular Momentum disk model shown in Figure 6. Note the large negative residuals in the blueshifted emission.

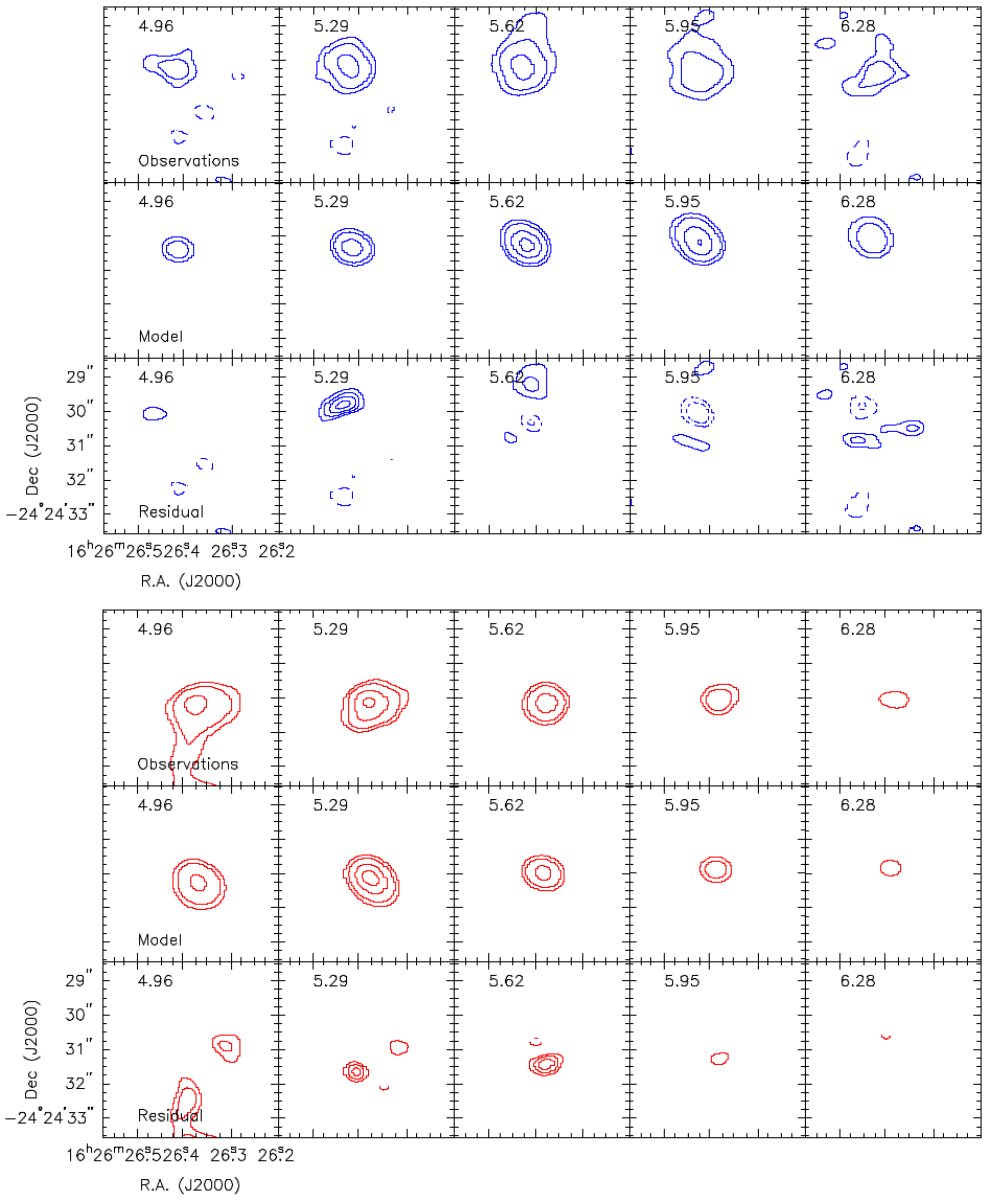

Figure 13: Same as Figure 10 but for the Infall plus Keplerian disk model shown in Figure 6.

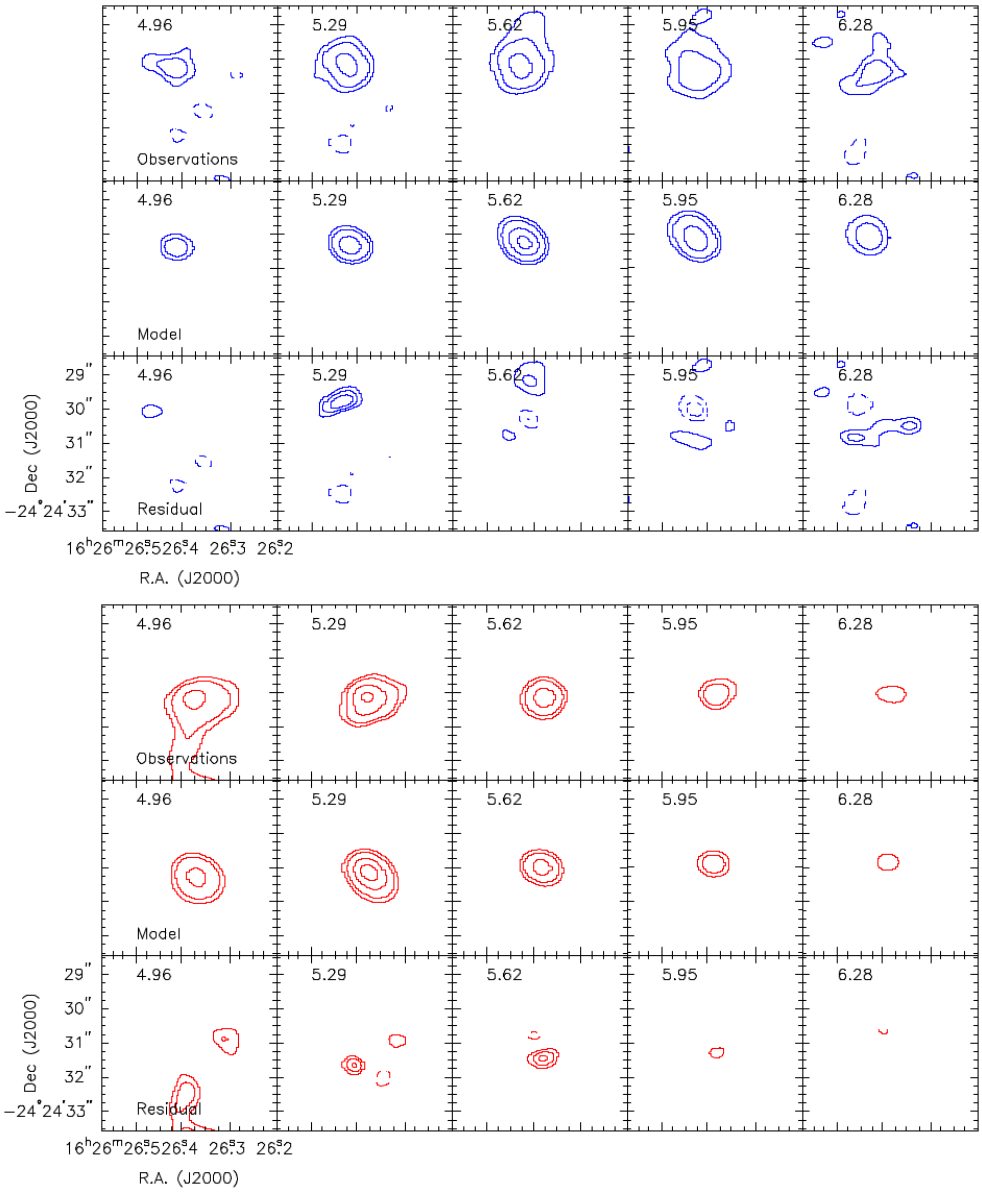

Figure 14: Same as Figure 10 but for the best fit pure Keplerian disk model shown in Figure 6.

Chapter 3

The physical and temperature structure of the disk-envelope interface

Evidence for disk shadowing from ALMA DCO^+ observations of VLA1623

Murillo, N. M., Bruderer, S., van Dishoeck, E. F.,
Walsh, C., Harsono, D., Lai, S.-P., and Fuchs, C. M.
2015, A&A, 579, 114

Abstract

Context Historically, due to instrumental limitations and a lack of disk detections, the structure of the transition from the envelope to the rotationally supported disk has been poorly studied. This is now possible with ALMA through observations of CO isotopologues and tracers of freezeout. Class 0 sources are ideal for such studies given their almost intact envelope and young disk.

Aims The structure of the disk-envelope interface of the prototypical Class 0 source, VLA1623A, which has a confirmed Keplerian disk, is constrained through modeling and analysis of ALMA observations of DCO^+ (3-2) and $C^{18}O$ (2-1) rotational lines.

Methods The physical structure of VLA1623 is obtained from the large-scale SED and continuum radiative transfer. An analytic model using a simple network coupled with radial density and temperature profiles is used as input for a 2D line radiative transfer calculation for comparison with the ALMA Cycle 0 12-m array and Cycle 2 ACA observations of VLA1623.

Results The DCO^+ emission shows a clumpy structure bordering VLA1623A's Keplerian disk. This suggests a cold ring-like structure at the disk-envelope interface. The radial position of the observed DCO^+ peak is reproduced in our model

only if the region's temperature is between 11 K and 16 K, lower than expected from models constrained by continuum data and source SED. Altering the density profile has little effect on the DCO^+ peak position, but increased density is needed to reproduce the observed $C^{18}O$ tracing the disk.

Conclusions The observed DCO^+ (3-2) emission around VLA1623A is the product of shadowing of the envelope by the disk observed in $C^{18}O$. Disk-shadowing causes a drop in the gas temperature outside of the disk on >200 AU scales, encouraging the production of deuterated molecules. This indicates that the physical structure of the disk-envelope interface differs from the rest of the envelope, highlighting the drastic impact that the disk has on the envelope and temperature structure. The results presented here show that DCO^+ is an excellent cold temperature tracer.

3.1 Introduction

Rotationally supported disks have been observed extensively among most protostellar and pre-main sequence evolutionary stages (Li et al. 2014). Recent studies have revealed the existence of such disks in the Class 0 deeply embedded phase (Choi et al. 2010; Tobin et al. 2013c; Murillo et al. 2013; Codella et al. 2014; Lee et al. 2014). In the early stages of star formation, the envelope is not yet dispersed and contains enough material to influence the evolution of the star-disk system. The boundary between the disk and the envelope, known as the disk-envelope interface, must then play a role in the formation process. This region, however, is largely unexplored owing to limitations in the resolution and sensitivity, as well as the lack of observed rotationally supported disks, until now. Class 0 sources with confirmed rotationally supported disks grant us the opportunity to study the chemical and physical structure of the disk-envelope interface region, which is crucial for the next step of understanding this region's role in star formation (Sakai et al. 2014c).

Whilst CO isotopologues are good tracers of rotationally supported disks, they freeze out onto dust grains below the evaporation temperature $T_{\rm ev}$ usually between 30-20 K (Jørgensen et al. 2005a). These low temperatures are reached at the edge of the embedded disk (Visser et al. 2009). As a result molecular species whose abundance is enhanced at low temperatures are needed to trace the disk-envelope interface. DCO^+ emission is known to be optically thin and its abundance is enhanced at a narrow range of temperatures below the CO freeze-out temperature tracing the so-called CO snowline (e.g., Wootten 1987, Roberts et al. 2003, Mathews et al. 2013). Thus, DCO^+ is a good candidate molecule to trace the chemical, physical and kinematic structure of the disk-envelope interface.

VLA1623-2417 (hereafter VLA1623) is a triple non-coeval protostellar system located in ρ Ophiuchus at d ∼120 pc (Murillo & Lai 2013). VLA1623A is the prototypical Class 0 source and emits predominantly in the (sub)millimeter range (André et al. 1993; Murillo & Lai 2013). From modeling of ALMA Cycle 0 $C^{18}O$ observations, Murillo et al. (2013, see chapter 2) found that VLA1623A supports a Keplerian disk with a radius of at least 150 AU and a central mass M_* of 0.2 $M_\odot$. The ALMA Cycle 0 observations also detected DCO^+ molecular line emission toward VLA1623A bordering the $C^{18}O$ disk. This grants us the opportunity to probe the disk-envelope interface of VLA1623A.

In this paper we present the results of our ALMA observations and simple chemical

modeling, aiming to understand the physical structure of the boundary between the envelope and the disk in a Class 0 protostar.

3.2 Observations

Using the Atacama Large Millimeter/submillimeter Array (ALMA) we observed VLA1623 (pointing coordinates α=16:26:26.419 δ=-24:24:29.988 J2000) during the early science Cycle 0 period on 8 April 2012. Observations were carried out using the extended configuration, comprised of 16 antennas with a maximum baseline of ∼400 m, in Band 6 (230 GHz). Total observing time was one hour with a 58% duty cycle. The spectral configuration was set to observe DCO^+ (3-2), $C^{18}O$ (2-1), and ^{12}CO (2-1) in addition to continuum. N_2D^+ was also observed but no significant detection was made. Data calibration was done with 3C 279, 1733-130, and Titan for bandpass, gain, and flux calibration, respectively.

In this paper, we present the results and analysis of the DCO^+ (3-2) (rest frequency: 216.11258 GHz) observations. The DCO^+ data were calibrated jointly with the continuum, $C^{18}O$ (2-1), and ^{12}CO (2-1) data. Further calibration details and results from the other observed lines can be found in Murillo et al. (2013, see chapter 2). The spectral set-up provided a velocity resolution of 0.0847 km s^{-1}. The synthesized beam size for the DCO^+ images is $0.85'' \times 0.65''$ with P.A. = 96°. The rms noise of the channel map is 12 mJy $beam^{-1}$ for a spectral resolution of 0.0847 km s^{-1}, giving a peak S/N = 7.

Our ALMA observations provide a maximum scale of $4''$ and a field of view (FOV) of $24''$, with emission between $4''$ and $24''$ largely filtered out by the interferometer. The FOV together with the beam size of $0.85''$ constrain the scale to which any analysis of the data can be done.

In addition to the ALMA Cycle 0 observations, we present the DCO^+ (3-2) results from our ALMA Cycle 2 Atacama Compact Array (ACA) observations carried out on 7 August 2014 (pointing coordinates α=16:26:26.390 δ=-24:24:30.688). Total observing time was 2 hours. Data calibration was done with J1517-243 and Mars for flux, J1625-2527 and Mars for gain, and J1733-1304 for bandpass. The rms noise of the DCO^+ channel map is 73 mJy $beam^{-1}$ for a spectral resolution of 0.021 km s^{-1}, with a synthesized beam of $8.6'' \times 4.2''$ with P.A. = -76°. These observations, with a mosaicked area of $6'$, provide the DCO^+ emission between $4''$ and $18''$ scales.

3.3 Results

3.3.1 ALMA 12-m Array Cycle 0

The detected DCO^+ emission (Fig. 1) is located between a velocity range of 2.8 to 5.2 km s^{-1} and shows a clumpy structure with two main clumps to the north and south of VLA1623A. The southern clump emission is stronger and is offset by about $2.5''$ (300 AU) from VLA1623A and in addition it borders the red-shifted emission of the disk traced in $C^{18}O$. The northern clump slightly overlaps the blue-shifted emission of the $C^{18}O$ disk and borders VLA1623B's continuum emission. A couple of clumps with emission between 3 and 10σ are observed near the continuum peaks of VLA1623A & B. No significant emission was detected toward VLA1623W, separated by $10''$ to the

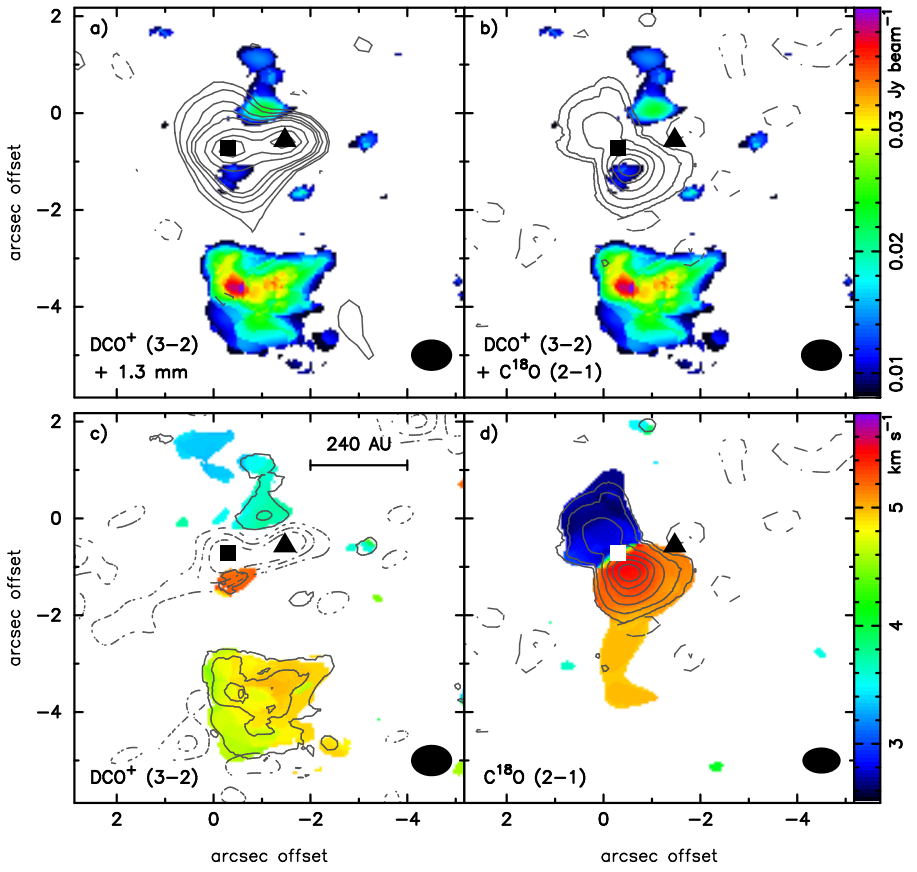

Figure 1: DCO^+ compared with continuum and $C^{18}O$ toward VLA1623A & B, marked with a square and triangle, respectively. The black ellipse shows the synthesized beam. Intensity integrated DCO^+ (color-scale) with (*a*) 1.3mm continuum and (*b*) $C^{18}O$. DCO^+ peaks at 0.0433 Jy beam^{-1} km s^{-1}. Contours are in steps of 3, 5, 10, 15, 20, 40, 60 and 78σ with σ = 1 mJy beam^{-1} for 1.3 mm continuum, and -5, -3, 3, 5, 10, 15, 20 and 25σ with σ = 13 mJy beam^{-1} km s^{-1} for $C^{18}O$. Velocity map (moment 1, color-scale) for (*c*) DCO^+ and (*d*) $C^{18}O$ overlaid with the corresponding intensity integrated map (contours). Contours are in steps of -10, -7, -4, 4, 7, 10 and 11σ with σ = 3 mJy beam^{-1} km s^{-1} for DCO^+, and the same as in (*b*) for $C^{18}O$.

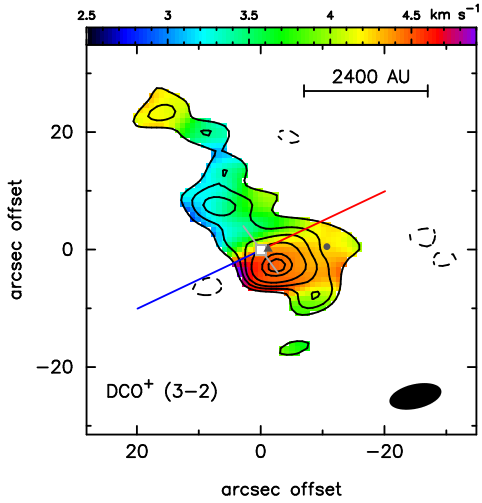

Figure 2: Intensity (contours) and velocity (color-scale) integrated maps of DCO^+ ACA observations. Note the 10 times larger scale of this figure compared with Fig. 1. The positions of VLA1623A, B and W are marked with a square, triangle and circle, respectively. The size of the filled square shows the size of the $C^{18}O$ disk. The red and blue lines indicate the outflow direction while the gray line shows the mayor axis of the disk plane. The black ellipse shows the synthesized beam. Contours are in steps of -3, 3, 5, 7, 10, 15 and 17σ with σ = 220 mJy beam^{-1} km s^{-1}.

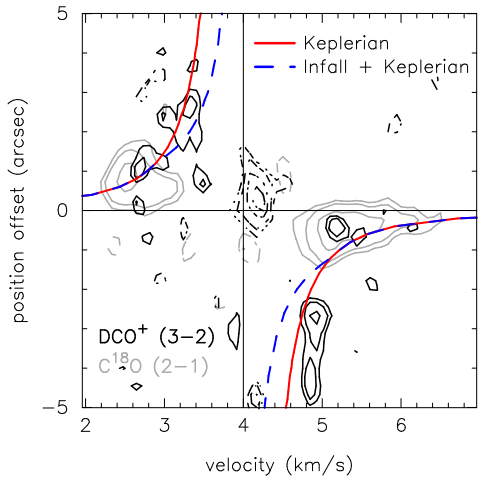

Figure 3: Cycle 0 DCO^+ (black) and $C^{18}O$ (gray) PV diagram. Cuts are made at P.A. = 26° for DCO^+ and P.A. = 35° for $C^{18}O$. Keplerian (solid line) and Infall plus Keplerian (dashed line) rotation PV models with $M_* = 0.2$ M$_\odot$ are overplotted (Murillo et al. 2013, see chapter 2). Contours are in steps of -3, 3, 5, 10 and 15σ with σ = 19 mJy beam^{-1} for $C^{18}O$, -7, -5, -3, -2, 2, 3, 4, 5σ with σ = 12 mJy beam^{-1} for Cycle 0 DCO^+

west from VLA1623A, possibly either because of the lack of DCO^+ or because the emission is too weak and filtered out.

The $C^{18}O$ line emission tracing the disk was found to be influenced by the outer envelope, with the blue-shifted emission being affected more than the red-shifted emission (Murillo et al. 2013, see chapter 2). We expect the same to hold true for the DCO^+ emission, thus potentially explaining why the northern blue-shifted clump emission is weaker than that for the southern red-shifted clump (Fig. 1 a & b).

The velocity weighted (moment 1) map of the DCO^+ emission (Fig. 1c) shows that its velocity gradient is similar to that of $C^{18}O$, with the northern clump being blue-shifted and the southern clump being red-shifted, but with a smaller velocity range. The Position-Velocity (PV) diagrams of DCO^+ and $C^{18}O$ emission (Fig. 3) are constructed and over-plotted with the best fitting thin disk models, Keplerian and Infall plus Keplerian out to 150 AU, obtained by Murillo et al. (2013, see chapter 2). It appears as though both line emissions are well described by pure Keplerian rotation out to 300 AU. However the DCO^+ emission is too weak, peaking at 7σ in the channel map, to carry out further kinematical analysis. The similar velocity signatures of the emission from both species may be due to the disk edge dragging along material from the envelope.

The above simple analysis of the observations indicates that the detected DCO^+ emission may be tracing a ring which borders the $C^{18}O$ disk. In addition, DCO^+'s velocity gradient and PV diagram suggest that the ring is undergoing Keplerian rotation, this is even more plausible given that the $C^{18}O$ (2-1) emission traces a rotationally supported disk with a Keplerian velocity profile (Murillo et al. 2013, see chapter 2).

3.3.2 ALMA ACA Cycle 2

The DCO^+ (3-2) emission traced with the ACA confirms that the emission is concentrated around VLA1623 (Fig. 2), it does not peak on VLA1623A and instead encircles it, forming a shell-like structure. The ACA detects only weak emission at the position of VLA1623W.

The DCO^+ emission mapped with the ACA shows the same velocity gradient (Fig. 2) as on the small scales, indicating that the kinematic structure is the same throughout.

3.4 Analysis

DCO^+ is detected at the disk-envelope interface of VLA1623A. Given that DCO^+ is optically thin and a good probe of temperature and CO freeze-out regions, we model the observed emission aiming to probe the physical and chemical structure of the disk-envelope interface. In this section we describe the model used and the results obtained from the model.

3.4.1 DCO^+ chemical network and model

We model the observed DCO^+ emission using a simple chemical network. Such a network, while it may not account for every possible reaction, is preferred as it gives insight into how the physical parameters of the temperature and density affect the observed emission. The network used is a steady-state analytic model that only takes the

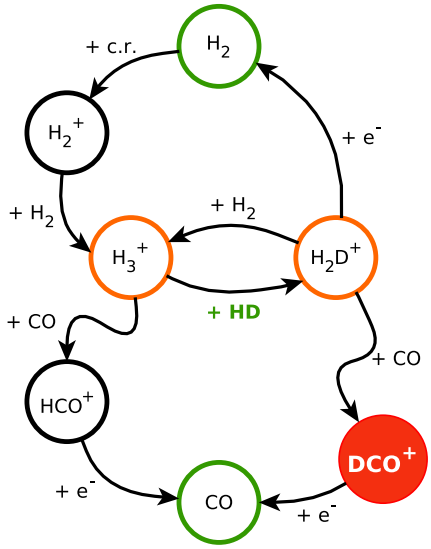

Figure 4: Cartoon of the chemical network used to analyze the observed DCO^+ emission. Red denotes the target molecule. Green the input molecular concentrations and orange the species involved in the bottleneck reaction.

Table 1: DCO^+ chemical network reactions and adopted rate coefficients

ID	Reaction	ζ^a s^{-1}	α^b $cm^3\ s^{-1}$	β^c	γ^d K	Ref.
1	$H_2 + cr \longrightarrow H_2^+ + e^-$	1.26 (-17)	...	...	...	1
2	$H_2^+ + H_2 \longrightarrow H_3^+ + H$	...	2.08 (-9)	0	0	2
3	$H_3^+ + HD \longrightarrow H_2D^+ + H_2$	...	3.50 (-10)	0	0	3, 4
4	$H_2D^+ + H_2 \longrightarrow H_3^+ + HD$	...	3.50 (-9)	0	220.0	3, 4
4a	$H_2D^+ + p\text{-}H_2 \longrightarrow H_3^+ + HD$	...	1.40 (-10)	0	232.0	5
4b	$H_2D^+ + o\text{-}H_2 \longrightarrow H_3^+ + HD$	...	7.00 (-11)	0	61.5	5
5	$H_2D^+ + e^- \longrightarrow HD + H$	...	6.79 (-8)	-0.52	0	5^e
6	$H_3^+ + CO \longrightarrow HCO^+ + H_2$	...	1.61 (-9)	0	0	6, 7
7	$HCO^+ + e^- \longrightarrow H + CO$	...	2.80 (-7)	-0.69	0	8
8	$H_2D^+ + CO \longrightarrow DCO^+ + H_2$	...	5.37 (-10)	0	0	4
9	$DCO^+ + e^- \longrightarrow D + CO$	...	2.40 (-7)	-0.69	0	4

Notes. The reactions 4a and 4b substitute the back reaction of the bottleneck (4) in the network when $o-H_2$ and $p\text{-}H_2$ are included.
$^{(a)}$ ζ is the cosmic-ray ionization rate of H_2. $^{(b)}$ α is the rate coefficient at $T = 300$ K. $^{(c)}$ β is the temperature coefficient. $^{(d)}$ γ is the activation barrier. $^{(e)}$ Value obtained by summing the rate coefficients for the reaction channels to three possible products.

References. (1) Black 1975; (2) Theard & Huntress 1974; (3) Gerlich et al. 2002; (4) Albertsson et al. 2013; (5) Walmsley et al. 2004; (6) Plessis et al. 2010; (7) OSU Database; (8) Amano 1990

basic reactions that lead to DCO^+ production and destruction into account (Table 1, Fig. 4). Since DCO^+ is formed by the reaction of H_2D^+ and CO, the rate-determining reactions in our network are

$$H_3{}^+ + HD \longrightarrow H_2D^+ + H_2 \tag{3.1}$$

with the back reaction

$$H_2D^+ + H_2 + \Delta E \longrightarrow H_3{}^+ + HD \tag{3.2}$$

where the activation energy due to the difference in zero point energy is $\Delta E \sim 220$ K. For reaction 5 in our network (Table 1), for simplicity, we adopt the total rate coefficient summing over all three pathways of the reaction. The rate coefficients for a two-body reaction are given by

$$k = \alpha \left(\frac{T}{300}\right)^{\beta} \exp\left(-\frac{\gamma}{T}\right) \text{ cm}^3 \text{ s}^{-1} \tag{3.3}$$

where T is the gas temperature, while

$$k = \zeta \text{ s}^{-1} \tag{3.4}$$

gives the rate coefficient for cosmic-ray ionization (reaction 1 from Table 1).

Our model takes as input a source density and temperature profile as a function of radius and the parameters needed to calculate the rate coefficients. The CO evaporation temperature $T_{\rm ev}$, desorption density $n_{\rm de}$ and CO abundance $X_{\rm CO}$ are free parameters. The CO abundance is assumed and not calculated. The CO evaporation temperature dictates when CO is in the gas phase ($T > T_{\rm ev}$) or freezes onto the dust grains ($T < T_{\rm ev}$). In a similar manner, the desorption density sets the boundary when the freeze-out timescales are too long ($n < n_{\rm de}$) compared to the lifetime of the core (Jørgensen et al. 2005a). We assume the density profile is equal to the H_2 density $n_{\rm H_2}$ and the abundance of HD $X_{\rm HD} = 10^{-5}$ with respect to the total hydrogen nuclei density $n_H = 2n(\rm H_2)$. The model returns the calculated concentrations as a function of radius. The results can then be input into excitation radiative transfer programs such as RATRAN (Hogerheijde & van der Tak 2000) for further analysis.

Given that CO is one of the parent molecules of DCO^+, we study the effect of CO abundance through the use of different abundance profiles following the models detailed in Jørgensen et al. (2005a) and Yıldız et al. (2010). The possible CO profiles are Constant and Drop abundance (Fig. 5). The former represents a fixed CO abundance throughout the core, whereas the latter, constrained by $T_{\rm ev}$ and n_{de}, is used to account for CO freeze-out in the chemical network. For the constant profile, the abundance is denoted by X_0. For the drop profile, the abundance in the inner, drop and outer regions are denoted by $X_{\rm in}$, $X_{\rm D}$ and X_0, respectively. Previous studies using multiline single dish $C^{18}O$ have found that the abundance at $X_{\rm in}$ is lower than X_0 for a number of sources (Alonso-Albi et al. 2010; Yıldız et al. 2010, 2013). One explanation is that some fraction of the CO ice is transformed into more complex and less volatile carbonaceous species in the cold phase. We thus take this effect in our model into account. A lower abundance of CO, due to freeze-out, allows an increase in the abundance of H_2D^+ (Mathews et al. 2013). However, since both molecules, CO and H_2D^+, are parent molecules of DCO^+, a balance must be reached before the

effective formation of DCO^+ takes place. This scenario is found to be common for the envelopes of early embedded protostars (Jørgensen et al. 2005a) where the outer region shielded from the protostellar and interstellar radiation heating has low enough temperature that CO freezes out onto dust grains.

In molecular clouds, and consequently in protostellar cores, H_2 chemistry plays a major role, hence the ortho-to-para ratio of H_2 influences the chemical reactions, and has been found to be crucial to the deuterium chemistry (Flower et al. 2006; Pagani et al. 2009b). The effect of ortho- and para-H_2 (o-H_2 and p-H_2) is studied in our model through the inclusion of the ortho-to-para ratio (o/p) and the distinction of o-H_2 and p-H_2 in the back reaction of the bottleneck (Eq. 3.2) in the chemical network. o-H_2 and p-H_2 are only added in the back reaction since it is here where the distinction has a significant effect (Table 1). We set a lower limit on o/p of 10^{-3} at low temperatures, as constrained by models and observations (Flower et al. 2006; Faure et al. 2013). The o-H_2 and p-H_2 reactions and their parameters for the rate coefficients are taken from Walmsley et al. (2004).

When o-H_2 and p-H_2 are included in the network, a thermal (LTE), upper- or lower-limit o/p ratio can be selected. In LTE, the ortho-to-para ratio is given by

$$\mathrm{o/p} = 9 \exp\left(\frac{-170}{T}\right) \tag{3.5}$$

where T is the gas temperature. Selecting the upper-limit ratio produces 3 times more o-H_2 than p-H_2. Since the back reaction with o-H_2 has a lower activation barrier γ than with p-H_2, the o/p upper-limit implies that H_2D^+ is being destroyed faster than generated, leading to a decreased production of DCO^+ (Fig. 14), since H_2D^+ is a parent molecule of DCO^+ (Fig. 4). The lower-limit ratio, on the other hand, implies more p-H_2 which has a higher activation barrier γ for the back reaction, thus H_2D^+ is generated faster than it is destroyed in turn increasing the DCO^+ production (Fig. 14).

As a starting point for our analysis of VLA1623A's DCO^+ emission, we use the density and temperature profile of VLA1623 obtained by Jørgensen et al. (2002) where 30 K is at ∼1.5" assuming a distance of 120 pc. The profile was obtained by fitting single dish JCMT continuum images and the spectral energy distribution (SED) with continuum radiative transfer modeling using DUSTY resulting in a power law density profile of the form $n \propto r^{-1.4}$. In the single dish continuum observations VLA1623A and B are unresolved and the density profile extends well beyond the ALMA field of view. It is expected, however, that VLA1623A dominates at 870 μm and that VLA1623B does not contribute much to the 450 μm continuum (Murillo & Lai 2013). Thus, the density and temperature profile obtained by Jørgensen et al. (2002) is representative of VLA1623A since VLA1623B is not significantly contributing to the continuum emission or the SED used to constrain the profiles.

The results of the analytic chemical network are run through the molecular excitation and line radiative transfer program RATRAN to generate line emission maps. Since the structure we are trying to reproduce is ring-like, we calculate the level populations with the 1-D version of RATRAN, and then run the level populations with the 2-D ray tracing to form the ring structure. The produced spectral image cubes are convolved with a Gaussian beam with the dimensions of the synthesized beam, continuum subtracted and then an intensity integrated map is generated. Radial profiles are extracted from the resulting images and compared with the observed profiles, which are integrated over the extent of the detected emission.

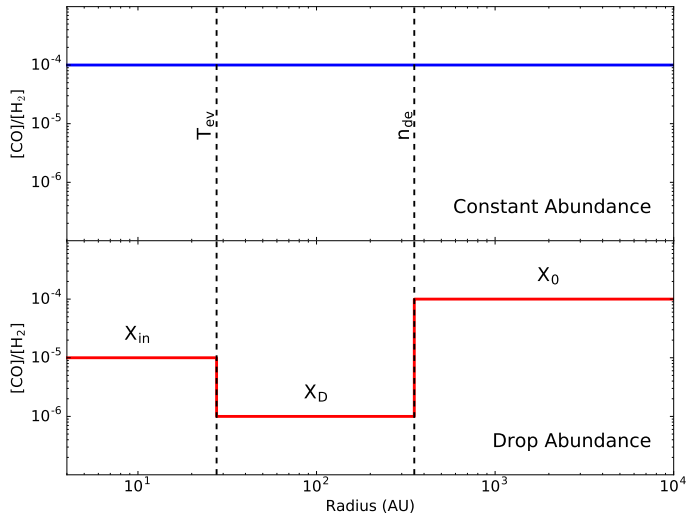

Figure 5: CO abundance profiles used in the model. The vertical dashed lines show the limits for the Drop abundance profile, evaporation temperature $T_{\rm ev}$ and desorption density n_{de}. X_0 denotes the abundance in the constant profile. $X_{\rm in}$, $X_{\rm D}$ and X_0 are the inner, drop and outer region abundances for the drop profile.

We find no significant difference in the peak position between the method used here and running the models through the ALMA simulator with the actual ALMA configuration or our Cycle 0 observations. However, the ALMA simulator does show that the emission $\geq 4''$ is indeed filtered out by the Cycle 0 observations, producing somewhat narrower radial profiles. Molecular data for DCO^+ and $C^{18}O$ are obtained from LAMDA (Schöier et al. 2005a; $C^{18}O$: Yang et al. 2010; DCO^+ extrapolated from Flower 1999). As DCO^+ is optically thin, the comparison mainly focuses on the position of the peak and the integrated intensity profile with respect to radius, the velocity profile has no effect on the resulting model integrated intensity. Thus, we assume a free-fall velocity profile with a central mass of 0.2 $M_\odot$ (Murillo et al. 2013, see chapter 2) and $T_{\rm dust} = T_{\rm gas}$. The RATRAN output maps are convolved with the observed beam ($0.85'' \times 0.65''$, P.A. 96.24°) and compared with the observed emission through radial cuts. In addition to comparing DCO^+, we also compare $C^{18}O$ in order to further constrain the physical structure of the disk-envelope interface. However, for $C^{18}O$ we assume a pure Keplerian velocity profile, in agreement with the rotationally supported disk it traces. For both emission lines, we use an inclination of 55° (90° = face-on), in accordance with the results obtained by Murillo et al. (2013, see chapter 2).

3.4.2 Modeling results

In this section the results of altering the CO abundance, density and temperature profiles in the chemical model are discussed. Figure 6 presents the models, with the light blue region showing the location of the observed DCO^+ peak emission with respect to VLA1623A's position. Model naming follows the scheme xYz where x is the test number from Table 3, Y is either C for constant or D for drop abundance, and z

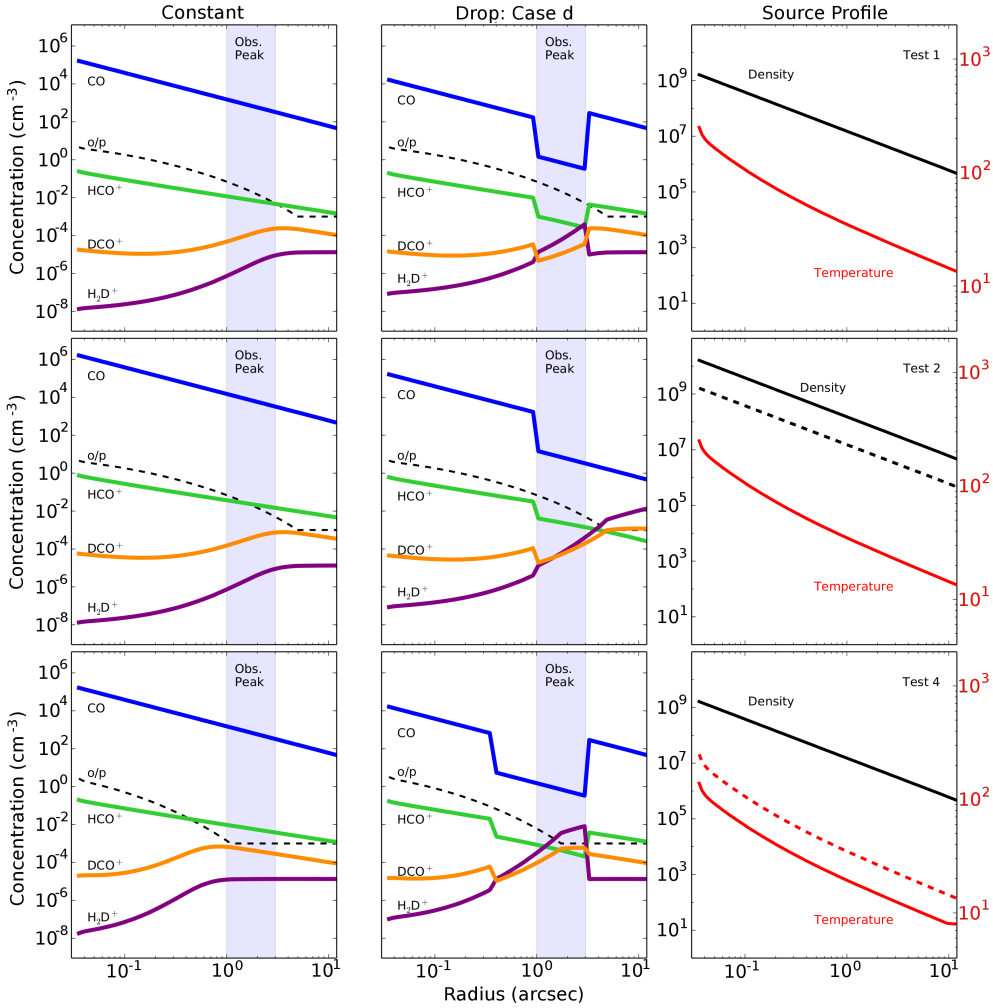

Figure 6: Chemical network model results. Left and center columns show the results for constant and drop CO abundance, respectively. Top, middle and bottom row show the results of Test 1, 2 and 4, respectively. Light blue shaded region shows the observed peak position of DCO^+. Right column shows the input source profile, where the original DUSTY source profile is shown with a dashed line so as to compare with the input for the specific test.

Table 2: Input CO abundance profiles

Case	CO profile	$T_{\rm ev}$ (K)	$n_{\rm de}$ (cm^{-3})	$X_{\rm in}$	$X_{\rm D}$	X_0
Fixed	Constant	...	...	...	...	10^{-4}
a	Drop	30	7×10^4	10^{-5}	10^{-6}	10^{-4}
b	Drop	35	3×10^6	10^{-5}	10^{-6}	10^{-4}
c	Drop	35	3×10^6	10^{-5}	5×10^{-6}	10^{-4}
d	Drop	35	3×10^6	10^{-5}	10^{-7}	10^{-4}
e	Drop	35	5×10^5	10^{-5}	10^{-6}	10^{-4}
f	Drop	35	3×10^6	10^{-5}	10^{-8}	10^{-4}

Notes. See Fig. 5 for definition of $X_{\rm in}$, $X_{\rm D}$ and X_0

Table 3: Input source profiles for each test

Test	$T_{\rm 4AU}$ (K)	$n_{\rm 4AU}$ (cm^{-3})	Source Profile
1	250.0	1.62×10^9	from Jørgensen et al. (2002)
2	250.0	1.62×10^{10}	Density increased 1 order of magnitude
3	250.0	1.62×10^8	Density decreased 1 order of magnitude
4	166.7	1.62×10^9	Temperature decreased by a factor of 1.5 with $T_{\rm lowlim} = 8$ K

is the case from Table 2.

Chemical properties

To probe the chemical conditions, we establish one case for the constant CO abundance with $X_{\rm CO} = 10^{-4}$ and six cases for the drop CO abundance with $X_{\rm D}$ ranging from 5×10^{-6} to 10^{-8} and varying $T_{\rm ev}$ and $n_{\rm de}$. Parameter ranges were selected based on trends found in previous work (Jørgensen et al. 2005a; Yıldız et al. 2010) and adapted to the current observations. Parameters for each case are listed in Table 2. As a zeroth order test, we compare the abundance profiles to the radial position of the observed DCO^+ peak in the ALMA 12-m array data in order to investigate which chemical conditions best approximate our observations. This comparison neglects the fact that the peak emission radius also depends on the DCO^+ excitation, which will be taken in Section 3.4.3 into account.

Figure 6 presents the model abundance profiles as functions of radius for different assumed CO abundances and physical structures. In general, the concentrations of CO and HCO^+ drop with radius whereas those of H_2D^+ and DCO^+ increase with radius due to the lower temperature farther away from the source. Constant CO abundance (Fig. 6, left column) does not appear to produce a DCO^+ peak within the expected region. Since the radial abundance profile of DCO^+ is not altered by changing $X_{\rm CO}$, we focus instead on the drop CO abundance profile.

While the drop CO abundance profile cannot alone alter the position of the peak, it produces several trends interesting to note. A kink in the abundance of DCO^+ forms at $T_{\rm ev}$ for all the cases examined, though in most cases it is relatively small. Altering the abundance in the drop $X_{\rm D}$ changes the shape of the peak but does not significantly

alter its position nor its abundance (Fig. 13). Decreasing the $X_{\rm D}$ below 10^{-7}, however, causes the abundance of the peak to drop by several orders of magnitude and become similar in magnitude to the kink at $T_{\rm ev}$, producing two peaks which are not observed (Fig, 13, case f). Varying $T_{\rm ev}$ and $n_{\rm de}$, in order to constrain the width of the drop, generates a very narrow peak which increases and drops quickly.

To test the effect of the o/p ratio on our chemical network, we vary the ratio from the thermalized value to the upper- and lower-limit for the drop CO abundance profile. In all cases, we find that setting o/p to the lower-limit does not change the position of the DCO^+ emission since the peak and bulk of the DCO^+ concentration for the thermalized o/p is already located in the o/p=10^{-3} range (Fig. 14). In fact, the peak of the modeled DCO^+ emission starts to decrease as the o/p ratio increases. The lower-limit o/p only alters the inner regions (<100 AU), which the data do not constrain. The upper-limit reduces the overall production of DCO^+ and pushes the peak outward to larger radii. In conclusion, altering the CO abundance and o/p ratio does not produce the observed results.

Physical properties

Altering the chemistry of the model does not reproduce the observed DCO^+ peak position, regardless of the case used. Thus we alter the density and temperature profile in order to find the conditions necessary to reproduce the observed emission. We set up 4 tests, including the original profile from Jørgensen et al. (2002) referred to as Test 1, by increasing or decreasing by a constant factor either the density or temperature profile. Parameters for each test are listed in Table 3.

Increasing or decreasing the density profile by one order of magnitude, Tests 2 and 3, does not generate a significant radial shift of the DCO^+ peak compared with the original profile (Fig. 6, middle row). Altering the density, however, affects the concentration of the peak upwards or downwards with an increase or decrease of the density, respectively.

The factor of 1.5 decrease in the temperature profile with cases *b* and *d* with $X_D \approx 10^{-6} - 10^{-7}$ shifts the modeled DCO^+ peak effortlessly to the observed position (Fig. 6). Decreasing the temperature profile between a factor of 1 to 2 moves the modeled DCO^+ peak inward (Fig.15). For the constant CO abundance, any alteration of the temperature either over-estimates the modeled DCO^+ abundance or produces a peak too far inward. For the drop CO abundance, a temperature drop less than a factor of 1.5 does not move the peak inward enough, whereas a larger factor moves it too far inward. Cases *b* and *d* with $X_D \approx 10^{-6} - 10^{-7}$ shifts the modeled DCO^+ peak effortlessly to the observed position (Fig. 6 bottom row). Changing the CO abundance in the drop (Table 2) does not alter the location of the peak, as expected from the results presented in Sec. 3.4.2. Examining the temperature profile shows that the DCO^+ emission peaks at a range of 11-16 K. This is lower than the expected 20 K at $\sim 3''$ inferred from radiative transfer modeling of the observed continuum data (Jørgensen et al. 2002). We limit the decrease in the temperature profile to not fall below 8 K (Zucconi et al. 2001), however this limit generates no significant change in the outcome of our model since the limit falls near and beyond the edge of the FOV of our observations (Fig. 6, bottom right panel).

From the results obtained from altering the chemical and physical conditions in our model, we can deduce that the DCO^+ emission is located at its observed position due to physical conditions, namely a lowered temperature, and not to special chemical

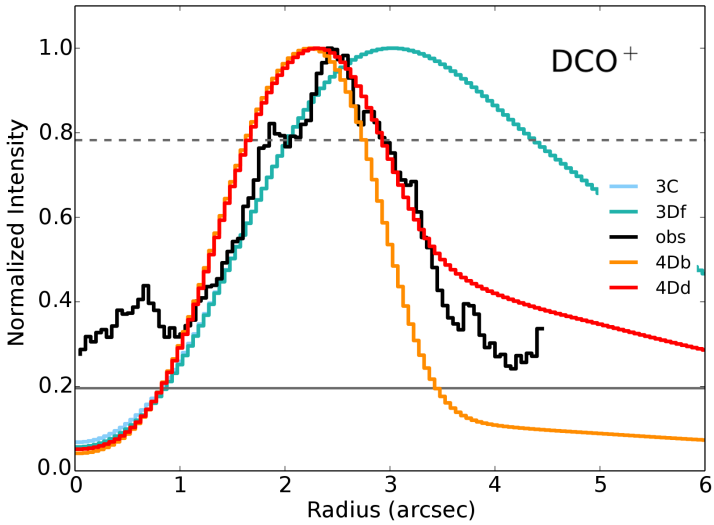

Figure 7: Comparison between observations and radiative transfer modeling of the chemical network results. Here the best approximations are highlighted, with model 4Dd being the preferred model. The models are referred to by test, abundance profile (Constant "C" or Drop "D") and case. Thus, 4Dd is the model for test 4 with Drop abundance and case d. Black line shows the DCO^+ observations integrated over the southern clump. Gray solid and dashed lines show the 1σ and 4σ levels, respectively.

conditions in the disk-envelope interface.

Comparison with full chemical network

To explore the limitations of the simple network, we compare the results to a full time-dependent deuterated chemical network, based on the RATE06 version of the UMIST Database for Astrochemistry (Woodall et al. 2007) extended with deuterium fractionation reactions (McElroy et al. 2013). Models with only gas phase chemistry and including gas-grain balance (freeze-out, thermal desorption, and cosmic-ray-induced photodesorption) are run. The models start with the same initial abundandances (H_2:HD:CO = 1:3×10^{-5}:1×10^{-4}) and the same physical structure as the simple network. We find that the large network confirms both the general trend found in the simple network and also reproduces the peak position and abundance of DCO^+ at the observed position for abundances extracted at early times ($\sim 10^5$ yr).

Inspection of the full network shows that in addition to the reactions listed in Table 1, the $HCO^+ + D \longrightarrow H + DCO^+$ reaction can become important if D/HD is large. The back reaction has a reaction barrier of ∼800 K, thus leading to fractionation of DCO^+ (Adams & Smith 1985). In practice, this reaction is only relevant for much lower densities than encountered in the VLA1623A envelope model. Similarly, dissociative recombination of H_3^+ with electrons cannot be neglected at low densities. At very early times ($< 10^3$ yr, depending on density), reactions with H^+ and D^+ become more significant than those with H_3^+ and H_2D^+. Finally, in full gas-grain models the bulk of the CO is frozen out in the cold outer envelope resulting in very low DCO^+ concentrations, unless an efficient non-thermal CO desorption process is included.

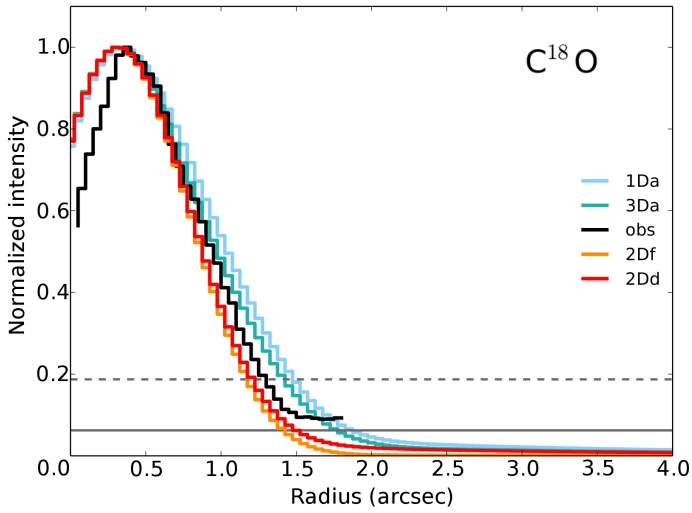

Figure 8: Same as in Fig. 7 but for $C^{18}O$, with 2Dd being the preferred model. Gray solid and dashed lines show the 1σ and 3σ levels, respectively. 2Dd, increased density profile, provides the best approximation to the observed $C^{18}O$.

3.4.3 Emission profiles

Aiming to better constrain the physical conditions of the disk-envelope interface we compare the models and observations of both DCO^+ and $C^{18}O$ emission computed with RATRAN. For the comparison, the observed southern red-shifted clump in the ALMA 12-m array data for both lines is selected. The reason is two-fold: i) the red-shifted emission of the $C^{18}O$ disk suffers less absorption from the outer envelope than the blue-shifted lobe as noted above (Murillo et al. 2013, see chapter 2); ii) the southern red-shifted clump traced by DCO^+ is the strongest and most prominent. Similarly, for the model of $C^{18}O$ only one lobe of the disk is selected for comparison.

Consistent with the abundance plots, the constant CO abundance profiles do not fit the observed DCO^+ emission in any of the four tests, producing very broad peaks between $3''$ and $5''$ away from the source for tests 1, 2 and 3; and a peak at $1''$ for test 4. In a similar manner, for the drop CO abundance scenario, tests 1, 2 and 3 all produce peaks beyond $3''$ with varying broadness, and thus do not approximate the observed DCO^+ emission. This occurs for all examined cases (Fig. 16). Models 4Db and 4Dd approximate the observed DCO^+ emission well (Fig. 7, orange and red lines, respectively). These results are in agreement with the conclusions drawn from the concentrations in the analytics chemical network model (See Sec. 3.4.2).

Comparing the results of the model with the observed $C^{18}O$ emission (Fig. 8), we find that in all four tests a constant CO abundance over-predicts the extent of $C^{18}O$, with the emission well above our 3σ level extending out to $3''$ or further, whereas we observe it only out to less than $2''$ from the central source. When the drop CO abundance is introduced, the source profile of VLA1623 from Jørgensen et al. (2002) overestimates the $C^{18}O$ emission in all cases, and generates a second peak at about $3''$ at half the intensity of the central peak in almost all cases. The width of the

drop does not have any significant effect on the modeled emission. The decreased density and decreased temperature profile tests do not fare better, as they again largely overestimate the $C^{18}O$ beyond 2″ and even produce secondary peaks. Case *a* (X_D = 10^{-6}) for the original profile and decreased density seem to show some promise, however the modeled emission is around 3σ at 1.5″ whereas observations at that radius are closer to 1σ. Surprisingly, we find that the increased density profile produces the best results with case *d* ($X_D = 10^{-7}$), the same as that for DCO^+ (Fig. 8, red line).

Hence we find that the DCO^+ and $C^{18}O$ observed emission are not reproduced by the same physical structure (Figs. 7 and 8). DCO^+ is well modeled by a temperature profile a factor of 1.5 lower than that needed to model $C^{18}O$, whereas $C^{18}O$ is reproduced by a density profile an order of magnitude higher than required for DCO^+. The abundance in the drop X_D necessary to reproduce the emission is the same for both lines, X_D=10^{-7}.

3.4.4 Large scale emission vs. model

We also compare the radial integrated intensity profile of the DCO^+ ACA observations with the model, both along the plane of the disk and perpendicular to the disk in the outflow direction, since these data probe larger spatial scales than the 12-m array data. For this purpose, the models were run through RATRAN's ray tracer *sky* again but instead using the cell size of the ACA observations (0.84″) and then were convolved to match the resolution of the ACA observations. The observed radial profiles are extracted from the red-shifted emission.

The profile along the plane of the disk (peak at ∼4″) is well described by the same model as in the small scale, the drop CO abundance profile for case d, with the temperature decreased by a factor of 1.5 (4Dd, Fig. 9). The temperature decreased by a factor <1.5 does not provide a better estimate. The constant CO abundance again overestimates the amount of DCO^+ produced in the outer regions.

On the other hand, the integrated intensity profile along the outflow direction (peak at distances ≈5″) is very well described by the model 1C (Fig. 9). This indicates that in regions that are not shadowed by the disk, the production of DCO^+ is as expected from dust continuum models.

3.5 Discussion

The results of our modeling show that the position of the DCO^+ emission (∼2.5″ = ∼300 AU) is closer to VLA1623A than expected based on the spherically symmetric dust continuum radiative transfer modeling from DUSTY (∼4″ = ∼480 AU). The results further show that the observed emission peaks at a dust temperature range of 11-16 K. Comparison of the radiative transfer results from RATRAN to the $C^{18}O$ emission from the disk suggest that the disk has a density higher by one order of magnitude than the emitting structure traced by DCO^+.

A possible explanation would be that VLA1623A is a Very Low Luminosity Object (VeLLO, Young et al. 2004, Dunham et al. 2008) undergoing episodic accretion and just coming out of the quiescent phase. This is highly unlikely, however, since Johnstone et al. (2013) find that the timescale for dust and gas to heat up after an accretion burst is short, on the order of hours to weeks. VLA1623A has been reported of having a bolometric luminosity between 0.4-2 $L_\odot$ from early observations to more recent work

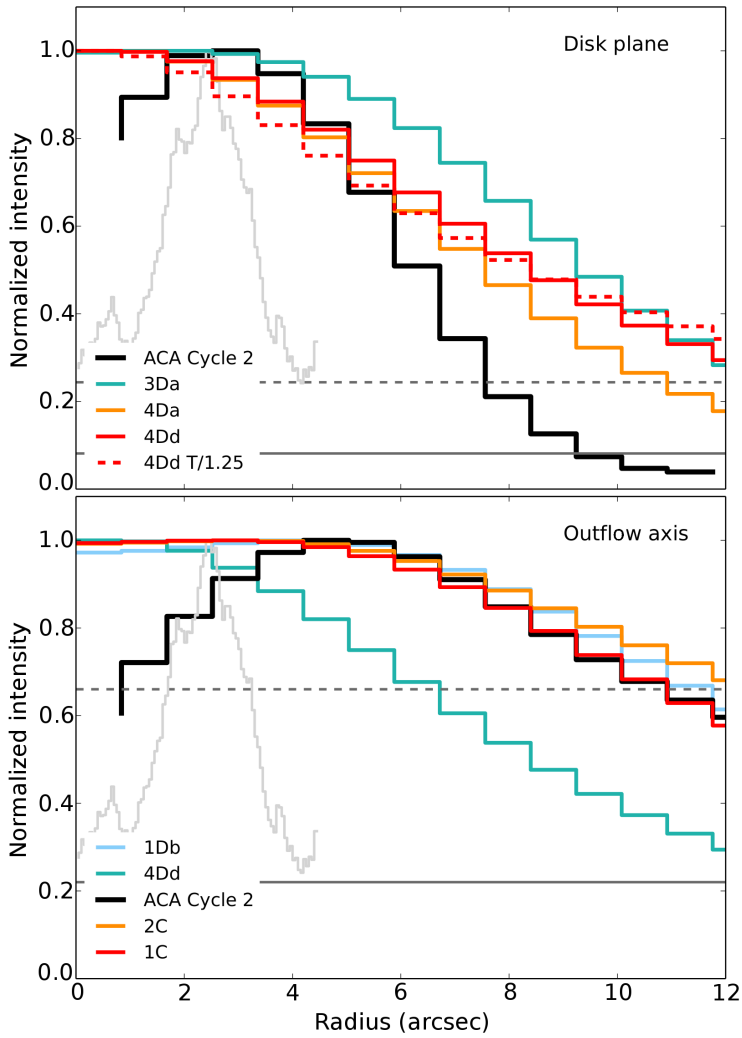

Figure 9: Radial profiles of the DCO^+ ACA observations along the disk plane (*top*) and along the outflow axis perpendicular to the disk (*bottom*) as shown in Fig. 2. Radial profile of the DCO^+ Cycle 0 observations is shown in light gray. Observed radial profiles are overlaid with models convolved to the resolution of the ACA observations. Gray solid and dashed lines show the 1σ and 3σ levels, respectively, of the ACA emission. These results evidence that the DCO^+ emission along the disk plane is best approximated by model 4Dd, whereas along the outflow is best described by model 1C.

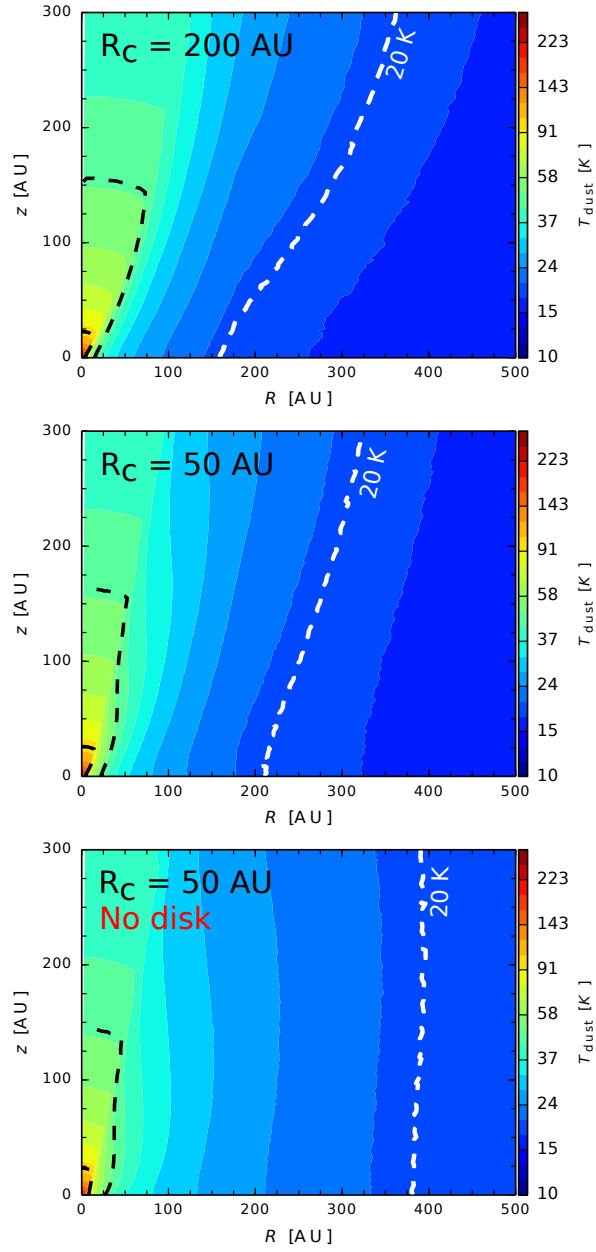

Figure 10: Radiative 2D models based on Harsono et al. (2013). For all models an envelope with $M_{\rm env} = 1$ M$_\odot$ irradiated by a 1 $L_\odot$ protostar is assumed, having an outflow cavity with a full opening angle of 30°. The dashed lines indicate the temperature contours for 100, 50 and 20 K. The top and middle panels include a 180 AU and 0.02 M$_\odot$ disk assuming a 0.1 AU scale height, with centrifugal radius $R_{\rm c} = 200$ AU (*top*) and 50 AU (*center*) orientated in the horizontal direction. The outflow cavity is oriented in the vertical direction. The bottom panel shows the envelope without a disk.

(André et al. 1993; Froebrich 2005; Murillo & Lai 2013; Chen et al. 2013), in contrast to the expected luminosity of 10^{-2} $L_\odot$ for VeLLOs. Hence VLA1623A has not recently come out of the quiescent accretion phase and the location of the observed DCO^+ emission can not be attributed to the relic of a previous phase of decreased accretion.

A more plausible explanation to the position and temperature of the region containing the DCO^+ emission is disk shielding. DCO^+ is observed to border VLA1623A's $C^{18}O$ disk in our present data. This could shield the outer parts of the disk from heating by the central protostar, thus moving in the freeze-out zone of CO, enhancing the production of DCO^+ closer to the protostar. This scenario is further supported by the result of our simple chemical model that the $C^{18}O$ disk is more dense than the region of the DCO^+ emission and than expected from Jørgensen et al. (2002)'s envelope density profile of VLA1623.

We test the possibility of the disk-shielding scenario with radiative 2D disk plus envelope models using radiative transfer methods as in Harsono et al. (2013) (Fig. 10). For the models, we assume a central protostellar source of 1 $L_\odot$ (Murillo & Lai 2013; Chen et al. 2013), an envelope with a mass of 1 $M_\odot$ (André et al. 1993; Froebrich 2005), with the addition of a disk mass of 0.02 $M_\odot$ and radius of 180 AU (Murillo et al. 2013, see chapter 2). The outflow cavity is assumed to have an opening angle of 30°. A thin disk with a scale height of 0.1 AU is adopted. Disk flaring is not included since we have no information on the flaring of VLA1623A's disk and the thin disk model approximates the $C^{18}O$ kinematics well. Two values for the centrifugal radius R_c, 200 AU and 50 AU, are chosen. Within the centrifugal radius the velocity structure of the disk is Keplerian. We find that even for such a thin disk the temperature along the plane of the disk is lower than for the envelope at the same radius (Fig. 10, top and middle panels), thus moving the CO freeze-out zone closer to the protostar along the edge of the disk than in other regions of the core. For either centrifugal radius the temperature beyond 200 AU drops well below 20 K. Finally, we test whether the presence of a disk makes a difference in the location of the CO freeze out region. Figure 10 bottom panel, shows the model with the same conditions as in Figure 10 middle panel, but without the disk. This shows that omitting the disk causes the CO freeze out region to move outward to ∼400 AU, 150 AU further out than the models including a disk.

The temperature conditions required to reproduce the observed DCO^+ emission with our simple chemical model are therefore in agreement with the results obtained from the 2D radiative transfer disk plus envelope model. These results strongly support the scenario where a disk can shield the regions at its edge from heating by the protostar. This shielding causes the CO freeze-out region to move inward toward the edge of the disk, bringing low-temperature enhanced molecules, such as DCO^+, closer to the central protostar along the plane of the disk. However, the rest of the envelope is largely unaffected by the disk and a shell of molecules such as DCO^+ forms at a radius predicted by spherically symmetric models. The ACA observations of DCO^+ toward VLA1623A provide further evidence for this effect. These results show that the DCO^+ emission peaks closer to the source along the disk plane than along the outflow direction.

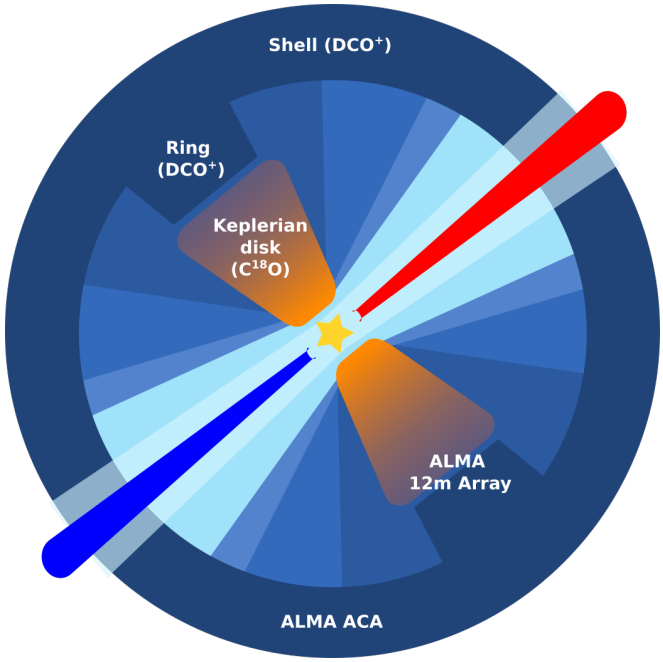

Figure 11: Cartoon of the disk and envelope of VLA1623A. The ring and disk, traced in DCO^+ and $C^{18}O$ respectively, are observed with ALMA 12-m array, while the outer spherically symmetric shell, traced in DCO^+, is observed with ALMA ACA.

3.6 Conclusions

This work presents the results and analysis of ALMA Cycle 0 Early Science Band 6 observations of DCO^+ (3-2) in the extended configuration toward VLA1623A probing subarcsec scales, as well as Cycle 2 ACA data probing the larger scales. A simple chemical network was setup taking ortho- and para-H_2 into account in the rate-determining reactions. The density and temperature profile of VLA1623A was obtained from fitting the SED and dust continuum data with radiative transfer modeling using DUSTY (Jørgensen et al. 2002). Our simple chemical model coupled with VLA1623A's physical structure served as input for line radiative transfer calculations with RATRAN with 2-D ray-tracing. The CO abundance, density and temperature profiles were altered to study the effect of each parameter on the location of the observed DCO^+ peak. The results of our observations and analysis can be thus summarized:

1. DCO^+ is observed to border the $C^{18}O$ disk around VLA1623A. Both emission lines show similar velocity gradients (blue-shifted to the north and red-shifted to the south), with DCO^+ emission between 2.8 to 5.2 km s^{-1}. The PV diagrams of $C^{18}O$ and DCO^+ suggest that both emission lines are well described by Keplerian rotation. However, the DCO^+ emission is weak, thus no further kinematical analysis was carried out, and whether the disk extends out to 300 AU cannot be confirmed.

2. Using a simple chemical network with the inclusion of ortho- and para-H_2 as well as non-LTE line radiative transfer, we model the observed DCO^+ emission. We find that using a constant CO abundance predicts a DCO^+ peak at around $4''$, twice further out than observed, irrespective of the adopted o/p ratio and density profile. Our model

results show that a drop CO abundance with a decreased temperature profile by a factor of 1.5 generates a peak at the same position as the observed emission. Thus, the observed DCO^+ peak is closer to VLA1623A and with a lower temperature (11-16 K) than that expected from a spherically symmetric physical structure constrained by continuum data and source SED.

3. The observed DCO^+ and $C^{18}O$ emission are not described by the same physical structure. In our model, the $C^{18}O$ emission is well reproduced by a drop CO abundance with the density profile increased by one order of magnitude at $1''$ ($\leq$120 AU) radii, in comparison with the density profile needed to reproduce the observed DCO^+ emission. A constant CO abundance and a decreased temperature profile over-predict the extent of the $C^{18}O$ emission.

4. Disk-shielding is the best possible explanation for the observed DCO^+ emission toward VLA1623A. Disk-shielding causes the inward shift of the CO freeze-out region along the plane of the disk, lowering the dust temperature to <20 K, generating a ring of molecules whose abundance is enhanced by low temperatures such as DCO^+. The rest of the envelope is largely unaffected by the disk, thus the CO freeze-out shell predicted by spherically symmetric radiative models is expected to be located further out. This prediction is confirmed by our recent ALMA Cycle 2 ACA observations, which show that the DCO^+ emission along the outflow axis lies at larger radii, $\sim 5''$, consistent with constant CO abundance models without any alteration to Jørgensen et al. (2002)'s temperature and density profile of VLA1623.

5. The disk-envelope interface in VLA1623A is shown to have a broken transition in density and temperature, with the impact generated by the presence of a disk being observable from small to large scales.

Our observations and modeling results for VLA1623A show the disk-envelope interface to have different physical conditions than other parts of the envelope. Our results also highlight the drastic impact that the disk has on the temperature structure at $\sim$100 AU along the plane of the disk, with the effect being observable even at large scales. We suggest performing further observations to determine whether the unequal physical and chemical conditions observed in the disk-envelope interface of VLA1623A is a common phenomenon in protostellar systems with rotationally supported disks or a special condition of the present source.

Appendix

3.A Modeling results: additional figures

Here we present additional figures illustrating details discussed in Section 3.4.2 and 3.4.3. Figures 12 and 13 show the effect of CO abundance X_{CO} in the drop on the DCO^+ peak for Test 1 and 4, respectively. Figure 14 highlights the effect of the upper and lower o/p limits on the DCO^+ abundance for the best approximation models to the DCO^+ observations. The effect of the factor used to decrease the temperature profile on the peak position of the modeled DCO^+ is explored in Figure 15. Figures 16 and 17 give a sampling of the observations compared with the radiative transfer modeling of the chemical network results for the different tests, CO abundance profiles and cases.

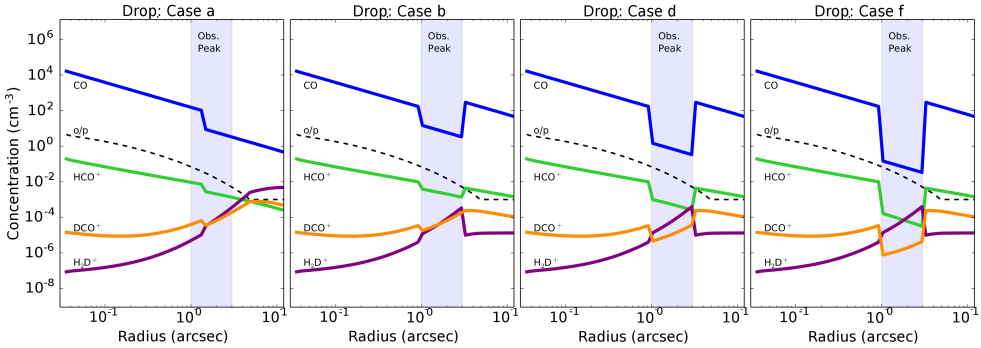

Figure 12: Chemical network results for Drop CO abundance with the Test 1 source profile from Jørgensen et al. (2002) for four cases (Table 2). Case d is the same as in the top row center panel of Fig. 6.

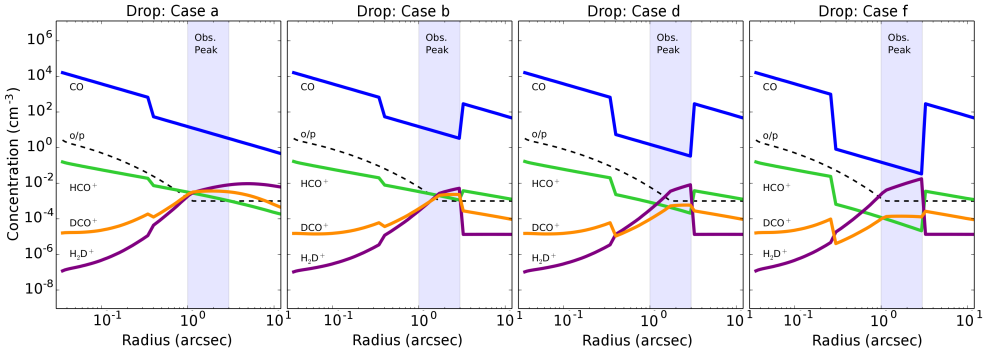

Figure 13: Chemical network results for Drop CO abundance with the decreased-temperature (Test 4) source profile for four cases (Table 2). Case d is the same as in the bottom row center panel of Fig. 6.

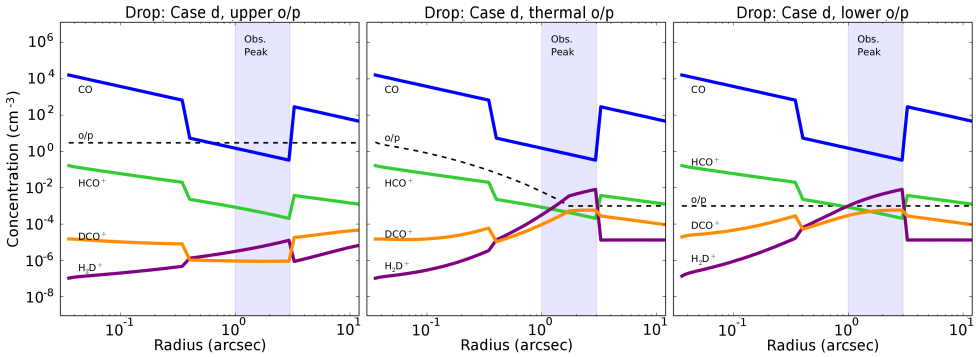

Figure 14: Chemical network results for Drop CO abundance with the decreased-temperature source profile (Test 4) for case a with upper-limit (*left*), thermal (*center*) and lower-limit (*right*) o/p ratio.

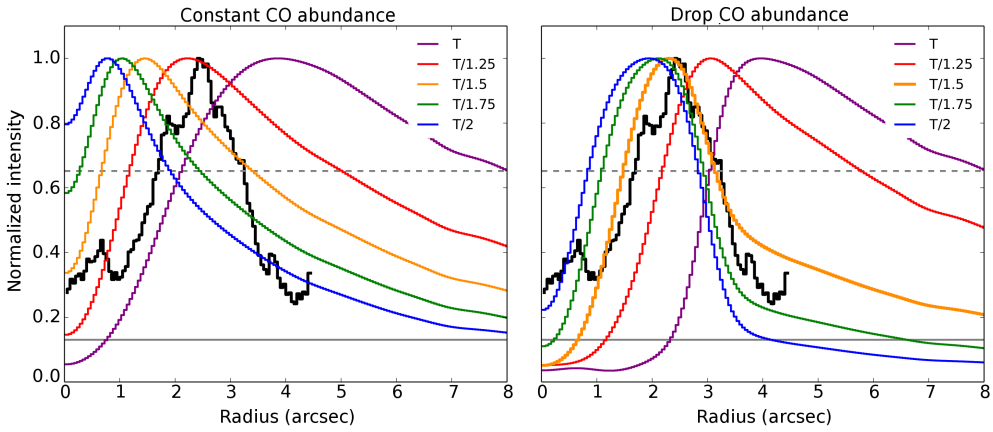

Figure 15: DCO^+ Cycle 0 observations compared with the radial profile of the constant and drop CO abundance models, showing the effect of the factor used to decrease the temperature, for case d. A factor of 1.5 with drop CO abundance provides the best approximation to the observed radial profile.

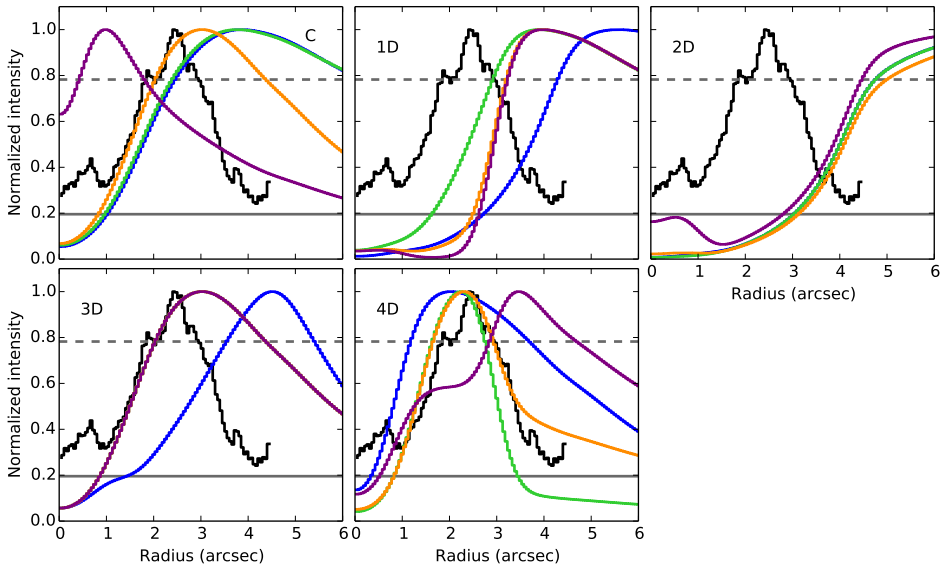

Figure 16: Comparison of the observations and radiative transfer modeling of the chemical network results. The black line shows the DCO^+ observations integrated over the southern clump, with the gray solid lines showing the 1σ and 4σ levels, respectively. Models are referred to by test, abundance profile (Constant "C" or Drop "D") and case. Color lines show tests 1 (blue), 2 (green), 3 (orange) and 4 (purple) for the top left panel, and cases a (blue), b (green), d(orange) and f (purple) for the other four panels.

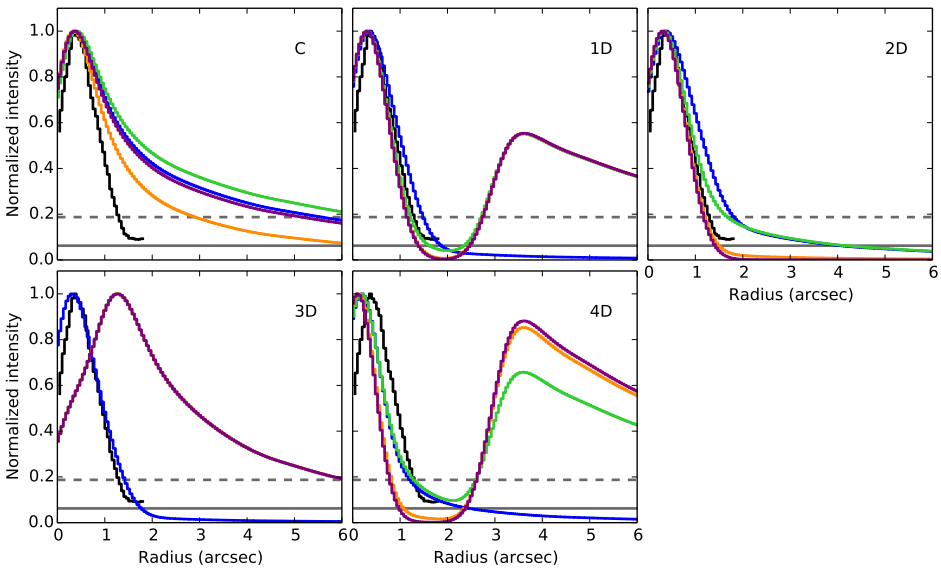

Figure 17: As in Fig. 16 but for $C^{18}O$. Gray solid and dashed lines show the 1σ and 3σ levels respectively. Note that constant CO abundance over-predicts the amount of $C^{18}O$ emission.

Chapter 4

Tracing the cold and warm physico-chemical structure of deeply embedded protostars

IRAS 16293-2422 versus VLA 1623-2417

Murillo, N. M., van Dishoeck, E. F., van der Wiel, M. H. D., Jørgensen, J. K., Drozdovskaya, M. N., Calcutt, H., Harsono, D.
submitted to A&A

Abstract

Context Much attention has been placed on the dust distribution in protostellar envelopes, but there are still many unanswered questions regarding the physico-chemical structure of the gas..

Aims Our aim is to start identifying the factors that determine the chemical structure of protostellar regions, by studying and comparing low-mass embedded systems in key molecular tracers.

Methods The cold and warm chemical structures of two embedded Class 0 systems, IRAS 16293-2422 and VLA 1623-2417, are characterized through interferometric observations. DCO^+, N_2H^+ and N_2D^+ are used to trace the spatial distribution and physics of the cold regions of the envelope, while c$-C_3H_2$ and C_2H are expected to trace the warm (UV-irradiated) regions.

Results The two sources show a number of striking similarities and differences. DCO^+ consistently traces the cold material at the disk-envelope interface, where gas temperatures are lowered due to disk shadowing. N_2H^+ and N_2D^+, also tracing cold gas, show low abundances towards VLA 1623-2417, but for IRAS 16293-2422, the distribution of N_2D^+ is consistent with the same chemical models that reproduce DCO^+. c$-C_3H_2$ and C_2H show different spatial distributions for the two systems, sometimes tracing the outflow cavity walls and in other cases the more quiescent envelope. In IRAS 1623-2422, c$-C_3H_2$ and C_2H are surprisingly anti-correlated.

Finally, hot core molecules are abundantly seen toward IRAS 16293-2422 but not toward VLA 1623-2417.

Conclusions We identify temperature as one of the key factors in determining the chemical structure of protostars as seen in gaseous molecules. More luminous protostars, such as IRAS 16293-2422, will have chemical complexity out to larger distances than colder protostars, such as VLA 1623-2417. Additionally, disks in the embedded phase have a crucial role in controlling both the gas and dust temperature of the envelope, and consequently the chemical structure.

4.1 Introduction

While there is a well-established outline of the physical evolution of protostellar systems (Evans 1999; Dunham et al. 2014; Li et al. 2014; Reipurth et al. 2014), there are still many questions regarding the physico-chemical structure of these systems. Several studies point out the chemical richness and diversity of young embedded protostars, most notably in the Class 0 stage, ranging from simple molecules to carbon chains and complex organics (see reviews by Herbst & van Dishoeck 2009; Caselli & Ceccarelli 2012; Sakai & Yamamoto 2013). In contrast, some other protostellar systems show much less chemical complexity (e.g., Jørgensen et al. 2005b; Maret et al. 2006; Öberg et al. 2014; Fayolle et al. 2015; Lindberg et al. 2014b, 2016, 2017; Bergner et al. 2017), a situation made more extreme when some starless cores have stronger molecular line emissions than the already formed protostars (e.g., Bergman et al. 2011; Bacmann et al. 2012; Friesen et al. 2014). It is interesting to explore the chemical structure and evolution of early stage protostars and what physical quantities dictate the resulting chemical structure as observed in the gas phase.

The chemical fingerprint generated in the early embedded stages of star formation may be transmitted to the later stages and eventually the protoplanetary disk, where planets and comets are formed (e.g., Aikawa et al. 1999; Aikawa & Herbst 1999; Visser et al. 2009, 2011; Hincelin et al. 2013; Drozdovskaya et al. 2014; Willacy et al. 2015; Yoneda et al. 2016). Which factors then generate a protostellar system's fingerprint? Protostellar cores may inherit their chemical composition from the parent cloud that eventually collapses to form protostars (e.g., Aikawa et al. 2012; Furuya et al. 2012; Tassis et al. 2012; Hincelin et al. 2016). It would then seem likely that protostars from the same parent cloud would have a similar chemical composition. However, this would require the cloud to have a homogeneous composition, which is not always the case (Bergman et al. 2011). Instead, other mechanisms could alter the chemical fingerprint. Turbulence and large-scale motions could stir the core around, moving material from the outer region of the core closer to the warmer regions of the system, kick-starting chemical reactions and producing enhancements of selected species. Formation of more complex chemical species likely occurs through solid-phase reactions (i.e., on ice and dust surfaces) instead of in the gas-phase, and such reactions proceed faster at higher dust temperatures which increases the mobility of radicals (Garrod & Herbst 2006). If material near outflow cavities is warmer than elsewhere in the envelope, this could generate pockets of chemically rich ices that, once heated above the sublimation temperature, would be released into the gas-phase (Drozdovskaya et al. 2015). Moreover, UV radiation can photodissociate CO and create free atomic carbon that leads to efficient formation of carbon-bearing molecules. UV irradiation together with age and variations in accretion rates would also produce different outcomes, even

with the same initial ingredients. In addition, simple warm-chemistry molecules can be the precursors to more complex molecules (Sakai & Yamamoto 2013).

The physical evolution of the individual protostars, e.g., the collapse time and structure, will also impact the chemical fingerprint. An important consideration regarding the physical structure is that disks may have formed already in the early stages, as shown by recent observations (e.g., Tobin et al. 2012b; Murillo et al. 2013; Harsono et al. 2014; Lindberg et al. 2014a; Codella et al. 2014; Yen et al. 2017). Not only do disks provide a high density long-lived reservoir preventing molecules from falling into the star, but they also affect the thermal structure of their surroundings. Thus the disk-envelope interface and the envelope itself must be studied (Murillo et al. 2015; Persson et al. 2016). The disk-envelope interface and the outer envelope of embedded systems are traced by cold-chemistry molecules, since these regions are usually shielded from heating by the central protostar (van Dishoeck et al. 1995; Jørgensen et al. 2004, 2005a; Sakai et al. 2014c; Murillo et al. 2015). Through the study of molecules sensitive to temperature, we can then understand the structure of embedded protostellar systems.

Aiming to explore the chemical evolution of the earliest embedded protostellar systems, i.e. Class 0, we compare two systems from ρ Ophiuchus ($d \sim 120$ pc, Loinard et al. 2008), IRAS 16293-2422 and VLA 1623-2417, separated by a projected distance of 2.8 pc. Most previous studies were based on single-dish studies. The advent of Atacama Large Millimeter/submillimeter Array (ALMA) now allows chemical studies on 100 AU scales that spatially resolve the different physical components of the system.

IRAS 16293-2422 (hereafter IRAS in the text) is a widely studied multiple system, located in L1689N, with a complicated outflow structure being driven by source A (Stark et al. 2004; Yeh et al. 2008; Loinard et al. 2013). IRAS-A and B, separated by about 620 AU, have different inclination angles, with A's disk-like structure being inclined and B orientated face-on with respect to the line of sight (Pineda et al. 2012; Jørgensen et al. 2016). Due to the different inclination angles, it is difficult to determine whether these systems are at the same evolutionary stage or not (Murillo et al. 2016, see chapter 5). Both components are chemically rich but show differences in structure (Bottinelli et al. 2004; Bisschop et al. 2008; Jørgensen et al. 2011).

VLA 1623-2417 (hereafter VLA in the text) is a triple protostellar system, located in L1688 (ρ Oph A), mostly studied for its prominent outflow in the region (André et al. 1990; Caratti o Garatti et al. 2006). The three components of the system, VLA-A, B and W are separated by 132 and 1200 AU, respectively, have similar inclination angles, and have also been found to be at different evolutionary stages (Murillo & Lai 2013; Murillo et al. 2013, see chapter 2). VLA has been shown to be largely line poor in single-dish studies (Garay et al. 2002; Jørgensen et al. 2004; Bergman et al. 2011; Friesen et al. 2014).

In this paper, we present observations of DCO^+, N_2H^+, N_2D^+, c$-C_3H_2$ and C_2H towards IRAS and VLA, using the ALMA, the Submillimeter Array (SMA) and the Atacama Pathfinder EXperiment (APEX), details of which are described in Sect. 4.2. DCO^+, N_2H^+ and N_2D^+ are known to be good tracers of cold gas where CO is frozen out. c$-C_3H_2$ and C_2H are usually seen in photon-dominated regions (PDRs) such as the Orion Bar (Pety et al. 2007; van der Wiel et al. 2009; Nagy et al. 2015) and the Horsehead Nebula (Cuadrado et al. 2015; Guzmán et al. 2015), with both species located at the irradiated, and thus warmer, edge of these regions. c$-C_3H_2$ and C_2H could thus be expected to trace the (UV-irradiated) outflow cavity walls, although

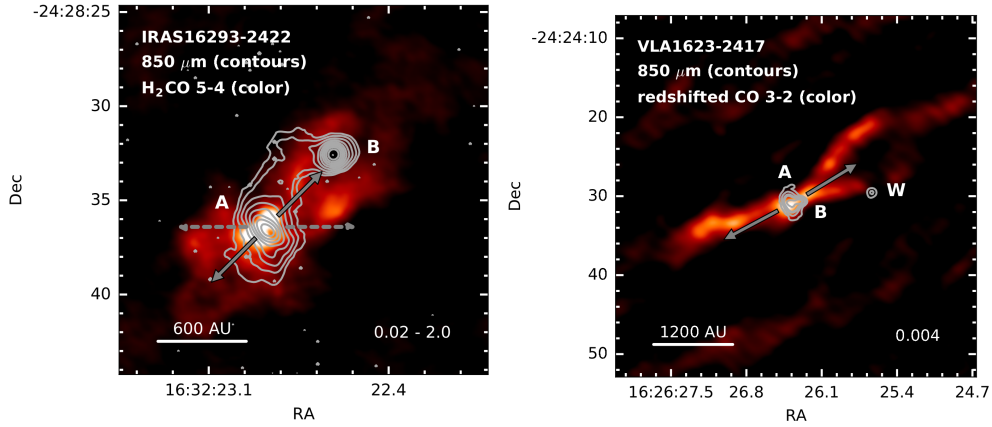

Figure 1: Continuum at 850μm (contours) for both systems, IRAS 16293-2422 (left) and VLA 1623-2417 (right), overlaid on H_2CO and redshifted CO (color-scale), respectively. For VLA 1623-2417, contours are in steps of 3, 8, 15, 20 and 50σ, with σ = 0.004 Jy beam^{-1}. For IRAS 16293-2422, the levels are logarithmically spaced between 0.02 and 2 Jy beam^{-1}, and highlight the ridge that spans between sources A and B. The arrows show the direction of red- and blue-shifted outflows from source A in each system.

both species have also been found just outside the disk-envelope interface (Sakai et al. 2014b). Besides mapping their distributions, multiple lines from a single molecule can also be used to trace physical conditions such as temperature and density (van Dishoeck et al. 1993; Evans 1999; van der Tak et al. 2007; Shirley 2015) and the current dataset allows this to be done for several species.

Section 4.3 describes the spatial distribution of each molecule for both systems. The observations are compared to chemical models and physical parameters are derived in Sect. 4.4. Sections 4.5 and 4.6 compare both systems studied here with other objects found in literature and place the results of our work in context.

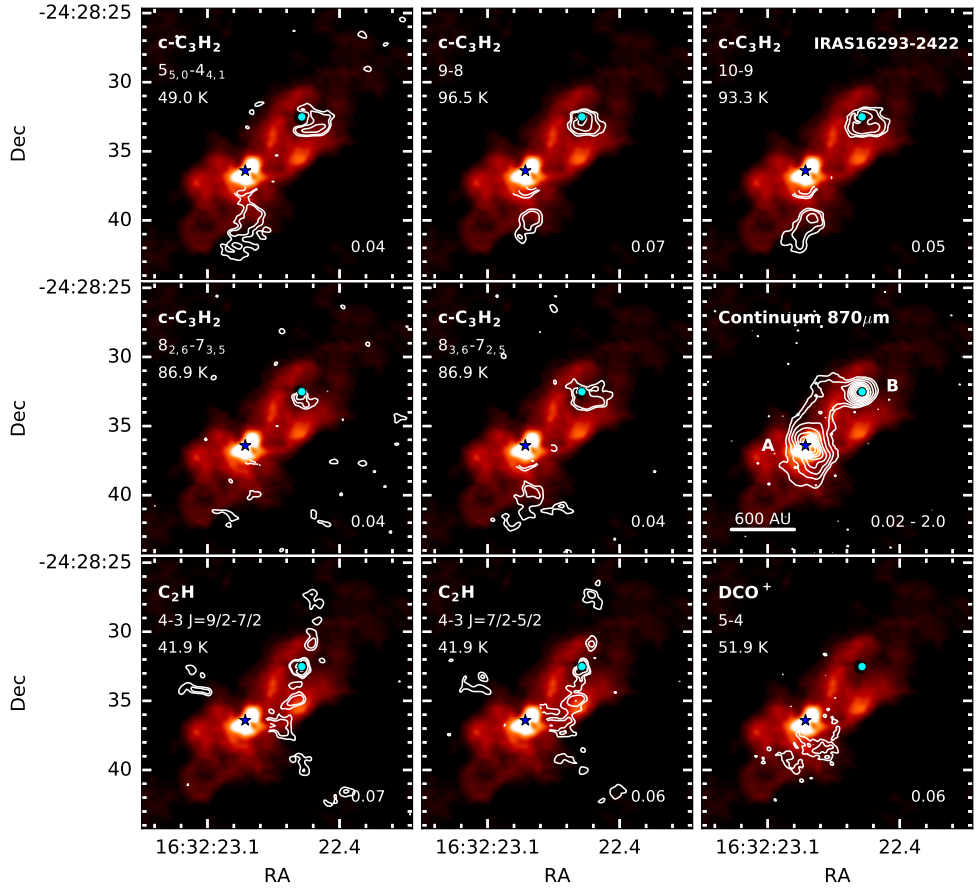

Figure 2: Intensity integrated maps (contours) of c$-C_3H_2$, C_2H, DCO^+ and continuum towards IRAS 16293-2422. H_2CO 5–4 is shown in color-scale. Contours show the respective lines in steps of 2, 3, 5, 20 and 60σ, with σ (Jy beam^{-1} km s^{-1}) indicated in the lower right of each panel. For continuum, the levels are logarithmically spaced between 0.02 and 2 Jy beam^{-1}, and highlight the ridge that spans between sources A and B. The positions of IRAS 16293-2422 A and B are indicated with a star and circle, respectively. For the c$-C_3H_2$ and C_2H panels, the emission centered on A is contamination from other molecule(s) and is masked out in a radius of 2″ from the position of A.

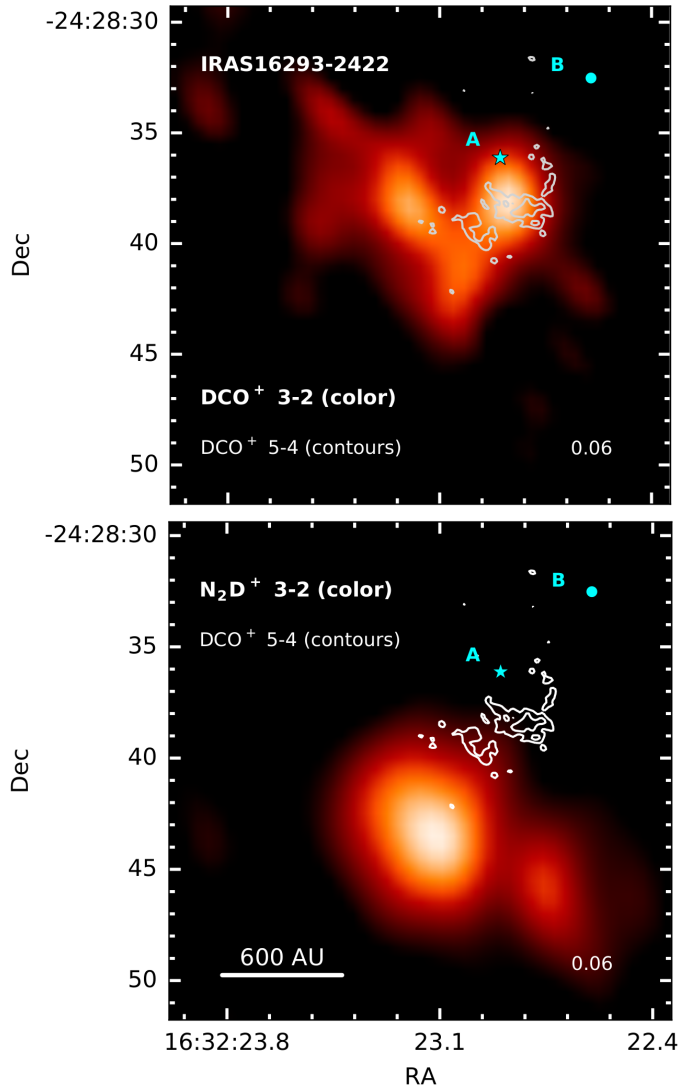

Figure 3: Intensity integrated maps of DCO^+ 3–2 (top) and N_2D^+ 3–2 (bottom) observed with the SMA, overlaid with DCO^+ 5–4 (contours) observed with ALMA. Contours are the same as in Fig. 2. The positions of IRAS 16293-2422 A and B are indicated with a star and circle, respectively. Both DCO^+ transitions match spatially, and N_2D^+ is located beyond the extent of the DCO^+ emission. Note the different center of this figure compared to Fig. 2.

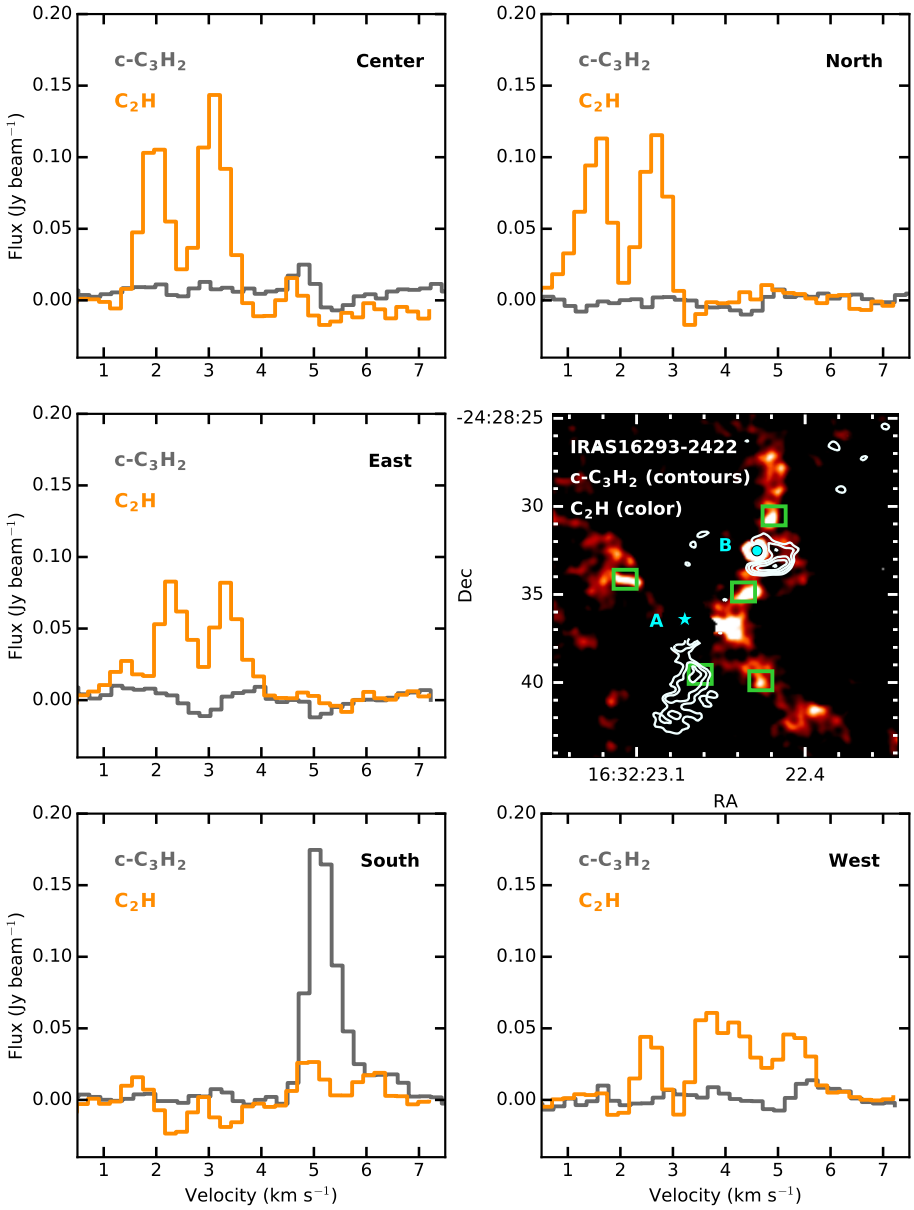

Figure 4: IRAS 16293-2422 c$-C_3H_2$ 5–4 and C_2H 4–3 J=9/2–7/2 spectra taken at 5 positions, indicated by the green boxes in the intensity integrated map presented in the left bottom panel. The anti-correlation of both molecules is seen at all positions. The region within a radius of 2″ from the position of source A is contaminated by other molecular species, and is masked out for these maps.

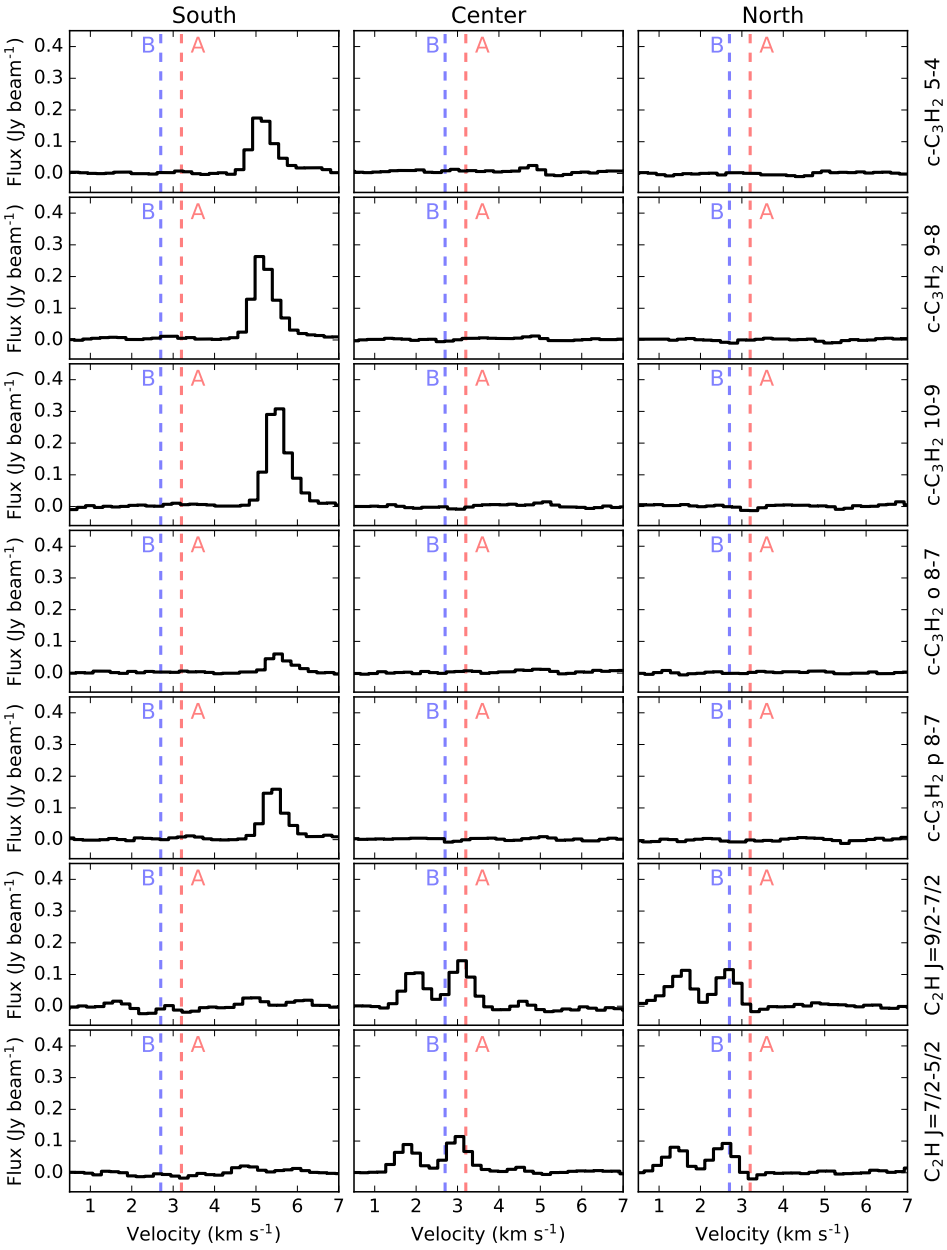

Figure 5: IRAS 16293-2422 ALMA spectra for all transitions of c$-C_3H_2$ and C_2H for each of the south, center and north positions shown in Fig. 4. The systemic velocities of sources A and B are marked with the vertical dashed lines. The anti-correlation of c$-C_3H_2$ and C_2H is also evident in the spectra shown here.

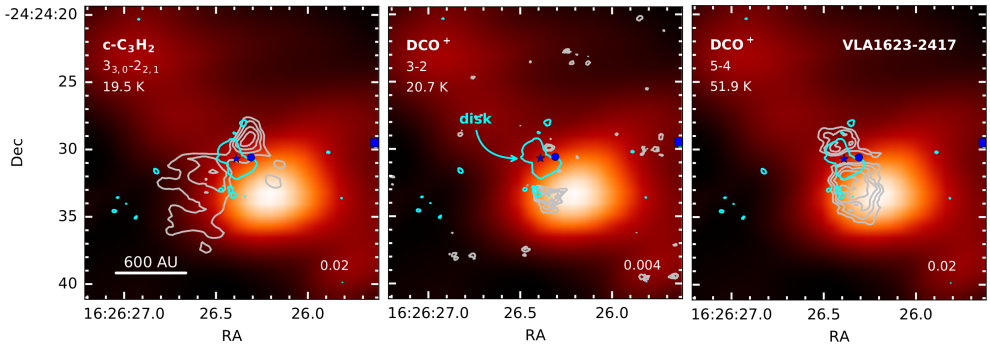

Figure 6: Intensity integrated maps (gray contours) of c$-C_3H_2$ and DCO^+ towards VLA 1623-2417. DCO^+ 3–2 from ACA observations is shown in color-scale. The cyan line is the 3σ contour of $C^{18}O$ in order to show the location and extent of the rotating disk centered on VLA 1623-2417 A. Gray contours show the respective lines in steps of 3, 4, 5 and 6σ, except for DCO^+ 3–2 where the contours start at 4σ. The value of σ (Jy beam^{-1} km s^{-1}) is indicated in the lower right corner of each panel. The positions of VLA 1623-2417 A, B and W are indicated with a star, circle and square, respectively.

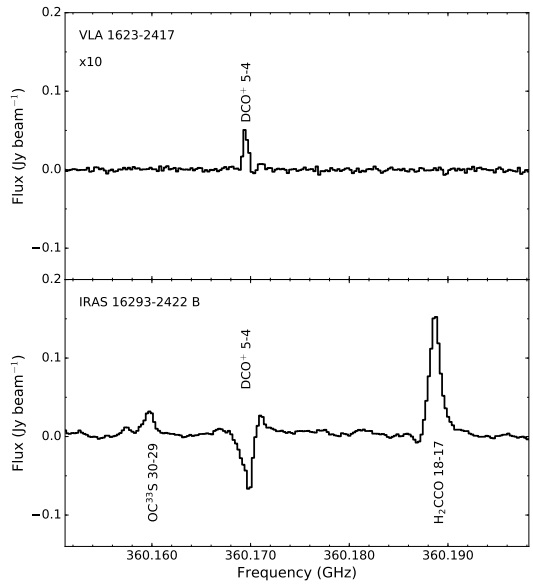

Figure 7: Comparison of the spectra centered on DCO^+ 5–4 of VLA 1623-2417 A and one beam offset from IRAS 16293-2422 B. The spectra for VLA 1623-2417 has been multiplied by a factor of 10 in order to compare more easily. Note the lack of molecular line emission toward VLA 1623-2417 in contrast to IRAS 16293-2422.

Table 1: Summary of line observations.

					IRAS 16293-2422		VLA 1623-2417	
Line	Transition	ν GHz	$\log_{10}$ A_{ij}	E_{up} K	Peak Flux mJy beam^{-1}	Line width km s^{-1}	Peak Flux mJy beam^{-1}	Line width km s^{-1}
				ALMA				
c$-C_3H_2$	$3_{3,0}$–$2_{2,1}$	216.27876	-3.33	19.46	...	...	190	0.5
c$-C_3H_2$	$5_{5,0}$–$4_{4,1}$	349.26400	-2.78	48.98	240[a]	1.0	...	...
c$-C_3H_2$	10–9[b]	351.78158	-2.61	96.49	410[a]	1.0	...	...
c$-C_3H_2$	9–8[c]	351.96597	-2.67	93.34	350[a]	1.0	...	...
c$-C_3H_2$	$8_{2,6}$–$7_{3,5}$	352.18554	-2.76	86.93	90[a]	1.0	...	...
c$-C_3H_2$	$8_{3,6}$–$7_{2,5}$	352.19364	-2.76	86.93	200[a]	1.0	...	...
C_2H	4–3 J=9/2–7/2 F=5–4	349.33771	-3.88	41.91	170	0.7	...	...
C_2H	4–3 J=9/2–7/2 F=4–3	349.33899	-3.89	41.91	140	0.7	...	...
C_2H	4–3 J=7/2–5/2 F=4–3	349.39927	-3.90	41.93	140	0.7	...	...
C_2H	4–3 J=7/2–5/2 F=3–2	349.40067	-3.92	41.93	110	0.7	...	...
DCO^+	3–2	216.11258	-2.62	20.74	...	...	90	0.7
DCO^+	5–4	360.16978	-2.42	51.86	10	1.0	290	0.7
N_2D^+	3–2	231.32166	-2.66	22.20	...	...	<8.58[d]	...
N_2H^+	4–3	372.67251	-2.51	44.71	...	...	<94.9[d]	...
				SMA				
DCO^+	3–2	216.11258	-2.62	20.74	1800	1.0	...	...
N_2D^+	3–2	231.32166	-2.66	22.20	1700	2.0	...	...

Table 1: continued.

					IRAS 16293-2422		VLA 1623-2417	
Line	Transition	ν	$\log_{10}$ A_{ij}	E_{up}	Peak Flux	Line width	Peak Flux	Line width
			APEX (T_{mb})					
C_2H	4–3 J=9/2–7/2 F=5–4	349.33771	-3.88	41.91	...	...	0.96 K	0.7
C_2H	4–3 J=9/2–7/2 F=4–3	349.33899	-3.89	41.91	...	...	0.62 K	0.7
C_2H	4–3 J=7/2–5/2 F=4–3	349.39927	-3.90	41.93	...	...	0.68 K	0.7
C_2H	4–3 J=7/2–5/2 F=3–2	349.40067	-3.92	41.93	...	...	0.34 K	0.7
DCO^+	3–2	216.11258	-2.62	20.74	...	...	4.8 K	0.8
DCO^+	5–4	360.16978	-2.42	51.86	...	...	2.2 K	0.8

Notes. [a] c$-C_3H_2$ peak fluxes and line widths taken from the south peak where there is no line confusion. [b] Blended $10_{0,10}$–$9_{1,9}$ and $10_{1,10}$–$9_{0,9}$ transitions of c$-C_3H_2$. [c] Blended $9_{1,8}$–$8_{2,7}$ and $9_{2,8}$–$8_{1,7}$ transitions of c$-C_3H_2$. [d] 1 σ noise level of N_2D^+ and N_2H^+ in 0.02 km s^{-1} channel

References. All rest frequencies were taken from the Cologne Database for Molecular Spectroscopy (CDMS) (Endres et al. 2016). The c$-C_3H_2$ entry was based on Bogey et al. (1987) with transition frequencies important for our survey from Bogey et al. (1986) and from Spezzano et al. (2012). The CCH entry is based on Padovani et al. (2009) with additional important data from Müller et al. (2000) and Sastry et al. (1981). The DCO^+ and N_2H^+ entries are based on Caselli & Dore (2005) and on Cazzoli et al. (2012), respectively. Information on the N_2D^+ rest frequency was taken from Pagani et al. (2009a).

4.2 Observations

4.2.1 IRAS 16293-2422

IRAS was targeted in the "Protostellar Interferometric Line Survey" (PILS) program (Project-ID: 2013.1.00278.S; PI: Jes K. Jørgensen; Jørgensen et al. 2016), an ALMA Cycle 2 unbiased spectral survey in Band 7, using both the 12m array and the Atacama Compact Array (ACA). The spectral set-up covers a frequency range from 329.147 GHz to 362.896 GHz, and provides a velocity resolution of 0.2 km s^{-1}. The pointing coordinate was α_{J2000} = 16:32:22.72; δ_{J2000} = −24:28:34.3, set to be equidistant from the two sources A and B at $v_{\rm lsr}$ = 3.2 and 2.7 km s^{-1}, respectively. The 12m array and the ACA observations were combined, producing a synthesized beam of 0.5″×0.5″. A detailed description of the observations and reduction is given in Jørgensen et al. (2016). Many complex molecules detected in this survey (e.g., Coutens et al. 2016; Jørgensen et al. 2016; Lykke et al. 2017) show relatively compact emission peaking close to the location of the two protostars. This work focuses on a few of the molecules detected in the spectral survey that show extended emission, namely DCO^+, c−C_3H_2 and C_2H. For c−C_3H_2 and C_2H the combined 12m array and ACA data cubes are used. For DCO^+, the combined data cube and the ACA data separately are considered. The typical RMS noise is about 7–10 mJy $beam^{-1}$ per 0.2 km s^{-1} channel, and the flux calibration uncertainty is ∼5% (Jørgensen et al. 2016). Transitions and line frequencies of the molecular species used in this work are listed in Table 1, as well as the peak fluxes and line widths.

Since the PILS survey did not cover lines of N_2D^+ 3–2 or DCO^+ 3–2, we include here the observations of these two molecules from a spectral line survey with the SMA (Jørgensen et al. 2011). A brief description of the observations is given here. The pointing coordinate was α_{J2000} = 16:32:22.91; δ_{J2000} = −24:28:35.5. For DCO^+ 3–2, the beam size is 5.5″× 3.2″, while for N_2D^+ 3–2 the beam size is 4.0″× 2.4″. The RMS noise is 0.24 Jy $beam^{-1}$ for a 0.56 km s^{-1} channel width for DCO^+, and 0.06 Jy $beam^{-1}$ for a channel width of 1.1 km s^{-1} for N_2D^+. Further details on the reduction and analysis are given in Jørgensen et al. (2011). These data are considered in order to directly compare the cold chemistry of IRAS with that of VLA. Additionally, two transitions of DCO^+ are needed to derive temperature and density from line ratios.

4.2.2 VLA 1623-2417

VLA was observed with ALMA in Cycle 0 using Band 6, with pointing coordinates α_{J2000} = 16:26:26.419; δ_{J2000} = 24:24:29.988. The spectral set-up was configured to observe DCO^+ 3–2 and N_2D^+ 3–2 together with $C^{18}O$ 2–1 and ^{12}CO 2–1, providing a velocity resolution of 0.0847 km s^{-1} and a synthesized beam size of 0.85″×0.65″. DCO^+ 3–2 data from the Cycle 0 obseravations were previously presented in Murillo et al. (2015, see chapter 3). The data reduction results of $C^{18}O$ and ^{12}CO can be found in Murillo et al. (2013, see chapter 2) and Santangelo et al. (2015).

ALMA Cycle 2 observations in Bands 6 and 7 were also carried out, with pointing coordinates α_{J2000} = 16:26:26.390; δ_{J2000} = −24:24:30.688. The Band 6 observations provided a spatial and spectral resolution of about 0.45″×0.25″ and 0.0211 km s^{-1}, respectively, with a typical RMS noise of about 7–9 mJy $beam^{-1}$ per 0.0211 km s^{-1} velocity channel. The spectral set-up covered DCO^+, $C^{18}O$ and ^{13}CO together with continuum and was observed in both the ACA and the 12m array. Band 6 ACA

Table 2: Tests of the temperature and density profiles of the two sources.

Test	IRAS 16293-2422 (Crimier et al. 2010)			VLA 1623-2417 (Jørgensen et al. 2002)		
	$T_{27\mathrm{AU}}$ K	$n_{27\mathrm{AU}}$ cm^{-3}	Note	$T_{4\mathrm{AU}}$ K	$n_{4\mathrm{AU}}$ cm^{-3}	Note
1	300.0	2.36×10^{9}	unchanged	250.0	1.62×10^{9}	unchanged
2	300.0	2.36×10^{10}	$n \times 10$	250.0	1.62×10^{10}	$n \times 10$
3	300.0	2.36×10^{8}	n / 10	250.0	1.62×10^{8}	n / 10
4	100.0	2.36×10^{9}	T / 3	166.7	1.62×10^{9}	T / 1.5

observations of DCO^+ were presented in Murillo et al. (2015, see chapter 3); $C^{18}O$ and ^{13}CO are treated elsewhere (Cheong et al. in prep.). Band 7 observations, with a spectral set-up covering N_2H^+ 5–4, DCO^+ 5–4 and H_2D^+ $1_{1,0}$–$1_{1,1}$ together with continuum with only the 12m array, provided a spectral and spatial resolution of 0.025 km s^{-1} and $0.87'' \times 0.54''$, respectively. Total observing time was 0.9 hr with a 46% duty cycle, using 34 antennas and a maximum baseline of 350 m. Data calibration was done with J1517-2422, J1625-2527 and Titan for bandpass, gain and flux calibration, respectively. DCO^+ was detected with a noise of 26 mJy beam^{-1} per 0.025 km s^{-1}. The system temperature was relatively high for the spectral windows containing N_2H^+ and H_2D^+, causing the noise to be of about 95 mJy beam^{-1} per 0.025 km s^{-1} velocity channel, despite flagging out the antennas that had the highest system temperature.

In this work we focus on the observations of the DCO^+ 3–2 and N_2D^+ 3–2 lines from Cycle 0 obsevations, in addition to DCO^+ 5–4, N_2H^+ 5–4 and H_2D^+ $1_{1,0}$–$1_{1,1}$ observations from Cycle 2. Line transitions and frequencies together with peak fluxes and line widths are listed in Table 1.

Additionally, single-dish APEX observations in the ON/OFF mode were carried out on 22 and 24 October 2016 using the heterodyne instrument SheFI with bands APEX-1 (213 – 275 GHz) and APEX-2 (267 – 378 GHz), targeting DCO^+ 3–2 and 5–4, as well as C_2H 4–3. These observations were taken to compare the location of C_2H in both VLA and IRAS, as well as to have a separate verification and comparison of the physical parameters derived from ALMA observations and single-dish. Several transitions of NO and HCN were detected, both of which can form in gas and surface reactions, whereas N_2H^+ and N_2D^+ only form in the gas. NO and HCN are not further analyzed in this work. The pointing was centered on VLA-A (α_{J2000} = 16:26:26.390; $\delta_{J2000} = -24$:24:30.688). The typical RMS noise was 100 mK for APEX-1 and between 50 – 80 mK for APEX-2 in 0.1 km s^{-1} channels. Peak temperatures (T_{mb}) and line widths for Gaussian fits to the single dish lines are listed in Table 1. The typical calibration uncertainties are about 10% for the APEX SheFI instruments in the 230 and 345 GHz bands. The main beam efficiencies used are $\eta_{\mathrm{mb}} = 0.75$ at 230 GHz, and $\eta_{\mathrm{mb}} = 0.73$ at 345 GHz.

Table 3: DCO^+ best approximation model parameters.

Parameter	IRAS 16293-2422	VLA 1623-2417
$T_{\rm peak}$ (K)	17–19	11–16
Drop boundaries:		
$T_{\rm sub}$ (K)	35	35
$n_{\rm de}$ ($\rm cm^{-3}$)	$\leq 10^6$	3×10^6
CO abundance:		
Inner $X_{\rm in}$	10^{-5}	10^{-5}
Drop $X_{\rm D}$	10^{-6}	10^{-7}
Outer X_0	10^{-4}	10^{-4}

4.3 Results

4.3.1 IRAS 16293-2422

The molecules c$-C_3H_2$, C_2H and DCO^+ from the PILS spectral survey (Jørgensen et al. 2016) are considered here, together with DCO^+ and N_2D^+ from the SMA spectral survey (Jørgensen et al. 2011) . The peak intensities and widths of each line are listed in Table 1. Intensity integrated maps of each line overlaid on H_2CO are shown in Fig. 2. H_2CO $5_{1,5}$–$4_{1,4}$ from the PILS survey (van der Wiel et al. in prep.) is used as a reference for the more extended envelope and one of the outflow directions. The nominal velocities at which most species emit at source A and B are $V_{\rm LSR}$ =3.2 and 2.7 km $\rm s^{-1}$. Velocity resolved maps can be found in Appendix 4.A. c$-C_3H_2$ and C_2H spectra at selected positions are presented in Fig. 4 and 5.

DCO^+ is detected in the 5–4 (PILS) and 3–2 (SMA) transitions, with a half-crescent shape centered around source A (Fig. 2 and 3). The peak is red-shifted and located $\sim2''$ south of source A in both transitions. Weak absorption is detected towards source B in the PILS observations. The DCO^+ emission south of source A is weak, peaking at 3 σ in the 5–4 transition and at 5σ in the 3–2 transition. It is slightly extended to the south along the outflow, but not as far as c$-C_3H_2$. In agreement with previous observations of DCO^+ and c$-C_3H_2$ for other objects (Spezzano et al. 2016b,a), these two molecules are spatially anti-correlated.

Five narrow (FWHM $\approx$ 1 km $\rm s^{-1}$) lines of c$-C_3H_2$ with $E_{\rm UP}$ ranging from 48 to 96 K were detected. The emission peaks to the south of A, seen clearly in the top row of Fig. 2. The lines are also seen near source B, at one ALMA beam offset from the source. The southern emission extends from the circumstellar region of source A, and peaks at $\leq5\sigma$ about $\sim4''$ away from the source position. Toward source A itself, the spectrum is too confused to identify the separate molecular lines. Thus the region is masked out in the maps within $2''$ from the source position. Comparing c$-C_3H_2$ with H_2CO (Fig. 2) suggests that it could arise from one side of the southern outflow cavity wall (van der Wiel et al. in prep.). Asymmetrical heating by source A of the outflow cavity could cause only one side to present c$-C_3H_2$ emission. The emission around source B may either be from the circumstellar region or the outflow cavity, but due to the orientation it is difficult to say.

C_2H is clearly detected in both spin doubling transitions with each transition showing a characteristic double hyperfine structure pattern. The emission within $2''$ of source A is masked out due to contamination from other molecular species. C_2H

emission is located in a filament-like structure extending from north to south, passing through source B (Fig. 2). A second, weaker structure formed by a string of clumps extends from north-east to south-west, apparently passing through source A. C_2H is diffuse and weak, peaking at $\lesssim 5\sigma$ on all off-source positions on the map (Fig. 4). The emission around source B is brighter, peaking at 10σ in the intensity integrated map. From the channel map, the emission appears to have a subtle velocity gradient from north to south at source B. However, the C_2H emission does not match the structure and extent of c$-C_3H_2$ (or H_2CO) in either transition (Fig. 4 and 5). It should be noted that neither C_2H or c$-C_3H_2$ coincide with the dust ridge seen in the continuum emission (Fig. 2; see also Jacobsen et al. submitted).

N_2D^+ 3–2 is mostly resolved out in the PILS survey, but it is detected south-east of DCO^+ with the SMA (Fig. 3), located $7''$ away from the continuum position of source A with a S/N = 7 (Jørgensen et al. 2011). Similar to DCO^+, there is no N_2D^+ emission towards B. No transition of N_2D^+ was covered in the Band 7 observations.

4.3.2 VLA 1623-2417

Two transitions of DCO^+ and one transition each of c$-C_3H_2$, N_2H^+ and N_2D^+ were observed with ALMA in Bands 6 and 7, with added ACA observations for Band 6. Additional APEX observations detected two transitions of DCO^+ and C_2H. Intensities and line widths are listed in Table 1. Fig. 6 shows the intensity integrated maps for the ALMA observations. In Appendix 4.A, velocity resolved maps of the ALMA observations can be found. All of these molecules trace material associated with VLA-A, but not the other two components of the system, VLA-B and W.

The DCO^+ 3–2 ALMA 12m array and ACA observations have been analysed in detail in Murillo et al. (2015, see chapter 3). The 3–2 ACA map shows a smooth distribution peaking south-west of the source, with the blue-shifted emission extending north-east, but no clear red-shifted counterpart south-west. Here we present additional ALMA band 7 12m array observations of DCO^+ 5–4. In both transitions of DCO^+ the red-shifted emission, located to the south of VLA-A, is clearly seen and is stronger than the blue-shifted emission located to the north. The DCO^+ 5–4 emission is three times stronger than the 3–2 emission with the 12m array, which makes the blue-shifted emission clearly visible. For both transitions the velocity gradients are consistent. The DCO^+ 3–2 emission borders the disk structure observed to be driven by VLA-A and is relatively compact. Even more interesting, however, is that DCO^+ in the 5–4 transition extends closer to the position of VLA-A than in the 3–2 transition (Fig. 6).

DCO^+ forms at temperatures below 20 K, where CO freezes out. The position of the DCO^+ 3–2 peak along the disk plane was found to be the product of disk-shadowing, which causes a temperature drop at the edge of the disk, whereas along the outflow direction no such effect was observed (Murillo et al. 2015, see chapter 3). The APEX observations of DCO^+ in both transitions show a single peak at the systemic velocity (3.7–4 km s^{-1}) and a peak intensity of 3.6 K for the 3–2 transition, the same as obtained from JCMT observations by Jørgensen et al. (2004). The beamsize for the APEX-1 and 2 bands covers approximately the full extent of the DCO^+ emission seen in the ACA map. For the DCO^+ 3–2 transition, the ALMA observations recover about 28% of the flux detected in the APEX observations (117.1 Jy km s^{-1} with 24 Jy/K), while 20% was recovered with the DCO^+ 5–4 ALMA observations (APEX: 53.7 Jy km s^{-1} with 24 Jy/K).

One low-lying transition of c$-C_3H_2$ is detected with the ACA but not the 12m array. The c$-C_3H_2$ emission is oriented perpendicular to the disk and seems to trace the cavity of the outflow driven by VLA-A out to 3″ from the source position. There is no detection of c$-C_3H_2$ emission in the disk traced by $C^{18}O$ or at the disk-envelope interface, down to the noise level. The material along the outflow cavity exhibits signatures of rotation, most notable in the south-east lobe, with a velocity range and gradient direction similar to that of DCO^+ and $C^{18}O$ (Murillo et al. 2013, see chapter 2).

C_2H is detected with APEX, with the hyperfine components of each transition being clearly distinguished. Both transitions are located at the systemic velocity of VLA-A (3.7–4.0 km s^{-1}) and show no broadening, indicating that the emission is most likely related to the envelope material of VLA-A.

N_2H^+ and N_2D^+ are not detected in our ALMA observations. Possible reasons could be either due to the emission being very extended and thus resolved out in the interferometric observations, or the abundance of these molecules being too low to be detected. This is a surprising contrast to several other young embedded Class 0 sources which do show N_2H^+ and N_2D^+ (Jørgensen et al. 2004; Tobin et al. 2013a). The non-detections of N_2H^+ and N_2D^+ are further analysed in Sect. 4.4.4. H_2D^+ is also not detected in our Cycle 2 band 7 observations, this is consistent with the JCMT observations reported by Friesen et al. (2014). H_2D^+ is not further treated in this work.

4.4 Analysis

4.4.1 DCO^+

DCO^+ appears to peak offset from the protostellar positions bordering the disk-like structures in both sources (Fig. 2 and 6). Here we analyze the peak position first through chemical modelling of the observed emission, and then using the line ratios to constrain the physical structure (temperature, density) and the associated chemistry.

DCO^+ distribution

In Murillo et al. (2015, see chapter 3) the distribution of DCO^+ around VLA was found to be altered by the presence of a rotationally supported disk, causing the emission to move inwards along the disk plane but not along other directions. In this section, the DCO^+ emission around IRAS is modelled, aiming to find whether the distribution of DCO^+ in IRAS is product of the same phenomenon as observed in VLA.

The DCO^+ chemistry is particularly sensitive to temperature. To model the observed emission for IRAS and VLA, a simple steady-state, analytic chemical network that accounts for the basic reactions leading to the production and destruction of DCO^+ is used.

Since CO and H_2D^+ are the precursors of DCO^+, the production of H_2D^+ will be the rate-determining reaction in the chemical network, since it will dictate the production of DCO^+. The H_2D^+ production and destruction reaction is given by

$$H_3{}^+ + HD \underset{\Delta E}{\rightleftharpoons} H_2D^+ + H_2 \tag{4.1}$$

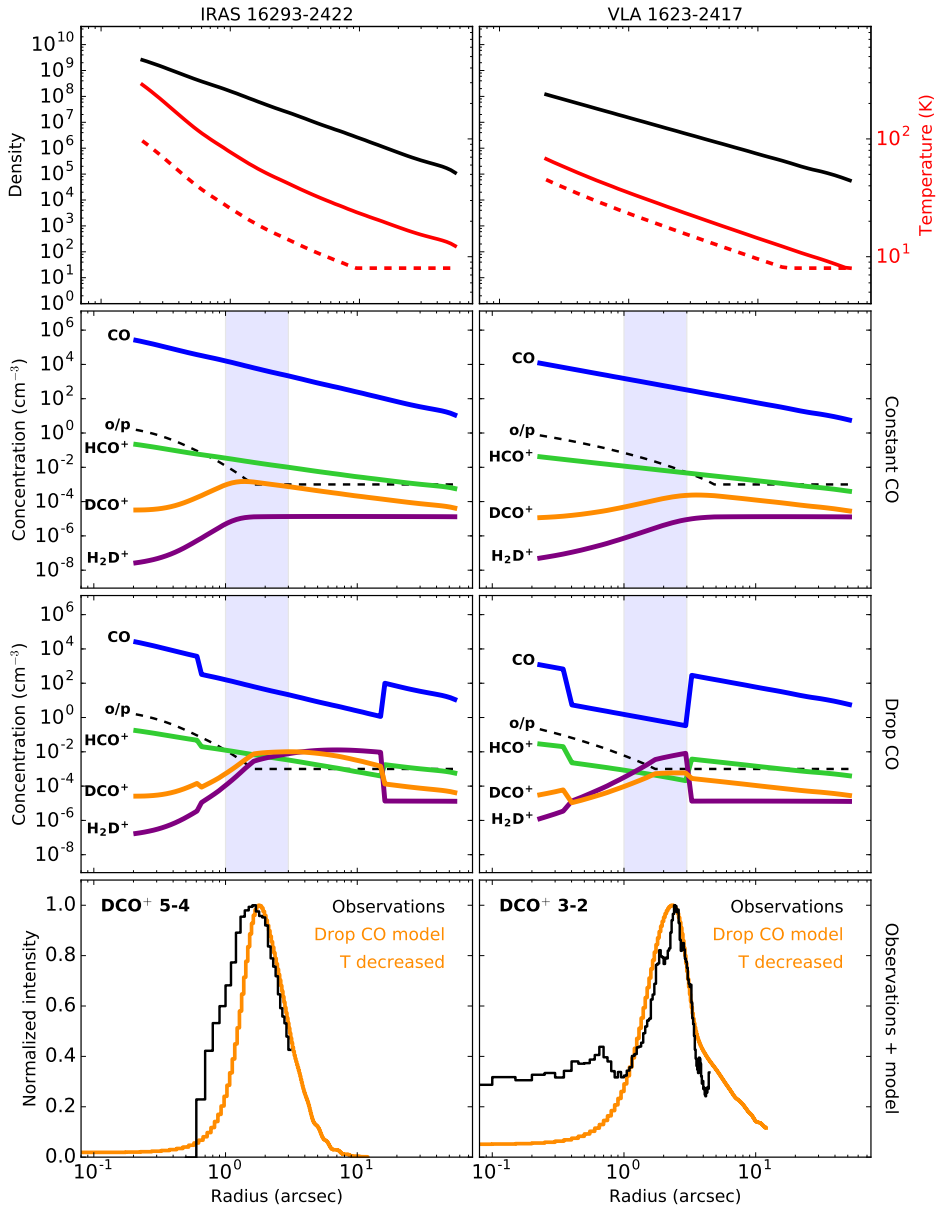

Figure 8: Results from modelling the observed DCO^+ peak with our simple analytic chemical model. The left column shows results for IRAS 16293-2422, while the right column shows those for VLA 1623-2417. The top row shows the input density (black) and temperature (red) as functions of radius for each system. The dashed red line shows the original temperature profile used for the constant CO model (second row panels). This model does not show a DCO^+ peak at the right position. The solid red line is the profile decreased by factors of 3 and 1.5 for IRAS 16293-2422 and VLA 1623-2417, respectively, and used for the drop CO model (third row panels). The lower limit on the temperature is set at 8K. In the second and third row, the shaded range is the location of the observed DCO^+ peak. The bottom row shows the observed radial profiles of DCO^+ overlaid with the Drop CO model.

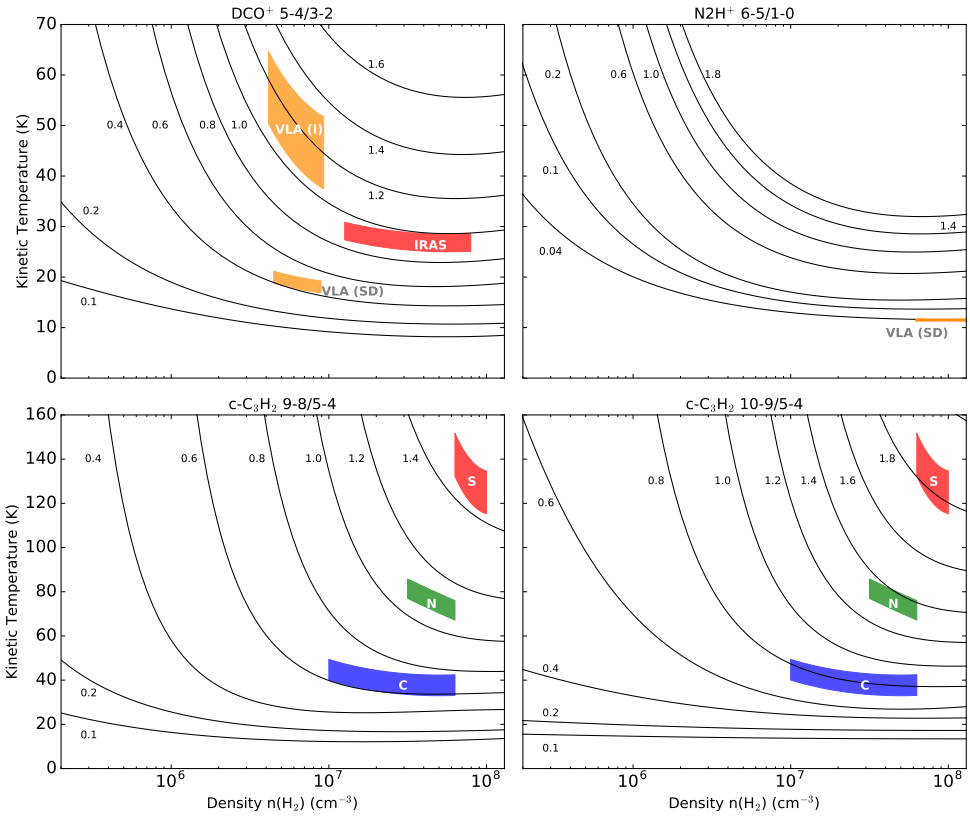

Figure 9: Calculated line ratios for DCO^+ 5–4/3–2, N_2H^+ 6–5/1–0 and c$-C_3H_2$ 10–9/5–4 and 9–8/5–4. Black lines show the modelled ratios assuming column densities of 2.5×10^{12} and 1.3×10^{13} cm^{-2} for DCO^+ and N_2H^+, respectively, and 2.5×10^{13} for both c$-C_3H_2$ ratios. Color areas indicate the observed line ratios drawn over the range of densities and temperatures that characterize the observed emission, for IRAS 16293-2422 with ALMA (red, blue and green) and VLA 1623-2417 (orange) with single-dish (SD) and interferometric (I) observations.

Table 4: DCO^+ intensities and line ratios, with inferred temperature and density.

Source	IRAS 16293-2422		VLA 1623-2417 - ALMA		VLA 1623-2417 - APEX	
Transition	5–4	3–2	5–4	3–2	5–4	3–2
Line width (km s^{-1})	1.0	1.0	0.6	0.6	0.7	0.7
Beam (arcsec)	0.5×0.5	4.11×2.45	0.87×0.65	0.85×0.54	17.3	28.9
Peak (Jy $beam^{-1}$)	5.3±0.4	1.8±0.2	0.29±0.02	0.087±0.008	...	...
Peak (K)	4.0±0.3	4.7±0.5	4.8±0.3	4.9±0.5	2.2±0.1	4.8±0.1
Line ratio	0.9±0.1		1.0±0.1		0.46±0.03	
Column density (cm^{-2})	3×10^{12}		2×10^{12}		2×10^{12}	
H_2 density (cm^{-3})	$1–8\times10^{7}$		$2–6\times10^{6}$		$4–9\times10^{6}$	
T_{kin} (K)	26–29		30–55		18–20	
τ	<1		<1		<1	

Table 5: c$-C_3H_2$ inferred parameters and abundance ratio for c$-C_3H_2/C_2H$

Position	Coordinates		9–8/5–4	10–9/5–4	n_{H_2}	T_{kin}	$N_{c-C_3H_2}$ [a, b]	N_{C_2H} [a]	c$-C_3H_2/C_2H$
	RA	Dec			cm^{-3}	K	cm^{-2}	cm^{-2}	
IRAS 16293-2422									
South	16:32:22.88	–24:28:39.78	1.7±0.08	1.4±0.07	5–10×10^7	120–155	9.3×10^{13}	3×10^{13}	≥3.1
Center	16:32:22.69	–24:28:35.16	0.7±0.3	0.7±0.3	1–6×10^7	37–44	1.3×10^{13}	2×10^{14}	≤0.07
North	16:32:22.55	–24:28:30.28	1.6±0.6	1.3±0.5	3–6×10^7	71–81	1.1×10^{13}	2×10^{14}	≤0.05
VLA 1623-2417					c$-C_3H_2$	$3_{3,0}$–$2_{2,1}$			
c$-C_3H_2$ [c]	16:26:26.39	–24:24:30.69	...	...	5–10×10^7	120–155	2.7–5.3×10^{13}	1–1.5×10^{13}	2.7–3.5

Notes. [a] For IRAS 16293-2422, column densities are for a beam of 0.5″. For VLA 1623-2417, column densities are for a beam of 1.6″ ×0.88″ for c$-C_3H_2$ and 17.3″ for C_2H. [b] An o/p = 3 was used to calculate the total column density of c$-C_3H_2$. [c] c$-C_3H_2$ parameters from the south position of IRAS 16293-2422 .

where the activation energy $\Delta E \sim 220$ K in the back reaction is due to the difference in zero-point energy. A crucial factor for deuterium chemistry is the ortho-to-para ratio of H_2 (Flower et al. 2006; Pagani et al. 2009b). This is included in the back reaction of the chemical network (Eq. 4.1), since it is here where the distinction has the most significant effect (Murillo et al. 2015, see chapter 3). The reactions and parameters for o$-H_2$ and p-H_2 were adapted from Walmsley et al. (2004). The ortho-to-para ratio is set to have a lower limit of 10^{-3} at low temperatures, as constrained from observations and models (Flower et al. 2006). The rate coefficient for two-body reaction is expressed as

$$k = \alpha \left(\frac{T}{300}\right)^{\beta} \exp\left(-\frac{\gamma}{T}\right) \text{ cm}^3 \text{ s}^{-1} \tag{4.2}$$

where T is the temperature of the gas. For cosmic ray ionization, important in the generation of $H_3{}^+$, the rate coefficient is given by

$$k = \zeta \text{ s}^{-1} \tag{4.3}$$

where $\zeta = 1.26 \times 10^{-17}$ is the cosmic-ray ionization rate of H_2. The reactions and rate coefficients used in this work are the same as those listed in Murillo et al. (2015, see chapter 3).

Since CO is a parent molecule of DCO^+, its abundance will impact the production of DCO^+. The profile of the CO abundance is taken to be either constant or with a drop used to simulate freeze-out. The drop is set by the CO sublimation temperature $T_{\rm sub}$ and desorption density $n_{\rm de}$. These limits dictate the boundary where CO is in the gas phase ($T > T_{\rm sub}$) or freezes onto the dust grains ($T < T_{\rm sub}$); and when the freeze-out time-scales for CO are too long ($n < n_{\rm de}$) compared to the lifetime of the core (Jørgensen et al. 2005c). The results of the chemical modelling are passed through RATRAN (Hogerheijde & van der Tak 2000), and then synthetic data cubes are generated in order to directly compare with the observations. The network and further details of the model and post-processing are given in Murillo et al. (2015, see chapter 3).

The model requires a density and temperature profile of the source as a function of radius. For IRAS, the power-law density and temperature profile from Crimier et al. (2010) is adopted. Two assumptions are made, namely that the density and temperature profile is centred on IRAS-A and that it is the main contributor to the luminosity of the core, consistent with the recent analysis of Jacobsen et al. (submitted). Thus, our assumptions should not introduce major issues in our modelling. While there have been several physical profiles derived for IRAS (e.g., Schöier et al. 2002), only one is adopted here since we alter the density and temperature profiles by an arbitrary factor, exploring the effects of these parameters on the production of DCO^+. For VLA, we adopt the power-law density and temperature profile from Jørgensen et al. (2002). Here again we assume the density and temperature profile is centred and dominated by VLA-A. Given that VLA-B does not contribute much to the line emission nor the continuum, and that VLA-W is $10''$ away, this should not produce issues in the resulting model. The temperature and density profile for VLA is also altered by an arbitrary factor to study the effect on DCO^+ production. The variations in the temperature and density profiles used in this work are listed in Table 2 for both systems.

For the DCO^+ models, we explore the parameter ranges of T_{sub} = 20–40 K, n_{de} = 10^5–10^8 cm^{-3} and X[CO] = 10^{-7} – 10^{-4}. The parameters for the best by-eye approximation to the observed DCO^+ peak position are listed in Table 3 for both systems. The best approximated model of the DCO^+ 3–2 emission around VLA (Murillo et al. 2015, see chapter 3) are reproduced here and compared with the results of DCO^+ toward IRAS.

For both systems we find that the constant CO abundance profile does not produce a DCO^+ peak where observed (too far outward), and the peak position does not shift with a change in the abundance. The drop CO abundance profile produces a peak within the drop boundaries, T_{sub} and n_{de}. Altering these parameters changes the shape but not the position of the DCO^+ peak.

Since the chemical conditions do not alter the peak position, the physical structure is examined. The original source density and temperature profiles for both sources also do not reproduce the position of the DCO^+ peak. Increasing or decreasing the density by one order of magnitude, causes the DCO^+ peak to either shift outwards or remain at a position similar to the unchanged density profile. Interestingly, only reducing the temperature profile by an arbitrary factor together with the drop CO abundance profile, causes the DCO^+ peak to shift inwards for both systems (Fig. 8). This is consistent with the results found for VLA's DCO^+ 3–2 in Murillo et al. (2015, see chapter 3), which explores the physical and chemical parameter space in more detail. Thus the observed DCO^+ peak position is produced by a drop in the temperature along the plane perpendicular to the outflow(s). This drop in temperature can be caused by a structure, such as a disk, which shadows the outer regions, allowing the peak emission of molecules whose abundance is enhanced in cold gas to move inwards.

It should be noted, however, that our simple chemical model cannot fully explain the inner part of the DCO^+ 5–4 emission observed centered on VLA-A. DCO^+ 5–4 emission at small radii could be located in the disk where both cold and warm chemical processes can contribute to its formation (Favre et al. 2015; Huang et al. 2017; Salinas et al. 2017).

Thus, the distribution of DCO^+ around both VLA and IRAS is product of the presence of a disk(-like) structure, which causes a drop in temperature on the envelope gas at the edge of the disk(-like structure), i.e. the disk-envelope interface. The presence of the disk(-like) structure generates an asymmetric temperature profile in the protostellar system.

Line ratios and implied physical conditions

Line ratios can provide an independent measure of the temperature of the region being traced by a molecule. The ratio of DCO^+ 5–4/3–2 will provide an independent test of the results obtained with the chemical model of DCO^+ described in the previous section.

Using RADEX (van der Tak et al. 2007), we performed non-LTE excitation and radiative transfer calculations to constrain the temperature and density of the regions being traced by comparing the ratios of observed molecular lines with those calculated by the non-LTE excitation. We limit the range of H_2 densities based on the source profile used for chemical modelling (Table 2 and Fig. 8) and the radial position of the emission being modelled. We assume the optically thin regime for all cases, which is valid for all low abundance species considered here. In this regime, the adopted column density does not affect the line flux ratios, only the absolute flux values. The

molecular data files are obtained from the Leiden Atomic and Molecular Database (LAMDA; Schöier et al. 2005b). In order to compare the observed peak intensities with the results from RADEX, the observed peaks are converted from Jy beam^{-1} to K using the relation $T_{\rm mb} = 1.36\ \lambda^2/\theta^2\ S_{\rm observed}$ where λ is the wavelength in centimetres of the molecular transition, θ is the beam of the observations and $S_{\rm observed}$ is the observed flux density in mJy beam^{-1}.

Here, we derive the physical parameters from the DCO^+ 5–4/3–2 ratio for both sources. Figure 9 shows the variation of the DCO^+ 5–4/3–2 ratio with H_2 density and temperature. For both IRAS and VLA, the red-shifted peak emission is considered, since it is the most prominent. The results for IRAS and VLA are compared in Table 4.

For IRAS, a ratio DCO^+ 5–4/3–2 = 0.9 ± 0.09 is obtained from the PILS band 7 observations and the SMA 230 GHz observations (Jørgensen et al. 2011). We adopt a line width of 1.0 km s^{-1} and a column density of 3×10^{12} cm^{-2}, a value that also reproduces the observed line intensities. For densities below 10^6 cm^{-3}, the critical density of the 5–4 transition, the line ratio is primarily sensitive to density; at higher densities, the ratio becomes a good temperature probe. According to the density structure presented in Fig. 8 (top panel), the density at the peak DCO^+ emission position is higher than the critical density, so a kinetic temperature between 20 and 30 K can be inferred for IRAS. This temperature is consistent with the chemical modelling of the DCO^+ peak position.

For VLA, the ALMA 12m array observations provide DCO^+ 5–4/3–2 = 1.0 ± 0.1. The beam-size of DCO^+ 5–4 ($0.87'' \times 0.65''$) is similar to that of the 3–2 transition ($0.87'' \times 0.54''$) and thus no beam dilution factor was added to the calculation. This line flux ratio implies a kinetic temperature between 30 and 55 K, adopting a column density of 2×10^{12} and a line width of 0.7 km s^{-1} to reproduce the observed peak intensities. This is higher than expected from the chemical modelling of DCO^+. The APEX observations are used to double check if this is the kinetic temperature of the bulk of the DCO^+ emission at the disk-envelope interface. The APEX DCO^+ data give a much lower line ratio, 5–4/3–2 = 0.46 ± 0.03. This line flux ratio is well reproduced by a kinetic temperature of 17 to 19 K, in agreement with the chemical model. It is likely that the ALMA 12m array observations are picking up both warm and cold DCO^+ emission in the 5–4 transition, but only cold DCO^+ in the 3–2 transition. On the other hand, the APEX observations are recovering DCO^+ emission from the cold regions at the edge of the disk and the envelope, but the beam size dilutes the emission from the inner regions. This then causes the discrepancy of derived kinetic temperatures that we obtain from interferometric versus single-dish data. The temperature from the interferometric data is driven up due to more emission being detected in the higher transition.

4.4.2 c−C_3H_2

To study the physical conditions of the region traced by c−C_3H_2, line ratios of the detected transitions, rather than chemical models, are used. Five transitions of c−C_3H_2 are detected towards IRAS. Temperature and density are derived from the c−C_3H_2 9–8/5–4 and 10–9/5–4 ratios (See Sect. 4.4.1). Figure 9 shows the line flux ratios as functions of H_2 density and kinetic temperature. The ortho-c−C_3H_2 molecular file is used for the RADEX calculations since the 5–4 transition (349.264 GHz) presented here is the ortho form (para-c−C_3H_2 5–4 is at 338.204 GHz). To convert to the total

(ortho + para) c−C_3H_2 column density, an o/p ratio of 3 was used. Three regions covering the south c−C_3H_2 peak and the C_2H peaks near the center and north of the map are selected to derive the temperature and c−C_3H_2/C_2H column density ratios (Fig. 4). Table 5 lists the positions. The IRAS-A and B positions are not modelled due to contamination from other molecular species.

Both c−C_3H_2 9–8/5–4 and 10–9/5–4 ratios are simultaneously fit for each position. Table 5 lists the ratios along with the adopted densities and derived kinetic temperature. The peak intensities for each transition at the three positions are listed in Table 6 We find that the temperature for the south c−C_3H_2 peak, corresponding to the outflow cavity of IRAS-A, is between 120–155 K, 2 to 4 times higher than for the positions where C_2H peaks. The central position shows the lowest temperature with 41–44 K. Comparing the temperatures obtained from c−C_3H_2 and DCO^+ line ratios, it is clear that c−C_3H_2 arises from a much warmer region than DCO^+. This is linked to the spatial anti-correlation found for these two molecules, both in our observations and other work (see Sect. 4.5).

Only one transition of c−C_3H_2 is available for VLA, with an upper level energy (19.5 K) lower than those observed toward IRAS ($\geq$ 49 K). Thus to obtain an idea of the column densities in the region traced by c−C_3H_2 towards VLA, we adopt the temperature and density from the c−C_3H_2 line ratios towards IRAS at the south peak. The c−C_3H_2 south peak of IRAS is chosen due to the fact that it traces the outflow cavity, as it does for VLA. Using the parameters of c−C_3H_2 from IRAS, the derived column density is a few times 10^{13} cm^{-2}, lower by about a factor of 2 or 3 than that found for the south peak of IRAS and similar to the column density found for the central position of the IRAS map.

4.4.3 C_2H

The same transitions of C_2H are observed towards both sources, with ALMA for IRAS and with APEX for VLA. The peak intensities are listed in Table 6. Since C_2H ratios are not sensitive to temperature or density given the similar upper eneriges E_{up} (Table 1), the method adopted for DCO^+ and c−C_3H_2 cannot be used here. Instead, the C_2H column density is derived by assuming the kinetic temperature and number density obtained from c−C_3H_2 line ratios. The results are listed in Table 5.

The south position in IRAS presents a column density of $\leq 3\times10^{13}$ cm^{-2}, about an order of magnitude lower compared to the centre and north positions which have a column density of 2×10^{14} cm^{-2}. Table 5 lists the c−C_3H_2/C_2H column density ratio for each position. It must be noted that the ratio at the south position is a lower limit, whereas for the central and north position, it is an upper limit. The differences in ratios between positions reflect the anti-correlation of the two molecules in the IRAS system. Most certainly, the anti-correlation is not due to critical densities, since the derived number densities of c−C_3H_2 (10^7 to 10^8 cm^{-3}) at all points are above the critical densities of both C_2H (8×10^4 to 6×10^5 cm^{-3}) and c−C_3H_2 (2–5×10^5 cm^{-3}).

For VLA, C_2H column densities are found to be a few times 10^{13} cm^{-2}, lower than the peaks of C_2H detected towards IRAS. The results are listed in Table 5. The c−C_3H_2/C_2H ratio of column density provides values similar to the south position towards IRAS.

4.4.4 N_2H^+ and N_2D^+

For VLA, the ALMA 12m array observations of N_2D^+ and N_2H^+ did not detect any emission. Since these molecules are readily detected in other sources (e.g., Tobin et al. 2013a), the cause of this non-detection is examined. Two cases are explored, extended and compact emission concentrated in a 1″ region. The details of the analysis are given in Appendix 4.B.

For the case of extended emission, the predicted N_2H^+ 4–3 peak intensity is the same as the noise level of our observations, while for the case of the emission concentrated in 1″ region, the S/N would be about 26. In a similar manner, the predicted N_2D^+ 3–2 peak intensity is expected to have a marginal detection in our observations for the extended emission case, and a $S/N = 40$ for the compact emission case. Thus, we should have detected both molecules in our observations if they arose from a compact structure.

4.5 Discussion

4.5.1 Comparison of IRAS 16293-2422 and VLA 1623-2417

The chemical structure of both systems is compared in this section. A cartoon of their structure is shown in Fig. 1.

The DCO^+ peak position in both sources is well described by a drop in the temperature profile. This drop can be explained by the presence of a disk which shadows the envelope, causing the DCO^+ emission to move inward, closer to the source along the disk plane. For VLA, the ALMA DCO^+ 5–4 observations are picking up emission coming from both the cold envelope at the edge of the disk (disk-envelope interface) and the warmer parts of the disk.

c$-C_3H_2$ traces the outflow cavity of IRAS-A and VLA-A. For VLA-A, c$-C_3H_2$ traces the full outflow cavity (extending out to 3″), whereas for IRAS-A only one side of the south outflow cavity wall is observed. It is possible that the c$-C_3H_2$ emission is product of UV radiation from the central source, and the warmer temperatures found in the outflow cavity. UV radiation liberates atomic carbon which leads to gas-phase formation of small hydrocarbons. Chemical models of the outflow cavity walls show that c$-C_3H_2$ is initially concentrated around the outflow wall, and progressively moves to the disk plane as the cavity widens with age, irradiating more envelope material (Drozdovskaya et al. 2015). Higher temperatures could accelerate certain chemical processes in the protostellar envelope, while movement of material through outflows, rotation and infall could bring dust with c$-C_3H_2$ precursors (e.g., CH_4, C_2H_2) closer to areas where they can be sublimated and thus enhance the c$-C_3H_2$ gas. Hence, the differences in the spatial distributions of c$-C_3H_2$ in IRAS-A ($L_{\rm bol} > 18$ L$_\odot$, Jacobsen et al. submitted) and VLA-A ($L_{\rm bol} \sim 1 L_\odot$) could be the product of age, luminosity, or core dynamics. In any case, the presence of c$-C_3H_2$ emission is due to the temperature of the region where it is observed.

C_2H does not present similar distributions in IRAS and VLA. Toward VLA, the single-dish C_2H emission peaks on VLA-A, and is most likely spatially correlated with c$-C_3H_2$. C_2H could arise from the envelope or outflow, given that it shows similar broadening with DCO^+ (Lindberg et al. 2017), but also with c$-C_3H_2$. For IRAS, the observed C_2H is found in the region one beam away from IRAS-B, but does not show

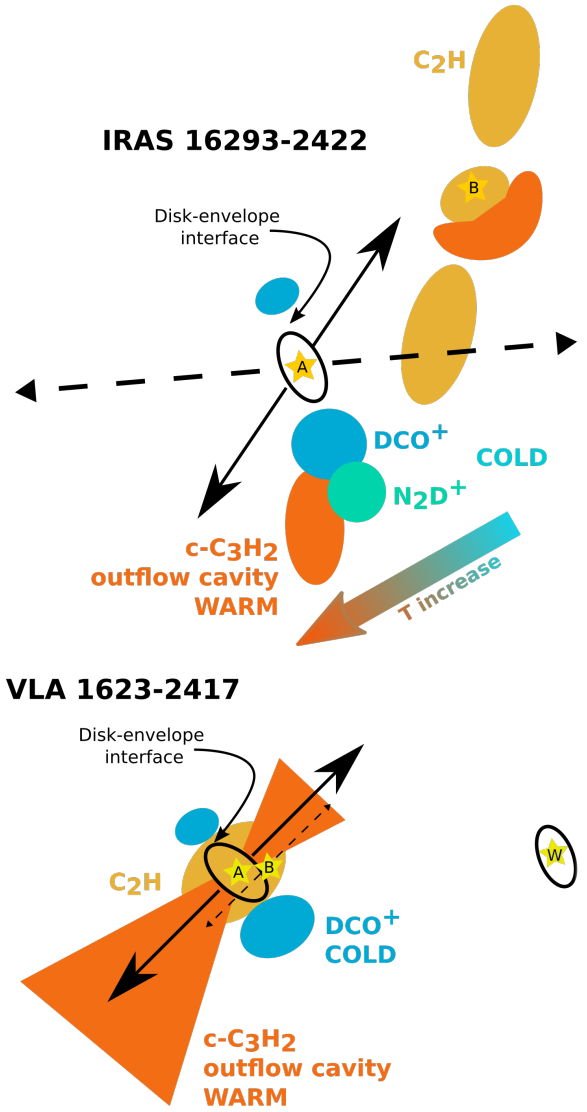

Figure 10: Cartoon showing the distribution of the molecules studied in this work towards both sources. The solid and dashed lines show outflow directions. Ellipses indicate disk structures.

relation with the position or outflow of IRAS-A, nor with the dust ridge connecting both sources. Beyond IRAS-B, C_2H and c$-C_3H_2$ are not spatially correlated (Fig. 4 and 5). This anti-correlation is unexpected from chemical models (e.g. Gerin et al. 2011; Drozdovskaya et al. 2015; Guzmán et al. 2015) or observations (see Sect. 4.5.2). The c$-C_3H_2/C_2H$ ratio is expected to be lowered with age, that is as the protostar evolves (O. Sipilä, private communication). If the different distributions of c$-C_3H_2$ and C_2H are product of age, it would suggest that IRAS is somewhat older than VLA; however, lowering the ratio with age does not explain the anti-correlation observed in IRAS.

A possible explanation may be top-down chemistry producing small hydrocarbons through UV destruction of large aromatic molecules as inferred for lower density PDRs (Guzmán et al. 2015), producing different amounts of the two molecules. Another possibility for the anti-correlation might be explained by the destruction of C_2H in reactions with sulfur, nitrogen, oxygen or carbon chains (Sakai & Yamamoto 2013). The full Band 7 spectrum is examined at the c$-C_3H_2$ peak position (Fig. 13– 15) in order to examine whether products of C_2H reactions are present. C_2S, product of C_2H reacting with sulfur (Drozdovskaya et al. in prep.), is not detected. In fact, little else is observed in the dense gas south of IRAS-A. Apart from c$-C_3H_2$, only H_2CS (Drozdovskaya et al. in prep.) and a few common species like HCO^+, H_2CO and CH_2OH are detected, which is unexpected given that outflow cavity would be irradiated and encourage chemical complexity (Drozdovskaya et al. 2015). Reactions of C_2H with carbon chains C_n would cause production of C_{n+2} and hydrogen, rendering these products undetectable due to lack of dipole moments. Overall, the strong anti-correlation of these molecules remains a chemical puzzle.

N_2D^+ is detected 7″ south of IRAS-A with the SMA (Fig. 3), bordering the DCO^+ emission (Jørgensen et al. 2011). In contrast, N_2D^+ and N_2H^+ are not detected with ALMA observations towards VLA. Single-dish observations show an offset between the position of VLA and the peak of N_2H^+ and N_2D^+ (Di Francesco et al. 2004; Liseau et al. 2015; Punanova et al. 2016; Favre et al. 2017). Since neither molecule is detected in our observations with ALMA (Sect. 4.4.4), it would suggest that N_2H^+ and N_2D^+ lines trace emission outside the VLA envelope (Liseau et al. 2015).

The presence of N_2D^+ in IRAS, but not in VLA, could be product of temperature differences. N_2 can be frozen out onto dust grains at temperatures below 20 K (Bisschop et al. 2006), a scenario also pointed out by Di Francesco et al. (2004). While other nitrogen-bearing molecules such as CN, HCN, HNC and NO can form in the gas and on grain surfaces, N_2H^+ and N_2D^+ only form in the gas phase if N_2 gas is present. This scenario is further supported by the low temperatures found for DCO^+. For VLA-A, DCO^+ has $T_{\rm kin}$ = 17 K, and the chemical modelling suggests dust temperatures between 11 to 16 K for where DCO^+ peaks. This would indicate that further out, the temperature is even lower. In addition, at densities below $\sim 10^4$ cm^{-3}, the dust and gas temperatures decouple, and without any additional external pressure, the gas temperature drops down to 10 K (Galli et al. 2002; Evans et al. 2001), which could cause N_2H^+ and N_2D^+ to recombine onto the dust grains or the precursor N_2 to freeze-out. In contrast, DCO^+ south of IRAS-A indicates $T_{\rm kin}$ = 30 K for the gas, and dust temperatures between 17 to 19 K from chemical modelling, evidencing that the envelope of IRAS-A is warmer than that of VLA (Jacobsen et al. submitted).

N_2H^+ and N_2D^+ are thought to be tracers of evolutionary stage (Emprechtinger

et al. 2009), as well as of the CO snowline (Jørgensen et al. 2004; Anderl et al. 2016; van't Hoff et al. 2017). These assumptions break down for very cold envelopes like that of VLA. Given that some starless cores do show N_2H^+ and N_2D^+ (Tobin et al. 2013a), including the starless cores north of VLA (Di Francesco et al. 2004), it cannot be said that the cold envelope itself is an indicator of evolutionary stage. It may be possible that the ridge of material north of VLA, which contains the starless cores, is being heated somehow from the side, but VLA is being shielded and thus much colder (Di Francesco et al. 2004; Bergman et al. 2011; Friesen et al. 2014). VLA-A itself is certainly heating up the disk and outflow cavity, evidenced by DCO^+ 5–4 emission on the disk and the presence of c$-C_3H_2$, but on much smaller scales (<100 AU) than in IRAS because of its lower luminosity.

4.5.2 Comparison with starless cores and low-mass protostars

In this section, IRAS and VLA are placed in the big picture of star formation. For this reason, the two systems described in the previous section are compared with observations of starless cores, embedded low-mass protostars and disks found in the literature. In addition, the multiplicity of the systems is also taken into consideration.

The starless core L1544 exhibits c$-C_3H_2$ close to the dense cloud core center and away from cold regions traced by DCO^+ (Spezzano et al. 2016b,a). This points to an anti-correlation between the chemistry traced by DCO^+ and that by c$-C_3H_2$, which is present in both IRAS and VLA. In the system NGC1333 IRAS4, C_2H is observed to peak on-source toward each component, including the starless core IRAS4C, which has the strongest emission (Koumpia et al. 2016, 2017). In the young embedded object IRAS15398, C_2H traces the red- and blue-shifted outflow cavity (Jørgensen et al. 2013). In contrast, L1527 presents both C_2H and c$-C_3H_2$ in the envelope and disk component, with enhancements at the centrifugal barrier (Sakai et al. 2010, 2014b, 2016), but no emission along the outflow cavity. The spatial distribution of C_2H and c$-C_3H_2$ is similar in L1527, with the emission from c$-C_3H_2$ being more compact than that of C_2H. In Oph-IRS67, C_2H and c$-C_3H_2$ exist in the same region, although the spatial extent is not the same (Artur de la Villarmois et al. submitted). In the protoplanetary disk TW Hya, C_2H and c$-C_3H_2$ are found to reside in the disk, bordering the millimeter dust, with both molecules showing an identical spatial distribution (Bergin et al. 2016). The c$-C_3H_2$ and C_2H distribution toward VLA is consistent with that observed in other protostellar systems; however, for IRAS the lack of correlation between the two molecules is still a puzzle, since no other source presents this situation.

In NGC1333 SVS13, N_2H^+ is detected around 2 of the 4 components of the system (Chen et al. 2009). From the system, SVS13B and SVS13C are Class 0 protostars, but the first has N_2H^+ emission while the second does not. Thus, the uneven distribution of material is not related to the evolutionary stage, but instead is most likely related to the varying envelope temperature.

Several of the systems mentioned above are multiple protostars, as are IRAS and VLA. The chemical structure is found to not be homogeneous among the individual components of these systems. Thus multiplicity in the embedded phase does not seem to affect the observed chemical structure, that is external heating from companions appears to have no significant effect. Altogether, the chemical structure of embedded protostellar systems for the molecules studied here seems to not be dependent on the

evolutionary stage, parent cloud or companion sources, but primarily on the central source heating its surrounding gas.

4.5.3 Comparison with diffuse clouds, PDRs and high-mass protostars

Looking to compare what structures are common throughout the interstellar medium, we compare the distributions found in IRAS and VLA with diffuse clouds and PDRs. Furthermore, given that IRAS is much warmer than VLA, it is also compared to high-mass protostars.

Towards the Horsehead nebula PDR, DCO^+ is observed far from the irradiated edge of the region, with no emission at the edge (Guzmán et al. 2015). The spatial anti-correlation between DCO^+ and c$-C_3H_2$ or C_2H suggests a temperature effect, as found for IRAS and VLA, highlighting that DCO^+ is a really good tracer of cold regions.

c$-C_3H_2$ and C_2H show close correlation in spatial distribution towards a number of PDRs, including the Orion Bar (Pety et al. 2007; van der Wiel et al. 2009; Nagy et al. 2015) and the Horsehead Nebula (Cuadrado et al. 2015; Guzmán et al. 2015), with both molecular species sitting at the irradiated, and thus warmer, edge of the region. In addition, a tight correlation between c$-C_3H_2$ and C_2H in diffuse clouds has been found (Lucas & Liszt 2000; Gerin et al. 2011; Liszt et al. 2012). The column density c$-C_3H_2/C_2H$ ratios calculated toward IRAS in the center and north positions (c$-C_3H_2/C_2H$ = 0.05–0.07) reflect the values found for diffuse clouds (c$-C_3H_2/C_2H$ = 0.048; Lucas & Liszt 2000; Liszt et al. 2012) and the envelope of L1527 (c$-C_3H_2/C_2H$ = 0.035 – 0.06; Sakai et al. 2014b).

In high-mass star-forming regions, c$-C_3H_2$ and C_2H are also strongly correlated, with both lines presenting similar spatial distributions (Pilleri et al. 2013; Mookerjea et al. 2012, 2014). Thus, the warmer envelope of IRAS does not provide a solution to the puzzle of why c$-C_3H_2$ and C_2H are anti-correlated in this system. The cause is most likely not related to the physical structure of IRAS, but the chemical processes occurring in the envelope of this system.

4.6 Conclusions

In this work, we present ALMA, SMA and APEX observations of DCO^+, c$-C_3H_2$, C_2H, N_2H^+ and N_2D^+ towards IRAS 16293-2422 and VLA 1623-2417, both multiple protostellar systems in ρ Ophiuchus. The spatial distribution of each molecule is compared for both systems. DCO^+ is studied using a simple analytic chemical network coupled with radiative transfer modelling, detailed in Murillo et al. (2015, see chapter 3), in order to determine the conditions leading to the observed peak position. Non-LTE molecular excitation and radiative transfer modelling of the observed line flux ratios is done to derive physical parameters of the regions being traced by the molecules. Finally, the observations and results of VLA 1623-2417 and IRAS 16293-2422 are compared, both between the two sources and other objects, ranging from low- to high-mass protostars, diffuse clouds and PDRs, in order to understand what structures are common.

From this work, we extract the following key points:

1. Temperature is a controlling factor of the chemical structure of a protostellar system. Disks can alter the temperature of the envelope, while UV heating can encourage the start of chemical processes in the outflow cavity.

2. An asymmetric DCO^+ structure is a good tell-tale sign for the presence of a disk, since a disk shadows the envelope at its edge, lowering the temperature and causing DCO^+ to move inwards only along the disk plane.

3. c$-C_3H_2$ traces the outflow cavity of IRAS 16293-2422 and VLA 1623-2417, but shows no disk component for either source.

4. Despite both VLA 1623-2417 and IRAS 16293-2422 being low-mass Class 0 embedded objects, their structure and chemical richness varies considerably, with VLA 1623-2417 being line poor. Its much lower luminosity, and consequently lower temperatures, coupled with a large cold disk, are likely at the root of this difference.

Although only two sources are studied in this work and some results in the literature, there is evidence pointing to a lack of correlation between multiplicity and the chemical structure of the envelope of these systems, at least in the embedded phase. Nevertheless, multiple systems do provide an interesting way to compare the structure with similar conditions. It would be possible, however, that the heating from companion sources would affect the chemistry as the envelope clears. Further comparison of embedded multiple protostellar systems is needed to confirm these results.

Appendix

4.A Velocity integrated maps

The velocity integrated maps of the molecules presented in this work are shown in Fig. 11. For IRAS 16293-2422 A, the velocity gradient goes from north-east (blue-shifted) to south-west (red-shifted). This gradient is consistent for H_2CO and all the transitions of c$-C_3H_2$. DCO^+ is only observed to have a red-shifted component. This is consistent with the DCO^+ observations with the SMA and ACA. The velocity gradient of IRAS 16293-2422 B is less clear, which is most likely due to it being orientated face-on.

4.B Peak intensities and line ratios

The observed peak intensities of C_2H and c$-C_3H_2$ are listed in this appendix (Table 6). The peak intensities are used in Sect. 4.4.2 and 4.4.3. In addition, the detailed calculation of expected peak fluxes for N_2H^+ and N_2D^+ are also summarized here (Table 7).

Single-dish observations of low-J transitions of CN, HCN and HNC show strong detections relative to other embedded systems (Jørgensen et al. 2004). Our recent APEX observations also detected NO towards VLA. However, single-dish observations of NH_3 (Wootten et al. 1994; Liseau et al. 2003) and N_2H^+ (Liseau et al. 2015; Punanova et al. 2016) indicate that these molecules have very low abundances at the

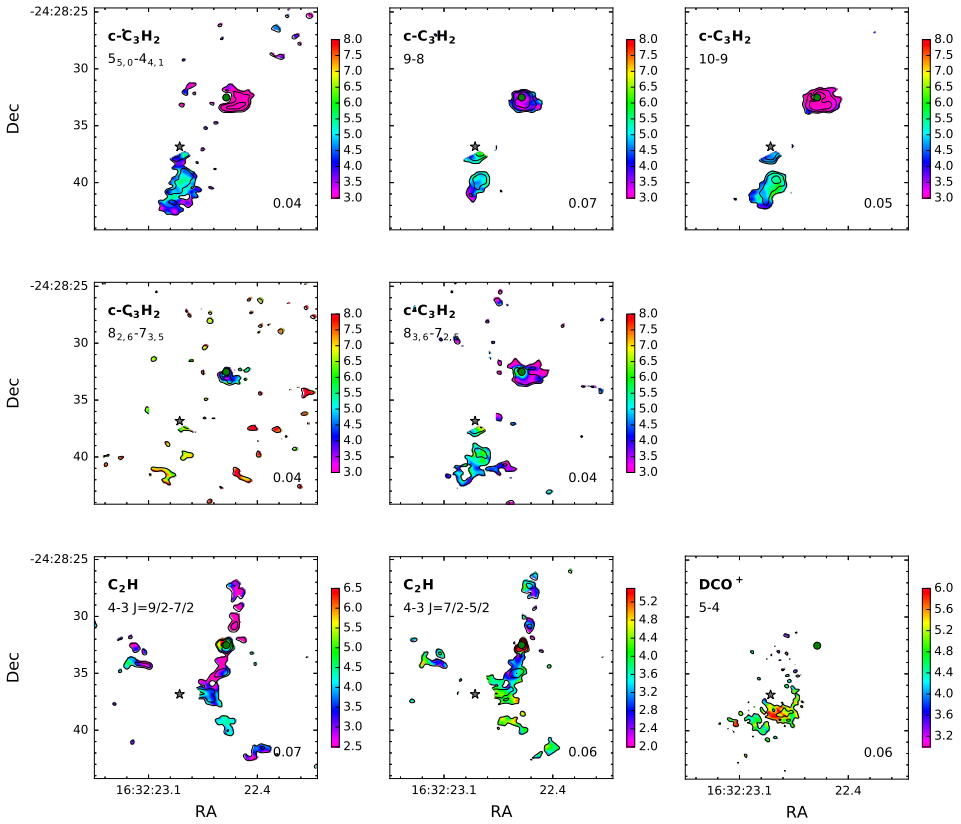

Figure 11: Intensity (contours) and velocity (color-scale) integrated maps of c$-C_3H_2$, C_2H and DCO^+ towards IRAS 16293-2422. The color-bar shows the velocity range in km s^{-1} for each panel. Contours show the respective line in steps of 2, 3, 5, 20, 60 and 80σ, with σ (Jy $beam^{-1}$ km s^{-1}) indicated in the lower right corner of each panel. The postions of IRAS 16293-2422 A and B are indicated with a star and circle, respectively.

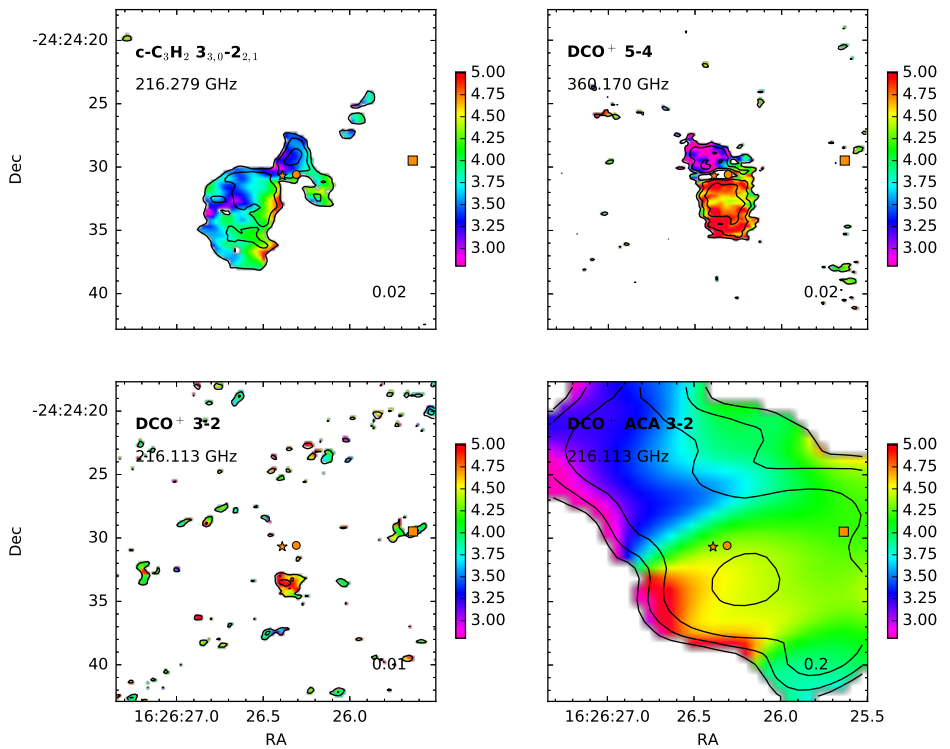

Figure 12: Intensity (contours) and velocity (color-scale) integrated maps of c$-C_3H_2$ and DCO^+ towards VLA 1623-2417. The color-bar shows the velocity range in km s^{-1} for each panel. Contours show the respective lines in steps of 2, 3, 5, 15, 20 and 30σ, with σ (Jy beam^{-1} km s^{-1}) indicated in the lower right of each panel. The positions of VLA 1623-2417 A, B and W are indicated with a star, circle and square, respectively.

position of VLA. N_2D^+ also exhibits the same behaviour (Punanova et al. 2016). Furthermore, *Herschel* observations of high-J N_2H^+ towards VLA (Liseau et al. 2015; Favre et al. 2017)) show that the molecule is detected up to the J = 6–5 transition peaking at ∼0.1 K km s^{-1} but the emission is extended. The observed parameters of N_2H^+ and N_2D^+ from Punanova et al. (2016) and Favre et al. (2017) are listed in Table 7.

Using the observed transitions of N_2H^+ and N_2D^+, we derive density and excitation temperature with the method described in Sect. 4.4.1. The different beam sizes of the observations require a beam dilution correction factor that is given by $T'_{\rm mb} = T_{\rm mb,obs} \frac{\theta^2_{\rm source}}{\theta^2_{\rm source}+\theta^2_{\rm beam}}$, where $T'_{\rm mb}$ and $T_{\rm mb,obs}$ are the corrected and observed main beam temperature, respectively, $\Omega_{\rm beam}$ is the solid angle of the single-dish beam and $\Omega_{\rm source}$ is the solid angle subtended by the source. We assume the emission is concentrated in the region of the smaller beam, which would be of 26.5″ for N_2H^+ and 16.3″ for N_2D^+.

To compare with our ALMA observations, the expected peak for N_2H^+ 4–3 and N_2D^+ 3–2 is derived from the observations of Punanova et al. (2016) and Favre et al. (2017). The N_2H^+ molecular data file without hyperfine structure is used to calculate the kinetic temperature of both molecules. Since LAMDA does not have a molecular data file for N_2D^+, the data file for N_2H^+ is used, selecting the corresponding transition rather than frequency. For the predicted peak emissions for N_2H^+ 4–3 and N_2D^+ 3–2, two cases are examined: i) the observed emission is evenly distributed in the single-dish beam (i.e., beam filling factor = 1) and ii) the emission is concentrated in a 1″ region (i.e. beam filling factor < 1). The second case introduces a beam dilution correction. The results of the calculation are listed in Table 7.

The kinetic temperature and number density obtained in our calculations (∼11 K, $\sim10^{7-9}$ cm^{-3}) are slightly higher than those previously reported (7.7 K, 10^6 cm^{-3}; Punanova et al. 2016). The column densities, however, are similar to those reported in Punanova et al. (2016). For N_2H^+, our results are also consistent with those reported in Liseau et al. (2015).

Using the physical parameters obtained from the DCO^+ 5–4/3–2 ratio (Sect. 4.4.1 and Table 4), we calculate a column density of 1.5–2×10^{13} cm^{-2} for N_2D^+. If instead we use the physical parameters obtained from the N_2D^+ observations towards VLA, we find a column density of 4–5×10^{13} cm^{-2} for N_2D^+ 3–2 towards IRAS. For both sets of parameters, the column density is higher by one order of magnitude in comparison to the N_2D^+ toward VLA.

4.C PILS full spectra

The PILS survey spectra (Jørgensen et al. 2016) is reproduced here for the south c−C_3H_2 peak position and at one beam away from the position of IRAS-B. Figures 13, 14 and 15 present the full spectra for both positions. At the south c−C_3H_2 peak position, the spectra is multiplied by a factor of 10 to bring out the features. Few molecular lines are detected at this position, apart from common molecules like HCO^+ and CO, only c−C_3H_2 and H_2CS are detected.

Table 6: c−C_3H_2 and C_2H peak intensities.

Molecules	c−C_3H_2					C_2H			
Transition	5–4	9–8	10–9	8–7	8–7	J=9/2–7/2 F=5–4	J=9/2–7/2 F=4–3	J=7/2–5/2 F=4–3	J=7/2–5/2 F=3–2
IRAS 16293-2422 (rms = 10 mJy beam^{-1})									
South	240	410	350	90	200	≤20	30	10	20
Centre	40	30	30	20	30	170	140	140	110
North	30	50	40	20	20	150	130	110	110
VLA 1623-2417 - APEX (rms = 80 mK)									
A	...	...	...	...	...	960	616	680	342

Table 7: N_2H^+ and N_2D^+ parameters for VLA 1623-2417.

	Observed			
Parameter	N_2H^+ 1–0[a]	N_2H^+ 6–5[b]	N_2D^+ 1–0[a]	N_2D^+ 2–1[a]
$T_{\rm mb}$ (K)	3.3 ± 0.1	0.2 ± 0.1	0.57 ± 0.1	1.5 ± 0.2
$\Delta v_{\rm SD}$ (km s^{-1})	0.56 ± 0.01	0.7 ± 0.2	0.55 ± 0.03	0.55 ± 0.01
$\eta_{\rm mb}$	0.95	0.63	0.95	0.94
$\Omega_{\rm beam}$ ($''$)	26.5	36	32.1	16.3
Ratio	0.06 ± 0.03		2.6 ± 0.6	
Col. density (cm^{-2})	1.3×10^{13}		1.8×10^{12}	
H_2 density (cm^{-3})	5×10^7 – 7×10^9		5×10^7 – 7×10^9	
$T_{\rm ex}$ (K)	11 – 12		11 – 12	
$\Omega_{\rm source} = \Omega_{\rm beam}$	N_2H^+ 4–3		N_2D^+ 3–2	
$S_{\rm pred}$ (mJy beam^{-1})	99		22	
$\Omega_{\rm beam,obs}$ ($''$)	0.85		0.76	
$\sigma_{\rm obs}$ (mJy beam^{-1})	94.9		8.58	
S/N	1		2.6	
$\Omega_{\rm source} = 1''$	N_2H^+ 4–3		N_2D^+ 3–2	
$S_{\rm pred}$ (mJy beam^{-1})	2631		364	
$\Omega_{\rm beam,obs}$ ($''$)	0.85		0.76	
$\sigma_{\rm obs}$ (mJy beam^{-1})	94.9		8.58	
S/N	27		42	

Notes. [a] IRAM 30m observations from Punanova et al. (2016). [b] *Herschel* observations from Favre et al. (2017)

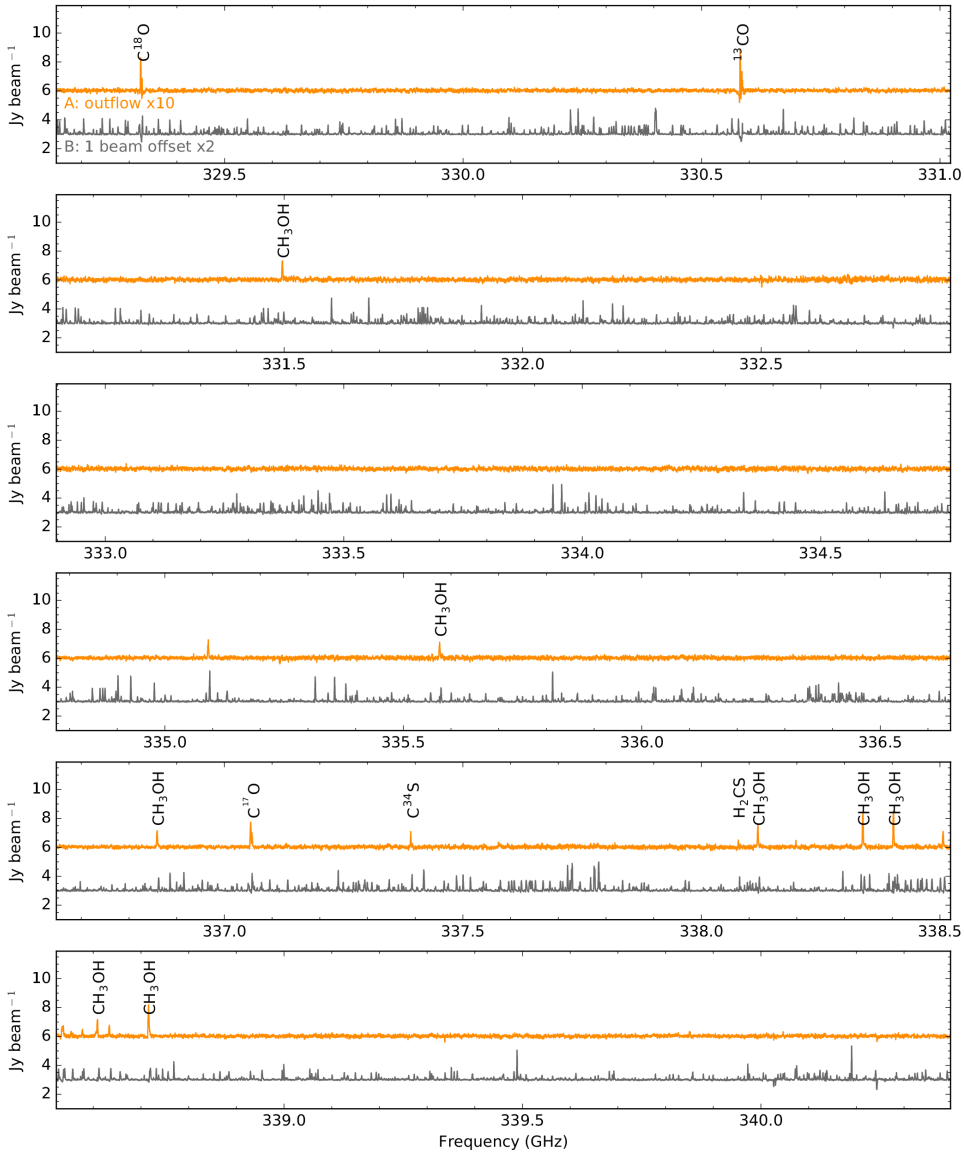

Figure 13: Full spectra obtained in the PILS survey for IRAS 16293-2422. Here the frequency range 329.15 to 340.4 GHz is shown. The rest of the spectra is shown in Fig. 14 and 15. The spectra for the IRAS 16293-2422 B is one beam away from the source position, note that it is multiplied by a factor of 2. The spectra for IRAS 16293-2422 A's outflow is centered at the observed peak of c$-C_3H_2$, note that it is multiplied by a factor of 10 and shows very little emission other than c$-C_3H_2$, CH_3OH, H_2CS, H_2CO and HCO^+.

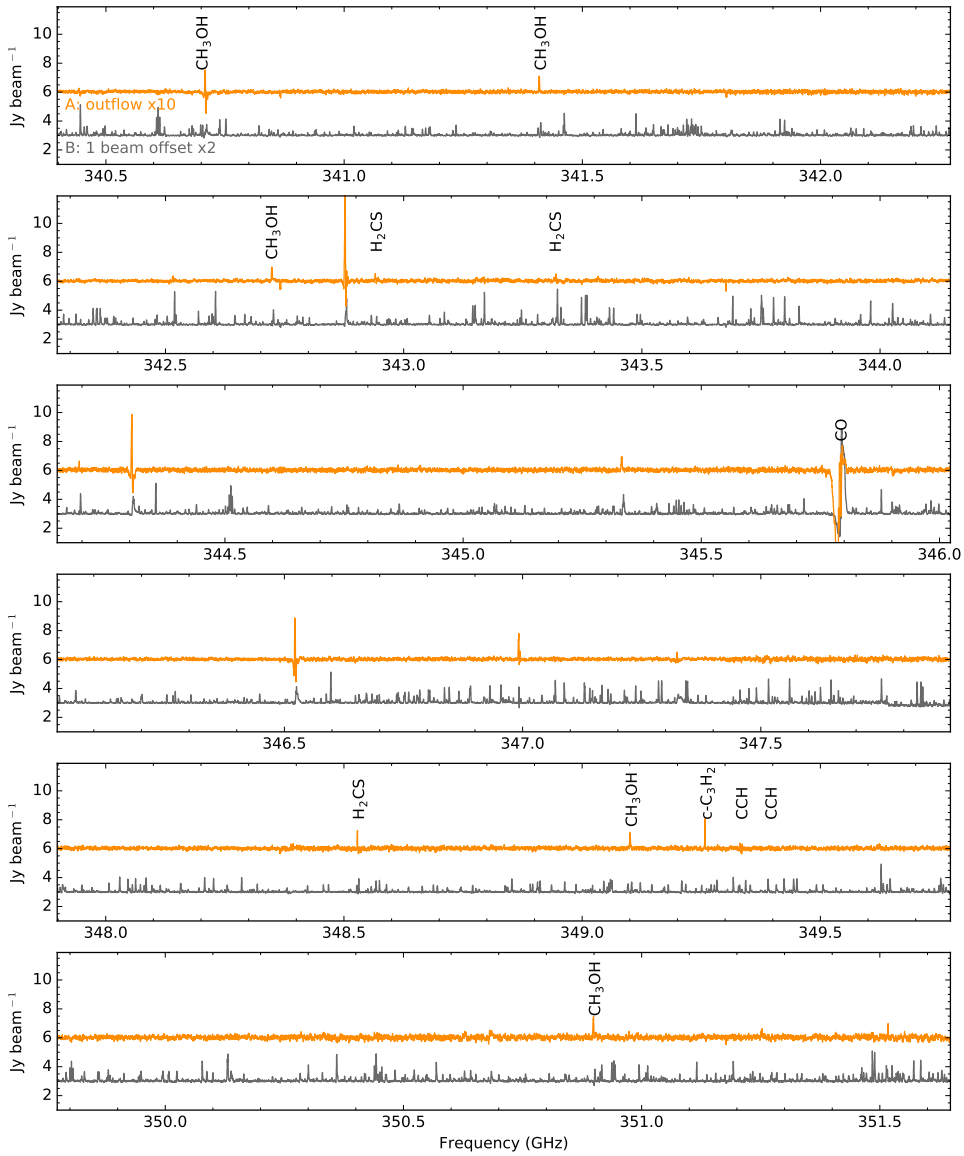

Figure 14: Same as in Fig. 13 but for the frequency range 340.4 to 351.65 GHz. C_2H is marked for reference.

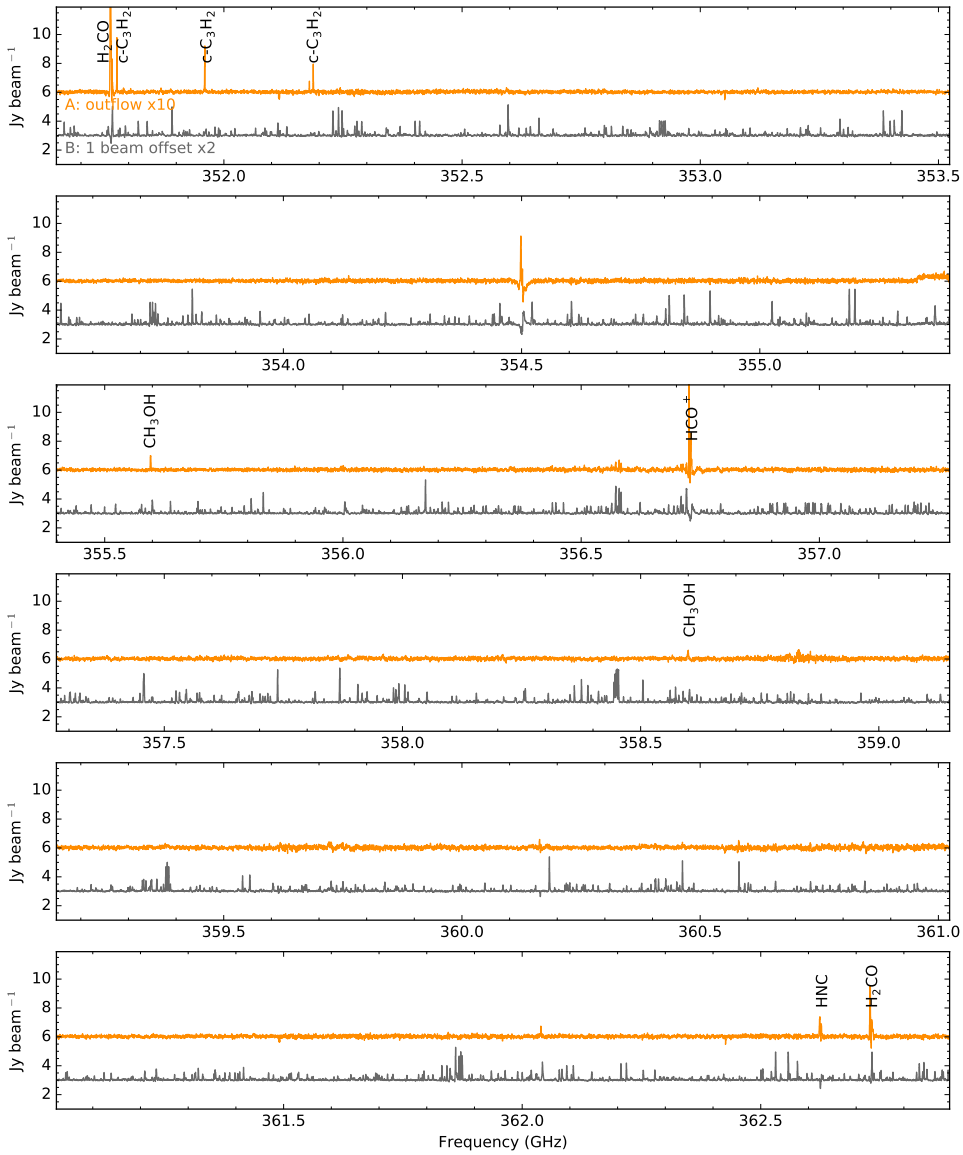

Figure 15: Same as in Fig. 13 but for the frequency range 351.65 to 362.9 GHz.

Chapter 5

Do siblings always form and evolve simultaneously?

Testing the coevality of multiple protostellar systems through SEDs

Murillo, N. M., van Dishoeck, E. F., Tobin, J. J. and Fedele, D.
2016, A&A, 592, 56

Abstract

Context Multiplicity is common in field stars and among protostellar systems. Models suggest two paths of formation: turbulent fragmentation and protostellar disk fragmentation.

Aims We attempt to find whether or not the coevality frequency of multiple protostellar systems can help to better understand their formation mechanism. The coevality frequency is determined by constraining the relative evolutionary stages of the components in a multiple system.

Methods Spectral energy distributions (SEDs) for known multiple protostars in Perseus were constructed from literature data. *Herschel* PACS photometric maps were used to sample the peak of the SED for systems with separations $\geq 7''$, a crucial aspect in determining the evolutionary stage of a protostellar system. Inclination effects and the surrounding envelope and outflows were considered to decouple source geometry from evolution. This together with the shape and derived properties from the SED was used to determine each system's coevality as accurately as possible. SED models were used to examine the frequency of non-coevality that is due to geometry.

Results We find a non-coevality frequency of $33 \pm 10\%$ from the comparison of SED shapes of resolved multiple systems. Other source parameters suggest a somewhat lower frequency of non-coevality. The frequency of apparent non-coevality that is due to random inclination angle pairings of model SEDs is $17 \pm 0.5\%$. Observations of the outflow of resolved multiple systems do not suggest significant

misalignments within multiple systems. Effects of unresolved multiples on the SED shape are also investigated.

Conclusions We find that one-third of the multiple protostellar systems sampled here are non-coeval, which is more than expected from random geometric orientations. The other two-thirds are found to be coeval. Higher order multiples show a tendency to be non-coeval. The frequency of non-coevality found here is most likely due to formation and enhanced by dynamical evolution.

5.1 Introduction

Multiplicity is common in stars: 46% of the solar-type field stars (Raghavan et al. 2010) and more than 82% of the O- and B-type stars (Chini et al. 2012) are multiple stars. Multiple stars are responsible for some of the more interesting phenomena in evolved stars, for example in the dust and gas shells of evolved stars (Maercker et al. 2012; Decin et al. 2015), phenomena such as type Ia supernovae (SNe), blue stragglers and cataclysmic variables that are generated through mass transfer in close binaries. Multiples are also laboratories in which to test models of stellar physics and the products of star formation (Duchêne & Kraus 2013).

Chen et al. (2013) and Tobin et al. (2016b) found that the frequency of multiplicity is highest for deeply embedded protostars and decreases to pre-main sequence and field stars in the separation range of 15 to 10000 AU. These authors used Submillimeter array (SMA) 1.3 mm and 850 μm archival data and Very Large Array (VLA) 8 mm and 1 cm observations, respectively. However, these surveys are incomplete toward small separations ($<$15 AU for the VLA and $<$600 AU for the SMA), and the derived frequency should be considered a lower limit. This clearly shows that stars are frequently born as multiple stellar systems.

While it is considered that fragmentation within the parent cloud is the mechanism through which multiples form, it is uncertain at which point in time and on what scale the fragmentation occurs. Models suggest one of two paths: turbulent fragmentation of the core ($\geq$1600 AU scales, e.g., Offner et al. 2010), or gravitational instability of the protostellar disk ($<$500 AU scales, e.g., Stamatellos & Whitworth 2009a; Kratter et al. 2010). While some mechanisms are thought to produce coeval systems, turbulence can cause density enhancements that can lead to non-coevality in multiple protostellar systems. Dynamical ejections of close binaires can, on the other hand, yield apparently non-coeval systems.

Early studies at disk scale ($\sim$100 AU) separations found that 15% out of 10 to 20 T Tauri and pre-main sequence binaries are formed of classical and weak-lined T Tauri stars, similar to mixed pairs in young binaries (Duchêne et al. 1999; Hartigan & Kenyon 2003). Classical T Tauri stars are generally considered to be younger and more actively accreting than weak-lined T Tauri stars (Duchêne et al. 1999; Kenyon & Hartmann 1995). Comparison of these binaries with isochrones showed that secondaries tend to be younger than primaries (Hartigan & Kenyon 2003), but it was suggested that this age difference would disappear with flatter isochrones. A larger study of 65 T Tauri stars in Ophiuchus, Taurus and Corona Australis also found classical and weak-lined T Tauri binaries, in agreement with earlier studies, as well as Class I and II binaries (McCabe et al. 2006) through comparison of color in K, L, [N] and 18 μm observations. This study noted that mixed pairs had a tendency of showing disks with low to no accretion, indicating different ages among the components, and supporting inside-out

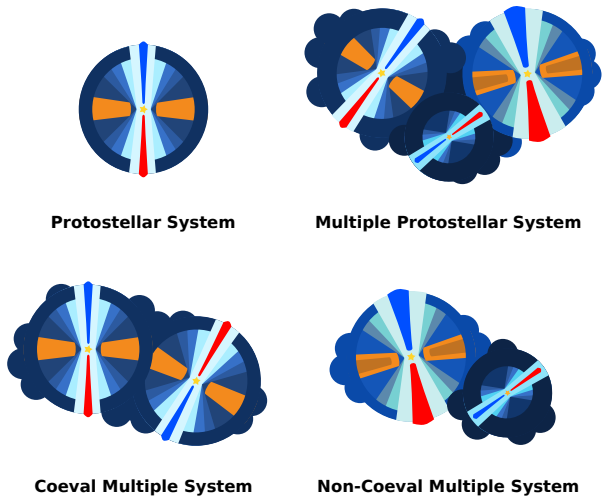

Figure 1: Cartoon of the definitions used in this work. More evolved sources are represented by larger disks, wider outflow cavities and less envelope material

disk evolution.

Kraus & Hillenbrand (2009) studied the 36 known binaries in the Taurus-Auriga region (d ∼145 pc) with separations >200 AU, known spectral types and flux ratios with the aim to probe the coevality of pre-main sequence binaries. Coevality of the sample of binaries was determined through comparison with a hybrid of two theoretical isochrones to estimate the ages of each component. Kraus & Hillenbrand (2009) found that two-thirds of the pre-main sequence binaries are coeval with a dispersion lower than 1.4 Myr (0.16 dex), with no trend between age and mass or separation, suggesting that coevality is a product of formation. It should be highlighted that only binaries were probed in Kraus & Hillenbrand (2009), which raises the question of whether the coevality frequency is different when higher order multiples are considered. This is related to the dynamic evolution of multiple systems, since higher order multiples tend to disintegrate more readily (Reipurth 2000), and fewer of them survive to main sequence stages (11% higher order multiples in solar-type stars, Raghavan et al. 2010).

While isochrones are considered the best technique to determine ages, age determination is plagued by large uncertainties, bias and the assumptions made to estimate the age, namely the definition of $\tau = 0$ (Soderblom et al. 2014). For embedded systems, determining the age is even more difficult due to the lack of information on the spectral type and stellar luminosity. Using color, mass accretion rates and inner disk holes to determine evolutionary classfication and ages, while useful for T Tauri stars and even for a few Class I protostars (Duchêne et al. 1999; Hartigan & Kenyon 2003; McCabe et al. 2006), becomes difficult for deeply embedded sources, where near- infrared detections are often lacking and accretion can be more variable (Audard et al. 2014). A more viable focus therefore is to probe the relative evolutionary stages of the components of multiple systems. While the age coevality will not be probed, the evolutionary coevality, which sets the conditions for the system's life, will be probed and can provide insight into the question.

The evolutionary stage of protostars is usually defined by the spectral energy distribution (SED) shape, infrared spectral index $\alpha_{\rm IR}$, bolometric temperature $T_{\rm bol}$ and

the ratio of submillimeter luminosity $L_{\rm submm}$ to bolometric luminosity $L_{\rm bol}$, which reflects the ratio of stellar mass M_* to envelope mass $M_{\rm env}$ (Froebrich 2005). The SED peak will tend to move toward the shorter wavelengths as the protostar evolves and disperses its envelope, changing the shape of the SED. It is expected that the parameters derived from the SED also reflect this, for example, $T_{\rm bol}$ will increase as the protostar sheds its natal cocoon and $\alpha_{\rm IR}$ will decrease as the protostar moves from the embedded phases to Class II. As the envelope is dispersed, the submillimeter luminosity will decrease and therefore $L_{\rm submm}$ / $L_{\rm bol}$ will also decrease. In-depth studies of some individual embedded multiple protostellar systems suggest non-coevality in embedded systems (such as L1448N A & B: Ciardi et al. 2003; NGC1333 SVS13: Chen et al. 2009; L1448C: Hirano et al. 2010; VLA1623: Murillo & Lai 2013) based on these criteria. However, the geometry, or in other words, the inclination and outflow cavity of the observed protostellar system, affects the shorter wavelength (≤ 70 μm) part of the SED. This in turn affects the derivation of parameters from the SED, some more strongly than others (Whitney et al. 2003; Robitaille et al. 2006; Crapsi et al. 2008), and the evolutionary stage classification (Enoch et al. 2009b; Dunham et al. 2014). Studies of modeled protostellar SEDs demonstrate that accurately constraining the inclination of the source provides more accurate estimates of the derived parameters and thus of the evolutionary stage classification (Offner et al. 2012b).

The inclination of the protostellar system with respect to our line of sight can be estimated from outflow observations and is derived with more precision from rotationally supported disk structures, if present. Protostellar systems alter their environment as they evolve, clearing out envelope material through widening of the outflow cavity (Arce & Sargent 2006), accretion and concentration of material onto the protoplanetary disk. Hence, the envelope and outflow can further constrain the evolutionary stage of the source through the chemical and physical structure of the envelope and core. As a consequence, to establish the evolutionary stage of a source and eventually the coevality of a multiple protostellar system, the SED, derived properties, inclination and environment must be accounted for.

In this work we present the construction and analysis of the SEDs of all identified protostellar systems in the Perseus molecular cloud, the largest sample of Class 0, I and II. Perseus is the main target of this work because it is a well-studied region whose multiplicity and environment are relatively well known. This provides data over a wide range of wavelengths and resolutions and both continuum and line emission towards most, if not all, of the region.

For this purpose, literature and archival data were used to construct the short ($<$70 μm) and long ($>$160 μm) wavelength regimes of the SEDs. *Herschel Space Observatory* Photodetector Array Camera and Spectrometer (PACS, Poglitsch et al. 2010) photometric maps were used to cover the peak of the SEDs (70, 100 and 160 μm), without which large uncertainties arise in the parameters derived from the SED. The *Herschel* PACS beamsize limits the range of component separations that can be probed to $\gtrsim 7''$, which at the distance of Perseus ($d \sim 235 \pm 18$ pc, Hirota et al. 2008, 2011) becomes $\sim$1600 AU. Below this angular resolution, the fluxes of multiple systems are difficult to disentangle. Therefore the coevality frequency, system alignment and properties derived in this work, as well as the environment, will provide constraints for fragmentation models only at core scales ($\geq$1600 AU).

In this paper we present the constructed SEDs of all identified and known systems in Perseus, with special focus on multiple protostellar systems. The SEDs are

constructed from literature and *Herschel* PACS data, compared with canonical SEDs for different stages from Enoch et al. (2009b). With this work, we aim to determine the frequency of coevality in multiple protostellar systems to provide constraints for multiple protostar formation scenarios. Section 5.2 defines the concepts used in this work. The data and sample studied in this paper, as well as the construction of SEDs and derivation of derived properties, are described in Sect. 5.3. The results, including an analysis of unresolved SEDs, are given in Sect. 5.4. Finally, the discussion and conclusions are given in Sects. 5.5 and 5.6, respectively.

5.2 Definitions

For consistency and clarity of the terms used throughout this work, definitions of certain terms are provided in this subsection. An illustration of these definitions is shown in Fig. 1.

Protostellar system is defined as a source and its surrounding environment composed of a disk, an envelope and a bipolar outflow.

Multiplicity or *multiple* is used to refer to a system consisting of two or more components or sources, regardless of whether they are stars or protostars. The terms binary, triples and higher order multiples are thus implicitly merged into this term.

Multiple protostellar system or simply *multiple system* here refers to two or more protostellar sources composing one system. Multiple systems are generally observed to share a common envelope and, in some cases, a common disk. We assume that a group of protostars is gravitationally bound unless there evidence to the contrary, if they were observed to have a common envelope in single-dish observations. An observed group of protostellar systems is considered a multiple when several observations and studies confirm its multiplicity through both continuum and molecular line emission.

Coevality is taken to mean the relative evolutionary stages of the components that make up a multiple protostellar system, accounting for the SED, derived properties, inclination and environment. Environment is taken here to mean the outflows, surrounding envelope,and disk(s), if any. A multiple system whose components show similar evolutionary stages is considered coeval, while a multiple system with different evolutionary stages is referred to as non-coeval.

Resolved multiple system is a system with confirmed multiplicity with separations $\geq 7''$ that can be resolved in the *Herschel* PACS maps.

Unresolved multiple system is a system with confirmed multiplicity down to $0.08''$ and separations $< 7''$ that cannot be resolved in the *Herschel* PACS maps.

5.3 Sample and data

5.3.1 Source sample

To study the coevality of multiple systems, the component protostellar systems must be identified. Perseus was chosen because of the large number of embedded young stellar objects in a single cloud at d<300 pc. Our source sample list and coordinates are obtained from Tobin et al. (2016b), who identified multiple systems in Perseus down to 15 AU separations in the VLA Disk and Multiplicity survey of Perseus protostars (VANDAM) survey. At the same time, the source sample was divided, based on

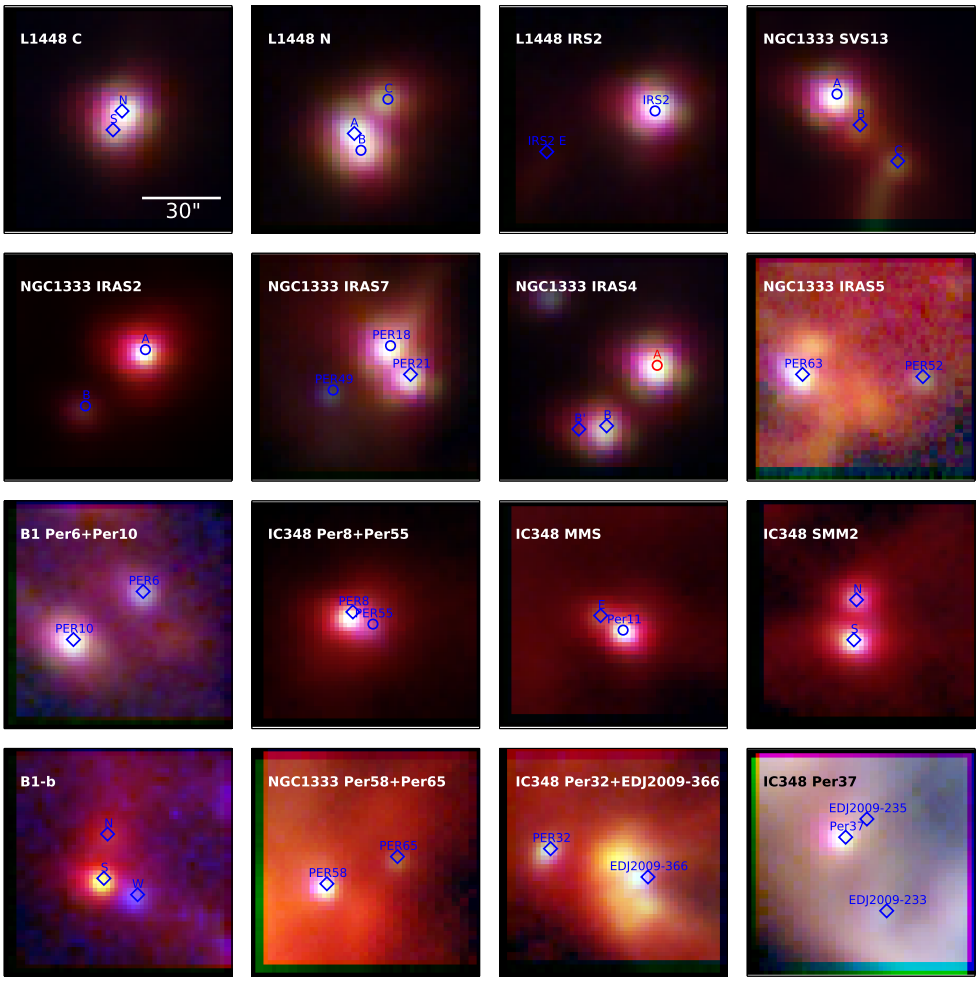

Figure 2: *Herschel* PACS stamps of resolved multiple protostellar systems in Perseus, except for NGC1333 IRAS4 which also shows IRAS4A, an unresolved protobinary. Each stamp is $80'' \times 80''$. 70, 100 and 160 μm are shown in blue, green and red, respectively. Blue symbols represent the components of a system, with circles denoting those with additional unresolved multiplicity and diamonds indicating those without (known) additional multiplicity. NGC1333 IRAS4A is marked in red.

the findings of Tobin et al. (2016b), into three categories: resolved multiple systems and unresolved multiple systems with our 7″ separation, and single protostars. The source sample is listed in Tables 1 and 2. Multiple systems and their components are referred to by their most common name. Components with designations PerXX up to 66 are shorthand for Per-emb XX from Enoch et al. (2009b). Sources with designations EDJ2009-XXX refer to sources from Evans et al. (2009). Duplicated systems in Tables 1 and 2 arise because some multiple systems have components that have been observed to be close binaries with separations <7″ (e.g., NGC1333 IRAS7 Per18, Tobin et al. 2016b). Half of the wide resolved multiple systems in our sample have a close unresolved companion, that is, 8 out of 16 systems. Of these 8 systems, 3 (L1448N, NGC1333 IRAS2 and NGC1333 IRAS7) have two resolved components with an unresolved companion each. Confirmed single protostellar systems are listed and discussed in Appendix 5.D.

The sources in our sample have all been confirmed to be protostars through studies at multiple wavelengths, ruling out background sources, AGB stars, or galaxies.

5.3.2 Literature data

Most star forming regions have been observed at infrared and (sub)millimeter wavelengths at different epochs and with varying resolutions. The first step to constructing SEDs is therefore a search of the available data in the literature. It needs to be noted, however, that even though there is much information in the literature, not all protostellar systems have been homogeneously observed or photometry reported, making it impossible to have all SEDs sampled at the same wavelengths.

The near- to mid-infrared regime of protostellar SEDs is well characterized from 2MASS and *Spitzer Space Telescope* observations with fluxes shortwards of 70 μm. The c2d catalog (Dunham et al. 2015) provides fluxes from 1.25 μm to 24 μm. The *Spitzer* 70 μm fluxes are not considered here given the large beam and saturation of the MIPS instrument for the 70 μm detector and the superior quality of the *Herschel* data. Sensitivity limits at each wavelength from the respective instruments are taken as upper limits for sources that lacked an entry in the c2d catalog. For NGC1333, integrated fluxes at wavelengths <70 μm were obtained from the compiled catalog of Rebull (2015) after conversion from magnitude to mJy units.

Submillimeter and millimeter integrated fluxes were collected from diverse interferometric continuum surveys (e.g., Looney et al. 2000; Jørgensen et al. 2007; Chen et al. 2013; Yen et al. 2015) as well as works reporting fluxes for individual protostellar systems (e.g., Chen et al. 2009; Hirano et al. 2010; Palau et al. 2014). Careful selection of the fluxes from literature was made to ensure that as much emission could be recovered from the observations as possible, while at the same time the individual sources could be clearly and easily separated. The VANDAM survey (Tobin et al. 2016b) provides fluxes from 8 mm to 1 cm for all sources in the Perseus star forming region. Interferometric observations are preferred over single-dish observations because of the resolution needed to separate the flux contribution from each component in a multiple system. The typical fraction of recovered flux varies by telescope configuration, sensitivity and structure being probed. Tobin et al. (2015) provided a comparison that gives an idea of the recovered flux in interferometric observations.

Although data from the literature can cover the near- to mid-infrared and (sub)millimeter regimes of the SED, the peak of the SED is not well sampled typically at 70 to 160

Table 1: Sample of resolved multiple protostellar systems (separation $\geq 7''$)

System	Component	RA[a] (J2000)	Dec.[a] (J2000)	Sep.[b] ($''$)
L1448 C	N	03:25:38.87	+30:44:05.40	...
...	S	03:25:39.14	+30:43:58.30	8.1
L1448 N	A	03:25:36.53	+30:45:21.35	...
...	B	03:25:36.34	+30:45:14.94	7.3
...	C	03:25:35.53	+30:45:34.20	16.3
L1448 IRS2	IRS2	03:25:22.40	+30:45:12.00	...
...	IRS2E	03:25:25.66	+30:44:56.70	46.9
NGC1333 SVS13	A	03:29:03.75	+31:16:03.76	...
...	B	03:29:03.07	+31:15:52.02	14.9
...	C	03:29:01.96	+31:15:38.26	34.7
NGC1333 IRAS2	A	03:28:55.57	+31:14:37.22	...
...	B	03:28:57.35	+31:14:15.93	31.4
NGC1333 IRAS7	Per18	03:29:11.26	+31:18:31.08	...
...	Per21	03:29:10.67	+31:18:20.18	13.3
...	Per49	03:29:12.96	+31:18:14.31	27.5
NGC1333 IRAS4	B	03:29:12.01	+31:13:08.10	...
...	B'	03:29:12.83	+31:13:06.90	10.6
NGC1333 IRAS5	Per52	03:28:39.72	+31:17:31.89	...
...	Per63	03:28:43.28	+31:17:32.90	45.7
B1 Per6+Per10	Per6	03:33:14.40	+31:07:10.88	...
...	Per10	03:33:16.45	+31:06:52.49	31.9
IC348 Per8+Per55	Per8	03:44:43.94	+32:01:36.09	...
...	Per55	03:44:43.33	+32:01:31.41	9.6
IC348 MMS	Per11	03:43:57.06	+32:03:04.60	...
...	E	03:43:57.73	+32:03:10.10	10.2
IC348 SMM2	S	03:43:51.08	+32:03:08.32	...
...	N	03:43:51.00	+32:03:23.76	16.1
B1-b	S	03:33:21.30	+31:07:27.40	...
...	N	03:33:21.20	+31:07:44.20	17.4
...	W	03:33:20.30	+31:07:21.29	13.9
NGC1333 Per58+Per65	Per58	03:28:58.44	+31:22:17.40	...
...	Per65	03:28:56.31	+31:22:27.80	28.9
IC348 Per32+EDJ2009-366	Per32	03:44:02.40	+32:02:04.89	...
...	EDJ2009-366	03:43:59.44	+32:01:53.99	36.6
NGC1333 PER37	Per37	03:29:18.89	+31:23:12.89	...
...	EDJ2009-235	03:29:18.259	+31:23:19.758	10.6
...	EDJ2009-233	03:29:17.675	+31:22:44.922	33.7

Notes. [(a)] Coordinates from Tobin et al. (2016b). [(b)] Separations are obtained from Tobin et al. (2016b) and are listed relative to the first component tabulated. Typical uncertainties in position are $<0.1''$.

Table 2: Sample of unresolved multiple protostellar systems (separation $< 7''$)

System	RA (J2000)	Dec. (J2000)	Sepearation[a] ($''$)
NGC1333 IRAS4A	03:29:10.51	+31:13:31.01	1.828
IRAS 03292+3039	03:32:17.95	+30:49:47.60	0.085
IRAS 03282+3035	03:31:21.00	+30:45:30.00	0.098
NGC1333 IRAS2A	03:28:55.57	+31:14:37.22	0.619
NGC1333 IRAS2B	03:28:57.35	+31:14:15.93	0.311
NGC133 IRAS7 Per18	03:29:11.26	+31:18:31.08	0.081
NGC1333 IRAS7 Per49	03:29:12.96	+31:18:14.31	0.313
L1448N C	03:25:35.53	+30:45:34.20	0.251
L1448N B	03:25:36.34	+30:45:14.94	0.226
Per17	03:27:39.09	+30:13:03.00	0.273
IC348 MMS Per11	03:43:57.06	+32:03:04.60	2.950
NGC1333 SVS13A	03:29:03.75	+31:16:03.76	0.3
L1448 IRS2	03:25:22.40	+30:45:12.00	0.751
L1455 FIR2	03:27:38.23	+30:13:58.80	0.346
B1-a	03:33:16.66	+31:07:55.20	0.391
EDJ2009-269	03:30:43.91	+30:32:46.28	0.539
IC348 Per55	03:44:43.33	+32:01:31.41	0.613
EDJ2009-183	03:28:59.32	+31:15:48.14	1.022
L1448 IRS1	03:25:09.54	+30:46:21.96	1.424
NGC1333 IRAS1	03:28:37.00	+31:13:27.00	1.908
EDJ2009-156	03:28:51.11	+31:18:15.41	3.192
Per32	03:44:02.40	+32:02:04.89	5.910
HH211	03:43:56.80	+32:00:50.21	0.3[b]
Per62	03:44:12.98	+32:01:35.40	0.121[c]

Notes. [(a)] Separations obtained from Tobin et al. (2016b). Typical uncertainties in position are $<0.1''$. [(b)] The companion reported in Lee et al. (2009) appears to be substellar with an orbital period of 3000 yr, which could explain the jet precession. Lee et al. (2010) also argued for a third component at <30 AU, proposing that it is a very low-mass system. [(c)] Possibly unresolved binary.

Table 3: *StarFinder* photometry parameters

Regions	λ μm	Beam[a] $''$	PSF[b] $''$	FWHM[c]	Deblend[d]	Flux error mJy
NGC1333, B1, IC348	70	9.6	13.0	1.0	N	20 - 30
...	100	7.2	8.0	1.0	N	7 - 10
...	160	12.8	13.0	1.0	N	10 - 15
L1448, L1455	70	9.6	13.0	0.7	Y	24 - 34
...	100	7.2	8.0	0.7	Y	8 - 16
...	160	12.8	13.0	0.7	Y	11 - 20

Notes. [(a)] Measured from the FWHM of the extracted PSF. [(b)] This refers to the mask applied to the PSF to include the PSF sidelobes. [(c)] Parameter to determine the smallest separation between close sources in terms of the FWHM. [(d)] Switch parameter to set whether detected sources are deblended.

μm. The lack of a well sampled SED peak can seriously underestimate the derived parameters and evolutionary classification of a protostar, and in turn the coevality determination of a system. *Herschel* PACS data are therefore crucial to this work.

5.3.3 *Herschel* PACS photometric maps

Archival photometric maps from *Herschel* PACS from the Gould Belt Survey (André et al. 2010; Pezzuto et al. 2012) were obtained from the Herschel Science Archive for the entire Perseus region. The maps made with JScanmap were selected for performing the photometry (see Appendix 5.A). From these data we can extract 70 μm $\leq S_\nu \leq$ 160 μm integrated fluxes. Due to the resolution of *Herschel* PACS observations, fluxes from each component in a multiple protostellar system can be extracted only for systems whose projected separations are $\geq 7''$.

Star-forming regions tend to be clustered, hence, crowded-field photometry techniques are employed to best exploit the *Herschel* PACS maps. While aperture photometry is a simple and straightforward method, it is not a viable solution for crowded protostellar fields. Point spread function (PSF) photometry presents a better solution to the problem at hand. The IDL-based program *StarFinder* (Diolaiti et al. 2000) was employed to perform photometry on the *Herschel* maps. The PSF was extracted from the maps themselves to account for the specific observation mode, which cannot be achieved as easily with modeled ideal PSFs. Single isolated sources were used to extract the PSF, with moderate brightness, thus avoiding spikes and negative spots, and little to no surrounding nebulosity. The extracted PSFs provide beam sizes of $9.6''$, $7.2''$ and $12.8''$ for 70, 100 and 160 μm, respectively. *StarFinder* allows deblending of sources and setting a lower limit for the FWHM for source separation, which proves to be very useful in separating multiple systems from PACS maps.

Postcard maps of each sub-region of Perseus, measuring 44' $\times$ 44', were extracted for ease of photometry. For postcard maps from the same larger map, the same PSF was used, which means that we required the PSF to be extracted only once per map using the best single-source targets. To avoid an overestimation of the measured fluxes and facilitate source deblending, the extracted PSF was then masked by introducing an aperture factor. The *StarFinder* parameters for the photometry used in this work for each subregion and the typical flux uncertainty per wavelength are listed in Table 3.

Table 4: Statistics from the constructed SEDs.

	L1448 & L1455	NGC1333	IC348	B1	Total
Multiple total	9	17	9	5	40
Resolved system	3	8	4	1	16
Unresolved system	6	9	5	4	24
Single	7	20	9	12	48
Total systems	16	36	18	17	88
Multiplicity frequency[a]	56.3%	47.2%	50.0%	29.4%	45.5%
Resolved: Coeval	3	6	2	2	14
Resolved: Non-coeval	1	3	2	1	7
Total determined systems	4	7	4	3	21
Non-coevality frequency[a]	25%	29%	50%	66%	33 ± 10%

Notes. [(a)] Calculated as the ratio of multiples or non-coeval systems over the total number of systems.

After PSF photometry was performed, PSF aperture and background corrections were applied to the raw fluxes. The values used for aperture correction are tabulated in Balog et al. (2014). A detailed explanation of the photometry with *StarFinder* is given in Appendix 5.A.

5.3.4 SED construction

Given the multiple names and identifiers each source has accumulated through surveys and literature, fluxes at different wavelengths were matched by means of the coordinates with a search radius of $\lesssim 4.5''$. The search radius was selected to be below the resolution limit of *Herschel* and similar to the FWHM lower limit for *StarFinder*, avoiding any confusion in source identification. Coordinates were obtained from (sub)millimeter interferometric observations given the higher angular resolution and because the source positions at these wavelengths are less likely to be contaminated by foreground stars (e.g., NGC1333 IRAS2B at $\lambda \lesssim 8$ μm, Rodríguez et al. 1999) or scattered light.

Care was taken that fluxes at all available wavelengths for each SED were separated from the other protostars in their system. At 160 μm this criteria breaks down for systems with separations smaller than 9 to $10''$. In these cases, the flux is flagged as combined and is noted in the plotted SEDs. Upper limits are also flagged and noted with a different symbol in the plots.

L1448 IRS1, an unresolved multiple systems, has fewer than three points in the SED. The same situation occurs for 7 single protostellar sources, listed in Table 9. Hence, these systems are not shown in Figs. 4 and 9.

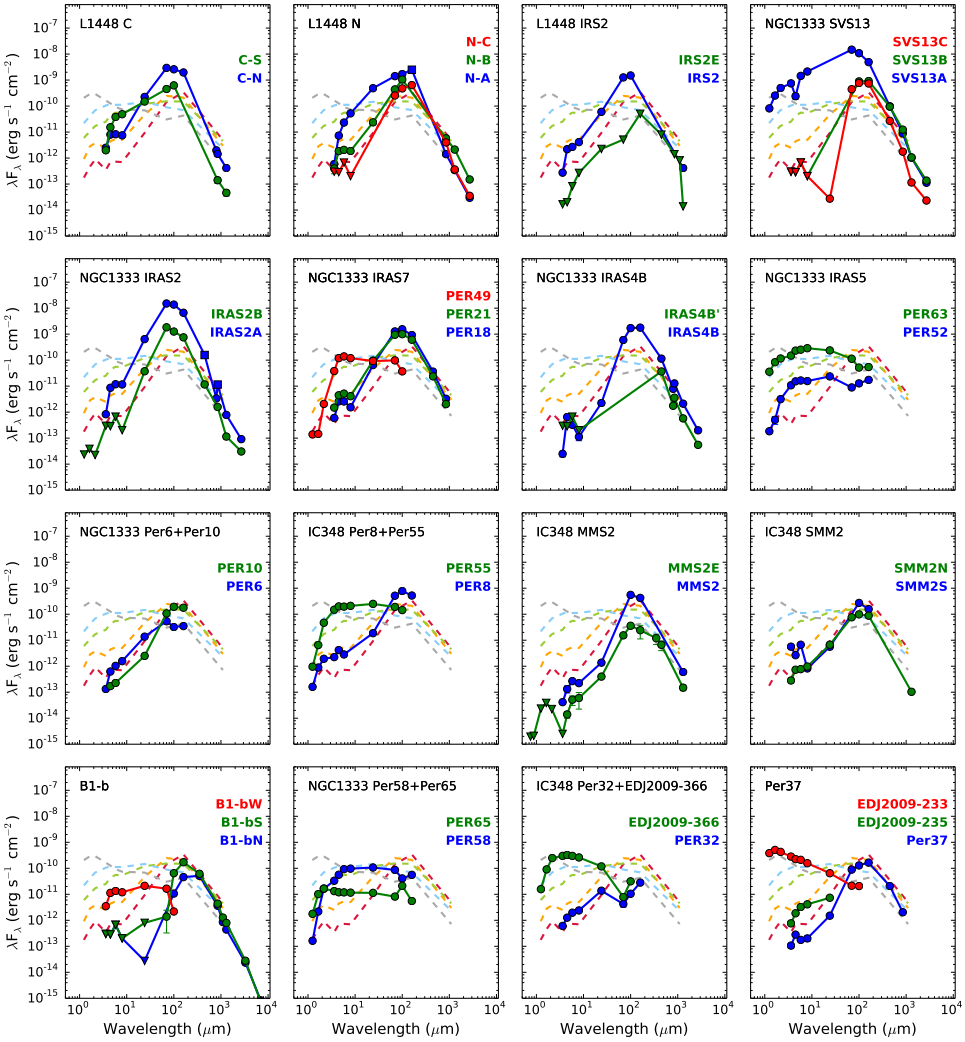

Figure 3: Constructed SEDs for resolved multiple protostellar systems. Filled circles denote the fluxes without contamination from nearby sources. Triangles indicate upper limits. Each SED is overlaid with the template SEDs from Enoch et al. (2009b) for comparison (dashed lines).

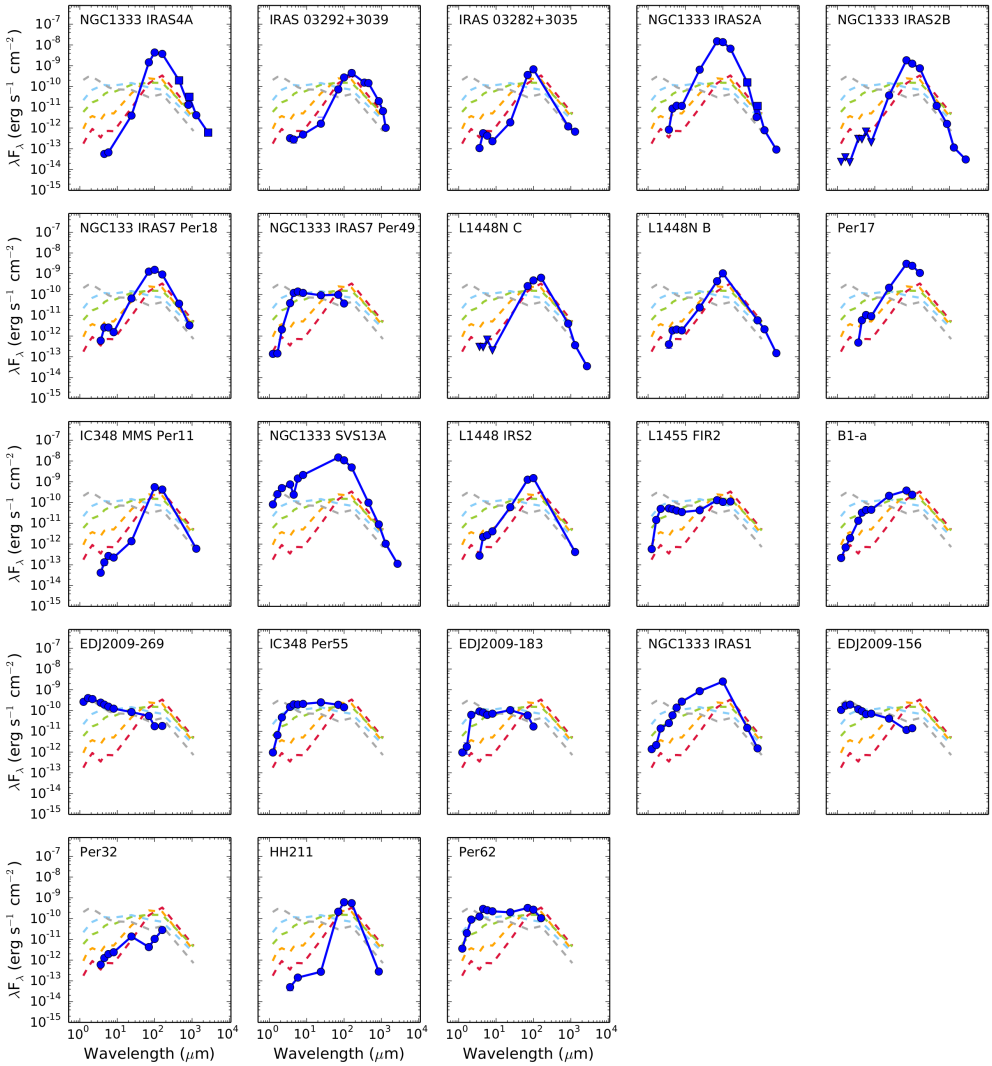

Figure 4: Constructed SEDs for unresolved multiple protostellar systems. Other details are the same as in Fig. 3.

Table 5: SED derived properties

System	Source	$T_{\rm bol}$ K	$L_{\rm bol}$ $L_\odot$	$L_{\rm fir}$ / $L_{\rm bol}$	$L_{\rm submm}$ / $L_{\rm bol}$	$\alpha_{3-24\mu m}$
L1448 C	N	49.5 ± 15.8	10.27 ± 1.59	0.479 ± 0.104	(7.7 ± 1.9)E-5	2.19 ± 0.38
...	S	82.6 ± 12.1	1.98 ± 0.31	0.416 ± 0.092	(3.2 ± 0.9)E-5	1.86 ± 0.65
L1448 N	A	57.3 ± 9.8	8.08 ± 1.27	0.566 ± 0.124	(9.4 ± 2.4)E-5	3.09 ± 0.72
...	B	47.0 ± 25.7	2.11 ± 0.33	0.632 ± 0.137	(1.8 ± 0.4)E-3	1.87 ± 0.37
...	C	43.3 ± 0.2	2.89 ± 0.44	0.412 ± 0.089	(5.3 ± 1.4)E-4	...
L1448 IRS2	IRS2	50.8 ± 11.9	4.30 ± 0.66	0.483 ± 0.105	...	2.48 ± 0.44
...	IRS2E	$<$ 30.9	$<$ 0.12	$<$ 0.882	$<$ 4.2E-2	$>$ 2.67
NGC1333 SVS13	A	74.6 ± 51.9	119.28 ± 18.31	0.140 ± 0.030	(4.2 ± 0.9)E-4	...
...	B	35.5 ± 0.1	10.26 ± 1.57	0.143 ± 0.031	(5.1 ± 1.1)E-3	...
...	C	38.0 ± 3.1	2.22 ± 0.34	0.670 ± 0.145	(5.8 ± 1.3)E-3	$>$ -1.40
NGC1333 IRAS2	IRAS2A	48.8 ± 9.5	47.06 ± 7.21	0.441 ± 0.095	(1.4 ± 0.3)E-3	3.09 ± 0.54
...	IRAS2B	47.7 ± 0.5	5.27 ± 0.81	0.412 ± 0.089	(1.2 ± 0.3)E-3	$>$ 2.58
NGC1333 IRAS7	Per18	46.4 ± 12.4	4.70 ± 0.72	0.522 ± 0.114	(3.6 ± 0.8)E-3	2.20 ± 0.52
...	Per21	51.7 ± 16.5	3.42 ± 0.53	0.478 ± 0.104	(3.3 ± 0.7)E-3	2.01 ± 0.36
...	Per49	315.1 ± 36.4	0.66 ± 0.11	0.058 ± 0.013	...	0.19 ± 0.39
NGC1333 IRAS4	B	34.2 ± 18.9	4.46 ± 0.68	0.778 ± 0.169	(1.2 ± 0.3)E-2	1.65 ± 0.93
...	B'	8.6 ± 0.1	1.76 ± 0.28	0.010 ± 0.002	(9.6 ± 2.1)E-3	...
NGC1333 IRAS5	Per52	306.8 ± 88.4	0.13 ± 0.02	0.158 ± 0.036	...	0.34 ± 0.09
...	Per63	476.5 ± 60.8	1.52 ± 0.25	0.061 ± 0.014	...	0.15 ± 0.17
NGC1333 Per6+Per10	Per6	72.7 ± 12.6	0.18 ± 0.03	0.307 ± 0.068	...	2.18 ± 0.34
...	Per10	44.5 ± 10.0	0.44 ± 0.07	0.576 ± 0.125	...	1.63 ± 0.08
IC348 Per8+Per55	Per8	51.8 ± 53.7	1.86 ± 0.29	0.507 ± 0.110	...	1.07 ± 0.23
...	Per55	334.1 ± 39.6	1.49 ± 0.25	0.068 ± 0.015	...	0.22 ± 0.07
IC348 MMS	MMS2	34.2 ± 35.7	2.23 ± 0.34	0.323 ± 0.070	...	1.61 ± 0.33
...	E	35.8 ± 64.9	0.10 ± 0.03	0.734 ± 0.306	(8.1 ± 3.8)E-2	$>$ 2.34
IC348 SMM2	S	42.3 ± 18.8	0.93 ± 0.14	0.182 ± 0.039	...	0.03 ± 0.68
...	N	47.4 ± 16.7	0.34 ± 0.05	0.584 ± 0.127	...	1.53 ± 0.19

Table 5: continued.

System	Source	$T_{\rm bol}$ K	$L_{\rm bol}$ $L_\odot$	$L_{\rm fir}$ / $L_{\rm bol}$	$L_{\rm submm}$ / $L_{\rm bol}$	$\alpha_{3-24\mu{\rm m}}$
B1-b	N	22.0 ± 0.1	0.16 ± 0.02	0.817 ± 0.177	(2.0 ± 0.4)E-1	> -1.40
...	S	23.5 ± 11.0	0.32 ± 0.05	0.985 ± 0.216	(1.2 ± 0.3)E-1	> 0.46
...	W	222.3 ± 16.7	0.10 ± 0.02	0.049 ± 0.012	...	0.70 ± 0.33
NGC1333 Per58+Per65	Per58	278.2 ± 43.0	0.66 ± 0.11	0.121 ± 0.027	...	0.50 ± 0.25
...	Per65	550.6 ± 58.6	0.11 ± 0.02	0.186 ± 0.042	...	-0.06 ± 0.03
IC348Per32+EDJ2009-366	Per32	124.4 ± 22.4	0.06 ± 0.01	0.352 ± 0.083	...	1.54 ± 0.14
...	EDJ2009-366	777.8 ± 52.8	1.23 ± 0.20	0.011 ± 0.002	...	-0.54 ± 0.09
NGC1333 Per37	Per37	36.6 ± 28.9	0.48 ± 0.07	0.687 ± 0.150	(2.1 ± 0.5)E-2	1.25 ± 0.31
...	EDJ2009-235	291.3 ± 14.4	0.02 ± 0.00	...	...	1.02 ± 0.31
...	EDJ2009-233	1276.3 ± 67.3	1.33 ± 0.21	0.010 ± 0.002	...	-0.77 ± 0.04

5.3.5 Source properties

Source properties derived from the constructed SED are expected to aid in the evolutionary stage classification. Constraining the peak of an SED improves the calculation of the protostellar system's derived properties, which makes the *Herschel* PACS observations crucial for this task. Five parameters were derived for each constructed SED: infrared spectral index, bolometric temperature and luminosity and two luminosity ratios.

For the infrared spectral index $\alpha_{\rm IR}$, the slope between 3 μm and 24 μm is given by

$$\alpha_{\rm IR} = \frac{d\,\log(\lambda\ {\rm F}_\lambda)}{d\,\log\,\lambda}$$

where F_λ is the flux at a given wavelength λ. If the flux at 24 μm is absent, $\alpha_{\rm IR}$ is not reported. When one or more of the fluxes in this range is an upper limit, $\alpha_{\rm IR}$ is a lower limit.

The bolometric temperature $T_{\rm bol}$ is expressed as

$$T_{\rm bol} = 1.25\ \times\ 10^{-11}\ \frac{\int_0^\nu\ \nu\ S_\nu\ d\nu}{\int_0^\nu\ S_\nu\ d\nu}$$

where S_ν is the flux at a given frequency ν.

The bolometric luminosity $L_{\rm bol}$ is derived using

$$L_{\rm bol} = 4\ \pi\ D^2\ \int_0^\nu\ S_\nu\ d\nu$$

where D is the distance. Submillimeter luminosity ($\lambda \geq 350$ μm) $L_{\rm submm}$ and far-infrared luminosity ($\lambda \leq 70$ μm) $L_{\rm fir}$ were derived from the same equation using the corresponding wavelength ranges. Both $T_{\rm bol}$ and $L_{\rm bol}$ were derived from the SEDs using trapezoidal integration.

In addition, two luminosity ratios were taken: submillimeter to bolometric $L_{\rm submm}/L_{\rm bol}$ and far-infrared to bolometric $L_{\rm fir}/L_{\rm bol}$. Both ratios were used since interferometric continuum observations resolve out much of the extended flux pertaining to the envelope, while the far-infrared fluxes from *Herschel* are expected to capture most of the envelope emission. These ratios are meant to reflect the envelope to central star mass ratio (André et al. 1993; Froebrich 2005), which is used to define the separate physical stages of protostars (Robitaille et al. 2006; Enoch et al. 2009b). Deeply embedded sources are expected to have luminosity ratios higher than 0.005, while less embedded protostars tend to show ratios lower than 0.005.

5.3.6 Caveats

The results in this work are limited by the resolution of the *Herschel* PACS maps. Multiple systems with separations $<7''$ cannot be resolved, making the frequency of non-coevality found in this work applicable to wider systems. Furthermore, the results obtained here can provide constraints for multiple protostellar system formation scenarios at the core scale ($\geq$1600 AU).

Some multiple systems lack reported resolved submillimeter fluxes, which means that the derived properties are under- or overestimated. This affects the evolutionary classification derived from these parameters. Care must then be taken to consider this aspect when classifying the systems, and the relations between components of a system are more relevant than the actual quantities themselves.

5.4 Results and analysis

The constructed SEDs are presented in Fig. 3 for resolved systems and in Fig. 4 for unresolved systems. Flux uncertainties are in general comparatively small, hence when plotted, the errors are not much larger than the symbols used for plotting.

The constructed SEDs are analyzed with the aim to study the coevality of multiple systems. All the parameters typically used to identify a protostellar system's evolutionary stage together with additional diagnostics are used in the classification. This is to ensure that there is as little bias as possible due to inclination, which tends to affect the derived SED parameters. In this section each method and the corresponding results are presented.

5.4.1 SED shapes

As the protostellar system evolves and clears out the envelope, the peak of the energy distribution shifts to shorter wavelengths. The wavelength at which the SED peaks can therefore be used as an indicator of the evolutionary stage. Average SEDs for the progressive evolutionary stages are shown in Figure 7. These SEDs were derived from the *Spitzer* c2d observations of a large sample of protostars in Perseus and Serpens by Enoch et al. (2009b) and divided into classes based on $T_{\rm bol}$. Figures 3 and 4 show the constructed SEDs for multiples compared with these average SEDs.

A quick look at the constructed SEDs makes it clear that several multiple systems have components with different SED shapes (e.g., IC348 Per8+Per55, IC348 Per32+EDJ2009-366), while others have components with similar SED shapes (e.g., NGC1333 IRAS 5, IC348 MMS2) or a combination (e.g., NGC1333 IRAS 7, L1448 N, NGC1333 SVS13, B1-b). The similar SEDs hint at coeval components, whereas non-coevality is suggested by the differing SEDs.

To obtain some simple statistics, we counted the systems and identified stages by eye in comparison to each other and to Fig. 7. The frequency of non-coevality found in this way is listed in Table 4. Higher order multiples were counted twice, once for the first pair and then a second time for the pair compared to the third component. For example, NGC1333 IRAS7 was counted once as coeval and once as non-coeval, since Per18 and Per21 appear to have the same evolutionary stage, but are non-coeval relative to Per49. This generates a total of 21 systems where coevality is probed, in contrast to the 16 systems in our sample. We found that 7 of 21 systems ($33 \pm 10\%$) show non-ceovality: L1448 N, NGC1333 SVS13, NGC1333 IRAS7, IC348 Per8+Per55, B1-b, IC348 Per32+EDJ2009-366 and NGC1333 Per37. We did not set a maximum separation limit for a multiple system, but it is interesting to see the change in non-coevality frequency in our sample as a limit is set. Assuming the characteristic size of protostellar cores ($30''$), we found that 6 of 15 systems ($40 \pm 13\%$) with separations $\leq 30''$ are non-coeval. An arbitrary separation limit of $\leq 20''$ shows 4 out of 14 systems ($33 \pm 14\%$) to be non-coeval. This means that the rate of non-coevality does not change significantly by limiting the separation of multiple systems.

For NGC1333 Per37, the EDJ2009-235 component is not detected in the *Herschel* PACS maps, but is detected in the c2d and VANDAM surveys. Tobin et al. (2016b) classified it as a Class II source, but based on the c2d fluxes, EDJ2009-235 appears to be an embedded source, closer in agreement with the classification from Young et al. (2015). A possible explanation for the discrepancy and its lack of *Herschel* PACS detection could be a highly extincted disk that might make a Class II source

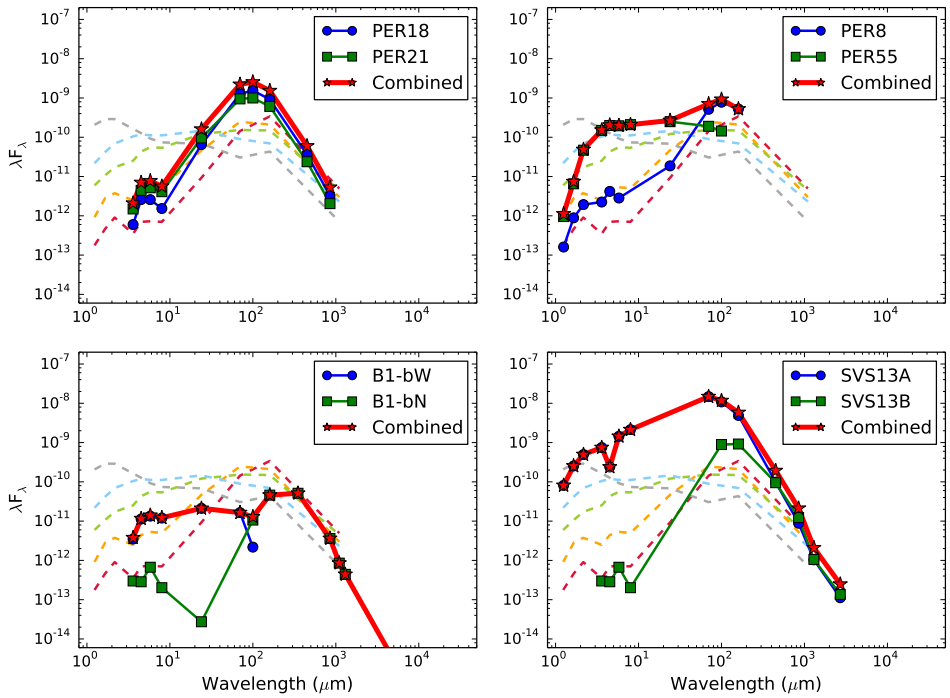

Figure 5: Summed SEDs from resolved multiple systems, showing how unresolved multiple systems might be composed. The dashed lines are the same as in Fig. 7.

look much younger. The IC348 systems Per8+Per55 and Per32+EDJ2009-366, which appear as proto-binaries at scales $\geq 7''$, have unresolved components (Table 2), which means they are higher order multiples. This would suggest that higher order multiples tend toward non-coevality.

5.4.2 Classification from derived properties

All the calculated parameters described in Sect. 5.3.5 and their errors are listed for each source in Table 5 for the resolved multiple systems. Comparing $T_{\rm bol}$ within the multiple systems indicates that the rate of non-coevality is much lower than found from the visual comparison of the SEDs. Based on $T_{\rm bol}$, 6 multiple systems are found to be non-coeval (NGC1333 IRAS7, IC348 Per8+Per55, B1-b, Per32+EDJ2009-366 and NGC1333 Per37 twice). Marginal non-coevality, that is, one source being slightly younger than the other (e.g., early Class 0 and late Class 0), can be seen toward 4 systems (L1448 C, NGC1333 SVS13, NGC1333 Per6+Per10 and NGC1333 Per58+Per65), while the remaining are quite coeval. The non-coevality frequency found based on $T_{\rm bol}$ is between 29 ± 10% and 48 ± 11%, with the latter value considering the marginally non-coeval systems in addition to the non-coeval systems.

Luminosity ratios, such as $L_{\rm fir}/L_{\rm bol}$ and $L_{\rm submm}/L_{\rm bol}$, are expected to be indicators of the evolutionary stage, with values above 0.005 indicating a Class 0 source. However, for these ratios to provide reliable information, a well-sampled SED at $\lambda \geq 70\mu$m is

Table 6: Derived parameters of combined SEDs

Source Source	$T_{\rm bol}$ K	$T_{\rm bol}$ Class	$L_{\rm bol}$ $L_\odot$	$L_{\rm fir}$ / $L_{\rm bol}$	L-ratio Class
Per18	46.4 ± 12.4	E 0	4.70 ± 0.72	0.52 ± 0.11	0
Per21	51.7 ± 16.5	L 0	3.42 ± 0.53	0.48 ± 0.10	0
Combined	**48.7 ± 11.57**	**E 0**	**8.13 ± 1.25**	**0.50 ± 0.11**	**0**
Per8	51.8 ± 53.7	L 0	1.86 ± 0.29	0.51 ± 0.11	0
Per55	334.1 ± 39.6	L I	1.49 ± 0.25	0.068 ± 0.015	0
Combined	**175.5 ± 36.8**	**E I**	**3.38 ± 0.53**	**0.32 ± 0.07**	**0**
B1-b	222.3 ± 16.7	E I	0.10 ± 0.017	0.049 ± 0.012	0
B1-bN	22.0 ± 0.1	E 0	0.16 ± 0.02	0.82 ± 0.18	0
Combined	**106.0 ± 16.6**	**E I**	**0.24 ± 0.04**	**0.59 ± 0.13**	**0**
SVS13A	74.6 ± 51.9	L 0	119.28 ± 18.31	0.14 ± 0.03	0
SVS13B	35.5 ± 0.1	E 0	10.26 ± 1.57	0.14 ± 0.03	0
Combined	**73.9 ± 51.9**	**L 0**	**121.07 ± 18.58**	**0.15 ± 0.03**	**0**

required. Not all the systems we studied here are well sampled in this regime. For most systems the $L_{\rm submm}/L_{\rm bol}$ ratio is underestimated or cannot be calculated at all, while the $L_{\rm fir}/L_{\rm bol}$ can be calculated in all cases but is also underestimated due to the lack of submillimeter flux. Systems relatively well sampled in the submillimeter regime in our sample are NGC1333 SVS13 and B1-bN & S. The $L_{\rm submm}/L_{\rm bol}$ ratio for NGC1333 SVS13 supports the non-coevality of this system, with the ratio for SVS13A being lower than 0.5%, the threshold for embedded sources, while SVS13B and C are (marginally) above the value, indicating they are embedded. In contrast, the $L_{\rm fir}/L_{\rm bol}$ ratio shows values well above 0.5% for all three sources, with SVS13A and B having equal values and SVS13C showing a higher value. This would seem to suggest that SVS13C is more embedded than its northern companions, and SVS13A and B are less embedded. B1-bN & S have a $L_{\rm submm}/L_{\rm bol}$ well above 0.5% and a high value for the $L_{\rm fir}/L_{\rm bol}$ ratio, consistent with their deeply embedded condition. A non-coevality frequency cannot be derived from the luminosity ratios in this work because they are not well determined for almost all sources.

The infrared spectral index $\alpha_{\rm IR}$, which is the slope of the SED between 3 and 24 μm, is assumed to be a good indicator of evolutionary stage, even when geometric effects affect the SED shape (Crapsi et al. 2008). Positive values indicate an embedded source (Class 0 and I), while negative values higher and lower than -1.5 point toward Class II and III, respectively. NGC1333 SVS13A and SVS13B lack a point at 24 μm and therefore the value was not calculated. SVS13C has a negative value, suggesting that it is a Class II source. For B1-bN & S, the northern source presents a negative value higher than -1.5 while the southern source has a positive value, which would indicate that the northern component is Class II and the southern component is an embedded source. The reason for these discrepancies relative to the other parameters is the sensitivity of the spectral index to the fluxes between 3 and 24 μm. For example, NGC1333 SVS13C's flux at 24 μm drops below the fluxes at shorter wavelengths, causing the slope and consequently the spectral index to be negative. The same occurs for B1-bN , whose flux at 24 μm is lower than for B1-bS. Interestingly, this parameter causes systems such as NGC1333 IRAS7 and IC348 Per8+Per55 to seem

coeval. A coevality frequency cannot be derived from the values of $\alpha_{\rm IR}$ for the sample in this work, since it is not well determined for all sources.

The derived properties suggest the non-coevality frequency to be lower than that obtained from a visual examination of the SEDs, when considering only non-coeval systems and not marginally non-coeval ones. Still, the derived properties are sensitive to inclination and SED sampling, which biases their classification of evolutionary stage. Hence, these parameters should not be taken at face value, but instead be considered together with the SED shape and other properties of the multiple systems.

5.4.3 Resolved versus unresolved SEDs of multiples

The SED of an unresolved multiple system is composed of the sum of SEDs of its individual components. This led us to analyze to which extent an unresolved SED reflects the parameters and evolutionary stage classification of its compoennts. To do so, the SEDs of resolved systems were summed and the resulting shape and derived properties compared to those of the individual components. This analysis does not generate a method to separate unresolved SEDs, but will provide insight into the coevality of close multiple systems. Figure 5 and Table 6 show the results of combining the SEDs of four systems: NGC1333 IRAS7 Per18 and Per21, IC348 Per55 and Per8, B1-bW and B1-bN, and NGC1333 SVS13 A and B.

From this simple analysis we find that there are mainly three cases. The first is that if the two components have almost identical SEDs, then the combined SED will simply be doubled. This case is shown by NGC1333 IRAS7 Per18 and Per21. The second case is when the two components are non-coeval, then the SED will not follow a specific SED shape but will appear odd shaped with two peaks. This is illustrated by the combined SEDs of IC348 Per8 and Per55, and B1-b and B1-bN. The final case occurs when one component is noticeably dimmer and younger than the other, then the brightest component dominates the combined SED. NGC1333 SVS13 A and B illustrate this scenario. Thus, different components can dominate different regions of the SED.

Figure 4 presents the SEDs of unresolved multiple systems. Examples of the second case from Fig. 5, such as L1455 FIR2, B1-a and Per62, are shown in Fig. 4. The first and third cases are next to impossible to identify without additional constraints, and systems such as IRAS03292, IC348 SMM22, EDJ2009-156, and HH211 could be examples of either case.

In all scenarios we find that $L_{\rm bol}$ for the unresolved SED is equal to the sum of both components. In contrast, parameters such as $T_{\rm bol}$ and $L_{\rm fir}$ / $L_{\rm bol}$ are an arithmetic average of the corresponding parameters of the two components. This, of course, affects the evolutionary classification of unresolved multiple systems. While taking the derived values and assuming each component contributes equally may be a good assumption in coeval cases, this could be an over- or underestimation of the true parameters in non-coeval systems.

5.5 Discussion

From the SED shapes of resolved multiple systems alone, we find a non-coevality frequency of 33 ± 10%. Higher order multiple systems contribute the most to this fraction, with all of five resolved systems (L1448 N, NGC1333 SVS13, NGC1333 IRAS7,

B1-b and NGC1333 Per37) showing indications of non-coevality. The other two systems, IC348 Per8+Per55 and Per32+EDJ2009-366, that appear as binaries at separations $\geq 7''$, show additional fragmentation at scales $<7''$ in one of the components (Table 2), which also makes them higher order multiples. Binaries, on the other hand, tend toward coevality in our sample. The non-coevality frequency found here is similar to that found by Kraus & Hillenbrand (2009) of one-third in pre-main sequence stars. However, their frequency was found from binaries alone, whereas higher order multiple systems are responsible for this frequency in our study. Kraus & Hillenbrand (2009) also probed down to small separations (>200 AU) an order of magnitude lower than the separations probed here ($\geq$1600 AU). The unresolved systems studied here that are suspected of non-coevality could account for the rest of that fraction. The question then arises whether the non-coevality frequency obtained here is real or a product of misalignment, that is, the difference in inclination (w.r.t. the line of sight) of each component in a multiple system.

Different SEDs do not necessarily indicate a non-coeval multiple system, but could also be due to geometrical effects, especially if the line of sight lies through the outflow cone. Inclination can alter the shape of the SED and derived parameters (Robitaille et al. 2006; Crapsi et al. 2008; Enoch et al. 2009b) and is crucial to attain an accurate determination of the evolutionary stage (Offner et al. 2012b). If the protostellar system is seen edge-on, the protostar is obscured and will seem younger. On the other hand, if the protostellar system is observed face-on, the protostar will be unobscured and appear more evolved. Hence, the alignment of multiple systems affects whether the differing SED shapes are a product of real non-coevality of inclination effects. Multiple system formation mechanisms suggest that ordered rotational fragmentation would produce systems with aligned inclination (Burkert & Bodenheimer 1993), whereas turbulent fragmentation is expected to produce random alignment (Offner et al. 2010). Work on pre-main sequence multiple systems shows that binaries have a tendency to be aligned, while higher order multiple systems are less likely to be aligned (Jensen et al. 2004; Monin et al. 2006). However, the numbers seen toward pre-main sequence multiple systems might not reflect the actual alignment at the time of formation because of the dynamical evolution (Reipurth 2000; Jensen et al. 2004). Although a handful of observations exist that show both aligned and misaligned multiple systems at every stage of evolution, there are no statistical numbers on the distribution of inclination and multiple system alignment at the time of formation.

The best method to obtain an accurate inclination estimate is through disk observations and modeling, but not all protostellar systems have confirmed and reported disks. Hence, the inclination of protostellar systems must be constrained through another technique.

5.5.1 Outflows

Outflows present a viable option, but they can provide only a broad inclination range and may not always be accurate, even more so in multiple systems where precession occurs due to companion perturbations (Fendt & Zinnecker 1998). The evolutionary stage of a protostar is closely linked to its outflow and circumstellar envelope. The envelope is dispersed as the protostar evolves and accretes part of its material (André et al. 1993), while the molecular outflow tends to become weaker with time and the outflow cavity broadens (Velusamy & Langer 1998; Arce & Sargent 2006).

Table 7: Random pair statistics based on synthetic SEDs

	Value	Aparent Non-coevality
Total number of models	10370	...
Total number of pairs	5185	...
Aligned (Δi = 0°)	9.5±0.4%	8.4±1.2%
Small misalignment (0° < Δi < 34°)	63.0±0.6%	12.4±0.6%
Large misalignment (34° < Δi < 69°)	25.5±0.6%	39.5±1.3%
Perpendicular (Δi = 69°)	2.0±0.2%	83.9±3.6%
Total	...	17 ± 0.5%

A point to highlight here is that misalignment of outflow axes on the plane of the sky is not the same as misalingment of inclination with respect to the line of sight. The former does not affect the observed SED, while the latter has a strong effect on a protostar's SED and derived parameters. Thus, we refer to the first case as the outflow position angle (P.A.) and the second case as inclination misalignment.

Lee et al. (2016) studied the outflows of 9 multiple systems in Perseus and found in all cases that the outflows of wide multiple systems have different P.A., that is, that they are misaligned on the plane of the sky. However, strong indications of inclination misalignment were not found.

To compare with the other parameters used to determine the evolutionary stage of components in a system, we explicitly examine here the outflows of a few systems, focusing on signs that are expected to indicate evolutionary stage and inclination misalignment. Specific comments on each resolved multiple system treated in this work are given in Appendix 5.C.

NGC1333 SVS13A shows molecular outflow lobes that are wide and shell-like, while SVS13C exhibits a collimated outflow with indications of being in the plane of the sky, meaning that the disk is seen edge-on (Plunkett et al. 2013; Lee et al. 2016). This possible inclination misalignment might be the reason that this system appears to be non-coeval based on the SEDs. However, SVS13A has been suggested to be a transition class0/I object based on its association with a Haro-Herbig object and the shell-like morphology of its outflow, making it somewhat older than SVS13B and C.

B1-bN and S have outflows that appear parallel to each other, but the blueshifted lobes are in opposite directions, a tell-tale sign of inclination misalignment. Even though their outflows suggest inclination misaglinment (Gerin et al. 2015), the SEDs appear to be similar, indicating coevality, which is consistent with the results obtained from the analysis of their environment (Hirano & Liu 2014). The inclination misalignment may therefore be small. B1-bW is expected to be older based on the SED, which is why it is not detected in the submillimeter because it has too little envelope material that might be the product of stripping from a neighboring outflow or jet (Hirano & Liu 2014).

This shows that inclination misalignment of the systems does not always generate an apparent non-coevality. To do this, one of the components of a system would need to be significantly inclined, tending toward the line of sight along the outflow cavity so that the source would appear much older.

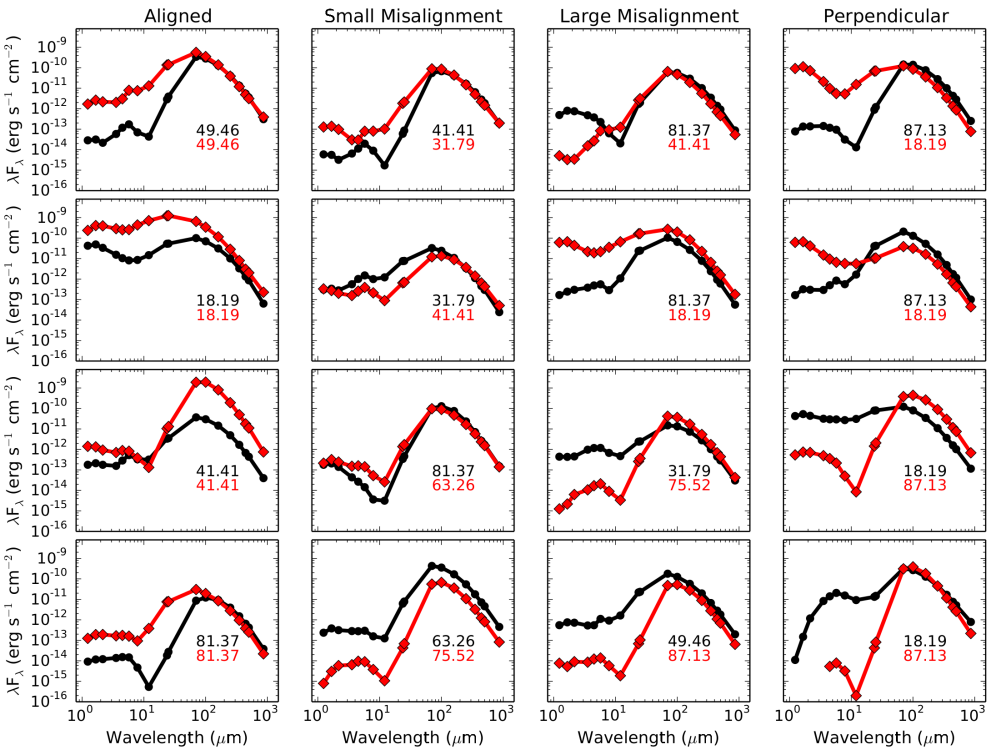

Figure 6: Randomly paired model SEDs in the four groups based on alignment. The numbers indicate the inclination of the respective component. Note that the SED pairs that appear non-coeval peak at the same wavelength for both components, which is not expected from components at different evolutionary stages.

5.5.2 Alignment and coevality

To assess the frequency of apparent non-coevality due to misalignment versus real non-coevality, we made a simple statistical test with the Robitaille et al. (2006) SED model grid[1]. This grid of models offers 10 inclination angles, evenly sampled in $cos(i)$, ranging from 87.13° to 18.19° with 0° being the disk seen face-on (i.e., looking down the outflow cone), which is ideally suited for our task. We constrained the number of models by choosing those for Class 0 sources, filtering by 2.0 $M_\odot \leq M_{\rm envelope} \leq$ 10.0 $M_\odot$ and $M_{\rm envelope} > M_{\rm star}$. The resulting set of model SEDs, a total of 1037 times 10 inclination angles, have stellar masses of up to 2.0 $M_\odot$ and outflow cavity angles ranging from 15 to 30°. The fluxes are obtained for similar wavelengths as our observations, including the *Herschel* PACS fluxes, and an aperture of 7000 AU (30″ at $d \sim 235$ pc).

Pairs of models with their respective inclinations are randomly drawn from the list of 10370 Class 0 synthetic SEDs, resulting in 5185 pairs. This is done to simulate, in a simplified manner, multiple systems and compare their SEDs and derived parameters. The random paired models are separated into four groups determined by the difference in inclination angles, that is, their degree of alignment. The four groups are perfectly aligned ($\Delta i = 0°$), small misalignment ($0° < \Delta i < 34°$), large misalignment ($34° < \Delta i < 69°$) and perpendicular ($\Delta i = 69°$). Perpendicular alignment is not equal to 90° because of the available inclination angles of the models, but is instead the difference between the edge-on (87.13°) and face-on cases (18.19°). To obtain the frequency of pairs in each group, the times each case occurs were counted based on Δi and are listed in Table 7. Perpendicular alignment is the least likely case (2 ± 0.2%), with small alignment the most common (63 ± 0.6%). Examples of SEDs from each case are shown in Fig. 6.

Apparent non-coevality was checked by first filtering with $T_{\rm bol}$, assuming that for apparently non-coeval pairs the $T_{\rm bol}$ difference is larger than a factor of 3. The reason for using $T_{\rm bol}$ to filter the models is based on three points: i) $T_{\rm bol}$ tends to be sensitive to inclination, ii) the thresholds for evolutionary stage classification (late Class 0 to early Class I: 100 K; late Class I to Class II: 650 K), and iii) the non-coeval resolved multiple systems in our sample identified from $T_{\rm bol}$ have a ratio of about 6 or higher. A factor of 3 was chosen to ensure that Class 0 and I pairs are also included, since for example a component with a $T_{\rm bol} = 50$ K may appear non-coeval with a companion having a $T_{\rm bol} > 150$ K. The paired SEDs filtered this way were then inspected by eye to subtract the SED pairs that did not appear non-coeval. The frequency of apparent non-coevality due to misalignment is found to be 17% ± 0.5%. Examining the frequency of apparent non-coevality in each of the four groups, we found that large misalignment and perpendicular have the most common occurrences of apparent non-coevality. This is mainly due to one component being face-on or close to face-on, in combination with the outflow cavity opening angle, causing one component to appear older. This was also suggested by the results of the outflows of multiple systems.

A characteristic of SEDs for different evolutionary stages is that the peak of the SED shifts to shorter wavelengths as the envelope is dispersed (see Fig. 7). While the SEDs can appear non-coeval as a result of inclination effects, the inspection by eye of these SED pairs revealed that the peak around $\lambda \sim$100 μm, characteristic of Class 0 sources, does not significantly shift to shorter wavelengths as a result of inclination,

[1]Retrieved Oct. 2015 from http://caravan.astro.wisc.edu/protostars/

even in the face-on case. Examples of this are shown in Fig. 6. In other words, even though one of the SEDs in the pair appeared more evolved than the companion, this apparently older source retained its peak around $\lambda \sim 100$ μm. This is in contrast to the SEDs of non-coeval resolved multiple systems discussed in this work. For example, in NGC1333 IRAS7, the peak of Per49 is located around 5.8 μm, whereas the peaks of Per18 and Per21 are around 100 μm. The same is true for B1-b, where B1-bW has a peak at 8 μm, while B1-bN & S peak at around 100 μm. On the other hand, NGC1333 SVS13 and L1448 N might appear non-coeval as a result of misalignment, given that the SED peaks of all three components are at about the same wavelength. For NGC1333 SVS13, the outflow and continuum detections of this object suggest that it might be transitioning to the Class I stage and therefore be slightly non-coeval with its companions.

5.5.3 On coevality and non-coevality

The frequency of non-coevality found in the sample of resolved multiple systems studied in this work can be safely assumed to be due to real non-coevality and not solely to misalignment, since most sources are expected to present small misalignment rather than one component close to face-on. Non-coevality in our resolved sample is exhibited by higher order multiples, except for IC348 MMS2, a triple with a component at a separation of $\sim 3''$ toward the western source (Table 2) that appears coeval. Protobinaries, on the other hand, tend toward coevality. Hence, protostellar siblings most of the time form and probably evolve simultaneously. This presents some interesting constraints to multiple system formation mechanisms and also raises questions.

For a multiple system to be non-coeval, the companion must either be formed after the first source or binary. In other words, fragmentation in the core must occur after the initial collapse and formation of the first protostar or protobinary. Hydrodynamical simulations predict that heated gas reduces the chance of further fragmentation, with only the cold gas tending to fragment (Stamatellos & Whitworth 2009b; Offner et al. 2010; Bate 2012). A possible explanation is that gas heating occurs along the outflow cavity while the dense envelope reduces heating of the surrounding gas, allowing further fragmentation to occur. Turbulence, on the other hand, is thought to be able to produce non-coevality through random density enhancements in the core.

For the coeval systems found in our resolved sample, fragmentation of the core would have occurred during the initial collapse and the system remained stable enough to hinder any further fragmentation and formation of younger companions, either through heated gas or lack of density enhancements and strong enough turbulence. Observational evidence for gas heating along the outflow cavity walls has been provided by van Kempen et al. (2009a) and Yıldız et al. (2015), including some of the multiple systems studied here.

Dynamical evolution, that is, the interaction that occurs in multiple systems, can cause these systems to evolve non-coevally, for example by expelling one of the companions, considerably reducing its envelope and thus truncating its accretion of material (Reipurth et al. 2010; Reipurth & Mikkola 2012). However, for embedded systems, not enough time has elapsed for dynamical evolution to play a major role in the appearance of the system. External factors, such as neighbouring outflows and jets, can affect a protostar in a system, for example by stripping material or possibly triggering further fragmentation. While these mechanisms, dynamical evolution and external

factors, are not formation mechanisms, they can alter the conditions of a multiple system and cause it to evolve non-coevally.

Given that only about a third of the multiple systems present non-coevality, the question then arises which factor or factors contribute to making some regions fragment and collapse even more while others do not. Probing the distribution of heated gas around multiple and single protostellar systems, in the case of multiples for both coeval and non-coeval, could provide insight.

5.6 Conclusions

This work presents the constructed SEDs of known resolved multiple protostellar systems in Perseus with separations $\geq 7''$. The SEDs were constructed from *Herschel* PACS photometric maps and *Spitzer* c2d catalogs, together with fluxes from the literature for the longer wavelengths. The properties were then derived from the observed SEDs. The SED shape and derived parameters were taken together with literature work on the envelope and outflow of these systems to determine the coevality of multiple systems. The literature, both from observations and models, lacks statistics on the frequency of alignment of multiple systems, but work is ongoing. A simple test whether the different SEDs might be due to misalignment was carried out in this work by randomly pairing model Class 0 sources from model SED grids with different inclinations with respect to the line of sight (Robitaille et al. 2006) and then counting the frequency of apparently non-coeval systems. The results of this work can be summarized in the following points.

1. From our sample of resolved multiple protostellar systems, which have separations $\geq 7''$, a coevality frequency of 66 $\pm$ 10% is found, suggesting that most wide multiples are born together.

2. From the observed SED shapes alone, a non-coevality frequency of 33 $\pm$ 10% is found, with higher order multiples being responsible for this percentage. Random pairing of model SEDs indicates that the frequency of apparent non-coevality that is due to misalignment of the components' inclinations is 17 $\pm$ 0.5%, with most occurrences in systems with large misalignments and perpendicular orientations. But most pairs tend toward small misalignment (63 $\pm$ 0.6%). This indicates that the observed non-coevality toward multiple systems in our sample is not due to misalignment, but is instead real.

3. Derived properties, such as $T_{\rm bol}$ and $\alpha_{\rm IR}$, suggest that the non-coevality frequency may be lower (21 $\pm$ 9%). However, the parameters derived from the observed SEDs produce contradicting results. Physical parameters derived from the synthetic SEDs demonstrate that these parameters are very sensitive to inclination or do not provide clear-cut evolutionary stage separations. As previously found in Offner et al. (2012b), the parameters are therefore unreliable for evolutionary stage classification, unless the inclination is well constrained.

4. Unresolved SEDs from multiple systems are not always dominated by the primary or brightest component, but can present an odd double-peaked shape that is due to non-coeval components. This can alter the fraction of non-coevality, but we did not take this into account because of the high uncertainty.

Owing to the limit on multiple system separations in this work, our results can only place constraints on formation mechanisms at core scales ($\geq$ 1600 AU). Higher order multiples show a stronger tendency to be non-coeval. This suggests that fragmentation at core scales can occur at different times, thus generating these types of systems.

The main conclusion of this work is then that real non-coeval multiple protostellar systems exist in the early stages of protostellar formation at core scales, which is most of the time due to formation, and can be enhanced by dynamical evolution (e.g., component ejection or envelope stripping by external influence, such as an outflow.). Several questions then arise. What causes some cores to fragment and collapse at different times? Which role do the already formed protostars play on the formation of their companions? Does temperature play an important role, and if so, to which extent? Future work, both from observations and models, is needed to address these questions.

Appendix

5.A HIPE map makers and photometry

The three HIPE map-makers (High Pass Filter; Jscan map; MADmap) were tested to determine the best map for performing photometry. The test was made only on the 70 μm maps for Perseus. The method used involved performing aperture photometry on the source and the surrounding background at four positions. The aperture (12") used was the same for all source and background measurements. Ten sources were selected from different regions of Perseus, ranging from isolated to clustered sources.

The flux was calculated in the following manner:

$$F_{source} = (F'_{source} - \frac{B_1 + ... + B_n}{n})A_{\rm corr}$$

where F'_{source} is the raw flux, B_i is the background flux, $A_{\rm corr}$ is the aperture correction factor, and F_{source} is the background corrected flux. Aperture correction values were taken from Balog et al. (2014). For an aperture of 12", the correction factor is of 0.802.

Table 8 lists the background and aperture corrected results. This shows that the difference between maps is not significant. We have adopted JScanmap for photometry.

5.B Evolutionary stage classification

The SEDs of the resolved systems are compared to average SEDs obtained by (Enoch et al. 2009b; Fig. 7) to determine by eye whether the multiple systems are coeval or not.

Physical parameters derived from the SED are known to be sensitive to inclination. This is confirmed by the properties derived from the model SEDs. The derived properties were calculated for the model SEDs in the same way as for the observed SEDs. Comparing the derived parameters, we find that $T_{\rm bol}$ varies widely with inclination, while $L_{\rm fir}/L_{\rm bol}$ are independent of inclination. These results confirm previous work on the subject (Jørgensen et al. 2009; Launhardt et al. 2013). Figure 8 shows the parameters for all the Class 0 models versus inclination.

Table 8: Aperture photometry results for 70 μm

Source	RA	Dec	HPF	JSM	MAD	Average	Std. Dev.
IRAS4C	03:29:13.81	31:13:56.11	2.72	2.74	2.75	2.74	0.014
SK1	03:29:00.77	31:11:57.59	1.42	1.43	1.37	1.41	0.026
NGC1333 S1	03:28:45.40	31:05:40.30	1.25	1.23	1.20	1.22	0.021
NGC1333 S2	03:28:34.49	31:00:50.20	3.22	3.20	3.11	3.18	0.049
IRAS03282	03:31:20.99	30:45:28.48	6.20	6.18	6.04	6.14	0.069
IRAS03292	03:32:17.95	30:49:46.46	2.55	2.55	2.47	2.52	0.039
L1448IRS1	03:25:09.54	30:46:20.80	2.62	2.61	2.52	2.58	0.044
IRAS5 Per63	03:28:43.54	31:17:31.61	2.01	2.04	1.96	2.00	0.035
IC348	03:33:27.40	31:07:10.00	4.28	4.35	4.24	4.29	0.049
L1455-FIR N	03:27:38.44	30:13:57.95	2.23	2.25	2.33	2.27	0.043

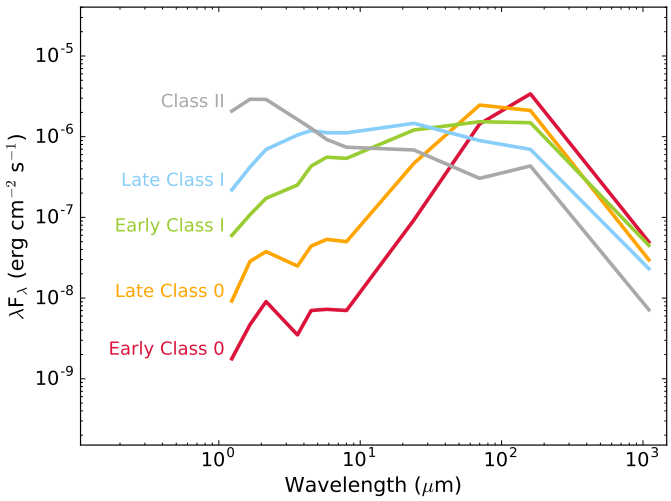

Figure 7: Average SEDs derived by Enoch et al. (2009b). The classifications are defined based on the bolometric temperature. These average SEDs are used to compare to the constructed SEDs in this work.

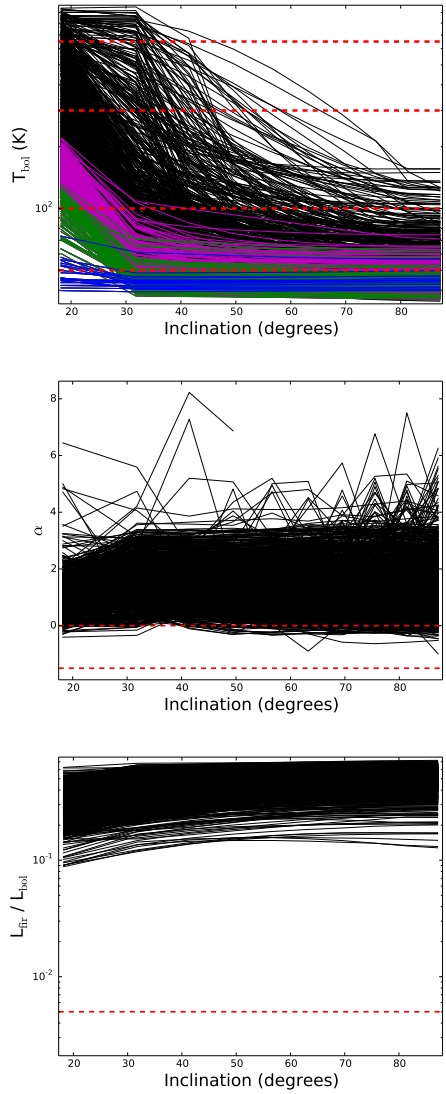

Figure 8: Physical parameters derived from the model SEDs from the grid of Robitaille et al. (2006) compared to the inclination w.r.t. line of sight. Edge-on is defined as 90°. The dashed red lines indicate the evolutionary stage boundaries. *Top:* Bolometric temperature $T_{\rm bol}$ varies largely as it inclines more toward face-on (0°). The blue lines are models with a small difference in $T_{\rm bol}$ with inclination; these have dense envelopes. Green and magenta show the models with an increase in $T_{\rm bol}$ when the inclination is close to face-on. *Middle:* The infrared spectral index from 2 to 24 μm oscillates without relation to inclination. This is most likely an effect of the ice feature at 8 μm. *Bottom:* The luminosity ratio $L_{\rm fir}/L_{\rm bol}$ is independent of inclination, but there is no clear boundary for systems at different evolutionary stages.

5.C Resolved multiple systems

5.C.1 NGC1333

NGC1333 SVS13: Located at the heart of NGC1333, SVS13 is a quintuple system with components SVS13A1 and 2, VLA3, SVS13B and C (Tobin et al. 2016b). Based on the velocity field, VLA3 and SVS13B are suggested to be a binary even though VLA3 is closer to SVS13A (Chen et al. 2009). One of the components in SVS13A is expected to be the driving source of HH 7-11 (Rodríguez et al. 1997; Looney et al. 2000). SVS13A is observed to have a prominent molecular outflow in the SE-NW direction with a moderate inclination angle and wide opening angles (Plunkett et al. 2013). These outflow characteristics together with the presence of a centimeter source and being the exciting source for HH 7-11 (Rodríguez et al. 1997) suggest that SVS13A is a Class 0/I transition object. SVS13C may be driving a N-S outflow possibly directed along the plane of the sky, but its outflow emission may be confused with other outflows (Plunkett et al. 2013). SVS13B does not show a clear outflow, which could be due to confusion with the outflow of SVS13A (Plunkett et al. 2013). SVS13 has been suggested many times to be non-coeval because components SVS13B and C are more embedded than SVS13A, which has an optical counterpart (Looney et al. 2000; Chen et al. 2009). SVS13B is not detected in the *Herschel* PACS 70μm maps, but is detected at $\lambda \geq$100μm, suggesting it is deeply embedded.

NGC1333 IRAS2: located in the west of the NGC1333 region, the IRAS2 system is composed of sources A, B and C (Sandell & Knee 2001), although source C is expected to be a starless core. IRAS2B is known to be confused with a field star at $\lambda \leq$8μm (Rodríguez et al. 1999). IRAS2A is typically classified as Class 0, while IRAS2B is considered Class I, but here we find them to be coeval. IRAS2A is well known because of its spectacular quadrupole outflow. The N-S outflow has a shell-like structure, while the E-W outflow is more collimated (Plunkett et al. 2013). Tobin et al. (2015) resolved components with a separation of 0.6″ toward IRAS2A and suggested that the southern component drives the E-W outflow, while the northern component drives the N-S outflow. The outflow of IRAS2B runs parallel to the N-S outflow of IRAS2A (Plunkett et al. 2013).

NGC1333 IRAS7: three systems in a common core (CLASSy N_2H^+ observations) of about 30″ diameter. Per49 is located in the SE edge of the dust and gas core, while Per18 is located at the peak with Per21 13″ to the SW. Per18 and Per49 were found to be close binaries with separations $\leq$0.3″ (Tobin et al. 2016b). This system of sources is associated with the Haro-Herbig object HH6. The outflow of this system has been less frequently observed, with candidate outflow lobes proposed to extend to around the NE of the SVS13A outflow (Plunkett et al. 2013). ^{12}CO observations with CARMA show outflow lobes associated with Per21, but no clear outflow signatures toward the other sources.

NGC1333 IRAS4: the region contains several systems and IRAS4B' can be resolved at the resolution of Herschel, but IRAS4A cannot. IRAS4B' (also referred to as IRAS4C, Looney et al. 2000, and IRAS4B2, Hull et al. 2014b) is not detected in the Herschel observations, which may mean that it is still deeply embedded. Hull et al. (2014b) detected outflows toward both sources, with IRAS4B showing an N-S outflow and IRAS4B' driving a weak E-W outflow.

NGC1333 IRAS5: located at the western edge of NGC1333, this protobinary composed of Per52 and Per63 does not show a prominent molecular outflow (Curtis et al.

2010).
NGC1333 Per58+Per65: located to the north of the NGC1333 core, there are indications of outflow from these sources, although their orientations are unclear because of confusion (Curtis et al. 2010).
NGC1333 Per37: located along a filament in the northernmost region of NGC1333, this triple protostellar system, identified by Tobin et al. (2016b), does not appear to have a strong outflow in the observations of Curtis et al. (2010).

5.C.2 L1448 and L1455

L1448 C: is a protobinary in the south of L1448, with the southern component having a projected position in the outflow of the northern source. L1448 C-N shows a more prominent high-velocity collimated outflow traced in ^{12}CO and SiO, with a low velocity conic cavity observed in ^{12}CO, while L1448 C-S shows a much weaker low velocity ^{12}CO collimated outflow (Hirano et al. 2010). Both outflows are not aligned, but do not show signs of significant misalignment along the line of sight either.
L1448 N: also commonly known as L1448 IRS3, this system is a sextuple, with the B and C sources containing three and two components, respectively (Lee et al. 2015). All three sources drive molecular outflows, with components B and C almost parallel to each other and source A perpendicular to B and C (Lee et al. 2015). The observed outflows suggest no significant misalignment along the line of sight. The outflow from L1448 C was suggested to induce fragmentation in this core (Barsony et al. 1998).
L1448 IRS2: Tobin et al. (2016b) found L1448 IRS2 to be a close binary (separation $\sim$0.7″). SCUBA 850μm observations showed a continuum peak to the east of L1448 IRS2, which Chen et al. (2010) referred to as IRS2E, and together with SMA and *Spitzer* upper limits proposed to be a first core candidate. Although SCUBA 850μm observations suggest a shared envelope, the separation of these two sources is 46″ and therefore cannot compose a multiple system. The outflow of IRS2 is observed to be conical in the SE-NW direction, while the suggested outflow of IRS2E is composed of only the red-shifted lobe directed toward the SW (Hull et al. 2014b; Chen et al. 2010).

5.C.3 IC348

IC348 Per8+Per55: this triple protostellar system shows a large-scale jet directed in the north-south direction and is associated with two Haro-Herbig objects, HH841 and HH842 (Walawender et al. 2006). Based on the large-scale jet, there is no indication of multiple components.
IC348 MMS: a protobinary located in the southwest of IC348 and associated with a strong north-south outflow where the overlapping of redshifted emission at the tip of the blueshifted lobe is suggested to be due to a change in environment and not a product of inclination; see Tafalla et al. (2006). The outflow is driven by the Class 0 western source, MMS2, and is also associated with HH797. The eastern source, MMS2E, was suggested to be a Class 0 proto-brown dwarf driving a weak outflow in the NE-SW direction by Palau et al. (2014). Both sources are found to be coeval, as suggested by Palau et al. (2014).
IC348 SMM2: also referred to as Per16+Per28, this protobinary shows jet emission in the east-west direction for both components and a large-scale S-shape bend in the flow (Walawender et al. 2006). The outflows appear to be short and clumpy (Eislöffel et al. 2003; Walawender et al. 2006).

IC348 Per32+EDJ2009-366: the H_2 emission around these sources appears to be clumpy, with bow shocks pointing east and possibly not all clumps belonging to the respective sources (Eislöffel et al. 2003). Per32 is a close protobinary ($\sim$6″) (Tobin et al. 2016b) and was also found to be a low luminosity object (Dunham et al. 2008; Hsieh et al. 2015).

5.C.4 B-1

B1 Per6+Per10: the outflows of this protobinary are not well determined owing to their location with several neighbouring systems whose outflows become entangled (Walawender et al. 2005; Hiramatsu et al. 2010). Per10 might drive a red-shifted outflow lobe directed NW, but it is uncertain whether the lobe belongs to Per10 or to a source about $\sim$70″ to the north (Hiramatsu et al. 2010). Per6 is also known as SMM3 and Per10 as SSTc2d J033314.4+310711.
B1-b: a triple system composed of Per41 to the west and B1-bN and B1-bS to the north and south, respectively. B1-bN and S are found to be very young based on 7 to 1.1 mm continuum data and lack of *Spitzer* detections at $\lambda \leq 24\mu$m (Hirano & Liu 2014). The outflows for both sources are directed E-W, but the location of the blueshifted lobes suggests that the two sources are misaligned, since the north source has the outflow directed to the west, while the south source has it directed to the east (Gerin et al. 2015). Per41 appears to be older, with no detection in the millimeter regime. It is suggested that there is no emission in the millimeter because the envelope of this system is being striped off by neighboring outflows, which makes it appear to be more evolved (Hirano & Liu 2014).

5.D Single protostellar systems

Single protostellar sources indentified in Perseus (Tobin et al. 2016b) are listed in Table 9 and the constructed SEDs are shown in Fig. 9. Not all sources have an SED, either due to lack of fluxes in the literature, non-detection in the *Herschel* PACS maps, or both. This is denoted in the last column of Table 9.

5.E *Herschel* Catalog

This appendix contains the *Herschel* PACS flux catalog for the Perseus star forming region obtained in this work through PSF photometry with *StarFinder* (Diolaiti et al. 2000). The fluxes have been background and aperture corrected, with the aperture correction values tabulated in Balog et al. (2014).

Table 9: Sample of single protostellar systems

Source	RA	Dec.	Constructed SED?
NGC1333 SK1	03:29:00.52	+31:12:00.68	Y
PER4	03:28:39.10	+31:06:01.80	Y
PER7	03:30:32.68	+30:26:26.48	Y
IRAS 03267+3128	03:29:51.82	+31:39:06.08	Y
NGC1333 IRAS4C	03:29:13.52	+31:13:58.01	Y
RNO 15 FIR	03:29:04.05	+31:14:46.61	Y
Per19	03:29:23.49	+31:33:29.48	Y
L1455-IRS4	03:27:43.23	+30:12:28.80	Y
Per23	03:29:17.16	+31:27:46.41	Y
PER24	03:28:45.30	+31:05:41.99	Y
PER25	03:26:37.46	+30:15:28.01	Y
B1-c	03:33:17.85	+31:09:32.00	Y
PER30	03:33:27.28	+31:07:10.20	Y
PER31	03:28:32.55	+31:11:05.21	Y
IRAS 03271+3013	03:30:15.12	+30:23:49.20	Y
PER38	03:32:29.18	+31:02:40.88	Y
PER39	03:33:13.78	+31:20:05.21	Y
PER43	03:42:02.16	+31:48:02.09	Y
PER45	03:33:09.57	+31:05:31.20	Y
PER46	03:28:00.40	+30:08:01.28	Y
IRAS 03254+3050	03:28:34.50	+31:00:51.09	Y
PER50	03:29:07.76	+31:21:57.21	Y
PER51	03:28:34.53	+31:07:05.49	Y
B5-IRS1	03:47:41.56	+32:51:43.89	Y
NGC1333 IRAS6	03:29:01.57	+31:20:20.69	Y
IRAS 03439+3233	03:47:05.42	+32:43:08.41	Y
PER57	03:29:03.33	+31:23:14.60	Y
PER59	03:28:35.04	+30:20:09.89	Y
PER60	03:29:20.07	+31:24:07.49	Y
PER61	03:44:21.33	+31:59:32.60	Y
PER66	03:43:45.15	+32:03:58.61	Y
PER64	03:33:12.85	+31:21:24.08	Y
PER-BOLO-58	03:29:25.46	+31:28:14.99	N
PER-BOLO-45	03:29:07.70	+31:17:16.80	N
L1451-MMS	03:25:10.21	+30:23:55.20	N
IRAS 03363+3207	03:39:25.20	+32:17:03.29	N
EDJ2009-161	03:28:51.48	+30:45:00.48	N
EDJ2009-263	03:30:27.45	+30:28:27.43	N
EDJ2009-285	03:32:46.94	+30:59:17.80	Y
IRAS 03295+3050	03:32:34.15	+31:00:56.22	Y
L1451 IRS2	03:27:47.49	+30:12:05.32	Y
EDJ2009-333	03:42:55.77	+31:58:44.39	Y
EDJ2009-385	03:44:17.91	+32:04:57.08	Y
EDJ2009-164	03:28:53.96	+31:18:09.35	Y
EDJ2009-172	03:28:56.65	+31:18:35.44	Y
EDJ2009-173	03:28:56.96	+31:16:22.20	Y
SVS3	03:29:10.42	+31:21:59.07	N
EDJ2009-268	03:30:38.23	+30:32:11.67	Y

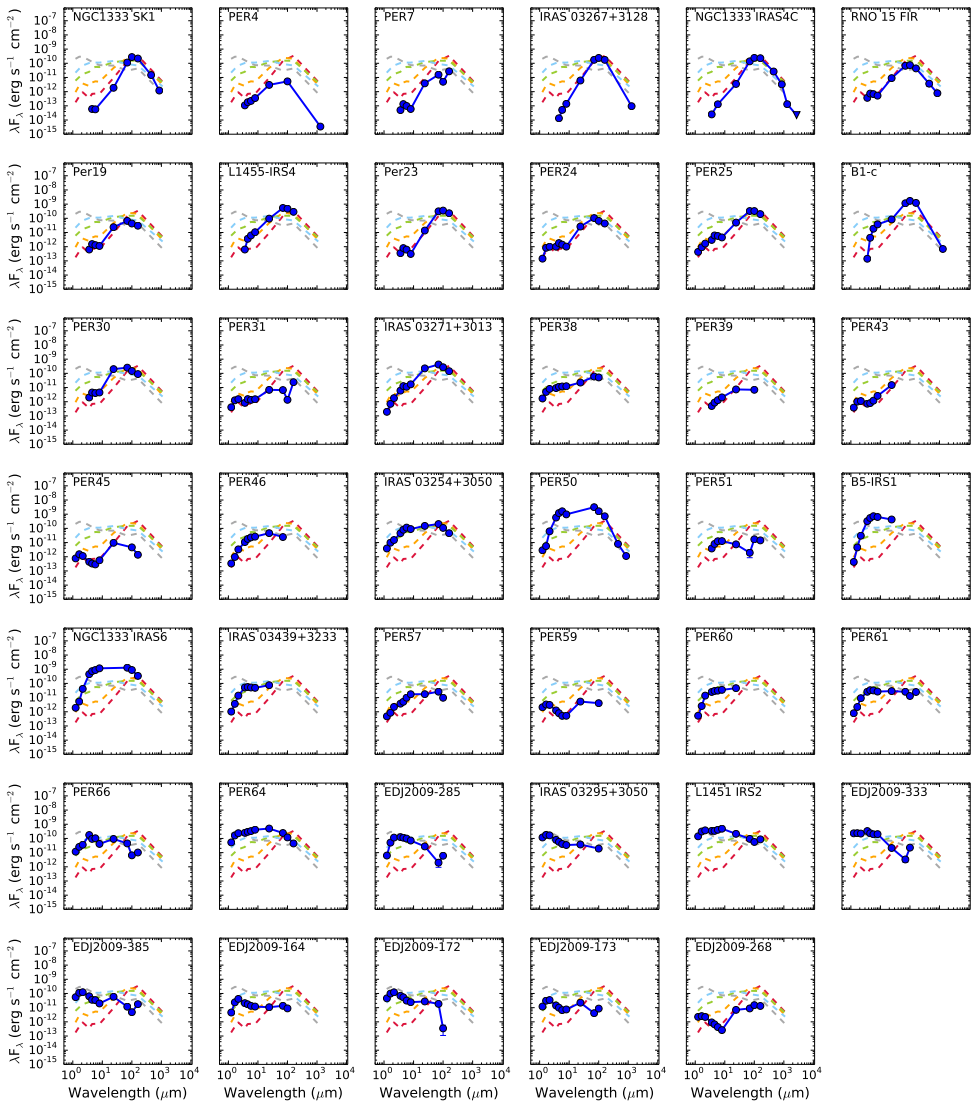

Figure 9: Constructed SEDs for single protostellar systems. Other details are the same as in Figure 3.

Table 10: *Herschel* PACS protostellar fluxes for Perseus

Source	RA	Dec.	$F_{70,\mathrm{int}}$ mJy	$F_{70,\mathrm{err}}$ mJy	$F_{100,\mathrm{int}}$ mJy	$F_{100,\mathrm{err}}$ mJy	$F_{160,\mathrm{int}}$ mJy	$F_{160,\mathrm{err}}$ mJy
L1448 IRS2	03:25:22.40	+30:45:12.00	29600.27	24.45	50315.79	9.35	...	...
L1448 IRS2E	03:25:25.66	+30:44:56.70	120.00	0.00	...	...	2700.00	0.00
L1448N C	03:25:35.53	+30:45:34.20	5975.70	25.02	15971.03	8.10	34348.59	12.01
L1448N B	03:25:36.34	+30:45:14.94	10245.52	45.09	35063.42	10.66	...	...
L1448N A	03:25:36.53	+30:45:21.35	33206.75	31.12	56855.07	10.66	133706.90	12.01
L1448C N	03:25:38.87	+30:44:05.40	68675.92	33.84	86927.75	9.23	105056.08	11.74
L1448C S	03:25:39.14	+30:43:58.30	10598.25	32.11	20902.32	8.74	...	...
Per25	03:26:37.46	+30:15:28.01	7640.36	24.54	10878.83	9.43	10587.80	11.71
L1455 FIR2	03:27:38.23	+30:13:58.80	3040.50	24.57	3573.99	9.88	6011.33	17.46
Per17	03:27:39.09	+30:13:03.00	70668.57	24.45	80705.92	9.29	58554.50	11.72
L1455-IRS4	03:27:43.23	+30:12:28.80	12583.17	31.19	15966.15	9.12	15317.03	11.69
L1451 IRS2	03:27:47.49	+30:12:05.32	2186.14	24.36	1897.01	14.88	4605.56	16.99
Per46	03:28:00.40	+30:08:01.28	575.09	24.51	...	...	...	...
Per31	03:28:32.55	+31:11:05.21	155.36	24.70	45.52	7.90	1279.57	11.78
IRAS 03254+3050	03:28:34.50	+31:00:51.09	4738.27	24.83	3613.08	7.93	2439.00	11.82
Per51	03:28:34.53	+31:07:05.49	44.76	24.71	567.30	7.90	763.32	11.89
Per59	03:28:35.04	+30:20:09.89	...	...	135.28	7.99	...	...
NGC1333 IRAS1	03:28:37.00	+31:13:27.00	...	...	83861.07	7.93	...	...
Per4	03:28:39.10	+31:06:01.80	...	...	177.23	7.91	...	...
NGC1333 IRAS5 Per52	03:28:39.72	+31:17:31.89	208.77	24.64	427.39	7.90	928.07	11.90
NGC1333 IRAS5 Per63	03:28:43.28	+31:17:32.90	2631.24	24.53	1733.94	9.54	2905.58	11.90
Per24	03:28:45.30	+31:05:41.99	2440.21	24.69	2218.64	7.92	2304.05	14.02
EDJ2009-156	03:28:51.11	+31:18:15.41	272.70	24.57	474.27	7.90	...	...
EDJ2009-164	03:28:53.96	+31:18:09.35	316.65	24.55	297.22	7.89	...	...
NGC1333 IRAS2A	03:28:55.57	+31:14:37.22	353085.72	24.59	457917.62	7.91	355028.75	11.90
NGC1333 Per65	03:28:56.31	+31:22:27.80	190.82	24.82	707.66	7.92	295.13	12.25
EDJ2009-172	03:28:56.65	+31:18:35.44	434.22	24.67	11.57	7.91	...	...

Table 10: continued.

Source	RA	Dec.	$F_{70,\mathrm{int}}$ mJy	$F_{70,\mathrm{err}}$ mJy	$F_{100,\mathrm{int}}$ mJy	$F_{100,\mathrm{err}}$ mJy	$F_{160,\mathrm{int}}$ mJy	$F_{160,\mathrm{err}}$ mJy
EDJ2009-173	03:28:56.96	+31:16:22.20	95.59	24.61	287.08	7.92	...	...
NGC1333 IRAS2B	03:28:57.35	+31:14:15.93	42904.02	24.61	42112.11	7.90	40297.80	11.90
NGC1333 Per58	03:28:58.44	+31:22:17.40	2023.94	24.51	1361.60	7.92	2993.06	13.89
EDJ2009-183	03:28:59.32	+31:15:48.14	1373.58	24.52	568.81	7.90	...	...
NGC1333 SK1	03:29:00.52	+31:12:00.68	2639.06	24.65	9202.65	7.93	11595.86	11.84
NGC1333 IRAS6	03:29:01.57	+31:20:20.69	29984.85	24.55	29552.15	7.91	18105.12	12.75
NGC1333 SVS13C	03:29:01.96	+31:15:38.26	10414.79	28.64	25758.22	9.50	39433.51	14.03
NGC1333 SVS13B	03:29:03.07	+31:15:52.02	...	...	29753.50	0.00	49162.50	0.00
Per57	03:29:03.33	+31:23:14.60	610.89	24.66	325.77	7.93	...	...
NGC1333 SVS13A	03:29:03.75	+31:16:03.76	346127.50	24.55	362422.36	9.35	262763.62	13.88
RNO 15 FIR	03:29:04.05	+31:14:46.61	1557.72	24.60	2464.90	7.91	2338.33	11.83
Per50	03:29:07.76	+31:21:57.21	73021.60	24.75	53860.12	7.90	38022.12	14.21
NGC1333 IRAS4A	03:29:10.51	+31:13:31.01	34177.79	24.54	145231.28	7.91	198935.09	11.79
NGC1333 IRAS7 PER21	03:29:10.67	+31:18:20.18	22177.79	25.30	33424.83	8.11	32656.71	13.73
NGC133 IRAS7 Per18	03:29:11.26	+31:18:31.08	29785.00	30.59	51718.19	10.33	49503.68	14.11
NGC1333 IRAS4B	03:29:12.01	+31:13:08.10	13967.95	24.47	57324.07	7.92	95091.14	11.87
NGC1333 IRAS4B'	03:29:12.83	+31:13:06.90	...	...	...	...	...	...
NGC1333 IRAS7 Per49	03:29:12.96	+31:18:14.31	2287.81	24.31	1234.96	7.93	...	...
NGC1333 IRAS4C	03:29:13.52	+31:13:58.01	3215.11	24.49	8028.17	7.93	12204.80	11.80
Per23	03:29:17.16	+31:27:46.41	7282.82	24.53	11712.11	7.92	12160.26	11.79
NGC1333 EDJ2009-233	03:29:17.675	+31:22:44.922	500.51	24.27	693.54	7.90	...	...
NGC1333 EDJ2009-235	03:29:18.259	+31:23:19.758	...	...	...	...	...	...
NGC1333 Per37	03:29:18.89	+31:23:12.89	2083.38	30.77	4311.49	7.91	8826.94	11.79
Per60	03:29:20.07	+31:24:07.49	...	...	...	...	...	...
Per19	03:29:23.49	+31:33:29.48	1539.06	24.38	1437.67	7.91	1615.74	13.53
IRAS 03267+3128	03:29:51.82	+31:39:06.08	4111.28	24.66	7984.09	7.92	9383.54	11.89
IRAS 03271+3013	03:30:15.12	+30:23:49.20	9835.80	24.40	8981.08	8.96	7599.56	13.28

Table 10: continued.

Source	RA	Dec.	$F_{70,\mathrm{int}}$ mJy	$F_{70,\mathrm{err}}$ mJy	$F_{100,\mathrm{int}}$ mJy	$F_{100,\mathrm{err}}$ mJy	$F_{160,\mathrm{int}}$ mJy	$F_{160,\mathrm{err}}$ mJy
Per7	03:30:32.68	+30:26:26.48	367.70	24.45	166.76	7.98	1453.21	14.87
EDJ2009-268	03:30:38.23	+30:32:11.67	206.44	24.38	501.70	7.96	704.23	11.75
EDJ2009-269	03:30:43.91	+30:32:46.28	1281.74	24.16	588.90	7.98	969.73	14.26
IRAS 03282+3035	03:31:21.00	+30:45:30.00	8447.13	24.59	22504.65	9.29	...	...
IRAS 03292+3039	03:32:17.95	+30:49:47.60	1700.00	180.00	9100.00	1300.00	24000.00	8400.00
Per38	03:32:29.18	+31:02:40.88	1391.34	24.58	1721.54	7.86	...	...
IRAS 03295+3050	03:32:34.15	+31:00:56.22	...	...	645.16	7.88	...	...
EDJ2009-285	03:32:46.94	+30:59:17.80	45.89	24.30	201.98	7.84	...	...
Per45	03:33:09.57	+31:05:31.20	...	...	153.45	7.85	73.99	11.99
Per64	03:33:12.85	+31:21:24.08	5666.66	24.37	3961.29	7.83	2369.53	11.77
Per39	03:33:13.78	+31:20:05.21	...	...	231.78	7.85	...	...
NGC1333 PER6	03:33:14.40	+31:07:10.88	1259.95	24.15	1076.28	7.87	1873.57	14.78
NGC1333 PER10	03:33:16.45	+31:06:52.49	2514.94	24.44	6431.20	7.86	9511.64	11.75
B1-a	03:33:16.66	+31:07:55.20	8844.80	24.24	7961.24	7.86	...	...
B1-c	03:33:17.85	+31:09:32.00	26917.64	24.01	56567.06	7.85	65357.92	11.83
B1-bW	03:33:20.30	+31:07:21.29	385.40	29.27	72.83	7.84	...	...
B1-bN	03:33:21.20	+31:07:44.20	...	...	356.37	7.87	2458.19	11.87
B1-bS	03:33:21.30	+31:07:27.40	32.30	24.68	2169.70	7.83	9152.34	13.65
Per30	03:33:27.28	+31:07:10.20	5885.32	24.09	4870.87	7.85	4753.57	11.81
Per43	03:42:02.16	+31:48:02.09	...	...	...	...	...	...
EDJ2009-333	03:42:55.77	+31:58:44.39	76.98	28.07	751.94	8.82	...	...
Per66	03:43:45.15	+32:03:58.61	1044.54	23.67	216.00	7.51	545.83	10.67
IC348 SMM2N	03:43:51.00	+32:03:23.76	1786.13	29.32	3298.55	8.93	4712.59	10.22
IC348 SMM2S	03:43:51.08	+32:03:08.32	...	...	9069.77	7.52	8418.18	11.32
HH211	03:43:56.80	+32:00:50.21	5008.66	23.38	20474.13	7.54	29631.02	16.35
IC348 MMS Per11	03:43:57.06	+32:03:04.60	...	...	18485.14	8.53	22651.04	13.02
IC348 MMS2E	03:43:57.73	+32:03:10.10	360.00	50.00	1200.00	100.00	1300.00	700.00

Table 10: continued.

Source	RA	Dec.	$F_{70,\mathrm{int}}$ mJy	$F_{70,\mathrm{err}}$ mJy	$F_{100,\mathrm{int}}$ mJy	$F_{100,\mathrm{err}}$ mJy	$F_{160,\mathrm{int}}$ mJy	$F_{160,\mathrm{err}}$ mJy
EDJ2009-366	03:43:59.44	+32:01:53.99	183.88	26.69	1053.86	8.26	...	...
Per32	03:44:02.40	+32:02:04.89	99.35	23.59	350.11	7.52	1506.45	10.04
Per62	03:44:12.98	+32:01:35.40	7627.83	23.53	8954.61	8.44	5590.77	10.06
EDJ2009-385	03:44:17.91	+32:04:57.08	274.20	23.32	160.37	8.48	942.41	11.49
PER61	03:44:21.33	+31:59:32.60	601.91	23.69	432.97	7.52	1326.28	10.08
IC348 Per55	03:44:43.33	+32:01:31.41	4451.78	29.90	4821.42	7.97	...	...
IC348 Per8	03:44:43.94	+32:01:36.09	12057.88	31.07	26087.98	8.49	28035.05	10.09
IRAS 03439+3233	03:47:05.42	+32:43:08.41	...	...	...	...	...	...
B5-IRS1	03:47:41.56	+32:51:43.89	...	...	...	...	...	...

Chapter 6

The role of environment and gas temperature in the formation of multiple protostellar systems

Molecular tracers

N. M. Murillo, E. F. van Dishoeck, J. J. Tobin,
J. C. Mottram, and A. Karska
in preparation

Abstract

Context What factors influence the formation of multiple protostellar systems? Simulations suggest radiative feedback resulting in gas heating is a key factor in the formation of multiple protostellar systems. Chemistry is a good tracer of the physical structure of a protostellar system, since it depends on the temperature structure.

Aims Study the relationship of multiplicity to envelope gas temperature.

Methods Single dish observations of various molecules that trace the warm and cold gas are used to probe the temperature structure of multiple and single protostellar systems.

Results Single, close binary and wide multiples present similar current envelope gas temperatures, as estimated from H_2CO and DCO^+ line ratios. The temperature of the outflow cavity, traced by c$-C_3H_2$, on the other hand, shows a relation with bolometric luminosity and anti-correlation with envelope mass. Although the envelope gas temperatures are similar for all objects surveyed, wide multiples do exhibit a massive reservoir of cold gas compared to close binary and single protostars.

Conclusions Although the sample of protostellar systems is small, no relationship between multiplicity and envelope gas temperature is found. The results suggest that temperature has little impact on fragmentation, and propose that mass, and density, may instead be key factors in fragmentation.

6.1 Introduction

Multiple protostellar systems are widely thought to be formed through fragmentation of the cloud core and/or disk. This process is expected to occur either induced by turbulence (Offner et al. 2010) or through instabilities in the disk that can lead to fragmentation of the disk material (Stamatellos & Whitworth 2009a; Kratter et al. 2010). Each mechanism is proposed to produce multiple protostellar systems with different separations between the components. Turbulent fragmentation predicts the initial formation of wide companions, whereas disk fragmentation can produce close companions, on scales of the disk radius. When these processes occur, upon initial collapse or after one component has formed, can also alter the resulting multiple protostellar system and its evolution. Aiming to understand how and when multiple protostellar systems are formed, the factors that influence fragmentation must be studied.

Radiative feedback and gas heating have been raised as key factors in the fragmentation of protostellar cores (Krumholz 2006; Bate 2012; Krumholz et al. 2014). Simulations and models show that fragmentation is halted by heated gas due to the increase in the Jeans mass for collapse. An accreting protostar heats up its surrounding gas, even as early as the first collapse of the core. Thus it is expected that fragmentation can be considerably suppressed even before the protostellar object forms. Numerical simulations show that as stars begin to form they can heat surrounding gas out to a few thousand AU, with the gas being continuously heated out to larger expanses as more objects form (Bate 2012). This is expected to considerably reduce fragmentation, and consequently the formation of multiple protostellar systems on envelope scales (few thousand AU).

Observations of early low-mass embedded protostellar systems, however, seem to show a different picture. Construction of the SEDs of all known embedded protostellar systems in the Perseus star forming region (d $\sim$ 230 pc, Hirota et al. 2011) found, for separations larger than $7''$, that higher order multiples have a tendency for one of its components to be at a different evolutionary stage than the rest, i.e. non-coeval systems (Murillo et al. 2016, see chapter 5). For these non-coeval systems to occur, one of the components must have been formed after the other protostars were formed. In contrast, objects undergoing accretion bursts, such as very low luminosity objects (VeLLOs), show no cases of multiplicity (Hsieh et al. in prep.). This is puzzling due to these objects having cold envelopes during the quiescent phase, which lasts on the order of 10^{3-4} yr which should be more conducive to fragmentation and collapse. Furthermore, the recently fragmented circumbinary disk of the deeply embedded protostellar system L1448 N (Tobin et al. 2016a) suggests that instabilities could overcome heating-suppressed fragmentation, since this disk is most certainly heated by both the central binary and through accretion. Based on these observations, it is very likely that other factors besides temperature can hinder or enhance fragmentation.

Relating the temperature structure and multiplicity of a protostellar system can provide constraints on the temperature-fragmentation relation. Simulations including radiative feedback would lead us to expect that single protostars and coeval binary protostellar systems have cloud cores heated out to larger extents than higher order multiples with non-coeval components. Thus, the temperature structure of protostellar systems needs to be characterized in order to test these models. Because heating is time-dependent and we cannot observe the temporal history of protostellar envelope

heating, protostellar objects at different evolutionary stages and having recently undergone processes such as accretion bursts and fragmentation need to be studied and compared.

Molecular excitation and chemistry provides an excellent tool to probe the temperature structure of a protostellar system. Using selected molecules that trace the cold and warm gas (Murillo et al. 2015, Murillo et al. subm., see chapters 3 and 4), it can be established how the gas heating is being distributed throughout the core. Relating this to the multiplicity and coevality[1] can then provide information on how temperature affects fragmentation.

This work presents single-dish observations of embedded multiple and single protostellar systems aiming to address the relation between temperature and fragmentation at the envelope scale. Sections 6.2 and 6.3 describe the source sample, and the Atacama Pathfinder EXperiment (APEX; Güsten et al. 2006) observations which probe the structure of the envelope on scales of 7000 AU, respectively. Results and analysis of the data obtained from the observations are given in sections 6.4 and 6.5, respectively. Comparison between single and multiple protostellar systems is made in section 6.6, considering evolutionary stage and whether they are located in a crowded or isolated environment. The conclusions of this work are given in section 6.7, along with the resulting insight on the temperature-fragmentation relation.

6.2 Source sample

The Perseus molecular cloud ($d = 230$ pc) large-scale structure has been well studied in continuum (e.g. Enoch et al. 2009b) and together with molecular line emission (e.g. Hatchell et al. 2005; Arce et al. 2010). The small scale structure of the region has been studied through the characterization of individual systems (e.g. Kwon et al. 2006; Hirano & Liu 2014; Ching et al. 2016). Recently, Tobin et al. (2016b) conducted an unbiased 8 mm survey of all protostars in Perseus down to 15 AU separation with the Karl G. Jansky Very Large Array (VLA). Additionally, the evolutionary stage of the protostars in the region have been characterized through the construction of spectral energy distributions (SEDs) and the parameters derived from the SEDs including *Herschel Space Observatory* PACS maps (Murillo et al. 2016, see chapter 5). Comparing the evolutionary stages of components in multiple protostellar systems, the coevality of these systems could be determined (Murillo et al. 2016, see chapter 5). Further examination of coevality, core structure and protostar distribution was done by Sadavoy & Stahler (2017), examining possible formation mechanisms. Disk kinematics of close binaries (separation $\leq$500 AU) are probed with Atacama Large Millimeter/submillimeter Array (ALMA) observations (Tobin et al. in prep.). The region has also been characterized with single-dish observations which probe the large scale structure, using both dust continuum and molecular line emission. In addition, envelopes and outflows driven by protostars in Perseus have been studied both at scales larger than 4000 AU (Davis et al. 2008; Curtis et al. 2010; Arce et al. 2010; Karska et al. 2014; Mottram et al. 2017) and below 2000 AU (Plunkett et al. 2013; Lee et al. 2016). Together, previous work provides an extensive database of the protostars in the Perseus molecular cloud.

[1] Coevality is here used as defined in Murillo et al. (2016, see chapter 5), which is the relative evolutionary stages of components in a protostellar system.

Table 1: Sample of protostellar systems

System	Component	RA	Dec	Separation (″)	Class	Region	$L_{\rm bol}$ ($L_\odot$)
			Wide multiples				
L1448N	A	03:25:36.53	+30:45:21.35	...	I	NC	5.88 ± 0.93
	B	03:25:36.34	+30:45:14.94	7.3	0		2.15 ± 0.33
	C	03:25:35.53	+30:45:34.20	16.3	0		1.22 ± 0.19
NGC1333 SVS13	A	03:29:03.75	+31:16:03.76	...	I	C	119.28 ± 18.31
	B	03:29:03.07	+31:15:52.02	14.9	0		10.26 ± 1.57
	C	03:29:01.96	+31:15:38.26	34.7	0		2.22 ± 0.34
NGC1333 IRAS5	Per63	03:28:43.28	+31:17:32.9	...	I	C	1.38 ± 0.21
	Per52	03:28:39.72	+31:17:31.9	45.7	I		0.12 ± 0.02
NGC1333 IRAS7	Per18	03:29:11.26	+31:18:31.08	...	0	C	4.77 ± 0.73
	Per21	03:29:10.67	+31:18:20.18	13.3	0		3.50 ± 0.54
	Per49	03:29:12.96	+31:18:14.31	27.5	I		0.65 ± 0.10
B1-b	S	03:33:21.30	+31:07:27.40	...	0	NC	0.32 ± 0.05
	N	03:33:21.20	+31:07:44.20	17.4	0		0.16 ± 0.05
	W	03:33:20.30	+31:07:21.29	13.9	I		0.10 ± 0.02
			Close binaries				
NGC1333 IRAS1		03:28:37.00	+31:13:27.5	1.908	I	C	11.00 ± 1.78
IRAS 03282+3035		03:31:21.00	+30:45:30.0	0.098	0	NC	1.49 ± 0.23
			Single systems				
IRAS03271+3013		03:30:15.00	+30:23:49.0	...	I	NC	1.62 ± 0.26
L1455-Per25		03:26:37.46	+30:15:28.01	...	0	NC	1.09 ± 0.17
NGC1333 SK1		03:29:00.00	+31:12:00.7	...	0	C	0.71 ± 0.11

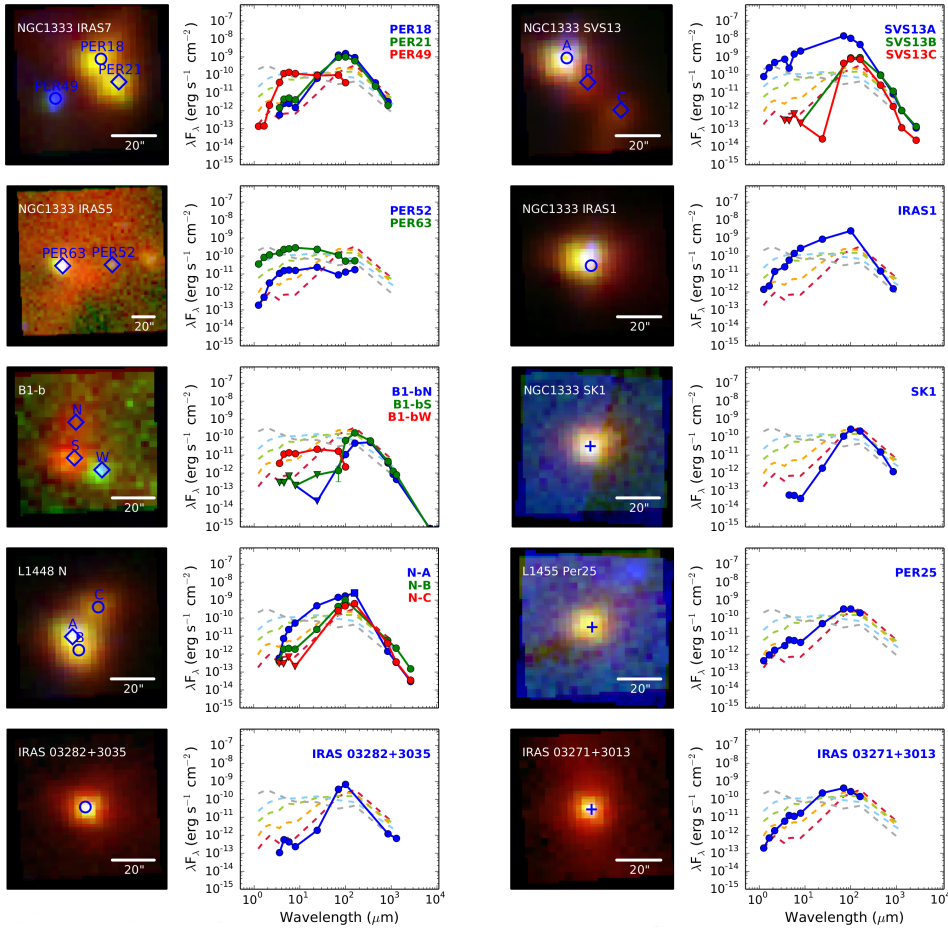

Figure 1: *Herschel* PACS stamps of the systems sampled in this work together with their respective SEDs. For the RGB stamps, 70, 100 and 160 μm are shown in blue, green and red, respectively. Each stamp spans a region of $80'' \times 80''$, except for NGC1333 IRAS5 whose components have a very wide separation. Blue symbols represent the components of a system and the positions of the APEX observations. Circles denote systems with additional unresolved multiplicity and diamonds indicating those without (known) additional multiplicity. The SEDs are overlaid on the average SEDs from Enoch et al. (2009) for reference, with early Class 0 (red), late Class 0, early Class I, late Class I and Class II (gray).

Table 2: Detected molecular species

Molecule	Transition	Frequency GHz	E_{up} K	$\log_{10} A_{ij}$
SO	5_5–4_4	215.22065	44.10	-3.92
DCO^+	3–2	216.11258	20.74	-2.62
c−C_3H_2	$3_{3,0}$–$2_{2,1}$	216.27876	19.47	-3.33
DCN	3–2	217.23863	20.85	-4.24
c−C_3H_2 [a]	6–5	217.82215	38.61	-3.23
c−C_3H_2	$5_{1,4}$–$4_{2,3}$	217.94005	35.42	-3.35
H_2CO	$3_{0,3}$–$2_{0,2}$	218.22219	20.96	-3.55
CH_3OH	$4_{2,2}$–$3_{1,2}$	218.44005	45.45	-4.33
H_2CO	$3_{2,2}$–$2_{2,1}$	218.47563	68.09	-3.80
H_2CO	$3_{2,1}$–$2_{2,0}$	218.76007	68.11	-3.80
C_2H	4–3 J=9/2–7/2 F=5–4	349.33771	41.91	-3.88
C_2H	4–3 J=9/2–7/2 F=4–3	349.33899	41.91	-3.89
C_2H	4–3 J=7/2–5/2 F=4–3	349.39927	41.93	-3.90
C_2H	4–3 J=7/2–5/2 F=3–2	349.40067	41.93	-3.92
H_2CO	$5_{1,5}$–$4_{1,4}$	351.76864	62.45	-2.92
DCO^+	5–4	360.16978	51.86	-2.42
DCN	5–4	362.04575	52.12	-3.13
HNC	4–3	362.63030	43.51	-2.64
H_2CO	$5_{0,5}$–$4_{0,4}$	362.73602	52.31	-2.86

Notes. [a] Contains both ortho- and para forms.

A sample of 10 low-mass protostellar systems in Perseus were selected from the work of Tobin et al. (2016b) and Murillo et al. (2016, see chapter 5). The sample is listed in Table 1, along with coordinates, component separations, type of region where they are located and the bolometric luminosity $L_{\rm bol}$ calculated from the SEDs. Figure 1 shows *Hersechel* PACS mini-maps of the sample along with the constructed SED from (Murillo et al. 2016, see chapter 5). Selected sources are young embedded protostars in the Class 0 and I evolutionary stages. Both single and multiple protostellar systems (i.e. binary and higher order multiples) are included, with the multiple systems spanning a range of separations from $\sim$0.1″ to 46″. Thus, both close and wide multiple protostellar systems are considered in this study. Finally, the sources are located in both clustered (NGC1333) and non-clustered regions (L1448, L1455 and B1). Selecting sources from both clustered and non-clustered regions (34 and 6 YSO pc^{-2}, respectively; Plunkett et al. 2013) allows to study if factors such as external heating have an impact on the measure gas temperature.

This sample then allows the evolutionary stage, multiplicity, and region to be compared with the envelope gas temperature. Since the temporal evolution of the temperature structure of a protostar cannot be probed, protostellar sources in Class 0 and I evolutionary stages need to be compared, as well as singles and multiple protostellar systems. Evolutionary classes are determined based on the shape of the SED, derived parameters such as bolometric temperature $T_{\rm bol}$, and the structure of the system (e.g. envelope, outflow opening angle). Thus, the temperature-multiplicity-age relation can be studied, which can in turn provide constraints to hydrodynamical models with radiative feedback.

6.3 Observations

APEX observations of our source sample were carried out with the SHeFi Heterodyne instrument in position switching mode. The APEX-1 band was used for observations on 1 December 2016 with PWV $\sim$ 1.6 mm (O-098.F-9320B.2016, NL GTO time) using one spectral setting with the central frequency set to 217.11258 GHz and a bandwidth of 4 GHz. This setting targeted the molecules DCO^+, DCN, c$-C_3H_2$ and H_2CO. In addition, SO and CH_3OH were detected. Typical noise levels for the observations ranged between 15 to 70 mK for a channel width of 0.4 km s^{-1} and a HPBW of 28.7″. The beam efficiency $\eta_{\rm mb}$ for observations at 230 GHz is 0.75. APEX-2 band observations were carried out from 7 to 12 July 2017 with PWV between 0.37 and 1.5 mm (M-099.F-9516C-2017) using two spectral settings with central frequencies of 350.33746 and 361.16978 GHz, and bandwidth of 4 GHz. The molecules targeted were C_2H, DCO^+, DCN and H_2CO. HNC was also detected. Typical noise levels range from 20 to 100 mK for a channel width of 0.4 km s^{-1}, a HPBW of 18 ″ and $\eta_{\rm mb}$ = 0.73. For both bands, calibration uncertainties are on the order of 20%. The molecules targeted in these observations (Table 2) probe the cold and warm gas of the envelope at scales of 7000 AU and temperature range of 20 to 100 K.

6.4 Results

The observed molecular lines trace the cold and warmer envelope gas of the systems in our sample. For the multiple protostellar systems, single pointing observations for

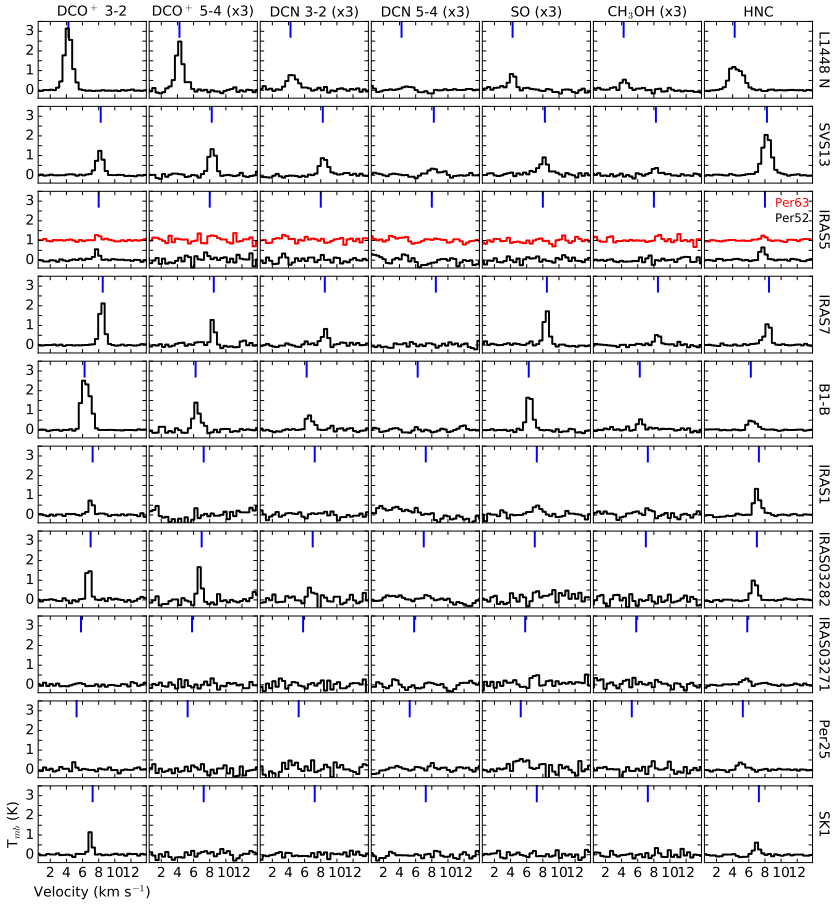

Figure 2: APEX single pointing observations of DCO^+, DCN, SO, CH_3OH and HNC. Except for DCO^+ and HNC, the spectra are multiplied by a factor of 3 to make the features more prominent. The spectra for the wide multiple systems are averaged for all the components, except for NGC1333 IRAS5. The vertical blue line marks the systemic velocity.

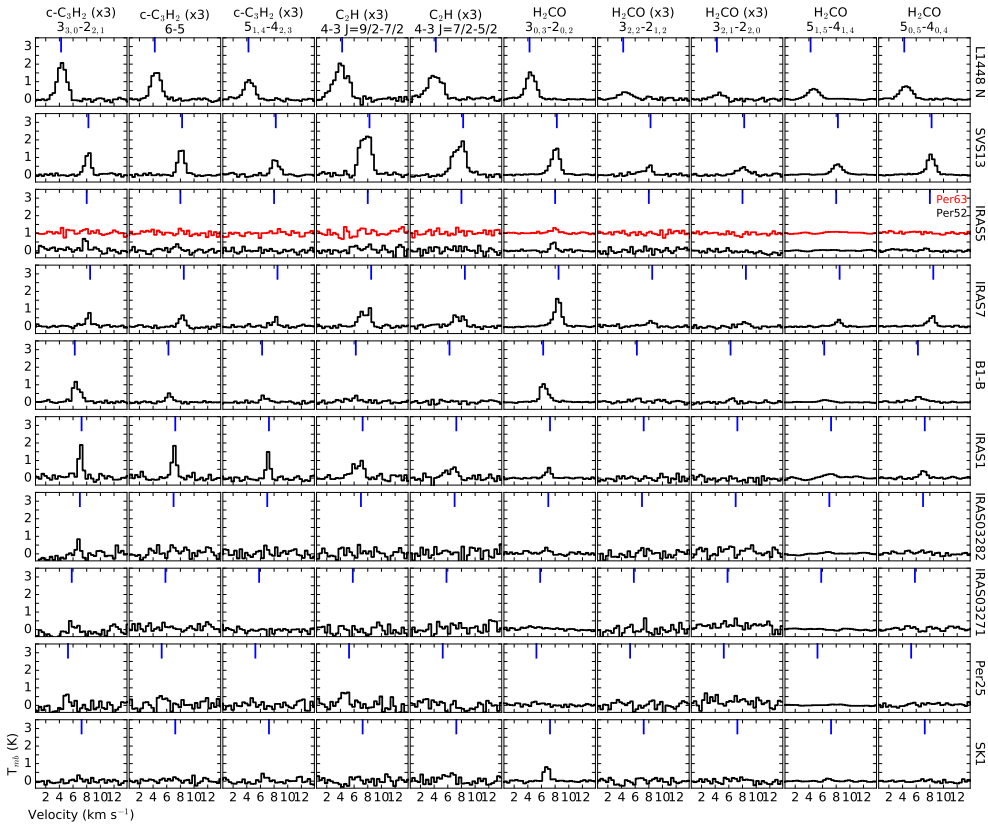

Figure 3: Same as Fig. 2 but for c−C_3H_2, C_2H and H_2CO.

each component were taken, however the beams of the observations (28 and 18″) are comparable to the component separations and the spectra of the individual components in a wide multiple system are very similar. As an example, the spectra of the individual components for NGC1333 IRAS7 is shown in Appendix 6.A. Thus the spectra of all three components in the wide multiple systems are averaged together, except for NGC1333 IRAS5 which has a separation of 45.7″ and is treated in this work as two separate single protostars Per63 and Per52. The results of the averaged spectra are discussed and analyzed in this work. Figures 2 and 3 show the resulting spectra for all the systems in our sample. Observed line peaks are listed in Tables 3 to 8, while the measured line widths and integrated fluxes can be found in Appendix 6.B.

HNC was detected toward all the systems in the sample (Fig. 2), however the other observed molecules were not always detected. Three out of the five wide multiple protostellar systems show detections with signal-to-noise (S/N) above 3 for a channel width of 0.4 km s^{-1} in all targeted molecular lines. B1-b, also a wide multiple system, shows above 3σ detections in all lines except H_2CO $3_{2,2}$–$2_{1,2}$, DCN 5–4 and C_2H 4–3 J=7/2–5/2. SO and CH_3OH were detected toward four wide multiple systems. IRAS5 Per63 has detections above 3σ only in DCO^+ 3–2, H_2CO $3_{0,3}$–$2_{0,2}$ and H_2CO $5_{0,5}$–$4_{0,4}$. In contrast, IRAS5 Per52 presents detections in DCO^+ 3–2, c−C_3H_2 3–2 and 6–5, and H_2CO $3_{0,3}$–$2_{0,2}$.

The close binary system NGC1333 IRAS 1 presents emission with S/N>3 in SO, DCO^+ 3–2, all transitions of the warm molecules c−C_3H_2 and C_2H, as well as H_2CO $3_{0,3}$–$2_{0,2}$. In contrast, IRAS03282+3035 presents emission only in both transitions of DCO^+, DCN 3–2 and H_2CO $3_{0,3}$–$2_{0,2}$.

The single protostellar systems show little to no emission. NGC1333 SK1 presents emission above 3σ in DCO^+ 3–2, H_2CO $3_{0,3}$–$2_{0,2}$ and H_2CO $5_{0,5}$–$4_{0,4}$; while L1455-Per25 shows only DCO^+ 3–2 emission. The other single protostar, IRAS03271+3013, presented no detection beyond HNC. This might be due to the protostar bieng a Class I protostar, howver, NGC1333 IRAS 1 and both components of NGC1333 IRAS5 are also Class I objects but show more line detections than IRAS03271+3013.

For all systems, DCO^+ presents strong emission (Fig. 2), suggesting cold envelope gas since DCO^+ is a good cold gas tracer. The low-lying transition of H_2CO is the strongest among the five transitions (Fig. 3), with peaks a factor of ∼10 higher than the higher-lying transitions. The peak intensities of c−C_3H_2 (Fig. 3), on the other hand, vary by less than a factor of 3 among all three transitions. The different systemic velocities of each region within Perseus are reflected in the observed spectra. For the systems located in NGC1333, there is also a slight difference in the systemic velocity among the sources located closer to the cluster center (NGC1333 SVS13, NGC1333 IRAS7 and NGC1333 IRAS5; $v_{\rm LSR}$ = 8.0–8.5 km s^{-1}) and those located in the outer part of the cluster (NGC1333 IRAS1 and NGC1333 SK1; $v_{\rm LSR}$ ∼ 7.3 km s^{-1}).

The molecules CH_3OH and SO trace shocks (Fig. 2), since CH_3OH ice and sulfur are sputtered off the grains back into the gas phase in shocked regions. DCO^+ and the low-lying transition of H_2CO, $3_{0,3}$–$2_{0,2}$, trace cold envelope gas. DCO^+ is formed from the reaction of H_2D^+ + CO, with H_2D^+ greatly enhanced at low temperatures. Furthermore, the presence of strong H_2CO in the low-lying transition but not in the other higher-lying transitions would suggest that the envelope gas is cold and not being currently heated. This is consistent toward all the observed systems. On the other hand, DCN is a warm gas tracer and can be formed and fractionated through a higher temperature route starting with CH_2D^+. Similarly to DCN, the higher-lying

transitions of H_2CO also trace warm gas. c$-C_3H_2$ and C_2H trace the warm irradiated gas, most likely located along the outflow cavity.

6.5 Analysis

The observed molecular line emission is compared to system luminosity and envelope mass in this section. Bolometric luminosity $L_{\rm bol}$ is obtained from the SEDs of the observed sources, with $L_{\rm bol}$ for the wide multiple systems derived from the combined SEDs (Murillo et al. 2016, see chapter 5). Envelope mass, listed in Table 9, is calculated from the 850μm flux and $L_{\rm bol}$ using the correction from Jørgensen et al. (2009) expressed as:

$$M_{\rm env} = 0.44 M_\odot \left(\frac{L_{\rm bol}}{1\ L_\odot}\right)^{-0.36} \left(\frac{S_{850\mu m}}{1\ {\rm Jy\ beam^{-1}}}\right)^{1.2} \left(\frac{d}{125\ {\rm pc}}\right)^{1.2}. \quad (6.1)$$

The 850μm flux used in this work is measured from the COMPLETE survey map for all of Perseus taken with JCMT using SCUBA (Kirk et al. 2006), which has a beam of 15″. The flux was measured with a circular region of 28.7″ (HPBW of the APEX-1 observations) centered on each source. For the wide multiple systems, the total flux of all 3 components is used. In addition, the observed line emission is comapred to the ratio of envelope mass to $L_{\rm bol}$ ($M_{\rm env}/L_{\rm bol}$), listed in Table 9. This ratio gives insight into the mass being heated by the central source. A protostar with a certain $L_{\rm bol}$ has more to heat with a massive envelope than with a less massive one.

6.5.1 Cold and warm gas

Figure 4, 5 and 6 show the line peaks versus envelope mass, bolometric luminosity $L_{\rm bol}$ and envelope mass to $L_{\rm bol}$ ratio $M_{\rm env}/L_{\rm bol}$. System type (wide multiple, close binary and single protostar) are indicated in the plots with different symbols in order to determine if there is any relation with respect to line emission or system parameters. For systems with molecular line non-detections, the upper limits in the plots are placed at 3σ. A linear fit to the data is used to identify trends in between the observed line emission peaks and source parameters.

Peak intensities are compared with the envelope mass in Fig. 4. The peak intensities of H_2CO $3_{0,3}$–$2_{0,2}$, both H_2CO 5–4 transitions, and both transitions of DCO^+ increase with envelope mass. Wide multiple systems have larger envelope masses than the close binaries and single protostars, with the exception of NGC1333 IRAS5, where Per63 and Per52 have envelope masses comparable to single protostars. This can be interpreted as wide multiple systems having massive reservoirs of cold gas compared to close binaries and single protostellar systems. On the other hand, the warm gas being traced by DCN and the two higher-lying transitions of H_2CO 3–2 do not show dependency on the envelope mass, degree of multiplicity or region type. Instead the line peaks are practically constant with envelope mass. Methanol, SO and the three transitions of c$-C_3H_2$ also do not show particular dependency on envelope mass either.

Figure 5 shows the observed line peak intensities compared with $L_{\rm bol}$. The warm molecules c$-C_3H_2$ and C_2H appear to be associated with $L_{\rm bol}$. Since these molecules are generally formed in irradiated regions, the correlation between c$-C_3H_2$ and C_2H and $L_{\rm bol}$ can be explained by the outflow cavity being irradiated by the central protostar. Thus, the more luminous the central protostar, the deeper the outflow cavity

Table 3: Peak antenna temperatures for DCO^+ and DCN

System	DCO^+ 3–2			DCO^+ 5–4			DCN 3–2			DCN 5–4		
	T_{mb} mK	Noise mK	S/N	T_{mb} mK	Noise mK	S/N	T_{mb} mK	Noise mK	S/N	T_{mb} mK	Noise mK	S/N
Wide multiples												
L1448N	3160	31	103	811	33	25	267	25	11	69	23	3
SVS13	1213	23	54	461	31	15	293	25	12	103	28	4
Per63	333	40	8	...	54	...	...	40	...	...	36	...
Per52	560	37	15	...	54	...	...	39	...	...	47	...
IRAS7	2267	27	85	468	33	14	267	24	11	...	37	...
B1-b	2627	21	123	446	30	15	253	19	14	...	30	...
Close binaries												
IRAS1	800	43	19	...	81	...	...	40	...	...	64	...
IRAS03282	1933	73	26	567	56	10	200	67	3	...	50	...
Singles												
IRAS03271	...	71	...	...	43	...	...	69	...	...	41	...
Per25	480	67	7	...	52	...	...	83	...	...	40	...
SK1	1173	37	31	...	53	...	...	40	...	...	40	...

Table 4: Peak antenna temperatures for SO, CH_3OH and HNC

System	SO 5_5–4_4			CH_3OH $4_{2,2}$–$3_{1,2}$			HNC 4–3		
	T_{mb} mK	Noise mK	S/N	T_{mb} mK	Noise mK	S/N	T_{mb} mK	Noise mK	S/N
Wide multiples									
L1448N	280	27	11	187	23	8	1219	24	51
SVS13	253	23	11	120	21	6	2070	26	81
Per63	...	35	...	...	40	...	256	46	6
Per52	...	45	...	...	39	...	667	40	17
IRAS7	600	23	26	187	23	8	1120	30	37
B1-b	627	21	29	187	23	8	490	24	20
Close binaries									
IRAS1	147	39	4	...	39	...	1284	58	22
IRAS03282	...	67	...	...	71	...	1030	44	23
Singles									
IRAS03271	...	77	...	...	60	...	324	47	7
Per25	...	75	...	...	65	...	370	38	10
SK1	...	39	...	...	40	...	611	46	13

Table 5: Peak antenna temperatures for $c-C_3H_2$

System	$3_{3,0}$–$2_{2,1}$			6—5			$5_{1,4}$–$4_{2,3}$		
	T_{mb} mK	Noise mK	S/N	T_{mb} mK	Noise mK	S/N	T_{mb} mK	Noise mK	S/N
Wide multiples									
L1448N	693	25	27	533	25	21	373	23	16
SVS13	440	23	19	507	19	27	293	23	13
Per63	...	47	...	...	35	...	...	40	...
Per52	320	40	8	121	36	3	...	35	...
IRAS7	267	24	11	213	24	9	200	20	10
B1-b	360	23	16	160	19	9	107	19	6
Close binaries									
IRAS1	667	44	15	613	40	15	493	33	15
IRAS03282	...	68	...	...	61	...	...	55	...
Singles									
IRAS03271	...	97	...	...	61	...	...	56	...
Per25	...	87	...	...	69	...	...	59	...
SK1	...	35	...	...	47	...	...	40	...

Table 6: Peak antenna temperatures for C_2H

System	4-3 J=9/2 – 7/2 f=5-4			4-3 J=9/2 – 7/2 f=4-3			4-3 J=7/2 – 5/2 f=4-3			4-3 J=7/2 – 5/2 f=3-2		
	T_{mb} mK	Noise mK	S/N	T_{mb} mK	Noise mK	S/N	T_{mb} mK	Noise mK	S/N	T_{mb} mK	Noise mK	S/N
Wide multiples												
L1448N	412	53	8	263	53	5	254	46	6	229	46	5
SVS13	742	35	21	608	35	18	594	29	20	431	29	15
Per63	...	49	...	...	49	...	...	50	...	...	50	...
Per52	...	56	...	...	56	...	...	53	...	...	53	...
IRAS7	335	24	14	276	24	11	208	29	7	221	29	8
B1-b	126	24	5	84	24	4	...	25	...	...	25	...
Close binaries												
IRAS1	337	39	9	258	39	7	215	37	6	138	37	4
IRAS03282	...	78	...	...	78	...	0	81	...	...	81	...
Singles												
IRAS03271	...	92	...	...	92	...	0	89	...	...	89	...
Per25	...	97	...	...	97	...	0	88	...	...	88	...
SK1	...	60	...	...	60	...	0	63	...	...	63	...

Table 7: Peak antenna temperatures for H_2CO 3–2

System	$3_{0,3}$–$2_{0,2}$			$3_{2,2}$–$2_{2,1}$			$3_{2,1}$–$2_{2,0}$		
	T_{mb} mK	Noise mK	S/N	T_{mb} mK	Noise mK	S/N	T_{mb} mK	Noise mK	S/N
Wide multiples									
L1448N	1520	23	67	132	24	6	109	23	5
SVS13	1520	27	57	147	20	7	132	21	6
Per63	253	37	7	...	40	...	...	32	...
Per52	533	40	13	...	40	...	...	37	...
IRAS7	1587	27	60	97	21	5	80	23	4
B1-b	1040	19	56	...	24	...	84	19	5
Close binaries									
IRAS1	573	36	16	...	45	...	...	41	...
IRAS03282	320	60	5	...	73	...	...	61	...
Singles									
IRAS03271	...	69	...	...	64	...	...	107	...
Per25	...	73	...	...	69	...	...	73	...
SK1	880	43	21	...	35	...	...	41	...

Table 8: Peak antenna temperatures for H_2CO 5–4

System	$5_{1,5}$-$4_{1,4}$			$5_{0,5}$-$4_{0,4}$		
	T_{mb} mK	Noise mK	S/N	T_{mb} mK	Noise mK	S/N
Wide multiples						
L1448N	595	21	28	758	40	19
SVS13	594	23	26	1130	27	41
Per63	...	55	...	82	29	3
Per52	...	40	...	...	48	...
IRAS7	374	33	11	568	32	18
B1-b	127	19	7	252	25	10
Close binaries						
IRAS1	230	57	4	423	41	10
IRAS03282	...	42	...	...	92	...
Singles						
IRAS03271	...	36	...	...	90	...
Per25	...	28	...	...	69	...
SK1	161	40	4	...	62	...

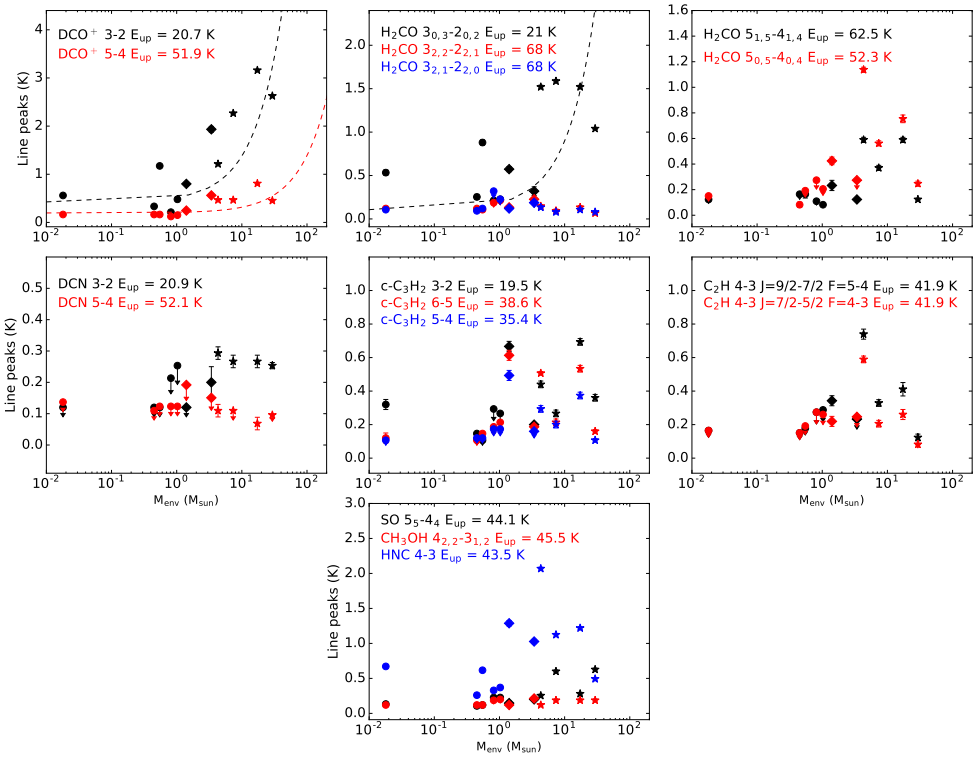

Figure 4: Peak intensities of the observed molecular lines compared to the envelope mass ($M_\odot$) of each source. The dashed lines are linear fits to the data for the cases where a correlation is found. Circles, diamonds and stars show single, close binary and wide multiple protostellar systems, respectively. Note that the more massive envelopes show an increase in the peak intensities of DCO^+ and the low-lying transition of H_2CO, which trace cold gas in the envelope. Molecules tracing warm gas have similar peak intensities regardless of envelope mass.

Table 9: Source parameters

System	850μm flux Jy	$M_{\rm env}$ $M_\odot$	$L_{\rm bol}$ $L_\odot$	$M_{\rm env}$ / $L_{\rm bol}$ $M_\odot$ / $L_\odot$
Wide multiples				
L1448N	25.06	17.30	13.08	1.32
SVS13	15.34	4.31	121.07	0.04
Per63	0.61	0.45	1.38	0.33
Per52	0.02	0.02	0.12	0.15
IRAS7	10.97	7.37	8.92	0.83
B1-b	15.38	29.38	0.59	49.80
Close binaries				
IRAS1	2.94	1.41	11.0	0.13
IRAS 03282	3.37	3.40	1.49	2.28
Singles				
IRAS03271	1.05	0.82	1.62	0.50
Per25	1.13	1.03	1.09	0.94
SK1	0.59	0.55	0.71	0.77

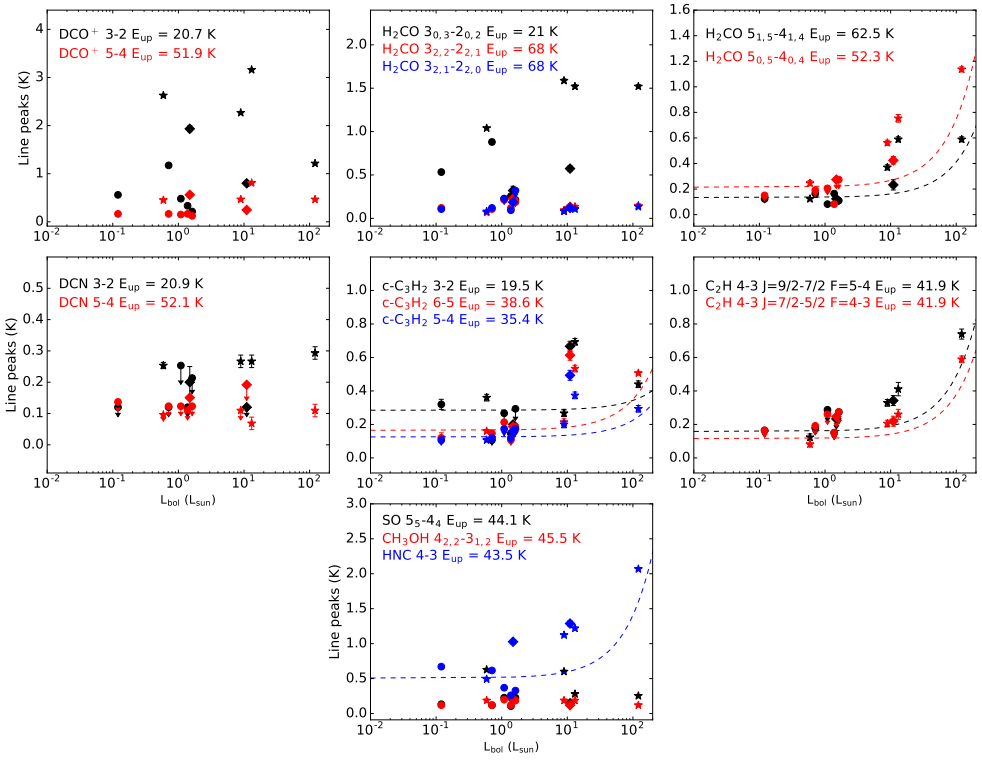

Figure 5: Peak intensities of the observed molecular lines compared to the bolometric luminosity $L_{\rm bol}$ ($L_\odot$) of each source. The dashed lines are linear fits to the data for the cases where a correlation is found. Circles, diamonds and stars show single, close binary and wide multiple protostellar systems, respectively. C_2H and c$-C_3H_2$ show somewhat higher peak intensities in sources with relatively higher luminosities.

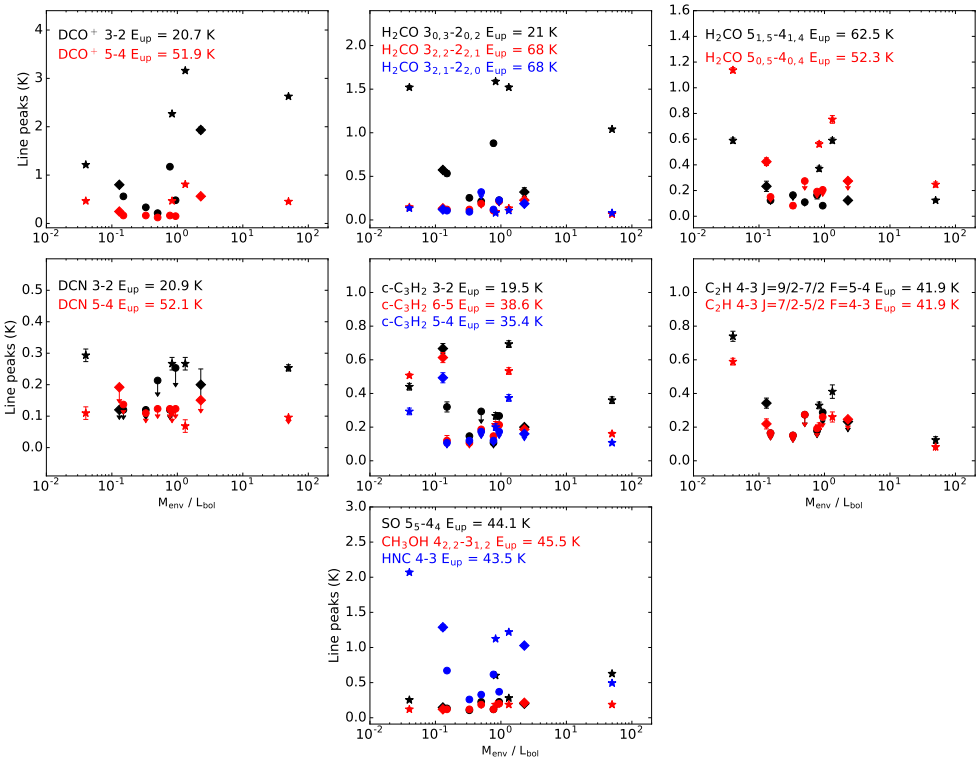

Figure 6: Peak intensities of the observed molecular lines compared to the envelope mass to luminosity ratio of each source. Circles, diamonds and stars show single, close binary and wide multiple protostellar systems, respectively.

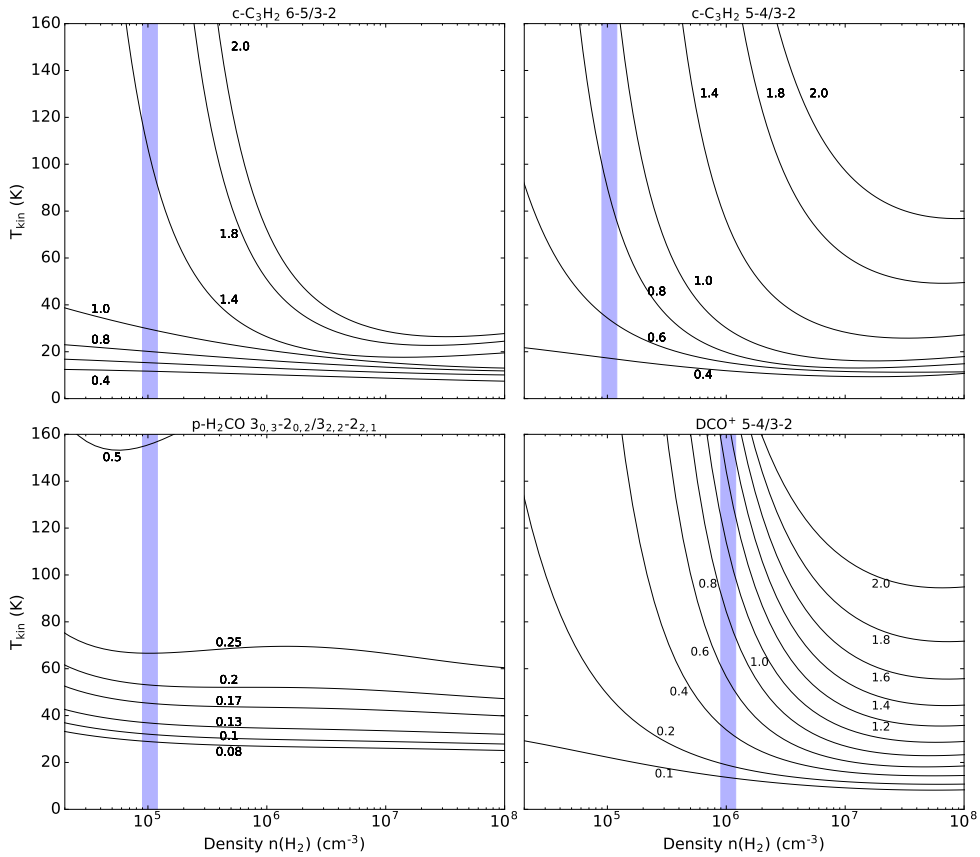

Figure 7: Calculated line ratios for c$-C_3H_2$ 6–5 / $3_{3,0}$–$2_{2,1}$ (left) and $5_{1,4}$–$4_{2,3}$ / $3_{3,0}$–$2_{2,1}$ (center), and H_2CO $3_{0,3}$–$2_{0,2}$ / $3_{2,2}$–$2_{2,1}$. The black lines show the modelled ratios assuming a column density of 10^{12} cm^{-2}. Lines between the 0.4 and 1.0 ratios of c$-C_3H_2$, are spaced evenly in steps of 0.2. The shaded area indicates the adopted H_2 density for the temperature calculations.

is irradiated and more c$-C_3H_2$ and C_2H is produced. The two transitions of H_2CO 5–4 and HNC also show relation to $L_{\rm bol}$. The other molecules do not present any correlation to bolometric luminosity, not even SO and CH_3OH which are expected to trace shocks, or the higher transitions of H_2CO 3–2 which tracer warmer gas.

Figure 6 presents the peak line intensities compared with $M_{\rm env}/L_{\rm bol}$. There appears to be no relation between any of the observed molecular line peaks and $M_{\rm env}/L_{\rm bol}$. This indicates that when the amount of mass being illuminated, and thus heated, by the central protostellar system is taken into account, the observed protostellar systems present similar molecular line intensities.

These results could be summarized as follows. The bulk of the cold envelope gas is traced by DCO^+ and H_2CO $3_{0,3}$–$2_{0,2}$ while the warm gas is traced by DCN and the two higher-lying transitions of H_2CO. c$-C_3H_2$ and C_2H trace the warm irradiated outflow cavity, rather than envelope material.

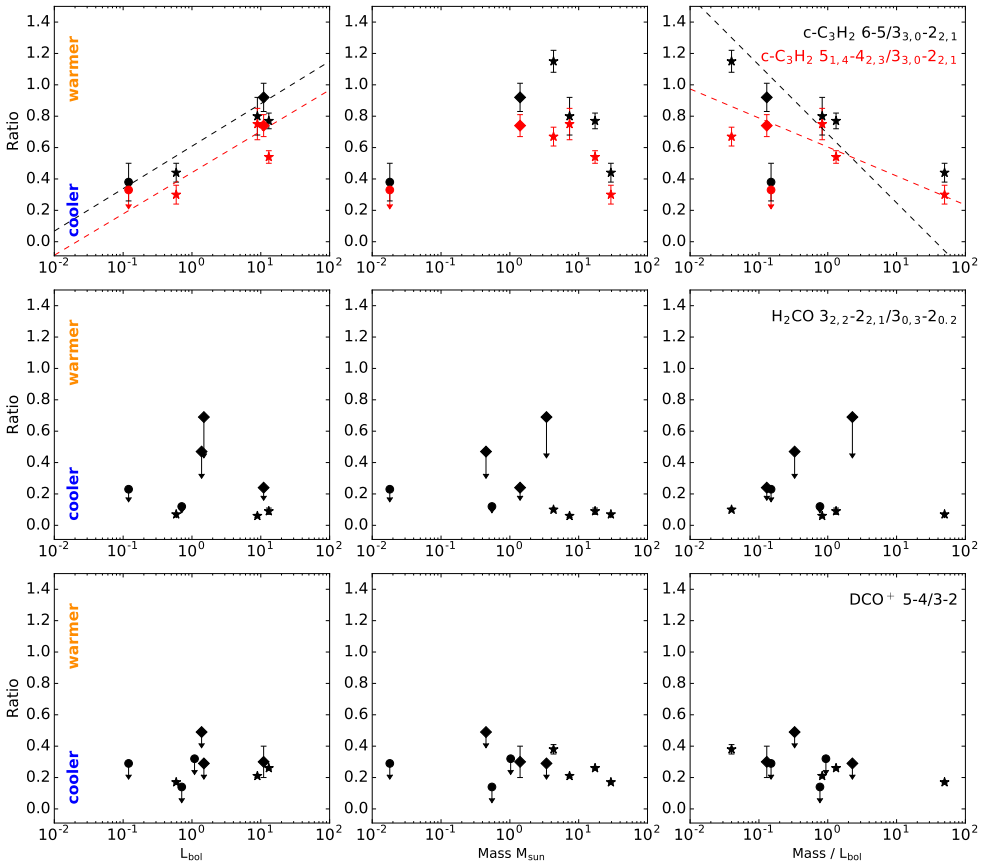

Figure 8: Calculated molecular line ratios of c$-C_3H_2$ (top row), H_2CO (middle row) and DCO^+ (bottom row) compared to the source parameters bolometric luminosity L_{bol} (left column), envelope mass M_{env} (middle column) and the envelope mass to luminosity ratio (right column). The dashed lines in the top row are linear fits to the data. Circles, diamonds and stars show single, close binary and wide multiple protostellar systems, respectively. The c$-C_3H_2$ ratios appear to be somewhat related to luminosity, whereas the ratios from H_2CO and DCO^+ are constant regardless of source parameter.

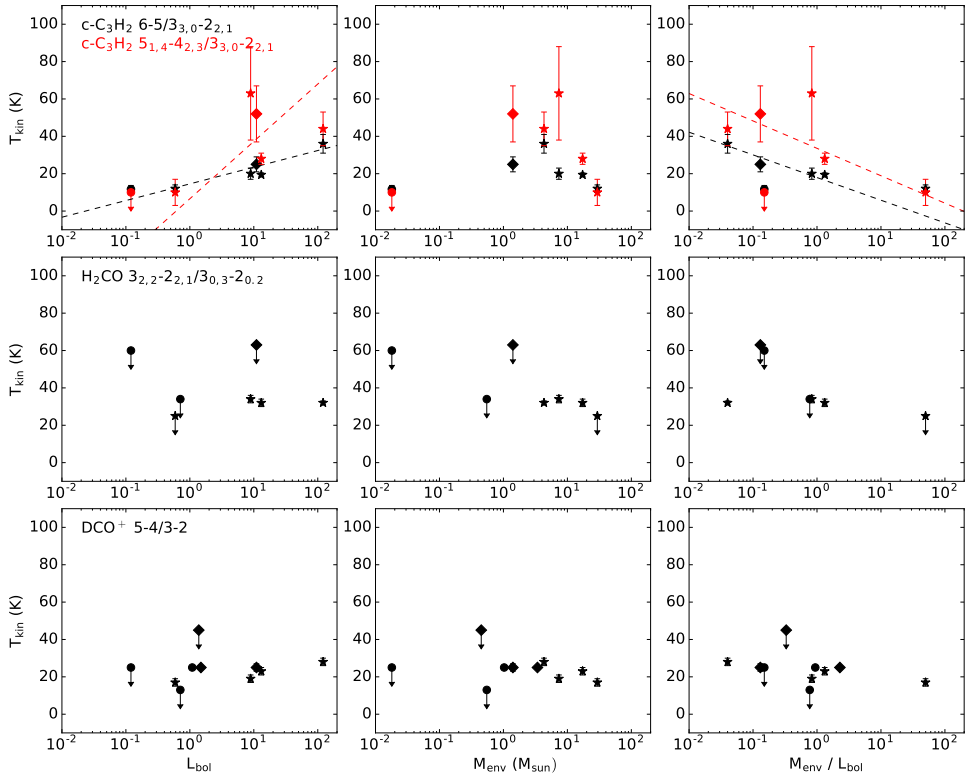

Figure 9: Kinetic temperature derived from c$-C_3H_2$ and H_2CO ratios compared to the source parameters bolometric luminosity L_{bol} (left column), envelope mass M_{env} (middle column) and the envelope mass to luminosity ratio (right column). Dashed lines show the best linear fit. Circles, diamonds and stars show single, close binary and wide multiple protostellar systems, respectively.

6.5.2 Line ratios and implied physical conditions

Since several transitions of c$-C_3H_2$ and H_2CO are present, as well as two transitions of DCO^+, we can probe the gas temperature structure. The ratio of DCN/DCO^+ can be used to compare the warm (DCN) and cold gas (DCO^+) from the envelope. The line ratios of c$-C_3H_2$, H_2CO, DCO^+ and DCN/DCO^+ are listed in Table 10. While two transitions of DCN were observed, ratios can only be obtained for half the systems, of which three are upper limits. These ratios are thus also listed in Table 10 but not further discussed. The variation of the c$-C_3H_2$, H_2CO and DCO^+ ratios with H_2 density and temperature is shown in Fig. 7. Ratios are not calculated for the systems with non-detections in both transitions used in the ratio (Tables 3, 5 and 7) and are thus not considered in the following analysis (Table 10). Upper limits are given when one of the transitions is a non-detection (Table 10), and are not considered for the linear fits but are shown in the figures for reference.

Figure 8 compares the calculated ratios with envelope mass M_{env}, bolometric luminosity L_{bol}, and M_{env}/L_{bol}. With respect to L_{bol}, both ratios of c$-C_3H_2$ show good correlation with luminosity. The H_2CO and DCN/DCO^+ ratios, on the other hand,

do not. c$-C_3H_2$ is the only molecule which shows an anti-correlation with $M_{\rm env}/L_{\rm bol}$.

Kinetic temperature is derived from the c$-C_3H_2$, H_2CO and DCO^+ ratios, and listed in Table 11. An H_2 density n_{H_2} of 10^5 cm^{-3}, typical in the envelopes of embedded protostellar objects on the scales of the beam, is considered for the c$-C_3H_2$ and H_2CO calculations. For DCO^+, an H_2 density of n_{H_2} of 10^6 cm^{-3} is used, since this value has been found in single dish observations toward other embedded protostars (Murillo et al. subm.). A column density of 10^{12} cm^{-2} is adopted for the line ratio calculations, ensuring that the lines are optically thin.

Both c$-C_3H_2$ ratios point to gas temperatures between 10 and 60 K (Fig. 9). Considering $n_{H_2} = 10^6$ cm^{-3}, lowers the derived temperatures to a range between 8 and 30 K for both transitions. The obtained kinetic temperatures appear to have no relation with the envelope mass, but in contrast, do seem to have a correlation with $L_{\rm bol}$, and an anti-correlation with the $M_{\rm env}/L_{\rm bol}$ ratio (Fig. 9). This is consistent with what is found when comparing the ratios with $L_{\rm bol}$ and $M_{\rm env}/L_{\rm bol}$ (Fig. 8). These results suggest that c$-C_3H_2$ is dependent on the central protostellar source luminosity and the amount of surrounding gas (Fig. 9). This makes sense if it is considered that c$-C_3H_2$ traces the outflow cavity, which is irradiated by the central protostar. At the same time, however, higher temperatures are traced by c$-C_3H_2$ if the envelope mass is lower, since less material needs to be heated than in the case of higher envelope mass. The separation of the components in multiple systems or their coevality does not show any effect on the temperature traced by the c$-C_3H_2$ ratio. While there is no difference in temperature between close binaries and wide multiples, the effect of multiplicity, on the other hand, cannot be fully determined, since none of the single protostars in our sample present c$-C_3H_2$ detections.

Temperatures obtained from the H_2CO ratio range between 20 and 60 K. Considering higher n_{H_2}, alters the temperature by only a few degrees for ratios above 4, otherwise the temperature stays mainly constant. In contrast to the kinetic temperatures obtained from the c$-C_3H_2$ ratio, temperatures derived from the H_2CO ratio show no relation with respect to either envelope mass, $L_{\rm bol}$ or $M_{\rm env}/L_{\rm bol}$ (Fig. 9). Similarly, DCO^+ suggests temperatures between 10 to 45 K, showing no relation to bolometric lumnosity, envelope mass or their ratio. In fact, temperatures derived from the H_2CO and DCO^+ ratios seem to vary little with any source parameters. System type, region and evolutionary stage do not present any correlation either (Fig. 9). Thus, all embedded protostars appear to have envelope gas with similar, and relatively cold, temperatures regardless of their multiplicity.

6.5.3 Statistical analysis

In order to determine if there is a relation between the observed line peaks and derived quantities, and the source parameters, the Generalized Kendall's rank correlation is used (Isobe et al. 1986). This method measures the degree of association between two quantities which contain upper limits (censored data), with the null hypothesis being that the values are uncorrelated. Thus, if the significance level $p > 0.05$, the values are uncorrelated, while $p < 0.05$ indicates correlated values. The standard normal score z and the significance level p of the Generalized Kendall's rank correlation are listed in Table 12. The significance level is calculated from the standard normal score z by the relation

$$p = 1 - 0.5(1 + erf\left(\frac{|z|}{\sqrt{2}}\right)) \tag{6.2}$$

Table 10: Line ratios

System	c$-C_3H_2$ 6–5 / $3_{3,0}$–$2_{2,1}$	c$-C_3H_2$ $5_{1,4}$–$4_{2,3}$ / $3_{3,0}$–$2_{2,1}$	H_2CO $3_{2,2}$–$2_{2,1}$ / $3_{0,3}$–$2_{0,2}$	DCO^+ 5–4/3–2	DCN 5–4/3–2	DCN/DCO^+ 3–2
Wide multiples						
L1448N	0.77 ± 0.05	0.54 ± 0.04	0.09 ± 0.02	0.26 ± 0.01	0.26 ± 0.09	0.08 ± 0.01
SVS13	1.15 ± 0.07	0.67 ± 0.06	0.1 ± 0.01	0.38 ± 0.03	0.35 ± 0.10	0.24 ± 0.02
Per63	...	...	<0.47	< 0.49	...	<0.36
Per52	0.38 ± 0.12	<0.33	<0.23	< 0.29	...	<0.21
IRAS7	0.8 ± 0.12	0.75 ± 0.1	0.06 ± 0.01	0.21 ± 0.01	< 0.41	0.12 ± 0.01
B1-b	0.44 ± 0.06	0.3 ± 0.06	<0.07	0.17 ± 0.01	< 0.35	0.1 ± 0.01
Close binaries						
IRAS1	0.92 ± 0.09	0.74 ± 0.07	<0.24	0.30 ± 0.10	...	<0.15
IRAS03282	...	...	<0.69	< 0.29	< 0.76	0.1 ± 0.03
Singles						
IRAS03271	...	...	...	...	...	...
Per25	...	...	...	< 0.32	...	<0.52
SK1	...	...	<0.12	< 0.14	...	<0.1

Table 11: Derived $T_{\rm kin}$ from line ratios

System	c$-C_3H_2$ [a] $6–5/3_{3,0}–2_{2,1}$ $T_{\rm kin}$ (K)	c$-C_3H_2$ [a] $5_{1,4}–4_{2,3}/3_{3,0}–2_{2,1}$ $T_{\rm kin}$ (K)	H_2CO [a] $3_{2,2}–2_{2,1}/3_{0,3}–2_{0,2}$ $T_{\rm kin}$ (K)	DCO^+ [b] 5–4/3–2 $T_{\rm kin}$ (K)
Wide multiples				
L1448N	19 ± 2	28 ± 3	32 ± 2	23 ± 2
SVS13	36 ± 5	44 ± 9	32 ± 1	28 ± 2
Per63	...	...	<150	<45
Per52	12 ± 2	<10	<60	<25
IRAS7	20 ± 3	63 ± 25	34 ± 2	19 ± 2
B1-b	12 ± 2	10 ± 7	<25	17 ± 2
Close binaries				
IRAS1	25 ± 4	52 ± 15	<63	25 ± 2
IRAS03282	...	...	<180	<25
Singles				
IRAS03271	...	...	...	...
Per25	...	...	...	<25
SK1	...	...	<34	<13

Notes. [a] Assuming a H_2 density of 10^5 cm^{-3} [b] Assuming a H_2 density of 10^6 cm^{-3}

where $erf(x)$ is the error function.

The results show some interesting statistically significant correlations (Table 12). The peak intensities of the molecules tracing cold gas, namely DCO^+ and H_2CO are associated with source envelope mass, but not with luminosity. On the other hand, the peak intensities of c$-C_3H_2$ and C_2H, both tracers of warm gas, are correlated with luminosity but not source envelope mass. The ratio of c$-C_3H_2$ shows correlations with source luminosity, but not envelope mass. The kinetic temperature $T_{\rm kin}$ derived from the H_2CO shows a correlation with envelope mass, while $T_{\rm kin}$ derived from c$-C_3H_2$ presents a relation to luminosity.

6.6 Discussion

6.6.1 Observed line detections

The observations present a tendency for wide multiple protostellar systems (separations >7″) to have more molecular line detections with strong peak intensities than close binaries (Fig. 10). In contrast, single protostars present very weak molecular line emission. NGC1333 IRAS5, is considered as two separate systems, Per63 and Per52, since the HPBW is smaller than the separation of the components.

There is no apparent relation between the bolometric luminosity $L_{\rm bol}$ and the number of line detections (Fig. 10a). The systems L1448 N, NGC1333 IRAS7 and NGC1333 SVS13, which have combined bolometric luminosities above 10 $L_\odot$, show strong detections of all the molecular species. NGC1333 IRAS1 also has a bolometric luminosity of 11 $L_\odot$ but only five line detections. B1-b exhibits strong line detections despite having a combined bolometric luminosity of less than 1 $L_\odot$. The remaining

Table 12: Results of the Generalized Kendall Correlation

Molecule	Transition	Mass		$L_{\rm bol}$		Mass / $L_{\rm bol}$	
		z	p	z	p	z	p
		Peaks					
SO	5_5–4_4	3.12	**0.00**	0.94	0.17	1.25	0.11
DCO^+	3–2	2.88	**0.00**	0.54	0.29	1.32	0.09
c$-C_3H_2$	$3_{3,0}$–$2_{2,1}$	1.41	0.08	1.56	0.06	-0.62	0.27
DCN	3–2	2.33	**0.01**	1.85	**0.03**	0.89	0.19
c$-C_3H_2$	6–5	1.96	**0.03**	2.58	**0.00**	-0.08	0.47
c$-C_3H_2$	$5_{1,4}$–$4_{2,3}$	1.57	0.06	3.30	**0.00**	-0.63	0.26
H_2CO	$3_{0,3}$–$2_{0,2}$	1.87	**0.03**	0.94	0.17	0.00	0.50
CH_3OH	$4_{2,2}$–$3_{1,2}$	1.44	0.08	-0.08	0.47	2.62	**0.00**
H_2CO	$3_{2,2}$–$2_{2,1}$	-0.39	0.35	1.02	0.15	-0.39	0.35
H_2CO	$3_{2,1}$–$2_{2,0}$	-0.94	0.17	0.63	0.26	-0.79	0.22
C_2H	4–3 J=9/2–7/2 F=5–4	1.63	0.05	3.35	**0.00**	-0.86	0.20
C_2H	4–3 J=9/2–7/2 F=4–3	0.70	0.24	2.11	**0.02**	-0.86	0.19
C_2H	4–3 J=7/2–5/2 F=4–3	0.62	0.27	2.34	**0.01**	-0.62	0.27
C_2H	4–3 J=7/2–5/2 F=3–2	0.08	0.47	1.48	0.07	0.08	0.47
H_2CO	$5_{1,5}$–$4_{1,4}$	1.27	0.10	2.22	**0.01**	-0.95	0.17
DCO^+	5–4	2.13	**0.02**	1.34	0.09	0.55	0.29
DCN	5–4	-1.67	0.05	-0.56	0.29	-1.04	0.15
HNC	4–3	1.48	0.07	1.95	**0.03**	-0.70	0.24
H_2CO	$5_{0,5}$–$4_{0,4}$	2.50	0.01	3.12	**0.00**	0.00	0.50
		Ratios					
DCN/DCO^+	3–2	-1.63	0.05	-0.18	0.43	-1.45	0.07
DCO^+	5-4/3-2	-1.26	0.10	0.90	0.18	-1.44	0.08
c$-C_3H_2$	6–5/$3_{3,0}$–$2_{2,1}$	-0.56	0.29	2.07	**0.02**	-1.69	0.05
c$-C_3H_2$	$5_{1,4}$–$4_{2,3}$/$3_{3,0}$–$2_{2,1}$	-0.56	0.29	0.56	0.29	-0.94	0.17
H_2CO	$3_{2,2}$–$2_{2,1}$/$3_{0,3}$–$2_{0,2}$	-1.88	**0.03**	-0.21	0.42	-0.63	0.27
		$T_{\rm kin}$ from line ratios					
DCO^+	5-4/3-2	-1.21	0.11	0.28	0.39	-1.39	0.08
c$-C_3H_2$	6–5 / $3_{3,0}$–$2_{2,1}$	-0.56	0.29	2.07	**0.02**	-1.69	0.05
c$-C_3H_2$	$5_{1,4}$–$4_{2,3}$ / $3_{3,0}$–$2_{2,1}$	-0.38	0.35	0.77	0.22	-0.77	0.22
H_2CO	$3_{2,2}$–$2_{2,1}$ / $3_{0,3}$–$2_{0,2}$	-1.9	**0.03**	-0.42	0.34	-0.63	0.26

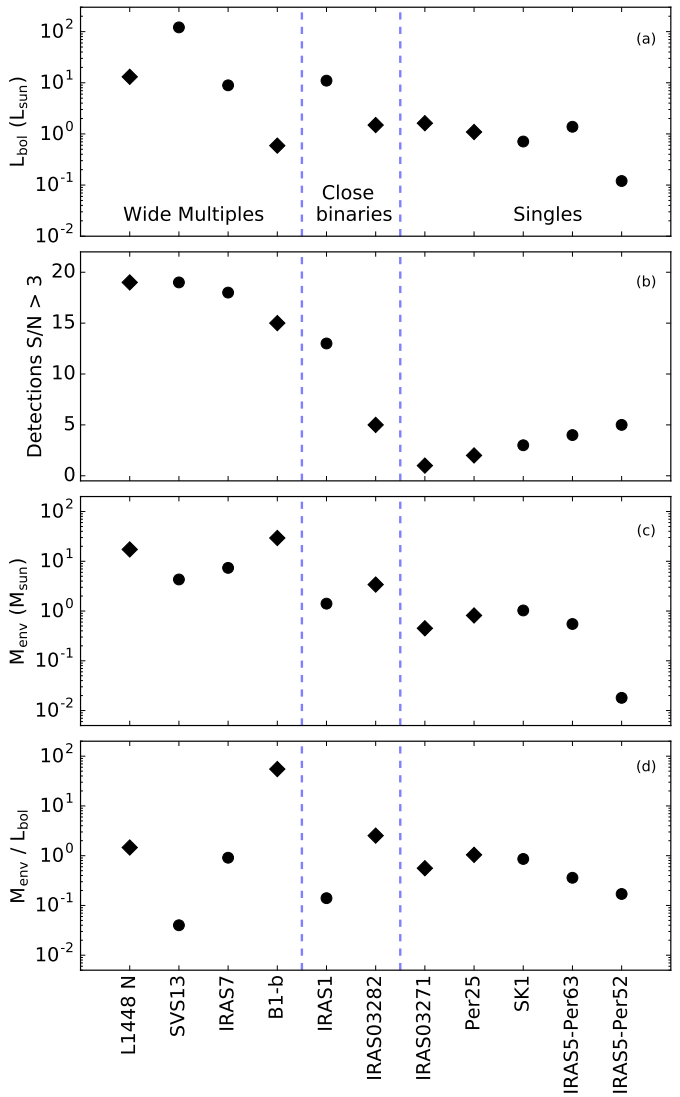

Figure 10: Bolometric luminosity (a), number of line detections (b), envelope mass $M_{\rm env}$ (c), and envelope mass to luminosity ratio $M_{\rm env}$ / $L_{\rm bol}$ (d) of each system in our sample compared to the region, clustered (circles) or non-clustered (diamonds), and source type. NGC1333 IRAS5 is considered here as two single protostellar systems, Per63 and Per52.

systems have luminosities compared to that of B1-b, but have five or less line detections.

Clustering does not seem to particularly enhance the line strength or number of line detections in the envelope (Fig. 10). L1448 N and B1-b are both located in non-clustered environments and present the same chemical richness as the multiple protostars located in NGC1333, which is a clustered region. The same holds for the close binaries and single protostars. NGC1333 IRAS 1 (close binary) and NGC1333 SK1 (single protostar), both located in a clustered region, do not show significant enhancements in line emission compared to IRAS03282+3035 (close binary) and L1455 Per25 (single), both located in less crowded environments.

Both Class 0 and I systems are present in wide multiples, close binaries and single protostellar systems, but no effect is seen on the line detections. For example, NGC1333 IRAS5 Per52 and IRAS03271+3013 are both Class I single sources, but the first shows five line detections, whereas the latter only shows a detection of HNC. For the close binary systems, NGC1333 IRAS1 is a Class I system, but IRAS03282 is a Class 0 protobinary, however IRAS1 has more molecular line detections than IRAS03282, despite IRAS1 having lower envelope mass than IRAS03282. All four wide multiple systems are non-coeval, however the combined SED of these systems would place them at either Class 0 (e.g. NGC1333 IRAS7) or Class I (e.g. B1-b; Murillo et al. 2016, see chapter 5), but no difference in these cases is exhibited.

There seems to be a relation, however, between the envelope mass and the number of molecular line detections, but not with the $M_{\rm env}/L_{\rm bol}$. This relation is again regardless of evolutionary stage and clustering. However, the envelope mass is larger for wide multiple protostellar systems in contrast to that of close binary and single protostars. Core mass would then be more related to formation of non-coeval wide multiple protostellar systems.

6.6.2 Envelope gas temperature and multiplicity

The H_2CO and DCO^+ ratios point to cool envelopes ($T_{\rm gas} < 60$ K at scales of 7000 AU) for all the sources in our sample, regardless of multiplicity, clustering and evolutionary stage. Only c$-C_3H_2$ presents a correlation with bolometric luminosity and an anti-correlation with $M_{\rm env}/L_{\rm bol}$, owing to the fact that the outflow cavity irradiation is dependent on the central source luminosity and the amount of material that is heated. Any non-detection of molecules such as c$-C_3H_2$ and H_2CO, which trace the outflow cavity and envelope gas, respectively, would point to cooler envelopes and outflow cavities. In addition, DCO^+, a cold gas tracer, is detected toward all but one system (IRAS03271+3013, single). Non-detections of warm gas tracers in addition to the presence of DCO^+ toward single and close binary protostellar systems could be explained by these systems being somewhat cooler than wide multiple protostellar systems. Another possibility could be the evolutionary dispersal of envelope material which would cause the warm gas to be located closer to the source and thus diluted in the observing beam. Despite this, wide multiple protostellar systems show a tendency toward non-coevality. Interestingly enough, H_2CO $3_{0,3}$–$2_{0,2}$ and DCO^+ appear to increase with an increase in envelope mass. In other words, H_2CO $3_{0,3}$–$2_{0,2}$ and DCO^+ present stronger emission in wide multiple protostars. This could indicate the presence of massive reservoirs of cold gas in these systems.

External heating seems to not play a significant role, as evidenced by a lack of

difference in all aspects between systems in clustered and non-clustered regions. However it is not clear why close binaries present less molecular line emission than wide multiple protostars, given that some components of the latter are often close binaries themselves (Fig. 1). A possible explanation would be the sensitivity of the observations. However, this would not explain why NGC1333 IRAS1 has more line detections than NGC1333 IRAS5 Per63 when both have sensitivities of ∼30 mK. The results presented in this work indicate that there is no significant difference in envelope temperature between single, close binary and wide multiple protostellar systems. The only difference temperature-wise arises from c$-C_3H_2$, which traces the outflow cavity. This is consistent with previous studies that find the central source heating is mainly channeled through the outflow cavity (Yıldız et al. 2012, 2015).

The lack of temperature difference in the envelope is surprising, given the tendency of wide multiple systems to be non-coeval, which are produced by further fragmentation of the core after the initial collapse has taken place (Murillo et al. 2016, see chapter 5; Sadavoy & Stahler 2017), and the recent formation of a protostar would be expected to heat the envelope considerably (Bate 2012) An interesting case is that of L1448 N, which has been found to have undergone recent fragmentation in the disk of one component (Tobin et al. 2016a). Although the recent fragmentation could have heated the envelope of this system, increasing its chemical richness, it is not the most likely explanation since the other wide multiple systems also show the same degree of chemical richness but no signs of recent fragmentation. Furthermore, while the presence of disks in close binary and single protostars could be considered to explain the low chemical richness of these systems at the observed scales, disks have also been found in wide multiple protostars (e.g. L1448 N, Tobin et al. 2016a)

6.6.3 Accretion bursts

Accretion of material onto the protostar is not a continuous process, but has been found from observations to be an episodic process (e.g., Visser et al. 2015; Frimann et al. 2017, Hsieh et al. in prep.). An accretion burst causes an increase in luminosity, and consequently heating of the envelope gas. The chemical composition of the envelope gas is altered, since cold chemistry molecules (e.g. DCO^+) move further out and molecules such as CO are evaporated off the grains. While the luminosity of the central protostar will decrease after the accretion burst has passed, it takes about 10^4 years for the gas to refreeze onto the dust grains.

Frimann et al. (2017) studied the presence of accretion bursts toward embedded protostars in Perseus. Their sample includes four of the systems studied in this work (L1448 N, NGC1333 SVS13, NGC1333 IRAS1 and IRAS03282), as well as two components of NGC1333 IRAS7, Per18 and Per21. Half of these systems (Per21, IRAS1 and IRAS03282) present indications of past accretion burst activity, while the others (L1448 N, SVS13 and Per18) do not. The results presented here do not show any difference among the sources that have evidence of having undergone an accretion burst, and those that have not. NGC1333 IRAS1 and IRAS03282, both close binary protostars, are suggested to have undergone an accretion burst. The difference found in this work is mainly that IRAS1 presents emission from warm molecules, while IRAS03282 only shows emission in cold molecules. For L1448N and SVS13, both wide multiple protostars, there is also no significant difference, since both systems present the same number of line detections, with similar peak intensities except for DCO^+ which is

stronger in L1448N. Analyzing NGC1333 IRAS7 Per18 and Per21 (Appendix 6.A) separately also points to a lack of difference among both sources. However, it must be noted that given their separation of 13″, the spectra of each component is contaminated by emission from the other.

6.7 Conclusions

Single-dish observations of a sample of 10 embedded protostellar systems in Perseus are presented here. The observations targeted molecular line emission that trace the cold and warm gas of the observed protostellar systems. The sample included wide multiple protostellar systems (separation ≥7″), close binary protostars (separation <2″) and single protostars, located in clustered and non-clustered environments, spanning Class 0 and I objects, and containing coeval and non-coeval systems. The results presented in this work examine the relation between fragmentation and temperature, since heated gas is expected to suppress fragmentation based on simulations including radiative feedback.

Although the sample presented here is small and there are several upper limits, the envelope gas temperature is found to be similar among multiple and single protostars, regardless of evolutionary stage, coevality or clustering. These results suggest that gas temperature may not have as strong a role in suppressing fragmentation as expected from models, a result that was also stated in Offner et al. (2010), which found that temperature does not suppress turbulent fragmentation. Instead, wide multiple protostellar systems present larger envelope masses and massive cold gas reservoirs in comparison to close binary and single protostars. It seems, then, that mass, along with other factors such as turbulence, density profile and magnetic fields, rather than envelope gas temperature plays a fundamental role in fragmentation. Larger, more massive cores, would then lean to further fragmentation that forms non-coeval wide multiple systems. A topic of further research would then be to determine what causes some cores to become more massive than others.

Appendix

6.A Single-pointing observations: NGC1333 IRAS7

APEX single pointing observations with the heterodyne instrument APEX-1 were made toward 5 wide (separation >7″) multiple protostellar systems in Perseus. These systems are referred to as wide multiple protostars since the components span separations grater than 7″ (which can be resolved with *Herschel Space Observatory* PACS photometric maps (Murillo et al. 2016, see chapter 5)) One pointing per component in a wide multiple system was observed. In the main text are the parameters of the lines obtained by averaging the spectra of the individual components for the corresponding system. This is because in all cases except NGC1333 IRAS5, the beam of APEX at 215 GHz overlaps partially overlaps another component in the system.

Here the spectra for the individual components for the system NGC1333 IRAS7 are presented (Fig. 11). This provides an example of the similarity of the spectra of the individual components. The spectra of the components Per21, which is expected to have undergone a recent accretion burst, and Per18, which has no evidence of episodic

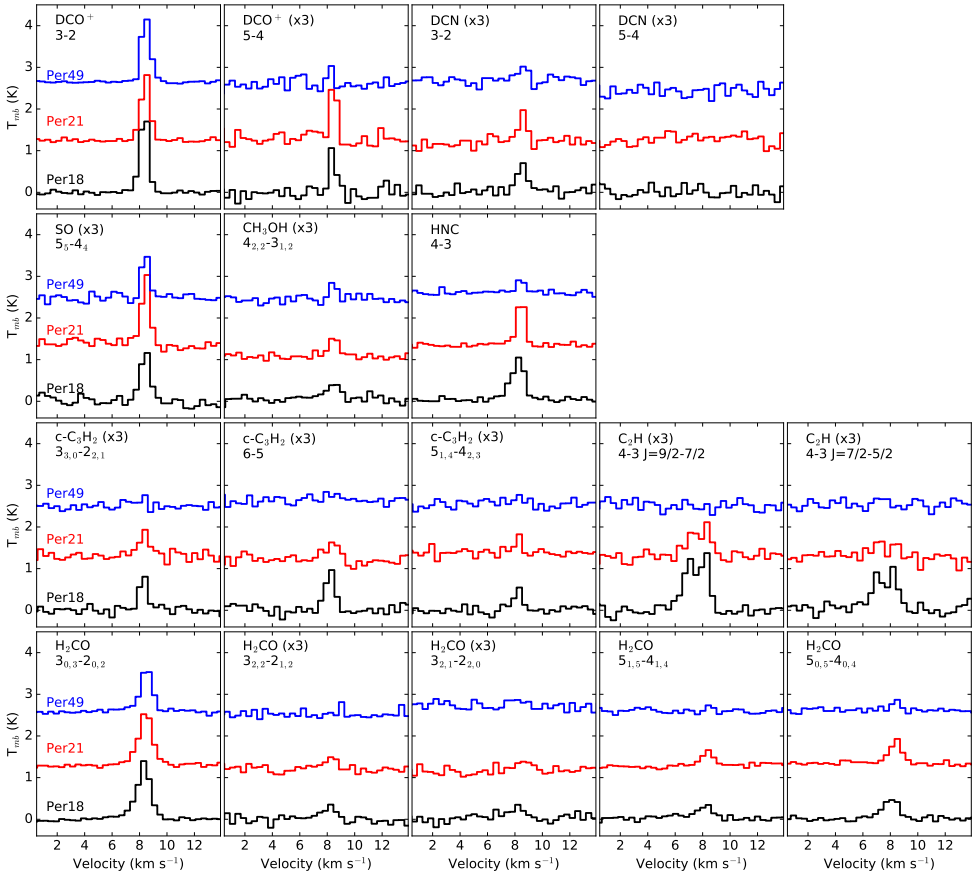

Figure 11: Spectra for the individual components of NGC1333 IRAS7. Note that some spectra are multiplied by a factor of 3 in order to enhance the line emission features. The spectra of Per21 and Per49 are offset by 1.3 K and 2.6 K from that of Per18 for clarity.

accretion, can also be compared. It is also interesting to note that the component Per49 presents much weaker emission than Per18 and Per21,

6.B Observed line widths and integrated fluxes

In this appendix the line widths and integrated fluxes are listed for the detected molecular lines from the APEX observations. These values were obtained with a simple Gaussian fit of the detected emission line.

Table 13: Line width and integrated intensity for DCO^+ and DCN

System	DCO^+ 3-2		DCO^+ 5-4		DCN 3-2		DCN 5-4	
	Width km s^{-1}	Integrated mK km s^{-1}	Width km s^{-1}	Integrated mK km s^{-1}	Width km s^{-1}	Integrated mK km s^{-1}	Width km s^{-1}	Integrated mK km s^{-1}
Wide multiples								
L1448N	1.13	3786.7	1.04	895	1.63	453.3	1.43	105
SVS13	1	1306.7	1.03	505	1.18	373.3	1.82	199
Per63	0.64	226.7	...	...	...	...	...	...
Per52	0.66	386.7	...	...	...	...	...	...
IRAS7	0.76	1866.7	0.56	281	0.8	266.7	...	...
B1-b	1.32	3680.0	0.92	438	1.05	280.0	...	...
Close binaries								
IRAS1	0.68	573.3	...	...	...	...	...	...
IRAS03282	0.6	1200.0	0.57	342	0.82	173.3	...	...
Singles								
IRAS03271	...	...	...	...	...	...	...	...
Per25	0.4	200.0	...	...	...	...	...	...
SK1	0.5	666.7	...	...	...	...	...	...

Table 14: Line width and integrated intensity for SO, CH_3OH and HNC

System	SO 5_5 – 4_4		CH_3OH $4_{2,2}$–$3_{1,2}$		HNC 4-3	
	Width km s^{-1}	Integrated K km s^{-1}	Width km s^{-1}	Integrated K km s^{-1}	Width km s^{-1}	Integrated K km s^{-1}
Wide multiples						
L1448N	0.99	30.7	1.02	200.0	2.00	2592
SVS13	1.5	413.3	1.1	133.3	1.32	2898
Per63	...	...	...	...	0.78	212
Per52	...	...	...	...	0.81	573
IRAS7	0.74	480.0	0.82	160.0	0.90	1068
B1-b	0.85	573.3	0.8	160.0	1.34	699
Close binaries						
IRAS1	1.4	266.7	...	...	0.89	1212
IRAS03282	...	...	...	...	0.84	917
Singles						
IRAS03271	...	...	...	...	1.03	357
Per25	...	...	...	...	1.07	422
SK1	...	...	...	...	0.70	457

Table 15: Line width and integrated intensity for c$-C_3H_2$

System	$3_{3,0}$–$2_{2,1}$		6—5		$5_{1,4}$–$4_{2,3}$	
	Width km s^{-1}	Integrated mK km s^{-1}	Width km s^{-1}	Integrated mK km s^{-1}	Width km s^{-1}	Integrated mK km s^{-1}
Wide multiples						
L1448N	1.56	1146.7	1.65	946.7	1.68	666.7
SVS13	0.99	453.3	1.1	586.7	1.3	400.0
Per 63	...	...	...	...	...	...
Per 52	0.5	173.3	0.94	121.3	...	...
IRAS7	0.7	200.0	0.97	226.7	0.59	121.3
B1-b	1.33	506.7	0.99	173.3	1.19	13.3
Close binaries						
IRAS1	0.66	466.7	0.75	480.0	0.62	333.3
IRAS03282	...	...	...	...	...	...
Singles						
IRAS03271	...	...	...	...	...	...
Per25	...	...	...	...	...	...
SK1	...	...	...	...	...	...

Table 16: Line width and integrated intensity for C_2H

System	4–3 J=9/2–7/2 f=5–4		4–3 J=9/2–7/2 f=4–3		4–3 J=7/2–5/2 f=4–3		4–3 J=7/2–5/2 f=3–2	
	Width	Integrated	Width	Integrated	Width	Integrated	Width	Integrated
	km s^{-1}	mK km s^{-1}	km s^{-1}	mK km s^{-1}	km s^{-1}	mK km s^{-1}	km s^{-1}	mK km s^{-1}
Wide multiples								
L1448N	2.14	937	2.47	693	2.16	584	2.61	637
SVS13	1.18	928	1.06	688	1.11	703	1.31	602
Per63	...	...	...	...	...	...	...	...
Per52	...	...	...	...	...	...	...	...
IRAS7	0.61	216	1.21	356	0.65	143	0.99	232
B1-b	0.80	108	0.04	840	...	...	...	...
Close binaries								
IRAS1	0.86	308	0.81	222	0.97	221	0.92	135
IRAS03282	...	...	...	...	...	...	...	...
Singles								
IRAS03271	...	...	...	...	...	...	...	...
Per25	...	...	...	...	...	...	...	...
SK1	...	...	...	...	...	...	...	...

Table 17: Line width and integrated intensity for H_2CO 3–2

System	$3_{0,3}$–$2_{0,2}$		$3_{2,2}$–$2_{2,1}$		$3_{2,1}$–$2_{2,0}$	
	Width km s^{-1}	Integrated K km s^{-1}	Width km s^{-1}	Integrated K km s^{-1}	Width km s^{-1}	Integrated K km s^{-1}
Wide multiples						
L1448N	1.68	666.7	2.2	306.7	1.67	200.0
SVS13	1.45	2333.3	1.5	240.0	2	293.3
Per 63	1.32	360.0	...	...	...	...
Per 52	0.76	400.0	...	...	...	...
IRAS7	1.16	1946.7	1.3	133.3	1.3	116.0
B1-b	1.3	1453.3	...	...	0.83	73.3
Close binaries						
IRAS1	0.86	520.0	...	...	...	...
IRAS03282	0.97	333.3	...	...	...	...
Singles						
IRAS03271	...	...	...	...	...	...
Per25	...	...	...	...	...	...
SK1	0.95	89.3	...	...	...	...

Table 18: Line width and integrated intensity for H_2CO 5–4

System	$5_{1,5}$-$4_{1,4}$		$5_{0,5}$-$4_{0,4}$	
	Width km s^{-1}	Integrated mK km s^{-1}	Width km s^{-1}	Integrated mK km s^{-1}
Wide multiples				
L1448N	2.00	1265	2.03	1639
SVS13	1.80	1136	1.38	1660
Per63	...	...	3.49	303
Per52	...	...	...	...
IRAS7	0.98	388	1.22	736
B1-b	1.92	260	2.52	677
Close binaries				
IRAS1	2.19	535	1.08	489
IRAS03282	0.00	0	...	...
Singles				
IRAS03271	...	...	...	...
Per25	...	...	...	...
SK1	0.92	158	...	...

Bibliography

Adams, N. G. & Smith, D. 1985, ApJ, 294, L63

Aikawa, Y. & Herbst, E. 1999, A&A, 351, 233

Aikawa, Y., Umebayashi, T., Nakano, T., & Miyama, S. M. 1999, ApJ, 519, 705

Aikawa, Y., Wakelam, V., Hersant, F., Garrod, R. T., & Herbst, E. 2012, ApJ, 760, 40

Akeson, R. L. & Jensen, E. L. N. 2014, ApJ, 784, 62

Albertsson, T., Semenov, D. A., Vasyunin, A. I., Henning, T., & Herbst, E. 2013, ApJS, 207, 27

Alonso-Albi, T., Fuente, A., Crimier, N., et al. 2010, A&A, 518, A52

Amano, T. 1990, J. Chem. Phys., 92, 6492

Anderl, S., Maret, S., Cabrit, S., et al. 2016, A&A, 591, A3

André, P., Martin-Pintado, J., Despois, D., & Montmerle, T. 1990, A&A, 236, 180

André, P., Men'shchikov, A., Bontemps, S., et al. 2010, A&A, 518, L102

André, P., Ward-Thompson, D., & Barsony, M. 1993, ApJ, 406, 122

Arce, H. G., Borkin, M. A., Goodman, A. A., Pineda, J. E., & Halle, M. W. 2010, ApJ, 715, 1170

Arce, H. G. & Sargent, A. I. 2006, ApJ, 646, 1070

Audard, M., Ábrahám, P., Dunham, M. M., et al. 2014, Protostars and Planets VI, 387

Bacmann, A., Taquet, V., Faure, A., Kahane, C., & Ceccarelli, C. 2012, A&A, 541, L12

Balog, Z., Müller, T., Nielbock, M., et al. 2014, Experimental Astronomy, 37, 129

Barsony, M., Koresko, C., & Matthews, K. 2003, ApJ, 591, 1064

Barsony, M., Ward-Thompson, D., André, P., & O'Linger, J. 1998, ApJ, 509, 733

Bate, M. R. 2009, MNRAS, 392, 1363

Bate, M. R. 2012, MNRAS, 419, 3115

Bate, M. R., Bonnell, I. A., & Bromm, V. 2002, MNRAS, 336, 705

Belloche, A. 2013, in EAS Publications Series, Vol. 62, EAS Publications Series, ed. P. Hennebelle & C. Charbonnel, 25–66

Bergin, E. A., Du, F., Cleeves, L. I., et al. 2016, ApJ, 831, 101

Bergman, P., Parise, B., Liseau, R., & Larsson, B. 2011, A&A, 527, A39

Bergner, J. B., Öberg, K. I., Garrod, R. T., & Graninger, D. M. 2017, ApJ, 841, 120

Bisschop, S. E., Fraser, H. J., Öberg, K. I., van Dishoeck, E. F., & Schlemmer, S. 2006, A&A, 449, 1297

Bisschop, S. E., Jørgensen, J. K., Bourke, T. L., Bottinelli, S., & van Dishoeck, E. F. 2008, A&A, 488, 959

Black, J. H. 1975, PhD thesis, HARVARD UNIVERSITY.

Bogey, M., Demuynck, C., & Destombes, J. L. 1986, Chem. Phys. Lett., 125, 383

Bogey, M., Demuynck, C., Destombes, J. L., & Dubus, H. 1987, J. Mol. Spectrosc., 122, 313

Boogert, A. C. A., Hogerheijde, M. R., Ceccarelli, C., et al. 2002, ApJ, 570, 708

Bottinelli, S., Ceccarelli, C., Neri, R., et al. 2004, ApJ, 617, L69

Breivik, K., Rodriguez, C. L., Larson, S. L., Kalogera, V., & Rasio, F. A. 2016, ApJ, 830, L18

Brinch, C., Crapsi, A., Jørgensen, J. K., Hogerheijde, M. R., & Hill, T. 2007, A&A, 475, 915

Burkert, A. & Bodenheimer, P. 1993, MNRAS, 264, 798

Caratti o Garatti, A., Giannini, T., Nisini, B., & Lorenzetti, D. 2006, A&A, 449, 1077

Caselli, P. & Ceccarelli, C. 2012, A&A Rev., 20, 56

Caselli, P. & Dore, L. 2005, A&A, 433, 1145

Cazzoli, G., Cludi, L., Buffa, G., & Puzzarini, C. 2012, ApJS, 203, 11

Chen, X., Arce, H. G., Zhang, Q., et al. 2013, ApJ, 768, 110

Chen, X., Arce, H. G., Zhang, Q., et al. 2010, ApJ, 715, 1344

Chen, X., Launhardt, R., & Henning, T. 2009, ApJ, 691, 1729

Ching, T.-C., Lai, S.-P., Zhang, Q., et al. 2016, ApJ, 819, 159

Chini, R., Hoffmeister, V. H., Nasseri, A., Stahl, O., & Zinnecker, H. 2012, MNRAS, 424, 1925

Choi, M., Tatematsu, K., & Kang, M. 2010, ApJ, 723, L34

Ciardi, D. R., Telesco, C. M., Williams, J. P., et al. 2003, ApJ, 585, 392

Codella, C., Cabrit, S., Gueth, F., et al. 2014, A&A, 568, L5

Commerçon, B., Launhardt, R., Dullemond, C., & Henning, T. 2012, A&A, 545, A98

Connelley, M. S., Reipurth, B., & Tokunaga, A. T. 2008a, AJ, 135, 2496

Connelley, M. S., Reipurth, B., & Tokunaga, A. T. 2008b, AJ, 135, 2526

Connelley, M. S., Reipurth, B., & Tokunaga, A. T. 2009, AJ, 138, 1193

Coutens, A., Jørgensen, J. K., van der Wiel, M. H. D., et al. 2016, A&A, 590, L6

Crapsi, A., Caselli, P., Walmsley, C. M., et al. 2005, ApJ, 619, 379

Crapsi, A., van Dishoeck, E. F., Hogerheijde, M. R., Pontoppidan, K. M., & Dullemond, C. P. 2008, A&A, 486, 245

Crimier, N., Ceccarelli, C., Maret, S., et al. 2010, A&A, 519, A65

Cuadrado, S., Goicoechea, J. R., Pilleri, P., et al. 2015, A&A, 575, A82

Curtis, E. I., Richer, J. S., Swift, J. J., & Williams, J. P. 2010, MNRAS, 408, 1516

Davidson, J. A., Novak, G., Matthews, T. G., et al. 2011, ApJ, 732, 97

Davis, C. J., Scholz, P., Lucas, P., Smith, M. D., & Adamson, A. 2008, MNRAS, 387, 954

Decin, L., Richards, A. M. S., Neufeld, D., et al. 2015, A&A, 574, A5

Di Francesco, J., André, P., & Myers, P. C. 2004, ApJ, 617, 425

Diolaiti, E., Bendinelli, O., Bonaccini, D., et al. 2000, in Society of Photo-Optical Instrumentation Engineers (SPIE) Conference Series, Vol. 4007, Adaptive Optical Systems Technology, ed. P. L. Wizinowich, 879–888

Drozdovskaya, M. N., Walsh, C., Visser, R., Harsono, D., & van Dishoeck, E. F. 2014, MNRAS, 445, 913

Drozdovskaya, M. N., Walsh, C., Visser, R., Harsono, D., & van Dishoeck, E. F. 2015, MNRAS, 451, 3836

Duchêne, G. & Kraus, A. 2013, ARA&A, 51, 269

Duchêne, G., Monin, J.-L., Bouvier, J., & Ménard, F. 1999, A&A, 351, 954

Dunham, M. M., Allen, L. E., Evans, II, N. J., et al. 2015, ApJS, 220, 11

Dunham, M. M., Chen, X., Arce, H. G., et al. 2011, ApJ, 742, 1

Dunham, M. M., Crapsi, A., Evans, II, N. J., et al. 2008, ApJS, 179, 249

Dunham, M. M., Offner, S. S. R., Pineda, J. E., et al. 2016, ApJ, 823, 160

Dunham, M. M., Stutz, A. M., Allen, L. E., et al. 2014, Protostars and Planets VI, 195

Dzib, S. A., Loinard, L., Mioduszewski, A. J., et al. 2013, ApJ, 775, 63

Eislöffel, J., Froebrich, D., Stanke, T., & McCaughrean, M. J. 2003, ApJ, 595, 259

Emprechtinger, M., Caselli, P., Volgenau, N. H., Stutzki, J., & Wiedner, M. C. 2009, A&A, 493, 89

Endres, C. P., Schlemmer, S., Schilke, P., Stutzki, J., & Müller, H. S. P. 2016, J. Mol. Spectrosc., 327, 95

Enoch, M. L., Corder, S., Duchêne, G., et al. 2011, ApJS, 195, 21

Enoch, M. L., Corder, S., Dunham, M. M., & Duchêne, G. 2009a, ApJ, 707, 103

Enoch, M. L., Evans, II, N. J., Sargent, A. I., & Glenn, J. 2009b, ApJ, 692, 973

Evans, II, N. J. 1999, ARA&A, 37, 311

Evans, II, N. J., Dunham, M. M., Jørgensen, J. K., et al. 2009, ApJS, 181, 321

Evans, II, N. J., Rawlings, J. M. C., Shirley, Y. L., & Mundy, L. G. 2001, ApJ, 557, 193

Faure, A., Hily-Blant, P., Le Gal, R., Rist, C., & Pineau des Forêts, G. 2013, ApJ, 770, L2

Favre, C., Bergin, E. A., Cleeves, L. I., et al. 2015, ApJ, 802, L23

Favre, C., Lopez-Sepulcre, A., Ceccarelli, C., et al. 2017, ArXiv e-prints [arXiv:1708.08247]

Fayolle, E. C., Öberg, K. I., Garrod, R. T., van Dishoeck, E. F., & Bisschop, S. E. 2015, A&A, 576, A45

Fendt, C. & Zinnecker, H. 1998, A&A, 334, 750

Flower, D. R. 1999, MNRAS, 305, 651

Flower, D. R., Pineau Des Forêts, G., & Walmsley, C. M. 2006, A&A, 449, 621

Frank, A., Ray, T. P., Cabrit, S., et al. 2014, Protostars and Planets VI, 451

Friesen, R. K., Di Francesco, J., Bourke, T. L., et al. 2014, ApJ, 797, 27

Frimann, S., Jørgensen, J. K., Dunham, M. M., et al. 2017, A&A, 602, A120

Froebrich, D. 2005, ApJS, 156, 169

Furuya, K., Aikawa, Y., Tomida, K., et al. 2012, ApJ, 758, 86

Galli, D., Walmsley, M., & Gonçalves, J. 2002, A&A, 394, 275

Garay, G., Mardones, D., Rodríguez, L. F., Caselli, P., & Bourke, T. L. 2002, ApJ, 567, 980

Garrod, R. T. & Herbst, E. 2006, A&A, 457, 927

Gerin, M., Kaźmierczak, M., Jastrzebska, M., et al. 2011, A&A, 525, A116

Gerin, M., Pety, J., Fuente, A., et al. 2015, A&A, 577, L2

Gerlich, D., Herbst, E., & Roueff, E. 2002, Planet. Space Sci., 50, 1275

Girart, J. M., Rao, R., & Marrone, D. P. 2006, Science, 313, 812

Goodwin, S. P. & Whitworth, A. 2007, A&A, 466, 943

Goodwin, S. P., Whitworth, A. P., & Ward-Thompson, D. 2004, A&A, 414, 633

Guilloteau, S. & Dutrey, A. 1998, A&A, 339, 467

Guilloteau, S., Dutrey, A., & Simon, M. 1999, A&A, 348, 570

Güsten, R., Nyman, L. Å., Schilke, P., et al. 2006, A&A, 454, L13

Guzmán, V. V., Pety, J., Goicoechea, J. R., et al. 2015, ApJ, 800, L33

Haisch, Jr., K. E., Barsony, M., Greene, T. P., & Ressler, M. E. 2002, AJ, 124, 2841

Haisch, Jr., K. E., Greene, T. P., Barsony, M., & Stahler, S. W. 2004, AJ, 127, 1747

Harris, R. J., Andrews, S. M., Wilner, D. J., & Kraus, A. L. 2012, ApJ, 751, 115

Harsono, D., Jørgensen, J. K., van Dishoeck, E. F., et al. 2014, A&A, 562, A77

Harsono, D., Visser, R., Bruderer, S., van Dishoeck, E. F., & Kristensen, L. E. 2013, A&A, 555, A45

Hartigan, P. & Kenyon, S. J. 2003, ApJ, 583, 334

Hatchell, J., Richer, J. S., Fuller, G. A., et al. 2005, A&A, 440, 151

Hennebelle, P. & Ciardi, A. 2009, A&A, 506, L29

Hennebelle, P., Whitworth, A. P., Cha, S.-H., & Goodwin, S. P. 2004, MNRAS, 348, 687

Herbst, E. & van Dishoeck, E. F. 2009, ARA&A, 47, 427

Herschel, W. 1803, Philosophical Transactions of the Royal Society of London Series I, 93, 339

Hincelin, U., Commerçon, B., Wakelam, V., et al. 2016, ApJ, 822, 12

Hincelin, U., Wakelam, V., Commerçon, B., Hersant, F., & Guilloteau, S. 2013, ApJ, 775, 44

Hiramatsu, M., Hirano, N., & Takakuwa, S. 2010, ApJ, 712, 778

Hirano, N., Ho, P. P. T., Liu, S.-Y., et al. 2010, ApJ, 717, 58

Hirano, N. & Liu, F.-c. 2014, ApJ, 789, 50

Hirota, T., Bushimata, T., Choi, Y. K., et al. 2008, PASJ, 60, 37

Hirota, T., Honma, M., Imai, H., et al. 2011, PASJ, 63, 1

Hogerheijde, M. R. 2001, ApJ, 553, 618

Hogerheijde, M. R. & van der Tak, F. F. S. 2000, A&A, 362, 697

Holland, W. S., Greaves, J. S., Ward-Thompson, D., & Andre, P. 1996, A&A, 309, 267

Hsieh, T.-H., Lai, S.-P., Belloche, A., Wyrowski, F., & Hung, C.-L. 2015, ApJ, 802, 126

Huang, J., Öberg, K. I., Qi, C., et al. 2017, ApJ, 835, 231

Hughes, A. M., Andrews, S. M., Espaillat, C., et al. 2009, ApJ, 698, 131

Hull, C. L. H., Plambeck, R. L., Bolatto, A. D., et al. 2013, ApJ, 768, 159

Hull, C. L. H., Plambeck, R. L., Kwon, W., et al. 2014a, ApJS, 213, 13

Hull, C. L. H., Plambeck, R. L., Kwon, W., et al. 2014b, ApJS, 213, 13

Isobe, T., Feigelson, E. D., & Nelson, P. I. 1986, ApJ, 306, 490

Jansen, D. J. 1995, PhD thesis, Leiden Observatory, Leiden University, P.O. Box 9513, 2300 RA Leiden, The Netherlands

Jensen, E. L. N., Mathieu, R. D., Donar, A. X., & Dullighan, A. 2004, ApJ, 600, 789

Jetsu, L. & Porceddu, S. 2015, PLoS ONE, 10 [arXiv:1601.06990]

Johnstone, D., Hendricks, B., Herczeg, G. J., & Bruderer, S. 2013, ApJ, 765, 133

Jørgensen, J. K., Bourke, T. L., Myers, P. C., et al. 2007, ApJ, 659, 479

Jørgensen, J. K., Bourke, T. L., Myers, P. C., et al. 2005a, ApJ, 632, 973

Jørgensen, J. K., Bourke, T. L., Nguyen Luong, Q., & Takakuwa, S. 2011, A&A, 534, A100

Jørgensen, J. K., Schöier, F. L., & van Dishoeck, E. F. 2002, A&A, 389, 908

Jørgensen, J. K., Schöier, F. L., & van Dishoeck, E. F. 2004, A&A, 416, 603

Jørgensen, J. K., Schöier, F. L., & van Dishoeck, E. F. 2005b, A&A, 437, 501

Jørgensen, J. K., Schöier, F. L., & van Dishoeck, E. F. 2005c, A&A, 435, 177

Jørgensen, J. K., van der Wiel, M. H. D., Coutens, A., et al. 2016, A&A, 595, A117

Jørgensen, J. K., van Dishoeck, E. F., Visser, R., et al. 2009, A&A, 507, 861

Jørgensen, J. K., Visser, R., Sakai, N., et al. 2013, ApJ, 779, L22

Jørgensen, J. K., Visser, R., Williams, J. P., & Bergin, E. A. 2015, A&A, 579, A23

Karska, A., Kristensen, L. E., van Dishoeck, E. F., et al. 2014, A&A, 572, A9

Kennicutt, R. C. & Evans, N. J. 2012, ARA&A, 50, 531

Kenyon, S. J. & Hartmann, L. 1995, ApJS, 101, 117

Kirk, H., Dunham, M. M., Di Francesco, J., et al. 2017, ApJ, 838, 114

Kirk, H., Johnstone, D., & Di Francesco, J. 2006, ApJ, 646, 1009

Klaassen, P. D., Juhasz, A., Mathews, G. S., et al. 2013, A&A, 555, A73

Klapp, J., Sigalotti, L. D. G., Zavala, M., Peña-Polo, F., & Troconis, J. 2014, ApJ, 780, 188

Koumpia, E., Semenov, D. A., van der Tak, F. F. S., Boogert, A. C. A., & Caux, E. 2017, ArXiv e-prints [arXiv:1705.00908]

Koumpia, E., van der Tak, F. F. S., Kwon, W., et al. 2016, A&A, 595, A51

Kratter, K. M. 2011, in Astronomical Society of the Pacific Conference Series, Vol. 447, Evolution of Compact Binaries, ed. L. Schmidtobreick, M. R. Schreiber, & C. Tappert, 47

Kratter, K. M., Matzner, C. D., Krumholz, M. R., & Klein, R. I. 2010, ApJ, 708, 1585

Kraus, A. L. & Hillenbrand, L. A. 2009, ApJ, 704, 531

Kristensen, L. E., van Dishoeck, E. F., Bergin, E. A., et al. 2012, A&A, 542, A8

Krumholz, M. R. 2006, ApJ, 641, L45

Krumholz, M. R., Bate, M. R., Arce, H. G., et al. 2014, Protostars and Planets VI, 243

Krumholz, M. R., Crutcher, R. M., & Hull, C. L. H. 2013, ApJ, 767, L11

Kwon, W., Looney, L. W., Crutcher, R. M., & Kirk, J. M. 2006, ApJ, 653, 1358

Ladd, E. F., Fuller, G. A., & Deane, J. R. 1998, ApJ, 495, 871

Larson, R. B. 1969, MNRAS, 145, 271

Launhardt, R., Stutz, A. M., Schmiedeke, A., et al. 2013, A&A, 551, A98

Lee, C.-F., Hasegawa, T. I., Hirano, N., et al. 2010, ApJ, 713, 731

Lee, C.-F., Hirano, N., Palau, A., et al. 2009, ApJ, 699, 1584

Lee, C.-F., Hirano, N., Zhang, Q., et al. 2014, ApJ, 786, 114

Lee, K. I., Dunham, M. M., Myers, P. C., et al. 2016, ApJ, 820, L2

Lee, K. I., Dunham, M. M., Myers, P. C., et al. 2015, ApJ, 814, 114

Li, Z.-Y., Banerjee, R., Pudritz, R. E., et al. 2014, Protostars and Planets VI, 173

Li, Z.-Y., Krasnopolsky, R., & Shang, H. 2011, ApJ, 738, 180

Lindberg, J. E., Charnley, S. B., & Cordiner, M. A. 2016, ApJ, 833, L14

Lindberg, J. E., Charnley, S. B., Jørgensen, J. K., Cordiner, M. A., & Bjerkeli, P. 2017, ApJ, 835, 3

Lindberg, J. E., Jørgensen, J. K., Brinch, C., et al. 2014a, A&A, 566, A74

Lindberg, J. E., Jørgensen, J. K., Green, J. D., et al. 2014b, A&A, 565, A29

Liseau, R., Larsson, B., Brandeker, A., et al. 2003, A&A, 402, L73

Liseau, R., Larsson, B., Lunttila, T., et al. 2015, A&A, 578, A131

Liszt, H., Sonnentrucker, P., Cordiner, M., & Gerin, M. 2012, ApJ, 753, L28

Loinard, L., Rodríguez, L. F., D'Alessio, P., Wilner, D. J., & Ho, P. T. P. 2002, ApJ, 581, L109

Loinard, L., Torres, R. M., Mioduszewski, A. J., & Rodríguez, L. F. 2008, ApJ, 675, L29

Loinard, L., Zapata, L. A., Rodríguez, L. F., et al. 2013, MNRAS, 430, L10

Lommen, D., Jørgensen, J. K., van Dishoeck, E. F., & Crapsi, A. 2008, A&A, 481, 141

Looney, L. W., Mundy, L. G., & Welch, W. J. 2000, ApJ, 529, 477

Loren, R. B. 1989, ApJ, 338, 902

Lucas, R. & Liszt, H. S. 2000, A&A, 358, 1069

Lykke, J. M., Coutens, A., Jørgensen, J. K., et al. 2017, A&A, 597, A53

Machida, M. N., Inutsuka, S.-i., & Matsumoto, T. 2014, MNRAS, 438, 2278

Machida, M. N., Tomisaka, K., Matsumoto, T., & Inutsuka, S.-i. 2008, ApJ, 677, 327

Maercker, M., Mohamed, S., Vlemmings, W. H. T., et al. 2012, Nature, 490, 232

Mannings, V. & Sargent, A. I. 1997, ApJ, 490, 792

Mardones, D., Myers, P. C., Tafalla, M., et al. 1997, ApJ, 489, 719

Maret, S., Bergin, E. A., & Lada, C. J. 2006, Nature, 442, 425

Masunaga, H. & Inutsuka, S.-i. 2000, ApJ, 531, 350

Masunaga, H., Miyama, S. M., & Inutsuka, S.-i. 1998, ApJ, 495, 346

Mathews, G. S., Klaassen, P. D., Juhász, A., et al. 2013, A&A, 557, A132

McCabe, C., Ghez, A. M., Prato, L., et al. 2006, ApJ, 636, 932

McElroy, D., Walsh, C., Markwick, A. J., et al. 2013, A&A, 550, A36

Mellon, R. R. & Li, Z.-Y. 2008, ApJ, 681, 1356

Michell, J. 1767, Philosophical Transactions of the Royal Society of London Series I, 57, 234

Monin, J.-L., Ménard, F., & Peretto, N. 2006, A&A, 446, 201

Mookerjea, B., Hassel, G. E., Gerin, M., et al. 2012, A&A, 546, A75

Mookerjea, B., Vastel, C., Hassel, G. E., et al. 2014, A&A, 566, A61

Mottram, J. C., Kristensen, L. E., van Dishoeck, E. F., et al. 2014, A&A, 572, A21

Mottram, J. C., van Dishoeck, E. F., Kristensen, L. E., et al. 2017, A&A, 600, A99

Müller, H. S. P., Klaus, T., & Winnewisser, G. 2000, A&A, 357, L65

Murillo, N. M., Bruderer, S., van Dishoeck, E. F., et al. 2015, A&A, 579, A114

Murillo, N. M. & Lai, S.-P. 2013, ApJ, 764, L15

Murillo, N. M., Lai, S.-P., Bruderer, S., Harsono, D., & van Dishoeck, E. F. 2013, A&A, 560, A103

Murillo, N. M., van Dishoeck, E. F., Tobin, J. J., & Fedele, D. 2016, A&A, 592, A56

Nagy, Z., Ossenkopf, V., Van der Tak, F. F. S., et al. 2015, A&A, 578, A124

Nakamura, F., Kamada, Y., Kamazaki, T., et al. 2011, ApJ, 726, 46

Nakamura, F. & Li, Z.-Y. 2003, ApJ, 594, 363

Öberg, K. I., Lauck, T., & Graninger, D. 2014, ApJ, 788, 68

Offner, S. S. R., Capodilupo, J., Schnee, S., & Goodman, A. A. 2012a, MNRAS, 420, L53

Offner, S. S. R., Dunham, M. M., Lee, K. I., Arce, H. G., & Fielding, D. B. 2016, ApJ, 827, L11

Offner, S. S. R., Klein, R. I., McKee, C. F., & Krumholz, M. R. 2009, ApJ, 703, 131

Offner, S. S. R., Kratter, K. M., Matzner, C. D., Krumholz, M. R., & Klein, R. I. 2010, ApJ, 725, 1485

Offner, S. S. R., Robitaille, T. P., Hansen, C. E., McKee, C. F., & Klein, R. I. 2012b, ApJ, 753, 98

Padovani, M., Walmsley, C. M., Tafalla, M., Galli, D., & Müller, H. S. P. 2009, A&A, 505, 1199

Pagani, L., Daniel, F., & Dubernet, M.-L. 2009a, A&A, 494, 719

Pagani, L., Vastel, C., Hugo, E., et al. 2009b, A&A, 494, 623

Palau, A., Zapata, L. A., Rodríguez, L. F., et al. 2014, MNRAS, 444, 833

Persson, M. V., Harsono, D., Tobin, J. J., et al. 2016, A&A, 590, A33

Pety, J., Goicoechea, J. R., Hily-Blant, P., Gerin, M., & Teyssier, D. 2007, A&A, 464, L41

Pezzuto, S., Elia, D., Schisano, E., et al. 2012, A&A, 547, A54

Pilleri, P., Treviño-Morales, S., Fuente, A., et al. 2013, A&A, 554, A87

Pineda, J. E., Maury, A. J., Fuller, G. A., et al. 2012, A&A, 544, L7

Pineda, J. E., Offner, S. S. R., Parker, R. J., et al. 2015, Nature, 518, 213

Plessis, S., Carrasco, N., & Pernot, P. 2010, J. Chem. Phys., 133, 134110

Plunkett, A. L., Arce, H. G., Corder, S. A., et al. 2013, ApJ, 774, 22

Poglitsch, A., Waelkens, C., Geis, N., et al. 2010, A&A, 518, L2

Price, D. J., Tricco, T. S., & Bate, M. R. 2012, MNRAS, 423, L45

Punanova, A., Caselli, P., Pon, A., Belloche, A., & André, P. 2016, A&A, 587, A118

Qi, C., Ho, P. T. P., Wilner, D. J., et al. 2004, ApJ, 616, L11

Raghavan, D., McAlister, H. A., Henry, T. J., et al. 2010, ApJS, 190, 1

Rebull, L. M. 2015, AJ, 150, 17

Reipurth, B. 2000, AJ, 120, 3177

Reipurth, B., Clarke, C. J., Boss, A. P., et al. 2014, Protostars and Planets VI, 267

Reipurth, B. & Mikkola, S. 2012, Nature, 492, 221

Reipurth, B., Mikkola, S., Connelley, M., & Valtonen, M. 2010, ApJ, 725, L56

Roberts, H., Herbst, E., & Millar, T. J. 2003, ApJ, 591, L41

Robitaille, T. P., Whitney, B. A., Indebetouw, R., Wood, K., & Denzmore, P. 2006, ApJS, 167, 256

Rodriguez, D. R., Kastner, J. H., Wilner, D., & Qi, C. 2010, ApJ, 720, 1684

Rodríguez, L. F., Anglada, G., & Curiel, S. 1997, ApJ, 480, L125

Rodríguez, L. F., Anglada, G., & Curiel, S. 1999, ApJS, 125, 427

Sadavoy, S. I. & Stahler, S. W. 2017, MNRAS, 469, 3881

Saigo, K., Tomisaka, K., & Matsumoto, T. 2008, ApJ, 674, 997

Sakai, N., Oya, Y., López-Sepulcre, A., et al. 2016, ApJ, 820, L34

Sakai, N., Oya, Y., Sakai, T., et al. 2014a, ApJ, 791, L38

Sakai, N., Oya, Y., Sakai, T., et al. 2014b, ApJ, 791, L38

Sakai, N., Sakai, T., Hirota, T., et al. 2014c, Nature, 507, 78

Sakai, N., Sakai, T., Hirota, T., & Yamamoto, S. 2010, ApJ, 722, 1633

Sakai, N. & Yamamoto, S. 2013, Chemical Reviews, 113, 8981

Salinas, V. N., Hogerheijde, M. R., Mathews, G. S., et al. 2017, ArXiv e-prints [arXiv:1707.06475]

Sandell, G. & Knee, L. B. G. 2001, ApJ, 546, L49

Santangelo, G., Murillo, N. M., Nisini, B., et al. 2015, A&A, 581, A91

Sastry, K. V. L. N., Helminger, P., Charo, A., Herbst, E., & De Lucia, F. C. 1981, ApJ, 251, L119

Schnee, S., Brunetti, N., Di Francesco, J., et al. 2013, ApJ, 777, 121

Schnee, S., Enoch, M., Johnstone, D., et al. 2010, ApJ, 718, 306

Schöier, F. L., Jørgensen, J. K., van Dishoeck, E. F., & Blake, G. A. 2002, A&A, 390, 1001

Schöier, F. L., van der Tak, F. F. S., van Dishoeck, E. F., & Black, J. H. 2005a, A&A, 432, 369

Schöier, F. L., van der Tak, F. F. S., van Dishoeck, E. F., & Black, J. H. 2005b, A&A, 432, 369

Seifried, D., Banerjee, R., Pudritz, R. E., & Klessen, R. S. 2013, MNRAS, 432, 3320

Shirley, Y. L. 2015, PASP, 127, 299

Shu, F. H., Adams, F. C., & Lizano, S. 1987, ARA&A, 25, 23

Soderblom, D. R., Hillenbrand, L. A., Jeffries, R. D., Mamajek, E. E., & Naylor, T. 2014, Protostars and Planets VI, 219

Spezzano, S., Bizzocchi, L., Caselli, P., Harju, J., & Brünken, S. 2016a, A&A, 592, L11

Spezzano, S., Gupta, H., Brünken, S., et al. 2016b, A&A, 586, A110

Spezzano, S., Tamassia, F., Thorwirth, S., et al. 2012, ApJS, 200, 1

Stamatellos, D. & Whitworth, A. P. 2009a, MNRAS, 392, 413

Stamatellos, D. & Whitworth, A. P. 2009b, MNRAS, 400, 1563

Stamatellos, D., Whitworth, A. P., & Hubber, D. A. 2011, ApJ, 730, 32

Stark, R., Sandell, G., Beck, S. C., et al. 2004, ApJ, 608, 341

Tafalla, M., Kumar, M. S. N., & Bachiller, R. 2006, A&A, 456, 179

Takakuwa, S., Saito, M., Lim, J., et al. 2012, ApJ, 754, 52

Tassis, K., Willacy, K., Yorke, H. W., & Turner, N. J. 2012, ApJ, 753, 29

Terebey, S., Shu, F. H., & Cassen, P. 1984, ApJ, 286, 529

Theard, L. P. & Huntress, W. T. 1974, J. Chem. Phys., 60, 2840

Tobin, J. J., Bergin, E. A., Hartmann, L., et al. 2013a, ApJ, 765, 18

Tobin, J. J., Chandler, C. J., Wilner, D. J., et al. 2013b, ApJ, 779, 93

Tobin, J. J., Dunham, M. M., Looney, L. W., et al. 2015, ApJ, 798, 61

Tobin, J. J., Hartmann, L., Bergin, E., et al. 2012a, ApJ, 748, 16

Tobin, J. J., Hartmann, L., Chiang, H.-F., et al. 2012b, Nature, 492, 83

Tobin, J. J., Hartmann, L., Chiang, H.-F., et al. 2013c, ApJ, 771, 48

Tobin, J. J., Kratter, K. M., Persson, M. V., et al. 2016a, Nature, 538, 483

Tobin, J. J., Looney, L. W., Li, Z.-Y., et al. 2016b, ApJ, 818, 73

Tohline, J. E. 2002, ARA&A, 40, 349

Tomida, K., Machida, M. N., Saigo, K., Tomisaka, K., & Matsumoto, T. 2010, ApJ, 725, L239

van der Tak, F. F. S., Black, J. H., Schöier, F. L., Jansen, D. J., & van Dishoeck, E. F. 2007, A&A, 468, 627

van der Wiel, M. H. D., van der Tak, F. F. S., Ossenkopf, V., et al. 2009, A&A, 498, 161

van Dishoeck, E. F., Blake, G. A., Jansen, D. J., & Groesbeck, T. D. 1995, ApJ, 447, 760

van Dishoeck, E. F., Jansen, D. J., & Phillips, T. G. 1993, in , 541–566

van Kempen, T. A., van Dishoeck, E. F., Güsten, R., et al. 2009a, A&A, 507, 1425

van Kempen, T. A., van Dishoeck, E. F., Salter, D. M., et al. 2009b, A&A, 498, 167

van't Hoff, M. L. R., Walsh, C., Kama, M., Facchini, S., & van Dishoeck, E. F. 2017, A&A, 599, A101

Velusamy, T. & Langer, W. D. 1998, Nature, 392, 685

Visser, R., Bergin, E. A., & Jørgensen, J. K. 2015, A&A, 577, A102

Visser, R., Doty, S. D., & van Dishoeck, E. F. 2011, A&A, 534, A132

Visser, R., van Dishoeck, E. F., Doty, S. D., & Dullemond, C. P. 2009, A&A, 495, 881

Walawender, J., Bally, J., Kirk, H., & Johnstone, D. 2005, AJ, 130, 1795

Walawender, J., Bally, J., Kirk, H., et al. 2006, AJ, 132, 467

Walmsley, C. M., Flower, D. R., & Pineau des Forêts, G. 2004, A&A, 418, 1035

Whitney, B. A., Wood, K., Bjorkman, J. E., & Wolff, M. J. 2003, ApJ, 591, 1049

Willacy, K., Alexander, C., Ali-Dib, M., et al. 2015, Space Sci. Rev., 197, 151

Woodall, J., Agúndez, M., Markwick-Kemper, A. J., & Millar, T. J. 2007, A&A, 466, 1197

Wootten, A. 1987, in IAU Symposium, Vol. 120, Astrochemistry, ed. M. S. Vardya & S. P. Tarafdar, 311–318

Wootten, A., Andre, P., Despois, D., & Sargent, A. 1994, in Astronomical Society of the Pacific Conference Series, Vol. 65, Clouds, Cores, and Low Mass Stars, ed. D. P. Clemens & R. Barvainis, 294

Yang, B., Stancil, P. C., Balakrishnan, N., & Forrey, R. C. 2010, ApJ, 718, 1062

Yeh, S. C. C., Hirano, N., Bourke, T. L., et al. 2008, ApJ, 675, 454

Yen, H.-W., Koch, P. M., Takakuwa, S., et al. 2015, ApJ, 799, 193

Yen, H.-W., Koch, P. M., Takakuwa, S., et al. 2017, ApJ, 834, 178

Yen, H.-W., Takakuwa, S., Ohashi, N., & Ho, P. T. P. 2013, ApJ, 772, 22

Yıldız, U. A., Kristensen, L. E., van Dishoeck, E. F., et al. 2012, A&A, 542, A86

Yıldız, U. A., Kristensen, L. E., van Dishoeck, E. F., et al. 2015, A&A, 576, A109

Yıldız, U. A., Kristensen, L. E., van Dishoeck, E. F., et al. 2013, A&A, 556, A89

Yıldız, U. A., van Dishoeck, E. F., Kristensen, L. E., et al. 2010, A&A, 521, L40

Yoneda, H., Tsukamoto, Y., Furuya, K., & Aikawa, Y. 2016, ApJ, 833, 105

Young, C. H., Jørgensen, J. K., Shirley, Y. L., et al. 2004, ApJS, 154, 396

Young, K. E., Young, C. H., Lai, S.-P., Dunham, M. M., & Evans, II, N. J. 2015, AJ, 150, 40

Yu, T. & Chernin, L. M. 1997, ApJ, 479, L63

Zucconi, A., Walmsley, C. M., & Galli, D. 2001, A&A, 376, 650

Nederlandse samenvatting

Meervoudige sterren, groepen van 2 of meer sterren die bij elkaar gehouden worden door de onderlinge zwaartekracht, komen veel voor in het universum. Bepaalde karakteristieken van deze stergroepen, zoals de veranderlijke helderheid, hebben er toe geleid dat deze sterren een belangrijke culturele rol speelde in de oudheid. Sindsdien zijn deze meervoudige sterren onderwerp van wetenschappelijk onderzoek geweest en met de komst van de telescoop is de kennis van deze objecten toegenomen. Door de verbeterde techniek om het universum te observeren, hebben we ontdekt dat meervoudige sterren verantwoordelijk zijn voor een groot aantal belangwekkende fenomenen, van supernovae en planetaire nevels tot samensmeltingen tussen zwarte gaten. Meervoudige sterren spreken tot de verbeelding en zijn veelvuldig het onderwerp van sciencefiction, in woord en beeld. Men vraagt zich af wat voor planeten in dit soort systemen kunnen voorkomen, en hoe een dageraad met meerdere sterren er uit zal zien. Recente observaties van ruimte missies zoals de Kepler satelliet hebben laten zien dat planeten rond meervoudige sterren kunnen bestaan. Dit leidt tot de vragen: hoe vorm je een meervoudig systeem en wat zorgt er voor dat een meervoudig systeem stabiel is. De eerste theorieën stelden voor dat één ster een andere ster uit zijn baan trok om een dubbel ster te vormen. Deze theorieën hadden grote tekortkoming. Zo moet een groot aantal sterren zich zeer dicht bij elkaar bevinden en is het nodig dat een derde ster het systeem stabiliseert. Een beter begrip van de vorming en evolutie van sterren is nodig om de vragen rond de formatie van meervoudige sterren op te lossen.

Wat men heeft geleerd uit observatie en modellen over het proces van stervorming kan als volgt kort worden samengevat. Roterende wolken van dicht gas en stof kunnen, onder de juiste condities, samentrekken om in het binnenste van de wolk een protosterren te vormen. Deze ster in wording is dan nog ingekapseld door een grote hoeveelheid gas en stof. Deze ingekapselde protosterren zijn verantwoordelijk voor energieke, zeer geconcentreerde uitstromen, een kenmerk van actieve stervorming. De rotatie en samentrekking van het materiaal naar de protoster zorgt voor de vorming van een vlakke (roterende) structuur in het gas en stof, een "schijf". Van deze schijf wordt verwacht dat die vroeg in het stervormingsproces vormt. Uit deze schijf worden uiteindelijk de planeten en kometen gevormd. Met het verstrijken van de tijd groeit de protoster en veranderd de interne structuur, tegelijkertijd verdwijnt er materiaal uit de wolk van gas en stof waar de ster uit aan het vormen is. Dit komt zowel door de accretie van materiaal op de ster, als door de krachtige uitstromen die een deel van de wolk weg duwen. Als al originele gas en stof uit de omgeving verdwenen is, houden we een enkele jonge ster en planeten, als die gevormd zijn, over. Waarnemingen van protosterren, van de diepst ingekapselde protosterren tot de jonge sterren, laat zien dat meervoudige sterren veel voorkomen. Dit wijst er op dat de meeste sterren als

deel van een meervoudige ster worden gevormd en dat dus ons beeld van stervorming moet worden herzien. Het feit dat meervoudige sterren als zodanig worden gevormd, roept een wirwar van vragen op. Dit proefschrift richt zich op een aantal van deze open vragen rond de formatie en evolutie van meervoudige protosterren, namelijk:

1. Wanneer vormen schijven en hoe beïnvloeden ze de meervoudige protosterren?
2. Vormen alle sterren in een meervoudige sterren groep op hetzelfde moment?
3. Welke factoren verhogen of verlagen vormingsefficiëntie van meervoudige protosterren
4. Hoe vergelijkt de structuur, zowel fysisch als chemisch, van het kapsel van enkele en meervoudige protosterren zich.

De eerste vraag wekt interesse omdat schijven, naast dat ze de uiteindelijke locatie van planeet en komeet vorming zijn, ook een belangrijke rol kunnen spelen in de vorming van een meervoudige ster in de eerste stadia van het stervormingsproces. De volgende twee vragen moeten inzicht geven in het processen waardoor meervoudige sterren vormen. Er wordt gedacht dat meeste meervoudige sterren vormen door het fragmenteren van de geconcentreerde wolk waaruit een ster kan vormen. Door het fragmenteren vormt deze wolk niet één maar meerdere sterren. Het is nog niet duidelijk, wanneer deze fragmentatie gebeurd en wat er toe leidt dat de wolk fragmenteert en een meervoudige ster vormt, en wat de effecten zijn op de evolutie van deze protosterren. De vierde vraag zoekt inzicht naar de verschillen in structuur rond vormende protosterren en of deze verschillen het product zijn van de meervoudigheid van een deel van deze systemen of dat een ander proces voor deze verschillen verantwoordelijk is.

Met als doel deze vier vragen te beantwoorden worden waarnemingen van moleculen en stof gecombineerd met fysische en chemische modellen om de structuur van de ingekapselde protosterren te beschrijven. De emissie van het stof wijst op de locatie van de protoster en uit de emissie kan het stadium van de evolutie van de protoster worden afgeleid. Moleculen zijn belangrijk omdat de emissie lijnen gebruikt kunnen worden om de kinetische structuur te bepalen, de temperatuur en dichtheid van het gas te bepalen en omdat de chemische structuur van de geobserveerde protosterren kan worden bepaald. Verder kan de chemie ons helpen in het begrijpen van processen die plaats vinden in het universum.

Dit proefschrift

Hoofdstuk 1 van dit proefschrift bevat een gedetailleerde introductie tot het huidige begrip van stervorming van zowel enkele als meervoudige sterren. De observaties die in dit proefschrift worden gepresenteerd spannen het elektromagnetisch spectrum van millimetergolven tot het nabije infrarood. Zowel observaties vanaf de grond als vanuit de ruimte zijn gebruikt. De *Atacame Large Millimeter/submillimeter Array*, ook wel bekent als ALMA, is een radio interferometer die staat op het Chajnantor plateau in de Atacama woestijn in Chili. ALMA is gebruikt om de chemische and fysische structuur van meervoudige protosterren op schalen van 100 astronomische eenheden (1 astronomische eenheid is de gemiddelde afstand tussen de zon en de aarde) waar te nemen. Het *Atacama Pathfinder Experiment* (APEX), gesitueerd op hetzelfde plateau als ALMA, is een schotel antenne die gebruikt is om protosterren op schalen van wolk

kernen (1000 AE) te bestuderen. Uit de archieven van de *Herschel Space Observatory* en de *Spitzer Space Telescope* zijn de helderheidskaarten gebruikt.

Hoofdstuk 2 richt zich op de vraag wanneer schijven vormen. Voor dit doel is een zeer jonge ingekapselde protoster bestudeerd, VLA 1623-2417. VLA 1623-2417 is een drievoudige protoster in het midden van ρ Ophiuchus op een afstand van 391 lichtjaar. De drie componenten verschillen significant, waarschijnlijk omdat alle drie de protosterren zich in een ander evolutionair stadium bevinden. Een van de componenten, VLA 1623-2417 A, heeft een vlakke schijfachtige structuur die zichtbaar is in zowel het stof als in de moleculaire lijn emissie. De studie van de kinematica van $C^{18}O$ met een simpel model wijs er op dat de emissie inderdaad afkomstig is van een roterende schijf, met een straal van ongeveer 150 astronomische eenheden, vijf keer zo groot als de afstand tussen Neptunus en de zon. Omdat VLA 1623-2417 A een hele jonge, diep ingekapselde protoster is, is het bestaan van deze schijf bewijs van de vroege formatie van deze structuren tijdens het stervormingsproces.

Roterende schijven kunnen vroeg in het stervormingsproces vormen, zoals beschreven in Hoofdstuk 2. Het is daarom te verwachten dat deze schijven ook effect hebben op de evolutie van de protoster. Dit onderwerp wordt behandeld in Hoofdstuk 3, door het materiaal rond de roterende schijf van VLA 1623-2417 A te bestuderen. Het molecuul DCO^+ wordt gebruikt om het koude materiaal van VLA 1623-2417 A in kaart te brengen, omdat dit molecuul vooral wordt gevormd bij temperaturen onder de 20 K. Een simpel chemisch model is gebruikt om de DCO^+ emissie te analyseren. De positie van de geobserveerde DCO^+ emissie is dichter de protoster dan verwacht uit een sferisch symmetrische dichtheids- en temperatuurstructuur. Dit zou het geval zijn als de protoster de directe omgeving in alle richtingen gelijkmatig zou opwarmen. Daarentegen wordt de DCO^+ emissie dichter bij de protoster gevonden in het verlengde van de roterende schijf, maar niet in de richting van de bipolaire uitstroom. De reden hiervoor is dat de schijf zorgt voor een lagere temperatuur aan de buitenste rand van de schijf omdat de schijf een schaduw slaat op het achterliggende materiaal waardoor dat minder opgewarmd kan worden door de protoster. Dit is een indicatie dat de aanwezigheid van de schijf een significant effect heeft op het omliggende materiaal door zowel de temperatuur als chemische structuur te veranderen.

De fysisch-chemische structuur van ingekapselde protosterren wordt verder bestudeerd in Hoofdstuk 4 met behulp van moleculen die het koude en warme gas van protostellaire wolkenkernen in kaart kunnen brengen. Twee meervoudige protosterren, IRAS 16293-2422 en VLA 1623-2422 worden bestudeerd. Beide systemen zijn te vinden in de ρ Ophiuchus wolk en zijn zeer diep ingekapseld in hun natale wolkenkern. IRAS 16293-2422 is een zeer heldere dubbelle protoster, terwijl VLA 1623-2417 de zwakkere drievoudige protoster is die ook al bestudeerd is in Hoofdstukken 2 en 3. VLA 1623-2417 A heeft een roterende schijf (Hoofdstuk 2) en ook IRAS 16293-2422 A wordt omgeven door een grote, vlakke schijfachtige structuur met een straal van ongeveer 200 astronomische eenheden. De andere bronnen in deze systemen hebben geen bevestigde schijfachtige structuren. Het koude gas wordt in kaart gebracht met emissie van de moleculen DCO^+, N_2H^+ en N_2D^+. Al deze moleculen vormen bij temperaturen onder de 20 K en zijn dus het meest aanwezig in de koudste delen van het gas. Voor het in kaart brengen van de warmere omgeving met temperaturen tussen de 50 en 100 K of het deel van het gas dat door de protoster wordt belicht met UV straling worden de moleculen $c-C_3H_2$ en C_2H gebruikt. De "koude" moleculen worden dichtbij de verschillende objecten gevonden door de aanwezigheid van de schijf-achtige structuren,

maar alleen in het verlengde van de schijf. N_2H^+ en N_2D^+ zijn niet gedetecteerd in VLA 1623-2417, dit komt waarschijnlijk door de zeer lage temperaturen, onder de 10 K, veroorzaakt door de schijf die het omliggende materiaal afschermt van de protoster. Dit komt overeen met de resultaten gepresenteerd in Hoofdstuk 3. Het "warme" molecule c$-C_3H_2$ volgt de rand van de holte gecreëerd door de uitstroom in beide meervoudige protosterren. Dit is consistent met de aanwezigheid van dit molecuul in warm en UV-belicht gas. In het algemeen zijn c$-C_3H_2$ en C_2H aanwezig in hetzelfde gebied. Dit geldt voor VLA 1623-2417 maar niet voor IRAS 16293-2422. Een interessant resultaat van deze studie is dat de meervoudigheid van deze systemen geen significant effect lijkt te hebben op de structuren rond de protosterren, alhoewel hier nog veel onderzoek naar gedaan moet worden.

In Hoofdstuk 5 wordt de vraag of alle sterren in meervoudige stergroepen op hetzelfde moment gevormd worden onder de loep genomen. Om deze vraag te beantwoorden, worden ingekapselde protosterren bestudeerd, in plaats van protosterren in een later stadium van het stervormingsproces. Bij ingekapselde protosterren zijn de omstandigheden van de formatie bijna volledig intact, terwijl protosterren in latere stadia significante veranderingen in de omgeving hebben veroorzaakt. Het bestuderen van de jongste protosterren komt met een ander probleem: de leeftijden van ingekapselde protosterren zijn bijna onmogelijk om met zekerheid te bepalen. In het algemeen wordt het evolutionaire stadium, oftewel de "leeftijd", van een protoster bepaald aan de hand van de distributie van de lichtkracht als functie van de golflengte van het licht. Dit staat in de literatuur bekent als de "Spectral Energy Distribution (SED)". Gedurende het ingekapselde stadium is de helderheid van de protoster vooral geconcentreerd op de lange golflengten door het kapsel van stof waarin de protoster gevormd wordt. Terwijl de protoster groeit, verdunt de wolk kern die het kapsel van de protoster vormt waardoor meer en meer licht op korte golflengte ons kan bereiken. Op het moment dat de protoster een ster wordt en waterstof gaat verbranden, wordt het grootste deel van het licht uitgezonden in het optische deel van het spectrum. Het is moeilijk om aan een SED een precieze leeftijd vast te plakken. Het is daarentegen relatief makkelijk om twee SEDs te vergelijken en te bepalen of de objecten in hetzelfde stadium van de evolutie zijn of niet. Deze relatieve leeftijdsmeeting is gebruikt om te bepalen of alle sterren in een meervoudig systeem op hetzelfde moment zijn gevormd. De SEDs voor alle geïdentificeerde protosterren in de Perseus moleculaire wolk (afstand 750 lichtjaar) zijn geconstrueerd met data uit de literatuur en uit helderheidskaarten uit de archieven van de *Herschel Space Observatory*. De SEDs van de componenten van de meervoudige systemen kunnen alleen worden onderscheiden als de afstand tussen de componenten minsten 1600 astronomische eenheden bedraagt, de resolutie van de Hershel Space Observatory. De oriëntatie van de protoster ten opzicht van onze zichtlijn heeft effect op de waargenomen SEDs. Een protoster die een uitstroom heeft die in de richting van onze zichtlijn staat kan worden gezien als ouder omdat het kapsel niet zichtbaar is. Daarom moet de oriëntatie van de protosterren, samen met de SEDs en fysische structuur mee genomen worden om te kunnen concluderen of alle sterren in een meervoudig systeem op hetzelfde moment zijn gevormd. Het resultaat van dit onderzoek is dat in een derde van de meervoudige protosterren de componenten niet op hetzelfde moment gevormd zijn. Dat wil zeggen dat sommige wolk kernen nog nieuwe protosterren vormen zelfs nadat ze al één of twee protosterren hebben gevormd, terwijl dat bij andere wolk kernen niet gebeurt. Dit is belangrijke informatie voor de theorie en modellen van meervoudige ster vorming, en roept op hetzelfde moment de vraag op,

wat zorgt er voor dat sommige meervoudige protosterren doorgaan met het vormen van nieuwe protosterren.

Hoofdstuk 6 onderzoekt een van de mogelijk factoren die invloed kunnen hebben op meervoudige stervorming: temperatuur. Modellen die het opwarmen van het gas en stof door de centrale protoster meenemen, suggereren dat als een protoster eenmaal gevormd is, het verwarmde gas en stof niet verder zou kunnen fragmenteren. Daarentegen suggereren de resultaten in Hoofdstuk 5 dat er andere factoren zijn die fragmentatie en het vormen van meervoudige sterren beïnvloeden. Om te onderzoeken of er een relatie is tussen temperatuur en fragmentatie, wordt het gas en stof op schalen van 1000 astronomische eenheden onderzocht. Observaties met de enkele antenne van APEX worden gebruikt om moleculen te observeren die dienst doen als thermometers, zoals DCO^+ en H_2CO. Daarnaast worden ook moleculen waargenomen die oplichten in de regio die wordt opgewarmd door de protoster, zoals c$-C_3H_2$ en C_2H. Deze moleculen worden waargenomen op zichtlijnen in de richting van een aantal geselecteerde protosterren in de Perseus moleculaire wolk. De selectie bevat zowel enkele als meervoudige protosterren. Omdat zowel enkele als meervoudige systemen worden waargenomen is het mogelijk om deze te vergelijken, wat kan helpen om de precieze rol van de temperatuur in het vormingsproces van meervoudige sterren. De observaties en de temperatuur kaarten die afgeleid zijn van de waargenomen moleculen, laten zien dat er geen duidelijke relatie is tussen temperatuur en enkele of meervoudige sterren. Er wordt juist gevonden dat meervoudige protosterren een groter reservoir van koud gas om zich heen hebben in vergelijking met enkele protosterren. Deze waarneming suggereert dat massa en dichtheid, in tegenstelling tot temperatuur, een belangrijke rol spelen in fragmentatie en als gevolg daarvan, in de formatie van meervoudige protosterren.

Conslusie

De resultaten van dit proefschrift dragen belangrijke stukjes bij aan de puzzel van meervoudige stervorming. Deze worden hier kort samen gevat. Grote schrijven kunnen in een vroeg stadium van het stervormingsproces vormen en kunnen de fysisch-chemische structuur van protosterren beïnvloeden. Dit is belangrijk voor stervorming in het algemeen omdat het ons beeld van de stervormingsprocessen verandert. Daarnaast kunnen beide factoren, schijven en fysisch-chemische structuur, de formatie van meervoudige protosterren beïnvloeden omdat ze invloed hebben op de fragmentatie. Niet alle protosterren in een meervoudig systeem vormen op hetzelfde moment. Dit is een indicatie dat in sommige gevallen, de omstandigheden in de wolk kern zodanig zijn dat verdere fragmentatie, nadat er al een protoster gevormd is, mogelijk is. Deze omstandigheden zijn niet gerelateerd aan de temperatuur maar zouden wel gerelateerd kunnen zijn aan de massa en dichtheid. De resultaten uit dit proefschrift zijn een stap vooruit in ons begrip van de vorming van meervoudige protosterren, maar de weg is nog lang. Het zou bijvoorbeeld interessant zijn om uit te zoeken of de resultaten gevonden voor de Perseus moleculaire wolk ook gelden voor andere stervormingsgebieden. Onze visie over het proces van stervorming zou moeten worden herzien om ook meervoudige stervorming uit te kunnen leggen, omdat het een zeer veel voorkomende uitkomst van het stervormingsproces is. Modellen en theorieën moeten worden aangepast aan de uitkomsten van observaties, zodat de uitkomsten van de modellen een nieuwe richting aan kunnen geven voor verder observaties.

English summary

Multiple stars, that is two or more stars composing a gravitationally bound system, are common in the universe. Characteristics such as their varying brightness have lead to these stellar systems being given cultural importance in ancient cultures. They have also been of the subject of academic study, and with the advent of the telescope, our knowledge of these systems grew. With the expansion of our capacity to observe the universe, multiple stars have been found to be the cause of many interesting phenomena, from supernovae and planetary nebulae, to binary black hole mergers. Multiple stars have fueled our imagination, both in written and visual fiction, wondering what planets around these stellar systems would be like, and how multiple sunrises might appear. Recent observations of missions like Kepler have shown that planets can exist around multiple stars. The question of how these systems are formed rises from our curiosity and interest in figuring out what would lead to stable multiple stellar systems. Early theories proposed that one star would pull another star into its orbit, thus forming a binary stellar system. However, this idea had serious problems, such as the need for close proximity of a large number of stars, and the involvement of a third star. Understanding how stars form and evolve can help solve the question of the formation of multiple stars.

Based on observations and models, the process of star formation can be briefly sketched as follows. Rotating clouds of dense dust and gas can, under the right conditions, collapse to form protostars embedded deep within the core of the clouds. These embedded protostars drive strong narrow outflows, a signature of ongoing star formation. Rotation and the infall of material toward the star eventually lead to the formation of a flattened (rotating) structure, a disk, which is expected to form at some point in the early stages of star formation. The disk will be the eventual site of planet and comet formation. As the protostar evolves and grows, the material in the cloud core decreases both from accretion onto the protostar and the clearing effect of the outflow. When most of the surrounding material has been cleared, a single young star and planets, if any formed, remain. Observations of protostars, from the earliest embedded stages to the resulting young stars, show that multiple stars are common. This points to the fact that most stars are born as multiple stellar systems, and that our picture of star formation needs to be revised.

The fact that multiple stars are born has brought a myriad of questions regarding these systems. This thesis addresses several open questions relating to the formation and evolution of multiple protostellar systems, namely

1. When do disks form and what is their impact on the protostellar systems?

2. Do all stars in a multiple stellar system form at the same time?

3. What factors enhance or hinder the formation of multiple protostellar systems?
4. How do single and multiple stars compare in structure, both physically and chemically?

The first question is interesting since disks are not only the eventual site of planet and comet formation, but can also play a role in forming multiple stars in the early stages of the star formation process. The next two questions deal with the way multiple star form. Fragmentation, the process of material break-up in the star forming cloud core, is widely considered as the main formation mechanism of multiple stars. But it is not yet clear when and what factors lead to fragmentation and the eventual formation of a multiple protostellar system, and how it could affect their evolution. The fourth question aims to understand whether single and multiple stars have differences in their structure, and if they are product of multiplicity or some other process.

With the objective to address these questions, observations of molecules and dust emission are combined with physical and chemical models to describe the structure of the observed protostars. Dust emission traces the location of the protostar, and can help determine the stage of formation of the protostar. Molecules are important since they can trace the kinematics, function as temperature and density meters, and reveal the chemical structure of the observed protostars. Chemistry can be a powerful tool to understand the processes in the universe.

This thesis

Chapter 1 of this thesis gives a detailed introduction to our current understanding of star formation, both of single and multiple stars. The observations presented in this work span from millimeter to near-infrared wavelengths, and were obtained with ground and space-based telescopes. The Atacama Large Millimeter/submillimeter Array, also known as ALMA, is a radio interferometer located in the Chajnantor plateau, Atacama desert, Chile, and was used to observe the chemical and physical structure of multiple protostars at scales of 100 astronomical units (1 astronomical unit is the distance from the Earth to the Sun). The Atacama Pathfinder EXperiment (APEX), located near ALMA, is a single-dish radio telescope and was used to probe protostars at scales of the cloud cores (1000 astronomical units). Archival photometric maps from the Herschel Space Observatory and the Spitzer Space Telescope were used in this work as well.

Chapter 2 addresses the question of when disks form. For this purpose, a very young embedded protostellar system, VLA 1623-2417, is studied. VLA 1623-2417 is a triple protostellar system located in the heart of ρ Ophiuchus (distance = 391 light-years). The three components show different characteristics, most likely product of being at different evolutionary stages. One of the components, VLA 1623-2417 A, presents a flattened disk-like structure both in dust and molecular line emission. Studying the kinematics traced by the molecule $C^{18}O$ with a simple model indicates that the emission is indeed tracing a rotating disk, with a radius of about 150 astronomical units, five times the radius of Neptune's orbit. Given that VLA 1623-2417 A is a very young, deeply embedded, protostar, finding a rotating disk around this source evidences that these structures can form very early in the star formation process.

Rotating disks can form in the early stages of star formation, as described in Chapter 2, thus their presence must impact the evolution of the protostar in some

manner. This question is addressed in Chapter 3, by studying the material surrounding the rotating disk of VLA 1623-2417 A. For this purpose, molecules typically associated with the cold material in the cloud core of protostars are studied. The molecule DCO^+ is used to trace the cold material of VLA 1623-2417 A, since this molecule is mainly formed at temperatures of 20 K or below. Combining the observations with a simple chemical model can help to analyze the DCO^+ emission. The position of the observed DCO^+ emission is found to be closer to the source than expected from a spherically symmetric density and temperature structure, that is if the protostar were heating up the surrounding material equally in all directions. Instead, the DCO^+ emission is observed to be closer to the protostar along the rotating disk, but not along the direction of the outflow. The reason for this is that the disk causes a drop in temperature at its edge because it is shadowing the material from heating by the protostar. This indicates that the presence of a disk has a significant impact on the surrounding material, by altering both its temperature and chemical structure.

The physico-chemical structure of embedded protostars is further studied in Chapter 4, using molecules that trace the cold and warm gas of protostellar cloud cores. Two multiple protostellar systems, IRAS 16293-2422 and VLA 1623-2422, are studied. Both protostellar systems are located in ρ Ophiuchus and are deeply embedded in their natal cloud core. IRAS 16293-2422 is a very bright protostellar binary, while VLA 1623-2417 is a dimmer triple protostellar system studied in Chapters 2 and 3. VLA 1623-2417 A has been found to have a rotating disk (Chapter 2), while IRAS 16293-2422 A presents a large, flattened disk-like structure with a radius of about 200 astronomical units. The other sources in each system have no confirmed disk(-like) structure. The cold gas is traced by the molecules DCO^+, N_2H^+ and N_2D^+, which form at temperatures below 20 K and thus characterize cold regions. For warm environments with temperature of 50 to 100 K or UV-irradiated by the central protostar, the molecules $c-C_3H_2$ and C_2H are good tracers. The cold molecules are found to be located closer to the source in both systems due to the presence of the disk(-like) structure, but not along any other direction. For VLA 1623-2417, N_2H^+ or N_2D^+ are not observed, most likely due to the low brightness of the protostar, and the very low temperatures (below 10 K) caused by the disk which shadows the material. This agrees with the results of Chapter 3. The warm molecule $c-C_3H_2$ traces the outflow cavity in both systems, consistent with the presence of this molecule in warm and UV-irradiated environments. The molecules $c-C_3H_2$ and C_2H tend to trace the same region. This is true for VLA 1623-2417, but not for IRAS 16293-2422. It is interesting to note that the multiplicity of these systems does not seem to have a significant impact in the chemical structure, however this needs to be explored further.

Chapter 5 examines the question if all stars in a multiple stellar system form at the same time. In order to answer this question, embedded protostars are studied, rather than protostars in later stages of the star formation process. This is because embedded protostars have the conditions of formation almost intact, while protostars in the later stages have undergone considerable evolution. However, this also poses a problem. The ages of embedded protostars are almost impossible to determine with certainty. On the other hand, the evolutionary stage of a protostar, its “age" in a way, is determined by the distribution of their brightness with respect to wavelength, also termed a spectral energy distribution (SED). During the embedded stage, the brightness of a protostar is mostly concentrated at long wavelengths due to the dust cocoon in which the protostar is formed. As the protostar evolves, the cloud core disperses

and the brightness of the protostar progressively shifts to shorter wavelengths, and as it becomes a hydrogen-burning star its brightness peaks in the visible regime. Thus, the evolutionary stage of a protostar relative to its siblings in a multiple protostellar system is used to determine whether all the protostars in the system formed at the same time or at different moments. The SEDs for all the identified protostellar systems in the Perseus molecular cloud (distance = 750 light-years) are constructed using data from literature and archival photometric maps from the Herschel Space Observatory. For multiple protostellar systems, the SEDs of the individaul components can only be disentangled for separations between the protostars of 1600 astronomical units, due to the resolution of the Herschel Space Observatory observations. The orientation of the protostar with respect to the line of sight can impact the constructed SED, since a protostar viewed along its outflow will appear older than it may actually be, since no envelope would be detected. Thus to determine whether the protostars within multiple systems are formed simultaneously or not, the orientation of the protostar, its physical structure and the SED are taken into consideration. The results of this study find that one-third of the time, the components of multiple protostellar systems are not formed at the same time. In other words, some cloud cores continue forming protostars even after one or two have formed, while others do not. This provides important information for theory and models of multiple star formation, and at the same time, leads to the question of what factors cause some multiple protostellar systems to continue forming protostars.

Chapter 6 examines one of the possible factors that can influence multiple star formation: temperature. Models that include the heating of the gas and dust by the central protostar suggest that once a protostar is formed, the heated gas and dust does not generally fragment further. However, the results from Chapter 5 suggest that there are other factors that influence fragmentation and the formation of multiple stars. To address whether there is a temperature-fragmentation relation or not, the gas and dust at scales of 1000 astronomical units is investigated. Single-dish observations with APEX are used to observe molecules that are good thermometers, such as DCO^+ and H_2CO, as well as molecules that trace regions irradiated by the protostar, such as $c-C_3H_2$ and C_2H. These molecules are observed toward a selected sample of protostellar systems in the Perseus molecular cloud which includes single and multiple systems. Including both types of systems allows the comparison of conditions in single and multiple stars, which can help determine whether temperature is a key element in multiple star formation. The observations, and derived temperature measurements from the observed molecules, show that there is no clear relation between temperature and multiple or single stars. In fact, the only observed difference is that multiple stellar systems have large cold gas reservoirs compared to single protostars. These findings suggest that mass and density, rather than temperature, play a role in fragmentation, and consequently, the formation of multiple protostellar systems.

Conclusions

The results from this thesis contribute useful pieces to the puzzle of multiple star formation, and are briefly summarized here. Large disks can form in the early stages of star formation, and they can impact the physicochemical structure of protostars. This is important for star formation in general, since it changes our view of the process of protostellar evolution. But in addition, both of these factors, disks and the physico-

chemical structure, can influence the formation of multiple protostellar systems, since they provide ingredients for fragmentation. Not all protostars in a multiple protostellar system form at the same time. This indicates that in some cases, the conditions in the cloud core are appropriate for further fragmentation. These conditions, however, are not associated with temperature and instead could be related to mass and density.

The results of this thesis provide a step forward in understanding the formation of multiple protostars, but additional research is needed. For example, it would be interesting to find out if the results found for the Perseus molecular cloud also apply to other star forming regions. Our understanding of the process of star formation needs to be revised to include the formation of multiple stars, since they are the most common outcome of star formation. Models and theory should be revised with the results of observations, and the predictions that come out of these models can then provide direction for our observations.

Resumen en español

Estrellas múltiples, es decir dos o más estrellas que forman parte de un sistema gravitacionalmente unido, son comunes en el universo. Características como variaciones en su luminosidad, les han dado significado cultural a estos sistemas estelares en distintas civilizaciones antiguas. También han sido objeto de estudio por parte de la academia; y con el desarrollo del telescopio, el conocimiento sobre estos cuerpos celestes aumentó de manera significativa. La expansión de la capacidad para observar el universo demostró que las estrellas múltiples son la causa de varios fenómenos interesantes; por ejemplo, algunos tipos de supernovas, nebulosas planetarias y fusión de agujeros negros binarios. Las estrellas múltiples han alimentado nuestra imaginación, tanto en forma escrita como visual. Se ha imaginado como serían los planetas alrededor de este tipo de estrellas, y la experiencia de ver múltiples amaneceres y atardeceres. Observaciones recientes, como las de la Misión Kepler, han demostrado que pueden existir planetas alrededor de estrellas múltiples. La pregunta de cómo estos sistemas son formados proviene de la curiosidad e interés por descubrir que produce sistemas de estrellas múltiples estables. Algunas teorías propusieron que una estrella capturaría a otra en su órbita, y así se formaría un sistema binario. Pero esta idea presenta serios problemas, como la necesidad de cortas distancias entre un gran número de estrellas, e involucraría una tercera estrella. El entender cómo las estrellas se forman y evolucionan puede ayudar a resolver el problema de la formación de estrellas múltiples.

Basado en observaciones y modelos, el proceso de formación de estrellas se puede describir brevemente de la siguiente forma: nubes densas de gas y polvo que rotan pueden, bajo las condiciones apropiadas, colapsar para empezar a formar estrellas en el centro de las nubes. Estas protoestrellas producen chorros y flujos bipolares, lo cual constituye evidencia del proceso de su formación. La rotación y acreción de material alrededor de la estrella eventualmente forma una estructura achatada y giratoria, también llamada disco, la cual se forma en algún momento durante las etapas tempranas de formación. El disco es el lugar donde eventualmente se formarán planetas y cometas. Con el crecimiento y evolución de la protoestrella, el material del núcleo protoestelar se reduce debido a la acreción y los flujos bipolares que dispersan el material de la nube. Al final, una estrella y sistema de planetas, si alguno se formó, persisten. Observaciones de protoestrellas en todas las etapas de formación demuestran que las estrellas múltiples son comunes. Esto indica que la mayoría de estrellas nacen como sistemas estelares múltiples, y que la teoría de formación de estrellas debe ser revisada. El hecho que las estrellas múltiples nacen genera numerosas preguntas. Por ello, esta tesis propone examinar varias preguntas relativas a la formación y evolución de protoestrellas múltiples, a saber:

1. ¿Cuándo se forman los discos y cuál es su impacto en los sistemas protoestelares?

2. ¿Se forman al mismo tiempo todas las estrellas en un sistema múltiple?

3. ¿Qué factores intensifican o dificultan la formación de protoestrellas múltiples?

4. ¿Cómo están estructuradas, en términos químicos y físicos, las estrellas en sistemas múltiples e individuales?

La primera pregunta es interesante ya que los discos no solamente son el sitio donde se forman los planetas y cometas, sino que también juegan un papel en la acreción de material a la protoestrella. Las dos siguientes preguntas tratan el mecanismo de formación de estrellas múltiples. Se considera que la fragmentación, el proceso por el cual el material del nucleo protoestelar se fracciona, es el proceso para formar sistemas estelares múltiples. Pero aún no se comprende bien cuáles factores inciden y cuándo ocurre la fragmentación, y cómo puede afectar la evolución de la protoestrella múltiple. La cuarta pregunta busca entender las diferencias en la estructura de estrellas múltiples e individuales, y si estas diferencias son producto de la formación o de otro proceso.

Con el objetivo de contestar estas preguntas, observaciones de la emisión de moléculas y polvo son combinadas con modelos físicos y químicos para describir la estructura de las protoestellas observadas. La emisión del polvo traza la ubicación de la protoestrella, y puede ayudar a conocer la etapa de formación de la misma. Las moléculas son importantes ya que trazan la cinemática de la protoestrella, al igual que funcionan como termómetros, medidores de densidad y describen la estructura química de estos sistemas. La química sirve como una herramienta para comprender el funcionamiento del universo.

Esta tesis

El primer capítulo de esta tesis da una detallada introducción del conocimiento actual sobre la formación de estrellas, tanto de estrellas individuales como múltiples. Por ello, las observaciones aquí descritas abarcan longitudes de onda desde lo milímetrico hasta cercano a infrarrojo. El Atacama Large Millimeter/submillimeter Array (ALMA) es un interferómetro de radio ubicado en el llano de Chajnantor, desierto de Atacama, Chile, el cual se utiliza para observar la estructura química y física de protoestrellas múltiples a escalas de 100 unidades astronómicas (una unidad astronómica es la distancia entre el Sol y la Tierra). El Atacama Pathfinder EXperiment (APEX), ubicado cerca de ALMA, es un radio telescopio de una antena y fue utilizado para observar los núcleos protoestelares (1000 unidades astronómicas). Mapas fotométricos obtenidos con el Observatorio Espacial Herschel y el Telescopio Espacial Spitzer también son utilizados en esta tesis.

El segundo capítulo trata acerca de cuándo se forman los discos. Con este propósito se estudió VLA 1623-2417, un sistema protoestelar muy joven. VLA 1623-2417 es un sistema triple protoestelar ubicado en el centro de ρ Ophiuchus (distancia = 391 años luz). Las tres protoestrellas muestran diferentes características, probablemente producto de estar en distintas etapas de evolución. Una de las protoestrellas, VLA 1623-2417 A, presenta una estructura achatada similar a un disco en emisión de polvo y molecular $C^{18}O$. La cinemática de esta estructura es examinada con un modelo físico, el cual indica que es un disco giratorio con un radio de 150 unidades astronómicas, cinco veces el radio de la órbita de Neptuno. Ya que VLA 1623-2417 A es una protoestrella

muy joven, los resultados son evidencia de que los discos giratorios pueden formarse en las etapas tempranas de formación estelar.

El tercer capítulo busca entender el impacto de los discos giratorios en las etapas tempranas de la formación de estrellas. Para ello, se estudia el material que rodea el disco giratorio de VLA 1623-2417 A mediante moléculas típicamente asociadas con material frío en los núcleos protoestelares. La molécula DCO^+ traza el material frío de VLA 1623-2417 A, ya que esta molécula se forma principalmente a temperaturas de 20 Kelvin o menos. Las observaciones de la emisión de DCO^+ son analizadas con un modelo químico simple. La posición de la emisión de DCO^+ se encuentra más cerca a la fuente protoestelar de lo esperado, esto basado en la estructura esféricamente simétrica de densidad y temperatura; es decir, la estructura como si la protoestrella estuviese calentando el material del núcleo de igual manera en toda dirección. En contraste, la emisión de DCO^+ se encuentra cerca de VLA 1623-2417^a, a lo largo del plano del disco giratorio, pero no en dirección del flujo bipolar. Esto indica que la presencia de un disco giratorio produce un impacto significativo en el material que lo rodea, alterando tanto su temperatura como su estructura química.

La estructura físico-química de protoestrellas jóvenes es estudiada más a fondo en el cuarto capítulo, usando moléculas que trazan las regiones frías y cálidas de los núcleos protoestelares. Dos sistemas muy jóvenes de estrellas múltiples son examinados, IRAS 16293-2422 y VLA 1623-2417, ambos ubicados en ρ Ophiuchus. IRAS 16293-2422 es un sistema binario muy brillante; mientras que VLA 1623-2417 es un sistema triple menos brillante y fue estudiado en los capítulos dos y tres de esta tesis. VLA 1623-2417 A tiene un disco giratorio (capítulo 2), mientras que IRAS 16293-2422 A presenta una estructura achatada similar a un disco con un radio de 200 unidades astronómicas. Las otras protoestrellas en los respectivos sistemas no presentan un disco ni estructura achatada. El gas frío es trazado por las moléculas DCO^+ N_2H^+ y N_2D^+, las cuales se forman a temperaturas bajo 20 Kelvin, y de esta manera caracterizan las regiones frías. Las moléculas c$-C_3H_2$ y c-C_2H son adecuadas para ambientes cálidos con temperaturas entre 50 y 100 Kelvin o irradiados por rayos ultravioleta por la protoestrella central. Las moléculas frías se encuentran más cerca de las fuentes protoestelares en cada sistema, debido a la presencia del disco, pero no en otras direcciones como la del flujo bipolar. Alrededor de VLA 1623-2417, las moléculas N_2H^+ y N_2D^+ no son detectadas. La causa de ello es el bajo brillo de la protoestrella y las temperaturas bajas del gas (por debajo de 10 Kelvin) causadas por la sombra que genera el disco en el material. Esto concuerda con los resultados del tercer capítulo. La molécula c$-C_3H_2$ traza la cavidad del flujo bipolar en ambos sistemas, consistente con la presencia de esta molécula en ambientes cálidos e irradiados con rayos ultravioleta. Las moléculas c$-C_3H_2$ y C_2H tienden a residir en el mismo ambiente. Mientras que esto es observado en VLA 1623-2417, no lo es en IRAS 16293-2422. Es interesante resaltar que el hecho que estos sistemas son múltiples no parece tener un impacto significativo en la estructura química; sin embargo, se requiere investigación adicional para corroborar este resultado.

El quinto capítulo examina la pregunta de si todas las estrellas en un sistema estelar múltiple se forman al mismo tiempo. Para responder esta pregunta, protoestrellas jóvenes, en lugar de protoestrellas en etapas tardías de evolución, son estudiadas. Esto porque las protoestrellas jóvenes tienen las condiciones de formación casi intactas, mientras que las protoestrellas en etapas tardías han cambiado considerablemente debido al proceso de formación. No obstante, el usar protoestrellas jóvenes presenta

un problema. Determinar las edades de protoestrellas jóvenes con certeza es casi imposible. Por otro lado, la etapa evolucionaria de una protoestrella, su edad en cierto sentido, es determinada por la distribución de su brillo con respecto a la longitud de onda, también llamado la distribución de energía espectral (DEE). Durante la etapa más temprana, el brillo de la protoestrella está concentrada en longitudes milimétricas de onda debido al núcleo de polvo en el cual la protoestrella es formada. Con la evolución de la protoestrella, el gas y el polvo del núcleo protoestelar se dispersa y el brillo de la protoestrella progresivamente se mueve hacia longitudes de onda en el infrarrojo, y cuando la estrella inicia fusión nuclear, su brillo se concentra en el espectro visible. En consecuencia, la etapa evolucionaria de una protoestrella relativa a las otras fuentes de un sistema protoestelar múltiple es utilizada para determinar si todas las protoestrellas en un sistema fueron formadas al mismo tiempo o en diferentes épocas. Las DEE para todas las protoestrellas identificadas en la nube molecular Perseo (distancia = 750 años luz) son construidas utilizando datos encontrados en la literatura y mapas fotométricos del observatorio espacial Herschel. La orientación de la protoestrella con respecto a la línea de vista del observador puede impactar la DEE, ya que una protoestrella vista a lo largo del flujo bipolar aparenta ser más desarrollada de lo que realmente es, ya que no se detectaría el polvo del núcleo protoestelar. Entonces, para determinar si las fuentes de un sistema protoestelar múltiple se forman simultáneamente o no, la orientación de la fuente, su estructura física y la DEE son consideradas en conjunto. Los resultados de este estudio encuentran que, en un tercio de sistemas múltiples, los componentes de estos sistemas no son formados simultáneamente. En otras palabras, algunos núcleos protoestelares continúan formando protoestrellas, aun luego de que una o dos se han formado. Esto constituye una pieza de información importante para la teoría y los modelos de formación de estrellas múltiples, y al mismo tiempo conduce a la pregunta de cuáles factores causan que algunos sistemas protoestelares múltiples continúen formando protoestrellas.

El capítulo sexto examina uno de los posibles factores que pueden influenciar la formación de estrellas múltiples: la temperatura. Modelos que incluyen el calentamiento del gas y polvo por la estrella central sugieren que cuando una protoestrella se ha formado, el gas y polvo caliente generalmente no se fragmenta. Sin embargo, los resultados del quinto capítulo sugieren que hay otros factores involucrados en la fragmentación y formación de estrellas múltiples. Para abordar el tema de si hay o no una relación entre temperatura y fragmentación, el gas y polvo a escalas de 1000 unidades astronómicas es investigado. El radiotelescopio APEX es utilizado para observar moléculas que funcionan como termómetros; por ejemplo, DCO^+ y H_2CO, al igual que moléculas que trazan regiones irradiadas por la protoestrella, como $c-C_3H_2$ y C_2H. Estas moléculas son observadas hacia una muestra seleccionada de sistemas protoestelares en la nube molecular Perseo. La muestra incluye tanto sistemas múltiples como individuales, lo cual permite comparar las condiciones en ambos tipos de sistemas y ayuda a determinar si la temperatura es un elemento clave en la formación de estrellas. Las temperaturas obtenidas mediante la comparación de las moléculas observadas demuestran que no hay una clara relación entre temperatura y la multiplicidad de estrellas. Estos resultados sugieren que la masa y la densidad juegan un papel importante en la fragmentación, y consecuentemente, en la formación de sistemas protoestelares múltiples.

Conclusiones

Los resultados de esta tesis contribuyen con información importante al campo de la formación de estrellas múltiples, y son brevemente resumidos a continuación. Discos con radios de 100 o más unidades astronómicas pueden formarse en las etapas tempranas de formación estelar, y pueden impactar la estructura físico-química de las protoestrellas. Esto es esencial para la formación de estrellas en general, ya que cambia la teoría del proceso de evolución protoestelar. Además, los discos y la estructura físico-química pueden impactar la formación de estrellas múltiples, ya que proveen los ingredientes para la fragmentación. No todas las fuentes en un sistema múltiple protoestelar se forman simultáneamente. Esto indica que, en algunos casos, las condiciones del núcleo protoestelar son apropiadas para continuar fragmentándose. Sin embargo, la temperatura no parece ser un factor significativo para la fragmentación, pero la masa y densidad si lo son.

Los resultados de esta tesis aportan un paso adelante en la comprensión de formación de estrellas múltiples, pero es necesario continuar investigando. Por ejemplo, sería interesante estudiar si los resultados encontrados en la nube molecular Perseo también podrían aplicarse a otras regiones de formación de estrellas. Nuestra comprensión del proceso de formación de estrellas necesita ser revisada para incluir la formación de estrellas múltiples, ya que son el producto más común. Los modelos y la teoría deben ser ajustados de acuerdo a lo que muestran las observaciones, y las predicciones de estos modelos pueden proveer la dirección para nuestras observaciones.

日本語の要旨

多重星，つまり重力的に拘束された2つ以上の星から成る系は，宇宙に普遍的に存在する。 これらの恒星系は，明るさの変動などの特性から，古代文化において文化的重要性を持っていた。 一方で，学術研究の対象となり，望遠鏡の発明に伴い我々の多重星に関する知識は増えていった。 我々の宇宙を観測する能力が拡大するにつれて，超新星爆発，惑星状星雲，バイナリブラックホール合体に至るまで，多重星が多くの興味深い現象の原因であることが明らかとなってきた。 多重星は小説や映画などのフィクションの中で，恒星系の周りの惑星がどのようなものになるのか，また複数の星による日の出がどのように見えるのだろうかと， 我々の想像力を掻き立てる。 ケプラー望遠鏡のような最近の観測ミッションは，惑星が多重星の周りにも存在することを明らかにしている。 何が安定した多重星系につながるかという我々の好奇心と興味から，これらのシステムがどのように形成されるのか，という問いが生まれる。 初期の理論では，1つの星が別の星をその軌道に引き寄せることで，連星系が形成されると考えられていた。 しかしこの理論には，多数の星が接近する必要があること，3つ目の星が関与するという深刻な問題がある。 星の形成と進化の理解は，多重星形成の問題を解決するのに役立つだろう。

観測とモデルに基づいた星形成過程の概要は以下である。 回転する，高密度のガスとダストから成る分子雲は，適切な条件下で重力収縮し，分子雲コア中に深く埋もれた原始星を形成する。 これらの埋もれた原始星は，星形成の兆候である，強力な細いアウトフローを引き起こす。 回転と星への物質降着は，星形成の初期段階のある時点で形成されると考えられる扁平な（回転する）構造，つまり円盤の形成をもたらす。 円盤は最終的に，惑星と彗星の形成の場となる。 原始星が進化して成長するにつれて，原始星への降着とアウトフローによる流出の両方により，分子雲コアの質量は減少する。 分子雲コアの大部分がなくなると，若い星と惑星が形成されていれば，それらが残る。 最も初期の埋もれた原始星の段階から若い星までの観測は，多重星が一般的であることを示している。 このことは，ほとんどの星が多重星系として生まれていること，そして星形成についての我々の理解が修正される必要があることを意味する。

多重星が生まれるという事実は，多くの疑問をもたらす。 本論文は，多重原始星の形成と進化に関するいくつかの未解決問題に取り組む，つまり

1. いつ円盤が形成され，系にどのような影響を与えるか？
2. 多重星系の中の全ての星は同時に形成されるのか？
3. 多重原始星系の形成を促進する，あるいは妨げる要因は何であるか？
4. 単一星と多重星系は，それらの物理的・化学的構造がどのように異なるか？

円盤は惑星形成・彗星形成の場となるだけでなく，星形成過程の初期段階で多重星形成の一因となり得るため，最初の問いは興味深い。 二つ目と三つ目の問いは，

多重星形成の仕方についてである。 星形成が起こる分子雲コアの中でガスが分裂する過程は，多重星の主要な形成機構と考えられている。 しかし，いつ・どのような要因が分裂につながり，最終的に多重原始星系が形成され，それらの進化に影響を与えるのかはよく分かっていない。 第四の問いは，単一星と多重星で構造に違いがあるかどうか，もし違いがあるならば，その違いが複数の星が存在することに起因するかどうか，を理解することを目的としている。

これらの問題に，分子輝線及びダスト連続波の観測と原始星の物理化学構造を記述するモデルを組み合わせることで取り組む。 ダスト連続波は原始星の位置を探り，原始星形成の進化段階を決めるのに有用である。 分子は，ガスの運動を探り，温度および密度計として機能し，原始星の化学構造を明らかにすることができるため重要である。 化学は宇宙で何が起こっているかを理解するための強力な道具となり得る。

本論文

本論文の第一章では，単独星と多重星形成に関する現状の理解について詳しく述べられている。 本研究で使用した観測データは，ミリメートルから近赤外までの波長に及んでおり，地上望遠鏡，及び宇宙望遠鏡により取得されたものである。 アタカマ大型ミリ波/サブミリ波干渉計（ALMA）は，チリのアタカマ砂漠にある電波干渉計である。 本研究では，ALMAを用いて100天文単位スケール(1天文単位は地球から太陽までの距離)で，多重原始星の化学的・物理的構造を観測した。 ALMAの近くにあるアタカマパスファインダー実験機（APEX）は，単一鏡の電波望遠鏡であり，分子雲コア（1000天文単位）のスケールで原始星を探査するために用いた。 Herschel 宇宙望遠鏡とSpitzer宇宙望遠鏡により取得された，アーカイバルの測光マップも本研究では用いた。

第二章では，円盤がいつ形成されるのかという問題に取り組んでいる。 この目的のために，まだ分子雲コアに埋もれた進化段階にある，非常に若い原始星VLA 1623-2417を研究する。 VLA 1623-2417は，へびつかい座ρ分子雲（距離391光年）の中心に位置する，三重連星系である。 三つの原始星は異なる特徴を示すため，異なる進化段階にある可能性が高い。 その1つであるVLA 1623-2417 Aは，ダスト連続波および分子輝線放射の両方において扁平な円盤状構造を示す。 $C^{18}O$分子輝線によりガスの運動を探り，単純なモデルによる解析から，放射は実際に回転円盤をトレースしていることが分かった。 円盤半径は約150天文単位であることが分かり，これは海王星の軌道半径の5倍である。 VLA 1623-2417 Aがコアに深く埋もれた非常に若い原始星であることを考えると，回転円盤構造が星形成過程の非常に早い段階で形成されることを示している。

第二章で述べたように，回転円盤は星形成の初期段階で形成し得る。 よって回転円盤は原始星の進化に何らかの影響を与えるに違いない。 第三章で，VLA 1623-2417 Aの回転円盤を取り巻く物質を研究することでこの問い取り組む。 この目的のために，典型的に分子雲コアの冷たい物質をトレースする分子を研究する。 DCO^+分子は主として20 K以下の温度で生成されるので，この分子をVLA 1623-2417 Aの冷たい物質をトレースするために用いる。 観測結果を単純な化学反応ネットワークモデルと組み合わせ，DCO^+分子輝線観測の解釈を行う。 観測されたDCO^+輝線の位置は，球対称な密度・温度構造（つまり，原始星が周囲の物質を等方的に加熱する場合に対応）から予想されるよりも，中心星に近いことが分かる。 またDCO^+輝線は，回転円盤方向に沿っては原始星近傍で観測されるが，アウトフローの方向ではそうではない。 この理由は，円盤が原始星からの輻射を遮ることで，円盤外縁部付近の物質の温度が低下するためである。 これは，円盤の存

在が温度と化学構造の両方を変えることにより，周囲の物質に大きな影響を与えることを示している。

分子雲コアに埋もれた原始星の物理化学構造は，冷たいガスと暖かいガスをトレースする分子を用いて，第四章でさらに研究されている。 IRAS 16293-2422とVLA 1623-2422の二つの多重原始星系が研究されている。 どちらの天体もへびつかい座ρ分子雲中に存在し，分子雲コアに深く埋もれている。 IRAS 16293-2422は非常に明るい原始連星である。 VLA 1623-2417は第二章と第三章で研究された，より暗い原始三重連星である。 VLA 1623-2417 Aは回転円盤を持ち（第二章），IRAS 16293-2422 Aは扁平な円盤状の構造（半径約200天文単位）を持つ。 それぞれの系の他の原始星には，円盤（状の）構造は見つかっていない。 冷たいガスは，DCO^+，N_2H^+およびN_2D^+によってトレースされる。 これらの分子は20 K以下の温度で生成される，すなわち冷たい領域に特徴的な分子である。 50-100 K程度の温かい環境，または中心星によって紫外線照射された領域では，c$-C_3H_2$とC_2H分子が良いトレーサー分子となる。 両方の天体において，冷たい分子は円盤方向には中心星近傍に存在するが，他の方向には同様の傾向は見られない。 これは円盤（状）構造の存在のためである。 VLA 1623-2417の場合，原始星が暗く，円盤に作られる影の効果によって非常に低温（10 K以下）のために，N_2H^+とN_2D^+は検出されていない。 これは第三章の結果と一致する。 両方の天体において，c$-C_3H_2$はアウトフローキャビティーをトレースする。 これはc$-C_3H_2$が温かく，紫外線照射された環境に存在することと整合的である。 c$-C_3H_2$とC_2Hは同じ領域をトレースする傾向にあるが， これはVLA 1623-2417には当てはまるが，IRAS 16293-2422には当てはまらない。 興味深いことに，これらの系が多重星系であることは化学構造に大きな影響を及ぼさないように思われるが，これについてはさらなる研究が必要である。

第五章では，多重星系を構成する全ての星が同時に形成されるかどうかを調べる。 そのために，星形成過程の後期段階にある原始星ではなく，埋もれた原始星を調べる。 後期段階にある原始星が形成後の進化を経ているのとは異なり，埋もれた原始星は形成時の状況をほとんど損なっていないためである。 しかしながら，この手法にも問題がある。 埋もれた原始星の年齢を精度よく決めることが，ほとんど不可能なことである。 一方，原始星の進化段階，ある意味では「年齢」は，波長に対する輝度の分布（スペクトルエネルギー分布，あるいはSED）によって決定される。 埋もれた段階の間，原始星の輝度は主に長波長側で大きい。 原始星が進化するにつれ，分子雲コアは消失し，原始星の輝度は徐々に短波長側にシフトする。 水素燃焼が星内部で始まると，その輝度は可視領域で最大となる。 よって，一つの原始多重星系の中で，それを構成する各原始星の進化段階を比較することで，系内の原始星がすべて同時に形成されるか，あるいは異なる時点で形成されるかを決定する。 ペルセウス分子雲（距離=750光年）で同定された全ての原始星系のSEDは，Herschel 宇宙望遠鏡のアーカイバル測光マップのデータおよび文献値を使用して構築した。 Herschel 宇宙望遠鏡の空間分解能のため，原始多重星系に属する個々の原始星に対するSEDは，原始星間距離が1600天文単位以上の場合のみ分離することができる。 視線方向に対する原始星の向きは，構築されたSEDに影響を及ぼす可能性がある。 例えばアウトフローに沿って観測された原始星は，エンベロープが検出されないため，実際よりも老いたように見えるだろう。 よって，多重星系の原始星が同時に形成されるかどうかを決定するために，原始星の向き，物理的構造およびSEDを考慮する。 研究の結果，3分の1の時間，原始多重星系の原始星は同時に形成されないことを見出した。 言い換えると，1つまたは2つの原始星が形成された後でさえ原始星が形成され続ける分子雲コアもあれば，そうではない分子雲コアも存在する。 これは，多重星形成の理論とモデルに重要な情報を

提供すると同時に，どんな要因によって，多重星系が原始星を形成し続けるのかという問題を提起する。

第六章では，多重星形成に影響を及ぼす可能性のある要因の一つ，温度について調べる。 コア中心に存在する原始星によるガスおよびダスト加熱を考慮したモデルは，原始星がいったん形成されると，加熱されたガスおよびダストは一般的にはさらに分裂しないことを示唆している。 しかし，第五章の結果は，ガスの分裂と多重星形成に影響する他の要因があることを示唆している。 温度と分裂に関係があるかどうかを調べるために，1000天文単位のスケールでガスとダストを調べる。 APEXを用いた単一鏡観測で，DCO^+およびH_2COのような温度計となる分子，ならびに原始星によって照射された領域をトレースする分子，c$-C_3H_2$およびC_2H，を調べた。 これらの分子を，ペルセウス分子雲中の原始星サンプルで観測する。 サンプルには単一星および多重星系が含まれている。 両方のタイプの系を含めることで，単一星と多重星系の状態の比較が可能になり，温度が多重星形成の鍵となる要素であるかどうかを判断するのに有用である。 結果として，温度と多重星系か否か，との間には明確な関係がないことを示す。 実際，観測される唯一の違いは，多重星系が単一星と比較して，大きな冷たいガスを持つことである。 これらの知見は，温度よりむしろ質量と密度が分裂，ひいては原始多重星系の形成に重要なことを示唆している。

結論

本論文の結果は多重星形成の理解の進展に大きく貢献する。 以下で簡潔に要約する。 巨大な円盤は星形成の初期段階で形成され，原始星系の物理化学的構造に影響を与え得る。 これは星形成・進化過程に対する私たちの理解を変えるため，星形成一般にとって重要である。 しかし加えて，円盤の存在およびその物理化学的構造への影響は，分裂を促進する可能性があり，原始多重星系形成に影響を及ぼし得る。 原始多重星系の全ての原始星が同時に形成されるわけではない。 これは，分子雲コアの物理状態の方が分裂に適している場合があることを示唆する。 しかし，分裂条件は温度に関連しておらず，むしろ質量および密度に関連している可能性がある。

本論文の結果は，原始多重星系形成の理解を進めるものであるが，さらなる研究が必要である。 例えば，ペルセウス分子雲の結果が他の星形成領域にも当てはまるかどうかを調べることは興味深い。 多重星形成が星形成過程の最も一般的な結果であるため，星形成過程に対する我々の理解は，多重星形成を含むように修正する必要がある。 モデルと理論は観測結果により修正されるべきであり，モデルによる予測は観測の指針となる。

Obaösterreichisch-Linzarische Zomfossung

A Meafochsteansystem bsteht aus mehrere Stern, die durch Schwerkroft zomgehoidn wern. Soiche Meafochsteansysteme hom die Menschheit scho imma fasziniert, und sie san a recht häufig im Universum verglichn mit Einzlsterna. Wegn ernare Hellikeitsschwonkungen und ondere scheinboa mysteriöse Eignschoften ham vaschiedenen Kulturn sie ois Götter, guade Omen oda ondare Vazeichn gsehn. A heizdog san Meafochsteansysteme des Zü von fü wissenschoftlicha Foaschung, und durchs moderne Teleskop is unsa Wissn enorm gwoxn. Meafochsteansysteme beflügln a heit unsa Fantasie, und sie san oft Ikonen in da Litaratur und Füm, ma denke nur an Sonnauf- oder Untagäng mit mehrare Sonnen auf an fremden Planeten. Heid wissn ma, dass soiche Systeme da Auslösa oda Uasprung fia füle intaressante Phenomene, wie zum Beispü Supernovas, Planetare Nöwi, und verschmözende Schwoaze Löcha, san. Wödraumteleskope wie Kepler ham bewiesen, dass zb. Exoplaneten in Meafochsteansystemen ned nur Fiktion san, sondern wiaklich existirn. Heute erforschen ma oiso ned mer ob, sondern wie soiche Systeme entstengan, und unter wöchen Bedingungen sie stabil bleibn. Früare wissnschoftliche Theorin san davon ausgonga, dass a Stean an ondaran einfongt, und so a Zwillingssysteme büdt. Olladings hom diese Onsätze graviernde Lückn ghobt, wei sie drauf basiern, dass vüle Sonnen noh beinonda entstengan oda zumindest a zusätzliche dritte Sonn no Einfluss nema miassad. Deswegen is es heizdog wichtig genau zu vasteh, wie a Sonn entsteht, damit ma die Entsteung von Meafochsteansystemen entschlüssln konn.

Basind auf astronomische Beobochtungn und Modölle ko ma den Prozess von da Sternenentstehung wie foigt beschreibn: Rotierade Gas- und Staubwoikn kolabiern und diaf in da Mittn von di Woikn büdn sie Protosterna. A Protostean erzeugt don an noch außen grichtetn Gasstrom, wos üblichaweis ois stoaka Hinweis drauf gsehn wird, dass a neiche Sonn entsteht. Dach die die Eigenrotation von der Sonn und des Material wos einizogen wird, wird die Woikn imma flocha und fongt on sich söwa a zum drahn. Des Endagebnis nennt ma don a Sternscheibn, und ma nimmt o, dass si die Scheibn irgndwonn am Onfong vom Entsteungsprozess büdt, und in ia donn speda a Planetn und Sternschnuppn entstengan. Die Woikn um den Protostan schrumpt donn mit da Zeit imma mea, da Matrial aus da Woikn vom Gasstrom wegtrogt wird oder indn Protostean foid. Üba Zeit verschwindt die Woikn don, und üba bleibt donn a neichs Sonnensystem mit Sterna und (eventuö) Planetn. Astronomische Beobochtungen vo olle Entwicklungstufn hom zagt, dass Systeme mit mehr ois aner Sonn die Regl san, ned die Ausnom. Des hast damit oiso a, dass die meistn Sonnen ned alan entstengan sondern in an Meafochsteansystem. Wa miaßn deswegn unsa bisherigs Konzept von

da Steanentsteung ändan.

Scho alan wegen ihra Existnz koman füle Frogn zua Entsteung und Entwicklung vo Meafochsteansystemen auf, und in diesa Doktoaobait gengan ma a boa davon aufn Grund:

1. Wonn entstengan die Staubscheiben und wos fia an Einfluss homs auf an Protostean?
2. Entwickln si olle Sonnen in an Sonnensystem zur söbn Zeid?
3. Wöche Eignschoftn regn oda behindan die Entwicklung von an Protostean zu Meafochsteansysteme anstöh vo an afochn Stean?
4. Is da kemische und physische Aufbau von an oafochn Stean vergleichboa mit Meafochsteansysteme?

Die erste Frog is voa ollem intaressant wei in Sternenscheibn ned nua Planetn und Sternschnuppn entstengan, sondern wei ma a was, dassi die Entsteung von Meafochsteansystemen beeinflussn. In die nextn beidn Frogn gehts um die Oat und Weis wia Meafochsteansysteme entstengan. Der Zafoi von Materieklumpn im Zentrum von aner Materiewoikn in mehrare Kernn, a Fragmentierung gnont, wird oigemein ois Hauptgrund für die Entsteung vo Meafochsystemen ongsehn. Dabei is owa ned kloa wos übahaupt die Framentierung auslöst, und wie genau die donn die weidare Entwicklung beeinflusst. Die letze Frog züt darauf wöche Untaschiede Meafoch- und Einzlsystemen Untaschiede im Aufbau hom, und ob die durch Mehrfochentwicklungen oder ondare Prozesse entstondn san. Diese Dissatation befasst si im Detai mit derane Frogn und verbindt Beobochtungen von Molekül und Staubemissionen mit phyikalische und kemische Modelle um die Struktur von Protosteana zu beschreibn und erfassn. Staufemissionen zeichnen die Region noch, in dem sich a Protostean befindt, und höffn dabei sei Evolutionsstadium zu erkennan. Moleküllinien ondaraseits san wichtig um die Kinematik von an Stern nochzvoiziehn, und fungiern ois Temperatur und Dichtemessa, und mochn damid die kemische Zusammensetzung von an Protostean sichtboa. Chemie is dahea a mächtigs Weakzeig zum Vasteh von die Voagänge im Wötraum.

Üwa diese Doktoaoabeit

Des easte Kapitl von diesa Dissatation enthoit a detailiate Einführung in die Sternenentstehung für einzelne und Mehrfochstern. Die Datn die dazu verwndt worn san stammen von die Teleskope ALMA (Atacama Large Millimeter/submillimeter Array) und APEX (Atacama Pathfinder EXperiment), und deckn Wellenlängen von Millimeter- bis zum Nah-Infratrotbereich ob. ALMA is a Radiointerferometer am Chajnantor Plateau in da Atacama Wüstn in Chile, und wir hams gnutzt um den kemischn und physikalischn Aufbau von mehrere Protosterne mit einer Durchschnittsgress vo circa 100 AE (Astronomischen Einheitn) zu studiern. APEX dagegen is a alleinsteendes Radioteleskop in da Nehe von ALMA. Wir hom APEX gnutzd um circa 1000 AU große Woikn um Protosterne zu beobochtn, und hom die Beobachtungen durch Archivdaten von die Weltraumteleskope Herschel und Spitzer komplementiad.

Im zweitn Kapitl wird anhand von VLA 1623-2417, an evolutionär jungen Protostean, untersucht wie Sternscheibn entstengan. VLA 1623-2417 is a Dreifochsystem

im Herzn vo ρ Ophiuchus und 391 Lichtjaa von uns entfernt. VLA 1623-2417 bsteht aus 3 Komponenten (Teile) und jede Komponentn waist vaschiedene Eigenschoftn auf, wos darauf hindeit, dass si die Teile in verschiedenen Phasn ihra Entwicklung befindn. Die easte Komponentn, VLA 1623-2417 A hod a floche, scheibnoatige Struktur mit Staub und Molekülhülle. Noch intensivem Stuidum von da Kinematik mit Hüfe vom Molekül $C^{18}O$ und oafache physikalische Modelle hot si zagt, dass die Emissionen von der Quelle a rotierende Scheibn mit circa 150 AE nochzeichnen, wos dem fünffochn Radius vom Neptunorbit entspricht. Wei VLA 1623-2417 A in ander sehr frühn Entwicklungsphase is, kenan ma oiso schliaßn, dass si rotierade Sternscheibn scho sehr früh ausbüdn kenan.

Da si rotirade Scheiben scho zu an frühn Entwicklungsstdium von an Stean büden kenan, miassns a des Endresultat von seina Entwicklung beeinflussen. Disa Schluss wird daher in Kapitl 3 eingehend beleutet, wo des koide Umgebungsmatrial und da Kern von da Woikn in da Scheibn von VLA 1623-2417 A genau betrocht wern. Dazu wird des Molekül DCO^+ benutzt, weis hauptsächlich bei Temperatuan um 20 K oder drunter gformt wird, und des koide Umgebungsmatrial daduach guad nochzeichnen wern ko. Die Beobachtungsdaten kombiniert mit an oafochn kemischn Modö erlaums die DCO^+ Emissionen genauer zu analysiern, und zagn dass die Position von DCO^+ nea am Kern is ois wie wenn da Protostean des Umgebungsmaterial gleichmäß aufhazen würd. Anstott auf a spherisch-symetrische Dichte und Temparaturstruktur hinzweisn, worn DCO^+ Emissionen längs von dea Scheibn näa om Protostern ois on die Endn. A Grund dafia is, dass die Scheibn die restliche Materiewoikn gegenüba dem Protostern beschottet, und dadurch an Temparaturabfoi verursocht. Des weist drauf hi, dass die Scheibn an direkten Einfluss aufs Umgebungsmaterial hod indems sei Temperaturverteilung und kemische Zusommensetzung vaendat.

In Kapitl 4 wiad die physikalisch-kemische Strukta von zwa eingebetteten Meafochprotosterna (IRAS 16293-2422 und VLA 1623-2417), anhond von Moleküln die woams und koids Gas im Zentrum von aner Protosternwoikn nochzeichnen, untasuacht. Beide von den Quön san a schon in Kapitl 2 und 3 analysiert worn, und san a sehr hella Doppiprotostean und a dunklara Dreifochstern, und san beide diaf eingebettet in ihr Materiewoikn in ρ Ophiuchus. Es is erkennboa dass VLA 1623-2417 A a rotierade Scheibn hod (siehe Kapitl 2), wohingegn IRAS 16293-2422 A a große, floche scheibnoatige Struktur mit Radius 200 AU hod. Bei di ondan Quön die beobocht worns san, san kane Scheibn oda scheibenoatige Strukturn sichtboa. DCO^+, N_2H^+ und N_2D^+ büdn si unter 20 K und zeichnen daduach koids Gas noch, wohingegn $c-C_3H_2$ and C_2H si zwischen 50 und 100 K oda unta UV-bestrohlung büdt, und damit woams Gas guad nochzeichnen. Die koidn Moleküle san dabei in beide Systeme enlong die scheibnoatign Strukturn noh an a Quön festgstöd woan, aowa ned in ondara Richtungen. Woascheinlich aufgrund von da geringen Helligkeit und da sehr niedrigen Temperatur unterhoib von 10 K afgrund vom Schottn von da Scheibn von VLA 1623-2417, hod ma ka N_2H^+ or N_2D^+ gfundn, sondern nur des woame Molekül $c-C_3H_2$, wos den Materialobfluss guad nochzeichnd. $c-C_3H_2$ und C_2H zeichnen beide die söwe Regionen noch, wos a bei VLA 1623-2417 nochgwiesen is, owa bei IRAS 16293-2422 ned verfizierboa woa. Insgesamt is hier vor ollem interessant, dass die Multiplizität von diese Systeme kan signifikantn Einfluss auf den kemischn Aufbau hod, und des soit in da Zukunft no genaua erfoascht wern.

In Kapitl 5 schaun ma uns o, ob olla Stern in an Mehrfochsystem si zur gleichen Zeid büdn, indem ma uns Protostane oschaun die no in ihr Woikn aibet san, denn bei denan

is da Umgebungszuastond no recht ähnlich wie zur Sternentsteung. Weidaentwicklde Steansysteme hom si dagegen scho vü steaka vaendat, wos die Oitasbestimmung donn owa a wieder sehr schwea oda goa unmöglich mocht. Ondaraseits wiad die Entwicklungsstufn von an Protostern, gewissamoßn sei Oita, durch sei Helligkeit auf diverse Wönlengen bestimmt, die Spektralenergievateilung (SED). In da Entwicklungsstufn wo a Protostern no in sei Woikn einbettet is, schein er wegn sein Staufkokon hauptsächlich auf längere Wönlengen hell. Wärend da weidaren Entwicklung vaziagt si don die Woikn, die Helligkeid vom Protostern verschiabt si don longsom zu die küzan Wönlengen, und da neiche Stern fongt on maxmimal Hell zum wern wenn er Wossastoff zum verbrenna ofongt. Deswegen wird des Helligkeitsverhötnis von Protosterna in an System releativ zuanonda verwendt um aussazfinden ob die Stern olla gleichzeitig entstondn san oda zeitlich unabhängig. In diesm Kapitl verwendn ma dahea die SEDs von olle ois Protostern identifizierte Systeme in Perseus (in circa 750 Lichtjoah Distanz) basierend auf Archivmaterial (Literaturmaterial und photometrische Koatn vom Wödraumteleskop Herschel). Auf Grund von da beschränktn Auflösung von Herschel kenan die SEDs von Meafochsystemen nur in Einzlkomponentn aufglöst wean, wenn die Protosteane mindestens 1600 AU ausanonda san. A die Orietierung von an Protostean im Raum ko die SED beeinflussn, denn a Protostean, endlong von seim Ausfluss betrocht, wird öda ausschaun ois aus aner ondan Perspektivn, wei des Umgebunsmaterial föd. Ma muas oiso nebman Aufbau und da SED a die Orientierung von an Stean analysian, wenn man bestimmen wü, ob die Komponentn von an Mehrfochsystem gleichzietig entstondn san oda ned. In diesem Kapitl kommen ma daher zum Schluss, dass in an Drittl von die Protosteannsystemen die Komponentn ned gleichzeitig entstondn san, und dass, söbst wenn a oda zwa Protosterna si scho büdt hom, si a no weidare Komponentn foamen kenan. Diese Resultate san daher sehr weatvoi und ergänzn die Theorie und von da Steanentstehung. Außerdem werfn sie die Frog auf, wöche Faktorn die Entstehung von weidare Protosteane in existierade Systeme auslösn.

In Kapitl 6 wiad aner von die meglichn Einflussfaktoan auf Meafochsteanentsteung betrocht: Temparatur. Gändige wissnschoftliche Modelle zagn, dass aufghazta Staub und Gas nimma zu weidara Framentierung füan, soboid da erste Protostern gformt worn is. Olladings zagt Kapitl 5, dass no ondare Faktorn die Entsteung von Mehrfochsteanen beeinflussn kenan. Um aussazfindn ob aner von die Faktoan die Temparatur is, wern deswegn in dism Kapitl Gas und Staub im Radius von 1000AU um a System betrocht. Die Datn dazu kuman aus APEX-Einzlschüsslbeobochtungen von Moleküln die guade Temperaturmesser san, zum Beispü DCO^+ und H_2CO, und soiche die von Protosteanen bestroite Regionen guad nochzeichnen, zum Beispü $c-C_3H_2$ und C_2H. Beobochtungen von diese Moleküle san in dem Kapitl deswegn füq vaschiedane Einzl- und Mehrfochprotosteansysteme in Perseus ongstöd worn, wos es ermöglicht ian Enwicklungsstond und die Vahötnisse zwischen Meafoch- und Einzlsteansystemen zu vagleichn, und damit donn höfn ko aussazfindn ob Temparatur waklich a Schlüsslfaktor in da Entsteung von Mehrfochsystemen is. Duach diesn Vagleich konntn ma zagn, dass es ka direkte Vabindung zwischen Temperatur und Mehrfochheit gibt, und im Gegenteil, die anzige Gemeinsomkeit is, dass Mehrfochsysteme üba a groß Reservoir aus koidn Gas vafügn ois Einzlsysteme. Die Ergebnisse weisn drauf hin, dass Masse und Dichte Einflussfaktorn fia Framentierung san, und damit a für die Entsteung von Meafochsteansystemen.

Schlusswoat

Diese Dissertation leistet mehrare wichtige Beiträge zum generellen Verständnis von da Sternentstehung, die im Foigendn noamoi kurz zommgfosst wern. Große Scheibn kenan si scho in am frühn Entwicklungsstdium entwickln, und sie kenan den physikalischkemischn Aufbau von Protosteanen beeinflussn. Des is inbesondere wichtig für den oigemeinen Sternentstehungsprozess, weils des grundlegendes Verständnis von da Entstehung von Protosterna vaändat. Zusätzlich kenan sowoi Scheibn ois a da physikalischkemische Aufbau die Entwicklung von Protosteannsystemen beeinflussn, wei sie Zutatn liefan die fia die Fragmentierung wichtig san. Protosterna in Mehrfochsystemen kenan sie a unobhängig vonananda büdn, oiso ned nur zeitgleich zuananda, wos darauf hinweist, dass in monche Fälle die Zuständ im Woiknkern no weidere Fragmentierung ermeglichn. Diese Umstände henagan olladings ned mit da Temperatur zom, kuntn owa mit da Masse und da Dichte von da Woikn zomhengan.

Die Ergebnisse die in diesa Dissertation präsentiert wern stelln an Schritt voaweats im Verständnis von da Stern- und Protosternentstehung, owa zagn a dass no weidare Forschung notwendig is um die damit einhergehendn neichn Frogn zu beontwurden. Zum Beispü wärs interssant aussazfindn, ob Schlüsse aus unsere Beobochtungen von Perseus a fia ondare Regionen zuadreffn. Unsa Büd vom da Sternentstehungsprozess muss genarell ana Revision untazogn werdn, um insbesondere a die Entwicklung von Meafochsteansystemen zu erklean, weil diese die wahrscheinlichstn und hiefigstn Endprodukte in da Sternentstehung san. A unsare physikalischen und kemischn Simulationen und die dahinta Theorie soit um die Eagebnisse die ma aus astronomischn Beobachtungen ergänzt werden, um don weidare Vorhersogn treffen zkena worauf ma in Zukunft unsa wissnschoftlichs Augnmeak richtn miassn.

Streszczenie w języku polskim

Układy wielokrotne – składające się z dwóch lub więcej gwiazd tworzących grawitacyjnie związany system – są powszechne we Wszechświecie. Ich szczególne własności, takie jak zmienna jasność, sprawiały że tego rodzaju systemy gwiazdowe kształtowały wyobraźnię już w czasach starożytnych. Były one również przedmiotem badań akademickich, zwłaszcza po skonstruowaniu pierwszych teleskopów. Wiedza na temat układów wielokrotnych gwiazd rosła wraz z coraz większymi możliwościami obserwacji Wszechświata. Pozwoliły one ustalić, że takie układy mogą być przyczyną występowania wielu ciekawych zjawisk, od supernowych i mgławic planetarnych, po zlewające się systemy dwóch czarnych dziur. Układy wielokrotne gwiazd regularnie pobudzały wyobraźnię na przykład w kontekście występowania wokół nich planet. W jaki sposób wyglądają układy planetarne wokół wielu gwiazd? Jak mogą przebiegać wielokrotne wschody i zachody gwiazd?

Niedawne obserwacje misji Kepler pokazały, że planety występują wokół gwiazd wielokrotnych. Pytanie w jaki sposób takie układy powstały jest naturalną konsekwencją naszej ciekawości i chęci zrozumienia, co powoduje powstawanie stabilnych układów wielokrotnych. Wczesne teorie koncentrowały się na scenariuszu, w którym jedna z gwiazd ściąga drugą na swoją orbitę i w ten sposób tworzą układ podwójny. Jednak ten pomysł miał poważne problemy, w szczególności potrzebę występowanie bardzo wielu gwiazd w niedużych odległościach od siebie i udział w procesie także trzeciej gwiazdy. Zrozumienie w jaki sposób gwiazdy powstają i ewoluują może pomóc rozwiazać zagadkę występowania układów wielokrotnych gwiazd.

Opierając się na obserwacjach i modelach, proces powstawania gwiazd może zostać naszkicowany w następujący sposób. Rotujące obłoki gęstego pyłu i gazu mogą, przy korzystnych warunkach, zacząć kolaps grawitacyjny i uformować protogwiazdę głęboko zanurzoną w gęstym jądrze takiego obłoku. Takie zanurzone protogwiazdy wyrzucają silne i wąskie wypływy molekularne, które są sygnaturą trwającego aktualnie procesu powstawania giwazdy. Rotacja oraz zapadanie się materiału na gwiazdę ostatecznie prowadzi do powstania spłaszczonej, rotującej struktury - dysku - która prawdopodobnie tworzy się na wczesnych etapach powstawania gwiazdy. Dysk w przyszłości stanie się miejscem powstawania planet i komet. W czasie gdy protogwiazda rośnie i ewoluuje, ilość otaczającej jej materii maleje, zarówno z powodu akrecji na protogwiazdę, jak i rozpraszania gazu i pyłu przez wypływ molekularny. Gdy większość materiału zostanie już usunięta, pozostaje już tylko pojedyńcza młoda gwiazda i planety, jeśli tylko powstały. Obserwacje wielu protogwiazd od etapu głęboko zanurzonego w materii do całkowicie z niej oczyszczonego pokazują, że układy wielokrotne gwiazd występują powszechnie. To z kolei sugeruje, że większość gwiazd rodzi się jako układy wielokrotne, a nasza wizja procesu powstawania gwiazd powinna uwzględnić ich ist-

nienie.

Fakt powstawania układów wielokrotnych gwiazd powoduje powstanie rozlicznych pytań dotyczących tych układów. Ta praca doktorska dotyka wielu otwartych pytań związanych z powstawaniem i ewolucją układów wielokrotnych gwiazd:

1. Kiedy powstaje dysk i jaki jest jego wpływ na układ protogwiazd?

2. Czy wszystkie gwiazdy w układzie wielokrotnym powstają jednocześnie?

3. Jakie czynniki wzmacniają lub utrudniają powstanie układów wielokrotnych gwiazd?

4. W jakim stopniu gwiazdy pojedyncze i układy wielokrotne są podobne jeśli chodzi o strukturę, zarówno fizyczną jak i chemiczną?

Pierwsze z powyższych pytań jest szczególnie interesujące, ponieważ dyski to nie tylko miejsca powstawania planet i komet, ale mogą również grać rolę przy tworzeniu układów wielokrotnych na wczesnym etapie procesu powstawania gwiazd. Następne dwa pytania związane są ze sposobem, w jaki układy wielokrotne powstają. Fragmentacja, jako proces rozrywania materiału w jądrze formującym gwiazdę, jest powszechnie uważana za główny mechanizm tworzenia układów wielokrotnych. Nie jest jeszcze jednak wiadomo kiedy i jakie czynniki wpływają na pojawienie się fragmentacji i ostateczne powstanie układu wielokrotnego oraz jego ewolucję. Czwarte pytanie ma na celu zrozumienie, czy pojedyncze i wielokrotne gwiazdy różnią się swoją strukturą [budową] i czy te różnice są wynikiem wielokrotności czy jakiegoś innego procesu.

Aby podjąć próbę odpowiedzi na powyższe pytania, wykonałam obserwacje emisji pochodzącej od molekuł i pyłu oraz skonstruowałam modele fizyko-chemiczne, aby opisać strukturę obserwowanych protogwiazd. Emisja pochodząca od pyłu pokazuje położenie protogwiazdy i pomaga określić etap, na którym znajduje się tworząca się protogwiazda. Molekuły są ważne, ponieważ umożliwiają badanie kinematyki obiektu, w funkcji temperatury i gęstości, i ujawniają strukturę chemiczną protogwiazd. Znajomość procesów chemicznych może być bardzo ważnym narzędziem przy próbie zrozumienia Wszechświata.

Ta praca doktorska

Rozdział 1 zawiera szczegółowe wprowadzenie do aktualnego stanu wiedzy z zakresu powstawania gwiazd, zarówno dla gwiazd pojedynczych i wielokrotnych. Obserwacje przedstawione w tej pracy doktorskiej obejmują zakres od fal milimetrowych do bliskiej podczerwieni i zostały uzyskane przy użyciu instrumentów naziemnych oraz satelitów kosmicznych. Sieć anten submilimetrowych ALMA (*ang.* the Atacama Large Millimeter/submillimeter Array), która pracuje jako interferometr radiowy położony na płaskowyżu Chajnantor na pustyni Atakama w Chile, została wykorzystana do obserwacji chemicznej i fizycznej struktury układów wielokrotnych protogwiazd w skalach przestrzennych rzędu setek jednostek astronomicznych (1 jednostka astronomiczna to odległość Ziemi od Słońca). Teleskop APEX (*ang.* the Atacama Pathfinder EXperiment), położony w pobliżu ALMA, to radioteleskop o pojedynczej antenie, który w tej pracy został użyty do badania protogwiazd w skalach przestrzennych podobnych do

wielkości jąder tworzących gwiazdy (tysiące jednostek astronomicznych). Wykorzystane również zostały archiwalne mapy fotometryczne z Kosmicznego Obserwatorium Herschela i Teleskopu Kosmicznego Spitzera.

Rozdział 2 poświęcony jest próbie odpowiedzenia na pytanie, kiedy powstaje dysk. Aby to zrobić, badany jest bardzo młody układ wielokrotny protogwiazd - VLA 1623-2417. VLA 1623-2417 jest układem potrójnym położonym w sercu ρ Ophiuchus (w odległości 391 lat świetlnych). Trzy składniki układu wykazują duże różnice, prawdopodobnie z powodu różnic w etapie ewolucyjnym. Jeden ze składników, VLA 1623-2417 A, posiada spłaszczoną strukturę przypominającą dysk widoczną zarówno w emisji molekuł, jak i pyłu. Badania kinematyki gazu przy użyciu molekuły $C^{18}O$ i prostego modelu pokazują, że ta emisja w istocie pochodzi z rotującego dysku o promieniu około 150 jednostek astronomicznych, czyli pięć razy większego niż orbita Neptuna. Ponieważ VLA 1623-2417 A jest bardzo młodą, głęboko zanurzoną protogwiazdą, znalezienie rotującego dysku wokół tego obiektu jest dowodem, że tego rodzaju struktury powstają na bardzo wczesnym etapie powstawania gwiazd.

Jak pokazuje Rozdział 2, rotujące dyski mogą się tworzyć podczas wczesnych etapów powstawania gwiazd. Stąd ich obecność musi w jakiś sposób wpływać na ewolucję protogwiazdy. Ten problem poruszony jest w Rozdziale 3 poprzez badanie materiału otaczającego rotujący dysk VLA 1623-2417 A. Wykorzystano w tym celu molekuły związane zwykle z chłodnym materiałem w obłoku molekularnym wokół protogwiazd. Molekuła DCO^+ użyta została do zbadania tego chłodnego materiału, ponieważ powstaje głównie w temperaturze 20 K lub niższej. Połączenie obserwacji z prostym modelem chemicznym pozwala na analizę emisji DCO^+. Zaobserwowana emisja w DCO^+ jest położona bliżej źródła niż przewidywałby model o sferycznie symetrycznym rozkładzie gęstości i temperatury tzn. sytuacji, gdyby protogwiazda ogrzewała otaczający ją materiał w sposób równomierny we wszystkich kierunkach. Zamiast tego, emisja w DCO^+ obserwowana jest bliżej protogwiazdy wzdłuż rotującego dysku, ale nie wzdłuż wypływu molekularnego. Spowodowane jest to obniżeniem temperatury na brzegu dysku z powodu zacienienia materiału od strony ogrzewającej go protogwiazdy. Wskazuje to na duży wpływ obecności dysku na otaczający materiał, skutkujący zmianami w rozkładzie temperatury i strukturze chemicznej.

Fizyko-chemiczna struktura zanurzonych protogwiazd jest dalej badana w Rozdziale 4 przy użyciu molekuł, które są wzbudzane przez chłodny i ciepły gaz obecny w jądrach protogwiazdowych. Badane są dwa układy wielokrotne – IRAS 16293-2422 i VLA 1623-2417. Oba systemy protogwiazd położone są w ρ Ophiuchus i są głęboko zanurzone w macierzystych jądrach materii. IRAS 16293-2422 jest bardzo jasnym układem podwójnym podczas gdy VLA 1623-2417 jest słabszym układem potrójnym protogwiazd badanym w Rozdziałach 2 i 3. W VLA 1623-2417 A został odkryty rotujący dysk (Rozdział 2), podczas gdy IRAS 16293-2422 A posiada dużą, spłaszczoną strukturę dyskopodobną o promieniu rzędu 200 jednostek astronomicznych. Inne składniki tych układów wielokrotnych nie posiadają potwierdzonych struktur dyskowych lub dyskopodobnych. Chłodny gaz był badany przy użyciu molekuł DCO^+, N_2H^+ i N_2D^+, które powstają w temperaturach poniżej 20 K i dlatego charakteryzują chłodne obszary. Dla ciepłych obszarów o temperaturach od 50 do 100 K i tych, które są ogrzewane przez promieniowanie UV od centralnej protogwiazdy użyteczne są molekuły $c-C_3H_2$ i C_2H. Molekuły pochodzące z chłodnego gazu są widoczne bliżej źródeł w obu systemach z powodu obecności dysku / struktur dyskopodobnych, ale nie w każdym kierunku. Dla VLA 1623-2417 N_2H^+ i N_2D^+ nie są zaobserwowane, prawdopodob-

nie z powodu niskiej jasności protogwiazdy i bardzo niskich temperatur (poniżej 10 K) spowodowanych ocienieniem materiału przez dysk. Jest to zgodne z wynikami z Rozdziału 3, w którym pokazano, że dysk ma dramatyczne znaczenie na strukturę fizyko-chemiczną protogwiazdy. Ciepła molekuła c$-C_3H_2$ dobrze pokazuje wnęki wypływów molekularnych u obu systemów, co jest zgodne z obecnością tej molekuły w ciepłym i oświetlanym przez promieniowanie UV otoczeniu. Molekuły c$-C_3H_2$ i C_2H czasem pochodzą z tego samego obszaru. Jest to prawdą dla VLA 1623-2417, ale nie dla IRAS 16293-2422. Warto zauważyć, że wielokrotność tych układów nie wydaje się mieć dużego znaczenia na strukturę chemiczną, choć dalsze badania są niezbędne.

W Rozdziale 5 zbadano czy rzeczywiście wszystkie gwiazdy w układach wielokrotnych powstają w tym samym czasie. Aby odpowiedzieć na to pytanie konieczne jest badanie protogwiazd na bardzo wczesnych etapach ewolucji, a nie tych późniejszych. Dzieje się tak dlatego, że warunki powstawania u młodych protogwiazd są praktycznie nienaruszone przez samą gwiazdę, podczas gdy na późniejszych etapach mamy do czynienia z wyewoluowanymi systemami. To jednak powoduje również problemy. Wiek zanurzonych protogwiazd jest praktycznie niemożliwy do określenia. Z drugiej strony etap ewolucyjny protogwiazdy, czyli właściwie jej "wiek", jest określony poprzez rozkład jasności w funkcji długości fali nazywany widmowym rozkładem promieniowania (*ang.* spectral energy distribution, SED). Podczas etapu zanurzonego, jasność protogwiazdy jest największa na długich falach z powodu kokonu pyłowego, w którym ona powstaje. Wraz z ewolucją protogwiazdy, materia wokół protogwiazdy ulega rozproszeniu i jasność protogwiazdy sukcesywnie przesuwa się ku krótszym falom. Gdy gwiazda zaczyna palić wodór w swoim jądrze, to jej jasność przesuwa się do zakresu widzialnego. Dlatego etap ewolucyjny protogwiazdy, w porównaniu do innych składników w układzie wielokrotnym, może być użyty do sprawdzenia czy wszystkie protogwiazdy w danym systemie powstały w tym samym czasie. SED dla wszystkich protogwiazd odkrytych w obłoku molekularnym Perseusza (w odległości 750 lat świetlnych) zostały zrekonstruowane przy użyciu danych literaturowych i fotometrycznych map z Kosmicznego Obserwatorium Herschela. Dla układów wielokrotnych SED poszczególnych składników mogły być rozwikłane przy odległościach pomiędzy protogwiazdami powyżej 1600 jednostek astronomicznych z powodu rozdzielczości Obserwatorium Herschela. Nachylenie protogwiazdy w kierunku linii widzenia może wpływać na wygląd SED, ponieważ protogwiazda widziana wzdłuż wypływu będzie wydawała się starsza niż jest w rzeczywistości, bo otoczka w ogóle może zostać niezauważona. Dlatego, aby wyznaczyć czy protogwiazdy w układach wielokrotnych powstawały jednocześnie czy nie, trzeba wziąc pod uwagę orientację protogwiazd, ich strukturę fizyczną i SED. Wyniki tego badania pokazują, że w jednej trzeciej przypadków składniki układów wielokrotnych nie powstają w tym samym czasie. Innymi słowy, niektóre obłoki molekularne tworzą protogwiazdy nawet długo potym gdy jedna lub dwie już zostały utworzone. Dostarcza to istotnej informacji dla teorii i modeli opisujących powstawanie gwiazd wielokrotnych i tym samym wskazuje na potrzebę zrozumienia czynników przyczyniających się do powstawania kolejnych protogwiazd w układach wielokrotnych.

W Rozdziale 6 badany jest jeden z możliwych czynników wpływających na powstawanie gwiazd wielokrotnych: temperatura. Modele, które obejmują ogrzewanie gazu i pyłu przez centralną protogwiazdę sugerują, że od momentu, w którym protogwiazda zostaje uformowana, podgrzany gaz i pył nie dzieli się już w więcej skupisk. Z kolei, wyniki z Rozdziału 5 pokazują, że są jeszcze inne przyczyny fragmentacji i pow-

stawania układów wielokrotnych gwiazd. Aby stwierdzić, czy istnieje zależność między temperaturą a fragmentacją, są prowadzone badania gazu i pyłu w skali tysięcy jednostek astronomicznych. Obserwacje teleskopem APEX skupiały się na molekułach, które są dobrymi miernikami temperatury, jak DCO^+ i H_2CO, oraz na $c-C_3H_2$ i C_2H, charakteryzujących regiony oświetlane przez protogwiazdę. Obserwacje tych molekuł wykonane zostały dla próbki wyselekcjonowanych systemów protogwiazdowych w obłoku molekularnym Perseusza, zarówno wielokrotne, jak i pojedynczych. Badanie obu typów systemów pozwala na porównanie warunków w pojedynczych i wielokrotnych gwiazdach, co może pomóc w stwierdzeniu, czy temperatura jest kluczowym elementem w tworzeniu się gwiazd wielokrotnych. Obserwacje molekuł i wyznaczone na ich podstawie temperatury gazu nie pokazują jasnej relacji między temperaturą a wielokrotnymi bądź pojedynczymi gwiazdami. Jedyną zaobserwowaną różnicą jest to, że wielokrotne systemy gwiazdowe mają ogromne zasoby chłodnego gazu w porównaniu z pojedynczymi protogwiazdami. To sugeruje, że masa i gęstość, bardziej niż temperatura, odgrywają rolę we fragmentacji, a w konsekwencji w formowaniu wielokrotnych systemów protogwiazdowych.

Wnioski

Wyniki tej pracy pozwalają na dołożenie kolejnych cennych elementów do układanki pod tytułem formowanie się gwiazd wielokrotnych i zostaną tu krótko przytoczone. Ogromne dyski mogą powstawać we wczesnych stadiach rozwoju protogwiazdy i wpływać na fizyko-chemiczną strukturę protogwiazd. Jest to istotne dla całego procesu formowania się gwiazd i zmienia nasze spojrzenie na ewolucję protogwiazd. Ponadto, oba czynniki - dysk oraz struktura fizyko-chemiczna, mogą wpływać na formowanie się systemów wielokrotnych poprzez fragmentacji. Nie wszystkie protogwiazdy w takim systemie tworzą się jednocześnie. To oznacza, że w niektórych przypadkach warunki panujące w gazowym jądrze sprzyjają dalszej fragmentacji. Te warunki nie są jednak związane z temperaturą, choć mogą być z masą i gęstością.

Wyniki te pozwalają wykonać kolejny krok na przód w rozumieniu formowania się systemów wielokrotnych, choć potrzebne są dalsze badania. Na przykład byłoby interesujące dowiedzieć się, czy wyniki uzyskane dla obłoku molekularnego Perseusza mają zastosowanie dla innych regionów powstawania gwiazd. Nasze rozumienie tego procesu musi zostać poszerzone o formowanie gwiazd wielokrotnych, gdyż są najczęstszym sposobem powstawania gwiazd. Modele i teorię należy zrewidować o wyniki obserwacji, co pozwoli na ukierunkowanie naszych dalszych badań.

中文總結

被萬有引力所束縛的，由兩個或更多恆星所組成的恆星系統在宇宙中普遍存在。這些恆星系統誠如光變等特徵，使得它們在古文化中被賦與重要地位。它們同時也是當今學術研究的課題。並且，我們對這些恆星系統的瞭解正循著望遠鏡效能的提升而增長。我們發現這些恆星系統是許多有趣現象的成因，例如超新星與行星狀星雲，以及雙黑洞合併。在科幻小說與科幻片中，恆星系統引發著我們對這些系統中行星的性質，以及一天當中有多次日出的光景的想像。最近的觀測任務，如Kepler mission，證實了行星可存在於這些具有複數恆星的系統。如何形成穩定的複數恆星系統引發了我們的好奇。某些早期的理論提出單一恆星可能牽引另一恆星進入其軌道，進而形成雙星系統。然而，這些理論存在嚴肅的問題，例如需要大量的恆星互相極為近鄰；該機制並需要有第三個恆星的參與。了解恆星們是如何形成的有助解答這些關於複數恆星系統形成的問題。

基於觀測與模型，恆星形成過程的輪廓可如下簡述。在適當情形下，帶有轉動的分子雲中的氣體與塵埃可經由塌縮，形成被包覆於氣體核與分子雲中的原恆星。這些仍被包覆的原恆星驅動著窄而強勁的噴流，可徵顯進行中的恆星形成。圍繞恆星旋轉並墜向恆星的物質被預期終將在恆星形成過程的早期形成一個扁平狀轉盤。而行星與慧星則終在該轉盤中形成。恆星周圍的氣體核物質在原恆星成長與演化的過程中逐漸耗失於恆星的吸積，或被噴流驅散。當所有圍繞的物質耗散之後，留存下來的便僅有年輕的恆星以及若有形成的行星系統。觀測顯示無論在尚被包覆的階段到成為裸露年輕恆星的階段，複數恆星的系統皆為普遍。這指向了大多數恆星皆以複數恆星系統形式形成的事實，使得上述恆星形成的圖像需被修正。

形成複數個恆星的現象掀起了無數針對這些系統的疑問。本論文針對如下關於複數原恆星系統形成以及演化的問題

1. 原恆星盤何時形成，以及它們如何影響原恆星系統？
2. 恆星系統內的恆星是否同時形成？
3. 哪些變因促使或阻礙了複數恆星系統的形成?
4. 單一恆星或是複數恆星系統內的恆星是否具有物理或化學上結構的差異。

第一個問題是有趣的，因為原恆星盤並不僅僅能形成行星與彗星，並可在恆星形成過程的早期對形成複數恆星扮演特定地位。接下來的兩個問題則針對複數恆星形成的機制。破碎化，一個將恆星形成雲氣核拆散的過程，廣泛地被認為是形成複數恆星的主要機制。然而，哪些變因主導了破碎化並使得最終形成複數個恆星，以及這些變因如何影響演化過程，尚未被分明。第四的問題的目的是為了了解若單一及複數恆個星是經由多重或是其它的程序而形成，則這些恆星的結構是否會有所不同。 以探討這些問題為目標的，對於星際分子與塵埃輻射的觀測，結合了物理與化學模型，來描述被觀測原恆星的結構。塵埃的輻射顯跡了原恆星的位置，並可幫助推定原恆星的演化狀

態。分子則作為對觀測的原恆星其動力學，溫度與密度結構，以及化學分佈的重要顯跡物。化學為了解宇宙中發生中的過程有力的工具之一。

論文概要

本論文的第一章提供了對當今對於單一與複數恆星形成的了解的詳細描述。本工作呈現了以地面及太空望遠鏡進行的，由毫米波到近紅外光波段的觀測。位於智利阿塔卡瑪沙漠中Chajnantor高原的阿塔卡瑪大型毫米及次毫米波陣列(Atacama Large Millimeter/submillimeter Array，縮寫作ALMA)被用來對原恆星系統在百天文單位尺度(一天文單位為地球到太陽的距離)的化學與物理結構進行觀測。鄰近ALMA的單天線電波望遠鏡，阿塔卡瑪開拓者實驗(Atacama Pathfinder Experiment，縮寫作APEX)則用以探測原恆星周千天文單位尺度的雲氣核。本工作並利用了文獻中的光學影像，以及赫雪爾太空望遠鏡(Herschel Space Observatory)以及史匹哲太空望遠鏡的數據。

第二章探討原恆星盤何時形成的問題，鑒此觀測了一個名為VLA 1623-2417的，極為年輕且尚被包覆的原恆星。VLA 1623-2417為一個位於蛇夫座 ρ 中心的三原恆星系統，距地約為391光年。這三個原恆星展現了截然不同的特徵，極可能因為它們處於不同的演化階段。塵埃與分子輻射展露了環繞其中名為VLA 1623-2417 A的成員的扁平原恆星盤。藉由簡易模型來研究以$C^{18}O$顯跡的動力學指出了塵埃輻射與分子譜線的確顯跡了一個半徑約為150天文單位的轉盤，為土星軌道半長軸的五倍大。由於VLA 1623-2417 A為一個極為年輕且尚被包覆的原恆星，發現圍繞於該原恆星的轉盤證實了這些結構形成於恆星形成過程中的早期。

據第二章所述，轉盤可在恆星形成過程中的早期形成，因此必定以某種形式影響著原恆星的演化。第三章藉由研究環繞於VLA 1623-2417 A轉盤周圍的物質來探討這個課題。據此目的，我們研究了那些通常發現於原恆星周圍氣體雲核中的低溫物質的分子。因DCO^+分子通常形成於低於絕對溫標20度的環境中，它被用來顯跡位於VLA 1623-2417 A的寒冷物質。結合觀測與簡易化學模型可幫助了解 DCO^+輻射。 被觀測到的DCO^+輻射所發出的位置，比由球對稱密度與溫度結構，亦即原恆星均向地加熱圍繞它的物質的情況下所做的預期，還更接近恆星。相對地， 在延著轉盤盤面的方向， DCO^+輻射在更靠近恆星的位置被測得；而在延著噴流的方向則無此現象。這個現象起因於原恆星盤遮擋了由原恆星所發出的輻射，使得溫度沿原恆星盤內緣至外降低。這明示了原恆星盤的存在對周圍物質的溫度分佈與化學結構具有顯著的影響。

第四章利用可顯跡形成原恆星的氣體雲核中，寒冷與溫暖的物質的各種分子，來對尚被包覆的原恆星的物理暨化學結構做更多的探究。名為IRAS 16293-2422及VLA 1623-2417的兩個複原恆星系統則為探究的目標。這兩個原恆星系統皆位於蛇夫座 ρ 之中，且尚被它們的原生氣體雲核所包覆。相較於在第二章及第三章中探討的，相對昏暗的三原恆星系統VLA 1623-2417 A，IRAS 16293-2422為一光度極高的原恆星雙星系統。對應於第二章中提及VLA 1623-2417 A中被發現轉盤，IRAS 16293-2422展露了巨大且扁平的，半徑約為200天文單位的類似轉盤結構。在這兩個原恆星系統中的其它原恆星則尚未被確認具有類似轉盤的結構。某些在低於絕對溫標20度的環境中形成的分子，如DCO^+, N_2H^+, 及N_2D^+，作為低溫區域的特徵，可顯跡低溫的氣體。如$c-C_3H_2$及C_2H等分子則可作為溫度介於絕對溫標50至100度的溫暖環境，或是受到中心恆星紫外輻射照射的區域，不錯的顯跡物。在這兩個系統中，由於原恆星盤的存在，低溫特徵的分子皆在較為靠近恆星處被測得。在VLA 1623-2417中並未測得 N_2H^+及N_2D^+。最有可能的解釋為原恆星的低光度，以及原恆星盤的遮擋使得物質溫度低於絕對溫標10度。這與第三章中的結果吻合。溫暖特徵分子$c-C_3H_2$在兩個系統中皆追蹤了噴流腔壁，與該分子顯現於溫暖或受紫外線照射的環境的特性吻合。 $c-C_3H_2$與C_2H傾向追蹤同樣的區域。這在VLA 1623-2417為真，在IRAS 16293-

2422則否。有趣的是，多重性似乎並未對這兩個系統的化學結構帶來顯著影像，然而尚待進一步的研究。

第五章檢視了是否複數恆星系統中的恆星為同時生成的問題。 為解答這個問題研究了尚在被包覆階段的原恆星，而非更後期的原恆星演化階段。這是由於尚被包覆的原恆星仍具備完整形成過程的狀態，而更晚期的原恆星則已受到演化過程可觀地影響。然而，這亦存在一個問題。在尚被包覆的階段，幾乎沒有任何的方法能精確推定原恆星的年齡。原恆星的演化階段，或稱它的年齡，可由原恆星的量度隨波長的分佈來推定(spectral energy distribution，縮寫作SED)。在尚被包覆的階段，因原恆星形成處的塵埃包層，原恆星輻射多集中於長波長。當包層隨原恆星的演化耗失，原恆星輻射的量度分佈則漸漸偏移到較短的波長。並且，亮度分佈的峰在點燃氫核反應後將移入可見光波段。據此，一個原恆星相對較於同系統內生成的其它原恆星的演化階段差別，可用來推論是否系統內的原恆星是在同一時間生成。利用文獻中的光學影像以及赫雪爾太空望遠鏡的數據，我建立了在距地約750光年的英仙座分子雲中所有以被辨認出的原恆星系統的 SEDs。受限於赫雪爾太空望遠鏡的角分辨率，在複數原恆星系統中，僅有在個別原恆星皆相距超過1600天文單位以上時，我們才能解析個別原恆星的SED。原恆星相對於視線的朝向亦影響它的SED。延著原恆星噴流的方向觀測原恆星將使得原恆星看起來比實際年齡稍大，因為在該方向缺乏能被探測得的包層。據此，為了辨別原恆星系統內的原恆星是否為同時形成，原恆星的朝向，物理結構，與SED需同時接受考量。本研究的結果發現有三分之一的複數原恆星系統，其中的原恆星並非同時生成。換句話說，某些但並非所有的雲氣何在形成首一二個原恆星後，仍持續地形成新的原恆星。這對關於複數恆星系統形成的理論與模型提供了重要的資訊，並演生出了因何變因使得某些系統持續地形成原恆星的問題。

第六章檢視了可能影響恆星系統形成的變因：溫度。模型若引入原恆星對周圍氣體與塵埃的加熱顯示當一個原恆星形成之後，這些被加熱的氣體與塵埃其分佈在一般情形無法更加破碎化。然而第五章的結果顯示有其它的變因亦影響破碎化的過程以及複數恆星的形成。為了探討溫度與破碎化呈度是否具相關性，我們研究了在1000天文單位尺度的氣體與塵埃。APEX單天線望遠鏡被用來觀測可用來測量溫度的分子，例如 DCO^+與H_2CO，以及可用來探測受恆星輻射照射區域的分子如c$-C_3H_2$與C_2H。在某些選擇於英仙座分子雲中的單一與複數原恆星系統，我們觀測了這些分子。兼具這兩類系統容許我們比較單一與複數原恆星系統中的狀態，有助於解答溫度是否為複數恆星系統形成的重要因子。由觀測的分子導出的溫度測量顯示系統為單一或複數恆星與溫度並無顯著關聯。事實上，觀測發現的唯一差異是複數恆星系統比起單一恆星系桶具備了更大的冷氣體庫。這些發現顯示質量與密度而非溫度，對破碎化以及隨之而來的複數原恆星形成，扮演重要角色。模型與理論需隨觀測做修正，使得利用它們所做的預測能對觀測提出指引。

結論

本論文貢獻數項有用的結果來解答關於複數恆星系統形成的謎題，茲簡要總結於下。大的原恆星盤可能在恆星形成過程中的早期便已形成，並且可能影響原恆星的物理與化學結構。這對恆星形成具普適地重要性，因其改變了我們對原恆星演化過程的圖像。並且，原恆星盤以及物理與化學結構這兩項因子皆可影響破碎化過程，故可影響複數恆星的生成。在一個複數恆星系統中，並非所有的原恆星皆同時生成。這表示在某些系統中，分子雲核具備更適於破碎化的條件。然而，這些條件與溫度並不相關，而更相關於質量與密度。 雖然本論文的結果促成對複數恆星系統的形成的進一步了解，更多的研究仍是必要的。例如，其它的分子雲是否具類似於對於英仙座分子雲的觀測結果是個有趣的課題。由於複數恆星系統為恆星形成過程最普遍的終產品，我們亦必須修正現有對恆星形成過程的了解來引入複數恆星的形成。

Curriculum vitae

I was born in San Jose, Costa Rica, on the 31st of August, 1988. Premature by a month and the youngest of three. My curiosity about travelling, learning and researching came from my dad, Carlos Murillo Zamora, a political scientist who often would inspire me to look at things from a different perspective. My interest in sewing, growing plants and understanding human behaviour and education came from my mom, Rosario Mejías Fernandez, a stay at home mom with an interest in child psychology.

I lived in Costa Rica until almost 5 years old, when my dad was appointed counsel of Costa Rica in Miami, Florida, USA. In 1994 we moved there for 4 years. I attended my last year of kindergarten in Dade County Elementary School. Although I could speak and read (upside down) Spanish, I learned to speak, write and read (right side up) English in 3 months, though I was stuck in ESOL courses for the next three years. Thus, English became, in a way, my first language. Moving house meant new school. Literally. I started in 1995 first grade in the newly built and inaugurated William Lehman Elementary School in Miami. I had wonderful teachers who encouraged and nurtured my curiosity, and love for doing research. Living in Miami, a melting pot of cultures and nationalities, exposed me to different languages, religions, cultures and people. Through my dad's work, I came into contact with diplomats and people involved in politics, humanities and sciences, which taught me how to talk with others and express my points of view. This exposure to people from all walks of life would not stop after leaving Miami, but has continued throughout my life.

In July of 1998, at the age of 9, we moved back to Costa Rica. I had to re-learn Spanish quickly before returning, this lead to many funny situations in school. During my first school summer vacation, while looking for something to do, I rekindled my love for research. I quickly found a deep interest in space, and as many children do, dreamed of becoming an astronaut and announced it to all my family. My dad took me seriously and found the only physics book in the house, Conceptual Physics by Paul Hewitt, turned to the chapter on relativity and handed it to me, suggesting I start there. I set out to read it happily, but understood little. Not being the kind to give up on a challenge, I turned to the first chapter and thus started learning about physics. When I reached concepts in physics I could not understand, I was determined to contact the author to ask him questions. After several attempts to find his contact information, and a call to his brother who owned a coffee farm in Costa Rica, I finally managed to contact Paul Hewitt. He became a mentor to me, encouraging me to learn and pursue studies in science, both in physics and chemistry.

We moved several times in the following years due to my dad's job as a university professor. I finished my final year of elementary school in the Escuela Jose Ezequiel Gonzalez Vindas, in San Pablo, Heredia, Costa Rica. Then went on to secondary

education at the Liceo Lic. Mario Vindas Salazar, or MAVISA for short. Despite the regulated education plan in schools in Costa Rica, I met there many teachers who further nurtured my curiosity and willingness to learn as well as my love for researching topics and presenting them in class. I quickly picked up French, found myself negotiating with teachers to do research in topics for classes rather than hand in boring homework, having discussions on literature, especially Don Quijote, with my Spanish teachers, convincing my math teacher to teach me calculus and discussing history and life with my social studies teacher. In the last two years, I also learned technical drawing and architecture, an interest that has not subsided and only grown with my travels.

During my teenage years, I confronted many health problems, obstacles that stopped me from going about my daily life. This lead me to see a myriad of doctors, specialists in many areas, and the realization I would not ever be allowed in any space program. Fortunately, by this time my interest had developed towards astronomy, understanding stars, galaxies and how all of it formed. My experience with medical specialists made me realize how human and subjective medicine is as a science, how much more there is to learn and the driving force of research. Despite every new obstacle, I was determined to move forward to my goals, one of them being to study abroad.

In my last year of secondary education, I applied for a scholarship to conduct my undergraduate studies in Taiwan. At the time, diplomatic relations between Costa Rica and Taiwan provided scholarships to Costa Rican students to study one year of language and four years of undergraduate studies in Taiwan, in any field of choice. I was granted the scholarship. Weeks before I turned 18 years old, to my dad's excitement and my mom's dismay, I boarded a plane off to another continent, 14 time zones away from home and my first time living alone. I arrived in Taiwan on the 15th of August 2006, mother's day in Costa Rica, at night on a hot and humid summer day that hit me like a wall as I stepped out of the Taoyuan airport in Taiwan. I spent my first year attending language lessons for 2 hours a day, and then roaming the city of Taipei and its county (now New Taipei city), reading as many menus and signs as I could understand. I quickly picked up the language. During this time I met people from all over Asia, exchanging anecdotes of life and culture.

In the summer of 2007, I obtained admission to the department of Physics in National Tsing Hua University, in Hsinchu. I was incredibly excited to finally attend university and study pure physics. Although I did not excel in my exams or grades, I pressed forward to find an opportunity to do research in astronomy, taking as many astronomy courses as possible. Through one of these courses, Observational Astronomy with Prof. Albert Kong, I had the opportunity to visit the optical one-meter telescope on Lulin Observatory, where I quickly found out an astronomer's nights are not always clear. At the end of the semester, there was the TIARA Winter school on star formation in January 2009. Encouraged by Prof. Albert Kong, I applied to attend the workshop and obtained a spot. Despite having an interest in gravitation and black holes, I found the lectures on star formation wonderfully immersive; the memory of Prof. Bo Reipurth presenting the multi-epoch observations of a jet and how it moved is still fresh in my mind. At the end of the workshop, Prof. Paul Ho went up on stage and asked the students for ways to improve astronomy in Taiwan. I raised my hand and stated I wanted more opportunities to get involved in astronomy, his reply was if given those opportunities would I take advantage of them? He offered attendance to his Saturday group meetings in Taipei for those interested. Prof. Shih-

Ping Lai also pointed out she had a weekly group meeting and interested students could attend. For the following semester I attended both meetings. By the summer of 2009, I started doing undergraduate research in Shih-Ping's group, looking at the outflow of NGC1333 IRAS4A. At the end of summer, I gathered all my courage and notes, and went up to Shih-Ping, explaining why I wanted to do research and that I was intent on studying multiple stars. Her reply was that she had some data on this source which had polarization measurements and was maybe a binary. That source turned out to be VLA1623, my new found obsession. I spent 3.5 wonderful years in her group, making long-lasting colleagues and friends.

During my first year of master studies, I took the opportunity to apply to Prof. Ewine van Dishoeck's PhD position in her astrochemistry group in Leiden University. After being rejected from three PhD programs in the USA, I did not expect to be considered for a spot in Leiden Observatory. To my great surprise, I was short listed and invited to an interview in the Netherlands. My first time to Europe. During the presentations and interviews, I was so nervous, seeing many others with research projects that to me seemed more advanced than mine. I enjoyed my visit to Leiden, but feared not obtaining a position thinking there were others more qualified than me. A couple of days after returning to Taiwan, Ewine offered me two positions, one part in MPE (Garching bei Munich, Germany) and part in Leiden, and the other in Leiden. I must have bounced off the walls from excitement. I waited until the weekend passed so I could tell Shih-Ping about it and then reply to Ewine with a most definite yes, and of course, a list of reasons why I would choose the MPE/Leiden position. Of course, Shih-Ping noted that now I had half a year to finish my master thesis.

After graduating from masters, I stayed in Taiwan for half a year to finish a project with Shih-Ping. On December 1st, 2012, I left Taiwan after 6.5 years of living there. I hopped on over to Costa Rica, to meet for the first time my nieces and nephew for Christmas, and then move to Europe. I arrived in Munich, Germany, on January 13th, 2013. I spent 3 years at MPE. During my time there, I met my wonderful Christian, who was doing his masters in computer science and on-board satellite computers. Afterwards, we moved together to the Netherlands for my last year of PhD, which turned to year and a half, and Christian started his PhD here in Leiden, continuing his work on dependability of satellite on-board computers.

My path continues onward with a post-doctoral position working on JWST with Ewine.

Acknowledgments

Many people have contributed to the years of work compressed in this thesis.

Simon, Agata and Davide, you made the time at MPE all the more enjoyable, and meeting you was wonderful. Simon, I am grateful to you for teaching me so much about modelling and physical processes in astronomy, discussions with you were always illuminating. Agata, conversations with you on science, Herschel and life are not to be forgotten, and I greatly enjoy every time we meet up; and I really appreciate your translation to polish of the summary. Davide, thank you for all the times we sat together to work with photometric maps, all the conversations in spanish or english, and Florence (as you once said, ah all the food, the food!). Thomas, Stefano and Paolo, although our time at MPE did not overlap for long, it was nice to share a building with you, and the conversations, either there or wherever we meet up, are always interesting.

My time spent at Leiden, whether short or long, was always well spent with everyone there. Daniel, ah Daniel, there is so much to thank you for, so I'll leave it at that, thank you for everything. I hope to continue poking you in person for the next 2.3 years. Catherine, I greatly appreciate all your help with chemistry and chemical modelling, you helped me greatly to become an astrochemist. Conversations with you, on any topic, are never dull. John, you are such a great colleague and officemate, talking about multiplicity, embedded stars and radio observations is always very useful, bothering Magnus made the days more fun. Magnus, you too were a wonderful officemate and Thirstday host, conversations on chemistry and embedded protostars were always interesting, sorry we bothered you so much (and still do, yes I know you do not listen to ABBA). Mihaela, fue un gusto conocerla. Merel, Sierk and Arthur, it is always enlightening to talk about science, music, sci-fi and fantasy, whatever comes up, and dutch culture. Arthur, thank you for your help in translating the summary of this thesis to dutch. Niels, it is always neat to have long conversations with you. Kenji, you were an awesome officemate in every way, and I agree, if you didn't bring your laptop to the office then its time to go home. I truly appreciate your translation of the thesis summary to Japanese. 可儒跟你說話很好玩，你的牛肉麵好好吃！ Łukasz and your outflows, please never stop asking where the outflows are, we need more people like you in conferences. Maria, you are awesome to work with and talk, thank you. Vianney, remerci de votre aide en chemie; practiquer l'espagnole avec vous c'est sympa, j'espere la prochaine fois je peut practiquer mon terrible française avec vous. Mihkel, I appreciated our conversations on methanol and Estonia. We should repeat dinner next time we meet, like the time in Garching. Joe, always great to sit and talk with you and Kirsty, and I am thankful for the help with Herschel data. Christian, it is nice to talk about life, travel and all sorts of things. Paola, las tardes buscando

galletas y chocolates para picar no son lo mismo sin ud. Alan, you have the most epic random unexpected conversation topics. Alvaro and Eleonora, it is awesome to share an office, but we should have more cookies.

Outside of Leiden, I have had many wonderful people help me along the way. Paul Hewitt, your mentoring and constant encouragement to seek more insight into physical concepts have stuck with me throughout all my studies. Now I can finally give you my book and with my own drawings! Paul Ho, thank you for challenging me to take advantage of opportunities, I hope I demonstrated that if given the chance, I will take it and use it to the fullest. Jeremy Lim, Saturday meetings in Taipei were always so interesting when you were leading them. Albert, learning about galaxies and optical observations was fun, though I'm still not sure what I would have seen by observing a black hole in optical. Maasaki, you are always fun and insightful, thank you for the many times you took us out in Tokyo.

謝天皓，慶道沖，洪肇伶, 王嘉瑋，林聖鈞，宋仁翔，李曉峰，許立承，段皓元我們一起過的時間我不會忘記了。你們都是好同學和朋友。非常謝謝你們。 謝天皓，跟你在705過夜，一起寫paper 還有參加開會是很好玩。謝謝你教我好多，但你教我的台語我都忘記了，ㄆㄢㄙㄟ。希望我們可以繼續合作。 慶道沖謝謝你教我怎麼reduce data和跟我討論原恆星的磁場。 洪肇伶，你讓705很熱鬧。 王嘉瑋，林聖鈞，宋仁翔，李曉峰，許立承，段皓元，你們好好玩，我還記得你們的故事。 Baobab， 謝謝你幫我翻譯總結。每次跟你聊天都很有趣，但我還是不了解為什麼那次你和道沖想賣我。。。 若亞呀呀 你好可愛喔！ 你和lasai讓大學年非常有趣。 謝謝你帶我去看宜蘭，還有因為你叫了我哪裡呀～

嘎幾嘎幾 嚴子晴～～ 已經十年了！ 其實沒有十年的感覺。非常謝謝你。從以開始你有幫我，不關什麼事。大學，研究所，小七，摩斯，晃晃, 坐在你家附近的鞦韆講髓便的喝珍珠奶茶吃雞排，不關做什麼 跟你過時間都很好玩。 謝謝你帶我去聽音樂會和讓我聽你拉小提琴彈鋼琴。為了你教我怎麼欣賞音樂，關淤臺灣的文化和語，還有跟我討論物理，你給我一個不一樣的想法。 也要謝謝台中中，你好好玩喔！

Christian, mijn süsser fuchs, danke dir für alles. Your company, encouragement and support throughout the years of my PhD have been wonderful and what has gotten me through many ups and downs. Bouncing off ideas with you has always been something I look forward to. Thank you for teaching me so much about computers, security and programming, for giving me a different perspective of the world, history and politics, and for letting me learn about space from your perspective. It makes me happy to think there is a bit of you in this thesis too, both as a collaborator and in the translation of the summary.

A pa y mama ositos, muchisimas gracias por todo su apoyo, tiempo y ayuda atraves del camino y los años. Hablar, aunque fuese un ratito o toda una noche, con uds ha ayudado tanto y de muchas maneras. Siempre tengo presente lo que todo el tiempo me decian: luchar para lograr mis metas y mejorarme cada dia sin pasarle por encima de otros. Y finalmente puedo poner un libro mio a la par de los suyos, pa. Tia Sara, aunque no llego a verme graduada y no siempre entendio lo que estaba estudiando, su apoyo en todo sentido fue constante y muy apreciado. A Don Diego, le agradezco tanto la oportunidad que ayudo a darme, me he esforzado para aprovecharla al maximo. A Gera, vago, siempre un gran amigo aunque nos hayamos reunido pocas veces en los ultimos años. Las conversaciones en sicologia y sociedad, y aveces ciencias, mezcladas con algunas locuras siempre son divertidas. Sip, siempre habran galletas.

There are so many people involved in doing this work. Inevitably, names will slip my mind and I may forget to mention someone. I apologize to those, and thank you.